Prediction of low-velocity/low-energy impact damage in the latest generation of carbon-epoxy laminated composites

Salim Chaibi

Université Fédérale Toulouse Midi-Pyrénées

THÈSE

ICA ONERA THE FRENCH AEROSPACE LAB

En vue de l'obtention du

DOCTORAT DE L'UNIVERSITÉ DE TOULOUSE

Délivré par : *l'Institut Supérieur de l'Aéronautique et de l'Espace (ISAE SUPAERO)*

Soutenance prévue le *16/09/2022* **par :**

Salim CHAIBI

Prévision des endommagements induits par un impact basse vitesse/basse énergie au sein de matériaux composites stratifiés carbone-epoxy de dernière génération

---

JURY

Rodrigue DESMORAT	Professeur à l'ENS Paris-Saclay	Rapporteur
Peter DAVIES	Ingénieur de Recherche HDR à l'IFREMER	Rapporteur
Carlos DÁVILA	Senior scientist at NASA Langley Research Center	Examinateur
Emmanuelle ABISSET	Professeure aux Arts et Métiers ParisTech	Examinatrice
Zoheir ABOURA	Professeur à l'UTC Compiègne	Examinateur
Jérémy BLEYER	Chercheur au laboratoire Navier (ENPC)	Examinateur
Christophe BOUVET	Professeur à l'ISAE SUPAERO	Directeur de thèse
Johann RANNOU	Ingénieur de recherche à l'ONERA	Encadrant
Fabrice CONGOURDEAU	Ingénieur de recherche DASSAULT Aviation	Invité
Frédéric LAURIN	Ingénieur de recherche HDR à l'ONERA	Invité
Julien BERTHE	Ingénieur de recherche à l'ONERA	Invité

École doctorale et spécialité :

MEGEP : Génie mécanique, mécanique des matériaux

Unités de Recherche :

Institut Clément Ader & ONERA

Remerciements

Ce manuscrit est l'œuvre de travaux de recherche menés pendant 3 années et 9 mois. Cette durée marque un épisode particulièrement important de ma vie. Le cheminement vers une maitrise scientifique de mon sujet s'est accompagné d'un travail sur moi sur le plan psychologique, éthique, humain. Durant cette thèse, j'ai développé une certaine humilité face à la grandeur de la science... Ces quelques mots à connotation philosophique laissent place aux remerciements sous-jacents.

Une thèse n'est jamais l'œuvre d'un loup solitaire, au contraire, elle est le fruit d'une collaboration avec de nombreuses "figures de l'ombre". En tout premier lieu, je souhaite témoigner ma profonde gratitude à mes encadrants. Un encadrement riche et d'une qualité indéniable. Ainsi, je souhaite remercier Christophe mon directeur de thèse, merci pour sa disponibilité (640 km nous separait), son expertise, ses conseils et son pragmatisme. Aussi, je souhaite exprimer mes remerciements à l'égard de mes encadrants à l'ONERA (Frédéric Laurin, Johann Rannou et Julien Berthe), notre proximité géographique nous a permis d'interagir régulièrement, de partager des moments de convivialité résultant d'une amitié qui s'est esquissée au fil de l'eau. À mon encadrement, sachez que vos lettres de $\mathcal{NOBLESSE}$ sont aposées sur ce manuscrit.

Je tiens à exprimer ma reconnaissance aux membres du jury d'avoir accepté d'évaluer mes travaux scientifiques. Plus particulièrement, je souhaite remercier messieurs Peter Davies et Rodrigue Desmorat en leur qualité de rapporteur et ce, durant la période de congé estivale. Enfin, merci à Carlos Davilà d'avoir fait le déplacement des USA pour ma soutenance.

Ma thèse a été réalisée dans le cadre d'un partenariat avec un acteur industriel de renom (Dassault Aviation). L'encadrement industriel mené principalement par Fabrice Congourdeau s'est montré complémentaire de l'encadrement académique. Les échanges réguliers avec l'équipe R&D de Dassault Aviation m'ont permis de me familiariser avec les problématiques industrielles autour de la tenue des structures composites d'aéronefs. Ainsi, je souhaite témoigner ma gratitude à l'égard de Fabrice Congourdeau, Dominique Martini, Vincent Jacques et Ldjoudi Manseri pour les interactions, les échanges et le suivi de ma thèse.

De nombreuses discussions avec les experts du département matériaux de l'ONERA ont été effectuées, des thématiques différentes de celles de l'impact ont été abordées, ce qui a contribué à mon enrichissement sur le plan scientifique. Ainsi, je souhaite remercier toute l'équipe MC^2, EPIC, CRD. J'exprime ma reconnaissance particulière envers Pascal Paulmier, Anne Mavel, Gérald Portemont et Julien Berthe pour les différents essais réalisés durant ma thèse. Nous avons fortement interagis durant les campagnes expérimentales. Vous avez fait preuve de pédagogies ce qui a contribué à mon éveil vers les sciences expérimentales. Si aujourd'hui les résultats présentés dans ce manuscrit sont de qualité c'est en partie grâce à vous. Aux doctorants de l'ICA et de l'ONERA (principalement MC^2), de véritables liens familiaux se sont tissés à travers nos afterworks, nos sorties run et kebab. Je tiens principalement à remercier Matthieu pour son aide sur LaTeX, Arthur pour son approvisionnement en confiseries et cocas durant la rédaction (généralement minuit passé), Ludo pour les aprem biblio, sorties kebab, foot, DJ, Jérémy Germain le frère aîné Marcos I et ancien co-bureau, et enfin Clément pour les nombreux échanges sur la culture, notre patrimoine français. Je ne puis malheureusement citer tous les autres doctorants, cependant sachez que je vous porte tous dans mon cœur.

Enfin... je n'aurai pas pu réaliser cette thèse sans le soutien inconditionnel et infaillible de ma famille. Le fait de revenir à Avignon quasiment chaque week-end rechargeait cette motivation pour déplacer n'importe quelle difficulté, fusse t-elle aussi lourde qu'une montagne. À ma mère et mon père qui ont traversé la méditerranée pour offrir un avenir à leurs progénitures. À leurs

sacrifices pour que je puisse recevoir une éducation de qualité et espérer avoir mon ticket d'or dans l'ascenseur social. À mon frère Achraf mon colocataire au Crous. Nous avons connu la galère depuis Marseille, mais il est temps de prendre notre revanche sur la vie ! À ma sœur Imane, elle aussi qui a tant sacrifié pour ses études et qui m'a précédée pour l'obtention de son grade de docteur. Tu as pu m'aider financièrement lorsque j'étais hors contrat pour terminer ma thèse, je t'en serai reconnaissant pour toujours. Et à mes deux dernières petites sœurs, l'innocence de vos âges m'ont permis de continuer à faire vivre cet enfant caché en moi.

Salim...

Contents

List of Tables

List of Figures

Acronyms

AIRT Active infrared thermography. vii, 17, 18, 24

BVID Barely visible impact damage. 8, 12

CAI Compression after impact. vii, ix, 4, 12, 14, 33, 57, 59, 60, 61, 62, 197

CDM Continuum damage model. 43, 46, 47, 48, 49, 53, 54, 137

CFRP Carbon Fibre Reinforced Polymers. viii, 1, 27

CT Computed tomography. ix, 74, 75, 78, 79, 83, 85

CT Compact tension. 43

CZM Cohesive zone model. viii, 39, 40, 41, 47, 132, 137

DI Destructive inspection. 16, 74, 75

DIC Digital image correlation. viii, ix, 26, 27, 57, 59, 61, 96

DPM Discrete ply model. viii, ix, 35, 42, 49, 61, 121, 134

DT Destructive technique. iii, 24, 63, 74, 75

FE Finite element. 46, 56, 122

FEA Finite element analysis. 15, 33, 57, 60

FEM Finite element modeling. viii, 34, 35, 36, 37, 43, 48, 62, 65, 122

FQ Frequency. 97

FS Frame size. 96

IR Infrared. viii, 26, 27, 33, 61

IRC Infrared cameras. 95

IRT Infrared thermography. 17, 26, 57, 59

LE/LV Low energy/Low velocity. viii, 5, 8, 15, 16, 24, 25, 26, 27, 31, 32, 33, 34, 35, 36, 39, 56, 57, 60, 64, 67, 73, 89, 113, 202

NDI Non-destructive inspection. 16, 17, 24, 25, 74, 75

NDT Non-destructive technique. iii, 18, 24, 63, 74, 75

OPFM ONERA Progressive Failure Model. 121, 122

QSI Quasi-static indentation. viii, 25, 42, 62, 96, 111

ROI Region of interest. 17

SEM Scanning electron microscope. viii, 17, 29, 46, 77, 85

SS Shutter speed. 97

TF Thermodynamic force. 129

UD Unidirectional. vii, ix, 1, 2, 28, 29, 32, 44, 45, 63, 64

UI Ultrasonic inspection. ix, 11, 77, 78, 83

UL Ultimate loading. 2, 8, 62

US Ultrasonic scans. viii, 13, 18, 19, 25

UT Ultrasonic testing. vii, 18, 19, 20, 21, 24, 74, 75, 88

VC Visible cameras. 95

Introduction

Global context in aircraft engineering

The aeronautical industry is marked by profound transformation due to global warming. Aerial transportation has to reduce its CO_2 emissions. To do so, aircraft manufacturers get a few leverages to play on:

- Adopting new kinds of power engines;
- Reducing the weight of structures significantly.

It involves a new design of the aircraft architecture with new component designs. The development of high-performance materials such as composite materials has enabled weight savings. Thus, composite materials are naturally an alternative to metallic materials. For the next generation of civil aircraft (Falcon 10X for instance), DASSAULT Aviation have introduced composite materials for the wings.

Laminated composite materials

Composite materials are heterogeneous materials composed of different constituents. CFRP is a family of composite materials where carbon fibers are embedded together using a resin to increase the stiffness and strength in one direction ([Berthelot, 1999]).

Different carbon fibres exist depending on the desired mechanical performances. For instance, if the need is stiffness, there are different categories of fibres (from low elastic modulus "LM" to ultra-high elastic modulus "UHM"). Moreover, the mass per unit area (g/m^2) and the strand size (10 K for 10 000 fibres in one strand) determine the thickness of the ply (the higher the strand and mass per unit area, the thicker the carbon fibre ply).

The resin is chosen to obtain a solid chemico-physical adhesion with fibres. There are actually two families of resins (thermoplastic and thermoset). Today in aeronautics, the most used are thermoset epoxy resins, especially a toughened epoxy resin reinforced with thermoplastic particles to increase the damage resistance. Nevertheless, the trend is shifting toward thermoplastic resins (PEEK, PEKK...) thanks to numerous advantages (recycling possibility, structural repairs, better impact resistance...).

A UD prepreg is a ply constituted by fibres oriented in the same direction and impregnated by a resin (ready to be cured). In the following, we will consider only UD plies with the material frame (1, 2, 3), where 1 is the longitudinal direction parallel to the fibres, 2 is the transverse direction perpendicular to the fibres, and 3 is the normal direction perpendicular to the plane 1-2. FIGURE 1 presents the UD

ply with its material frame. A global frame (x, y, z) is defined for the composite laminate, by stacking in the z-axis UD plies of different orientations, a laminate can be obtained. Composite laminates are designed according to the loading directions. For example, if the loading direction is parallel to the x-axis, fibres are oriented in that direction to sustain load, the resin ensures the loading transfer between fibres.

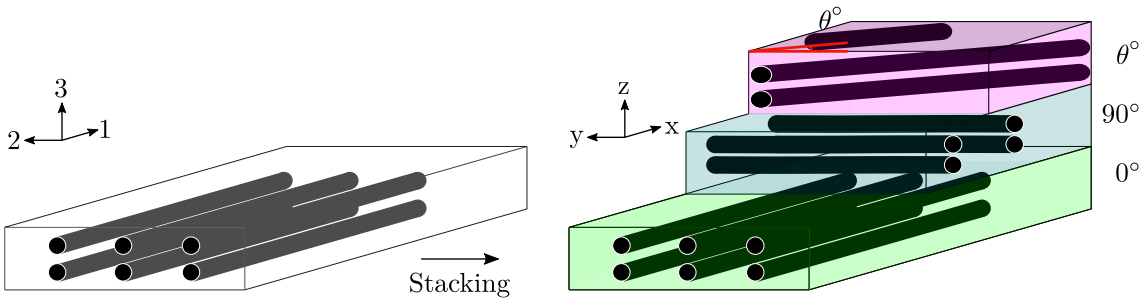

Unidirectional ply Composite laminate

Figure 1: UD ply and composite laminate

Certification of a composite structure

To certificate primary structures in aeronautics, the aircraft manufacturers have to demonstrate that the structure is compliant and can sustain Ultimate loading (UL) (UL is the limit load multiplied by a safety factor of 1.5. Damage is allowed and any component of the structure must withstand the UL without a catastrophic failure). This is currently a technological challenge as the mechanical behavior of composite materials is quite different from metallic materials, resulting in different certification rules for composite structures. As a matter of fact, with the advent of composite fuselage structure, the approach used to design with conventional approaches, such as aluminum aircraft structures, may no longer be sufficient to substantiate the same level of safety for the passengers. According to the FAA "*The structural static strength substantiation of a composite design should consider all critical load cases and associated failure modes*"[Hempe, 2010].

Actual limitations encountered for primary structure substantiation

The strength of the composite structures is demonstrated using important experimental campaigns occurring at different scales, starting from simple coupons to sub-structures or even primary structures. It requires performing numerous and expensive tests as composite structures are strongly dependent on structural design parameters (stacking sequence, laminate thickness, the geometry of the components...). This methodology is called the "building block approach" by industrials and is presented in FIGURE 2. At the coupon scales, numerous tests are performed to understand the material behavior. The structural effect and response are studied and analyzed when the scale is larger. Larger scales imply costly experimental testing.

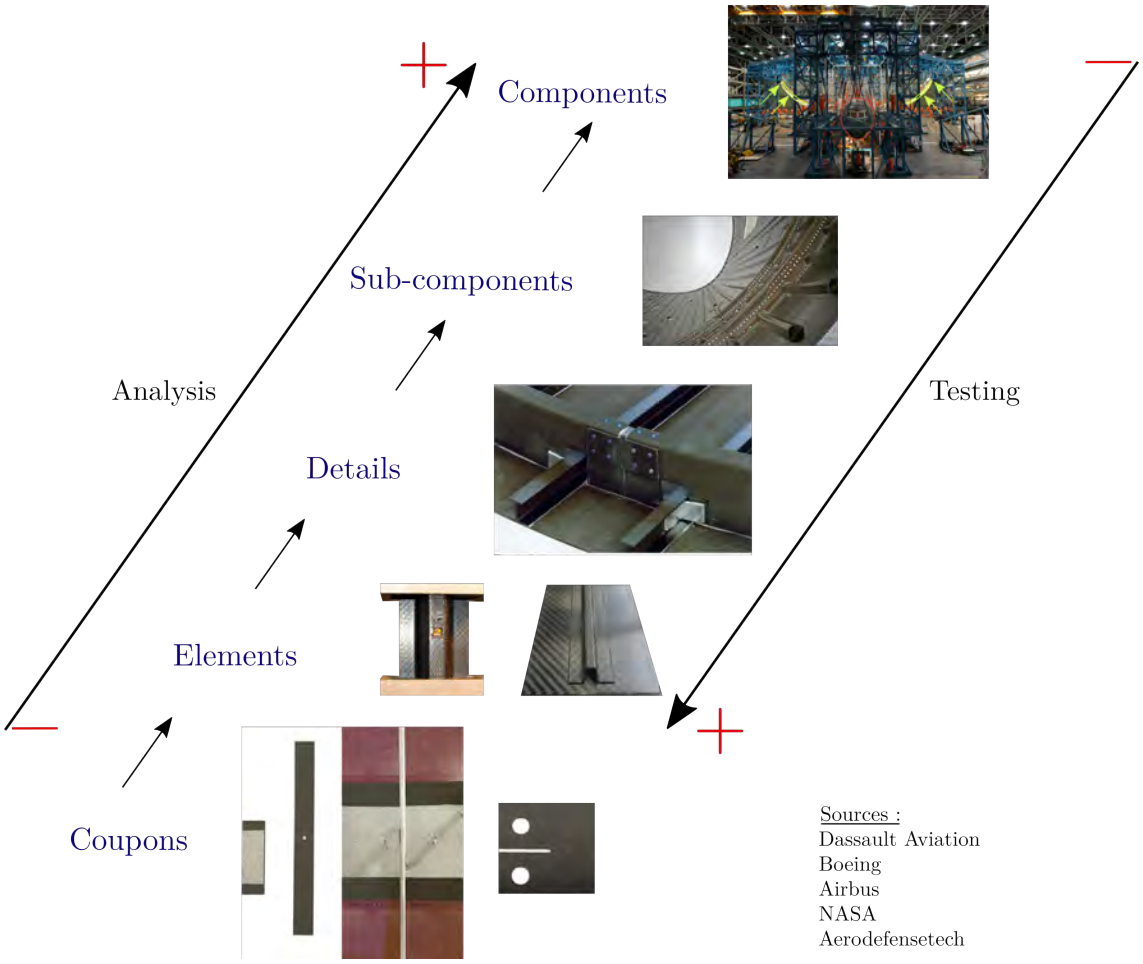

Figure 2: Building block approach for composite structures

MARCOS project

Industrial context

The failure of composite structures is preceded by complex mechanical degradation occurring in the material. The degradation of composite structures is highly dependent on the design parameters. Therefore, lengthy and costly experimental campaigns are performed by aircraft manufacturers to establish the sizing criteria based on the different design parameters. Moreover, these sizing criteria are available for a designated configuration; therefore, no extrapolation could be performed. Thus, the sizing criteria of composite structures introduce important safety margins that reduce the high-performance potential of such material.

For all these reasons, DASSAULT Aviation has wanted to collaborate with academic laboratories to evaluate more academic methodologies and compare them with industrial approaches. Thus, DASSAULT Aviation is associated with ONERA and ENPC in a 36-monthly project called MARCOS (Advanced failure of the failure of laminated composites).

Project challenges

The main challenge is to model the damage mechanisms in the sizing of the composite structures. Consequently, the introduction of numerical modeling will allow:

- The extrapolation of the untested configurations using simulations;
- To optimize the experimental test campaigns needed for the development of sizing criteria;
- To evaluate the design parameters, the uncertainties, and the effect of damages on composite structures.

Industrial and scientific objectives of the MARCOS project

Two objectives are defined:

- The first one is the simulation of the failure of laminated composite materials by modeling the damage initiation and propagation induced by an out-of-plane static or dynamic load;
- The second one is to enhance the CAI criterion using advanced modeling of the behavior of composite structures.

The first objective is linked to a scientific thematic, where an experimental study of the failure of composite laminates under out-of-plane load is performed. The second objective is the application of the academic analysis regarding the industrial need for composite structural sizing.

Thesis framework

The thesis is centered around an experimental and numerical study of impact damages. Four main parts have been defined to support the reader toward the actual problems of impact damages in composite laminates.

State-of-the-art of impact damages induced by low-energy/low-velocity on laminated composite materials

This chapter introduces the methodologies used by industrials and academics to deal with impact damages. Four sections have been defined. The first one brings forward the industrial procedure for the damage tolerance certification. The second and the third sections describe the experimental and numerical studies performed by academics to investigate the impact damages. The last section briefly provides information on the CAI residual strength estimation using experimental and numerical studies. The objective of this chapter is to establish the current limitations for impact damage predictions.

Investigation of impact damages using classical inspection methods

The experimental characterization of impact damages induced by a low-energy/low-velocity impact is performed on last-generation composite laminates reinforced with particles to improve the delamination resistance. Impact tests have been carried out for two stacking sequences and different impact energies (6.5–35 J) to investigate this specific material in the context of a tool drop. Different post mortem investigations have been considered to identify the mechanisms encountered in such material.

Experimental configuration for *in situ* monitoring of a LE/LV impact on composite material

This chapter aims to complete the previously established damage assessment and determine the chronology of the different damage mechanisms. Impact tests have been carried out with *in situ* damage monitoring. The instrumentation of the experimental setup has been enriched using high-speed infrared and visible cameras. Additionally, a comparison between quasi-static indentations and impacts has been performed to evaluate the sensitivity to strain rate effect and to reconstruct the damage scenario using quasi-static indentation.

Material degradation modeling and FE simulation of impact damages

This chapter is dedicated to the modeling of each damage mechanism based on the experimental investigations. Besides, two damage models with two different philosophies are presented (ONERA Progressive Failure Model) and DPM (Discrete ply models). Simulations of LE/LV impacts are carried out using FEA to evaluate the predictive capabilities of both models.

Chapter 1

State of the art of low velocity impact damages on laminated composite materials

Contents

1.1 Certification of a composite aircraft structure

1.1.1 Damage tolerance of composite structures

During the life cycle of an aircraft, impact threats are likely to occur, as shown in FIGURE 1.1. These threats can happen on the ground (runway debris, tool drop during maintenance operations) or during the flight (hail strike, bird strike ...) and can lead to a loss of functionality of the composite structure. While composite laminates are highly sensitive to impact, establishing general standards for damage tolerance evaluation is still challenging for composite structures, "*there are currently very few industry standards that outline the critical damage threats for particular composite structural applications with enough detail to establish the necessary design criteria or test and analysis protocol for complete damage tolerance evaluation*" [Hempe, 2010].

Therefore, regulation authorities rely on industrial expertise to bring substantiation. Aircraft manufacturers perform important experimental campaigns to demonstrate safety to regulation authorities as presented in FIGURE 1.2. Different impact tests on representative structures from coupons to large structures are carried out. The impact tests must consider different impact energies and impactor shapes (blunt or sharp) in order to "*cause the most critical and least detectable damage, according to the load condition (compression, shear ...)*". All of these impacts should be representative of impact threats occurring in service (vehicle collision, tool drops, ground debris...). It allows development of design criteria, inspection methods, and time intervals for maintenance inspections.

Regulation authorities have released five categories of damage as shown in FIGURE 1.3. These categories help aircraft manufacturers classify damages as a function of their severity. In this work, we will focus only on damage mechanisms caused by LE/LV impact. These impacts may occur during manufacturing or inspection with a dropped tool on the composite structure for instance. The impact damages generated at the outcome of a LE/LV impact are included in the category 1. It is interesting to notice that the category 1 excludes the need for repair when the damage remains under the Barely visible impact damage (BVID), which is the minimum impact damage surely detectable by scheduled inspection.

Indeed, after a LE/LV impact, the residual strength may not compromise the UL. The manufacturers have to prove that the residual strength of composite structures after a LE/LV impact may not affect the UL using a dedicated substantiation for this category.

1.1.2 Substantiation of category 1 impact damage for composite laminate structures

Two standards are currently available for composite coupons of 150×100 mm in order to measure the damage resistance after a drop-weight impact [AST, 2007b] and to measure the compressive residual strength [AST, 2007a] of composite laminates.

Impact damages resistance In the standard [AST, 2007b], a tool drop impact machine must be considered. A 16 mm diameter impactor is advised with a dropped mass of 5.5 kg. Concerning the boundary conditions, a composite plate of 150×100

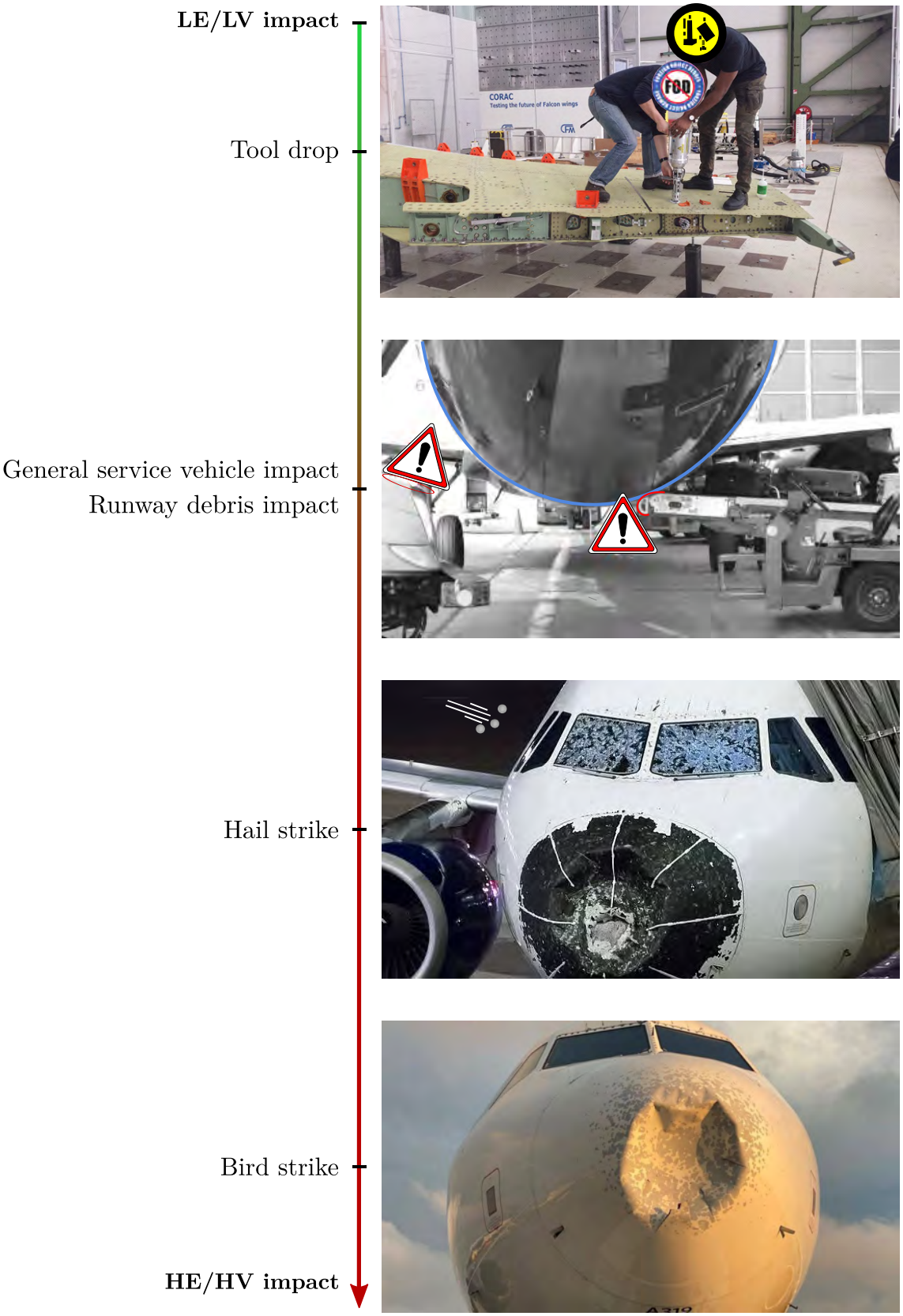

Figure 1.1: Impact threats occurring in aeronautics

mm is supported on an impact window of 125 × 75 mm. Four clamps restrain the plate during the impact. It is mentioned that "*the clamps shall have a minimum*

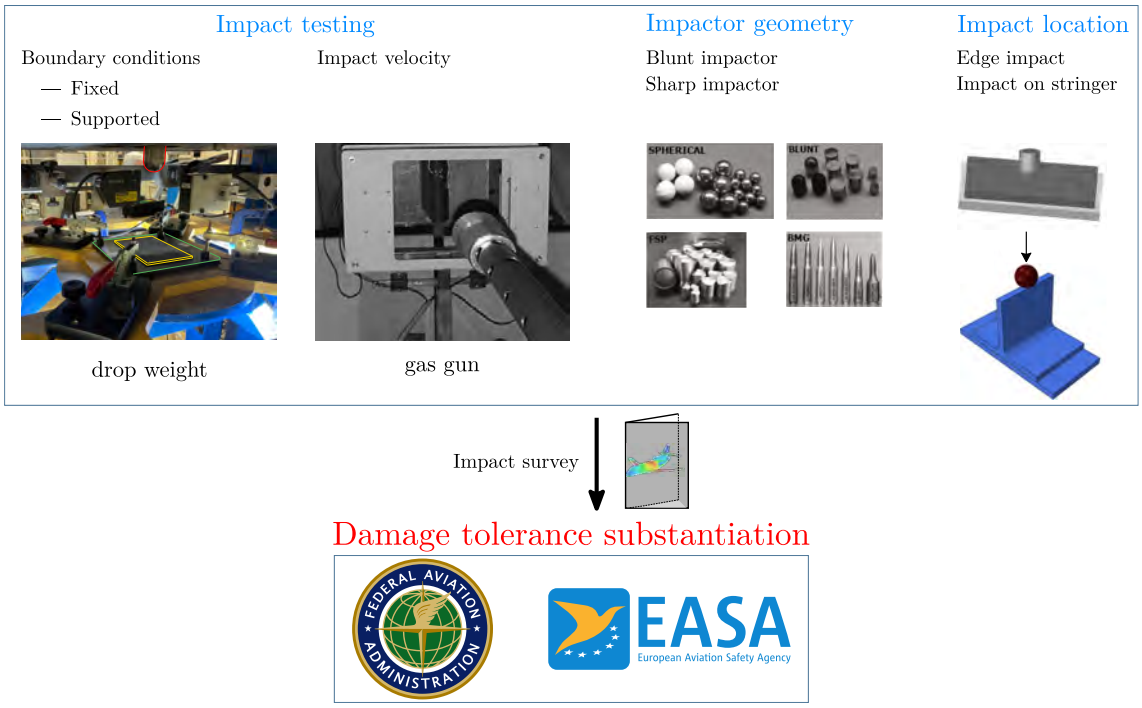

Figure 1.2: Variety of impact experimental configurations for impact survey establishment

holding capacity of 1100 N*, and the clamp tips shall be made of neoprene rubber*". The experimental setup is shown in FIGURE 1.4. Very few interests regarding the instrumentation are considered in the standard. Indeed, only two sensors are required, a cell load to measure the impact load during the impact event and a photo-diode sensor to measure the impact velocity. The information provided by these two sensors allows the computation of the impactor displacement and the dissipated energy due to impact in the composite plate.
The displacement $\delta(t)$ is calculated thanks to EQUATION (1.1)

$$\delta(t) = \delta_0 + v_0 t + \frac{gt^2}{2} - \int_0^t \left(\int_0^t \frac{F(t)}{m} \, \mathrm{d}t \right) \mathrm{d}t \tag{1.1}$$

where δ_0 is the displacement of the impactor at time $t = 0$ in mm, $F(t)$ is the measured impactor contact force at time t in N, m is the mass of the impactor in kg, g is the acceleration due to gravity ($9.81\,\mathrm{m\,s^{-2}}$) and v_0 is the velocity calculated just before impact in $\mathrm{m\,s^{-1}}$.
The impact energy is calculated according to EQUATION (1.2):

$$E = mgH \tag{1.2}$$

where H is the height. The energy dissipated by the composite material due to damage and due to dissipative mechanisms such as friction is calculated using EQUATION (1.3)

$$E_{\text{dissipated}} = \frac{1}{2} m(v_0^2 - v(t)^2) + mg\delta(t) \tag{1.3}$$

where $v(t)$ is the velocity calculated using the integral of the acceleration in $\mathrm{m\,s^{-1}}$

After the impact event, the physical response of the material can be determined using the load-displacement curve or load-time curves. These curves can provide

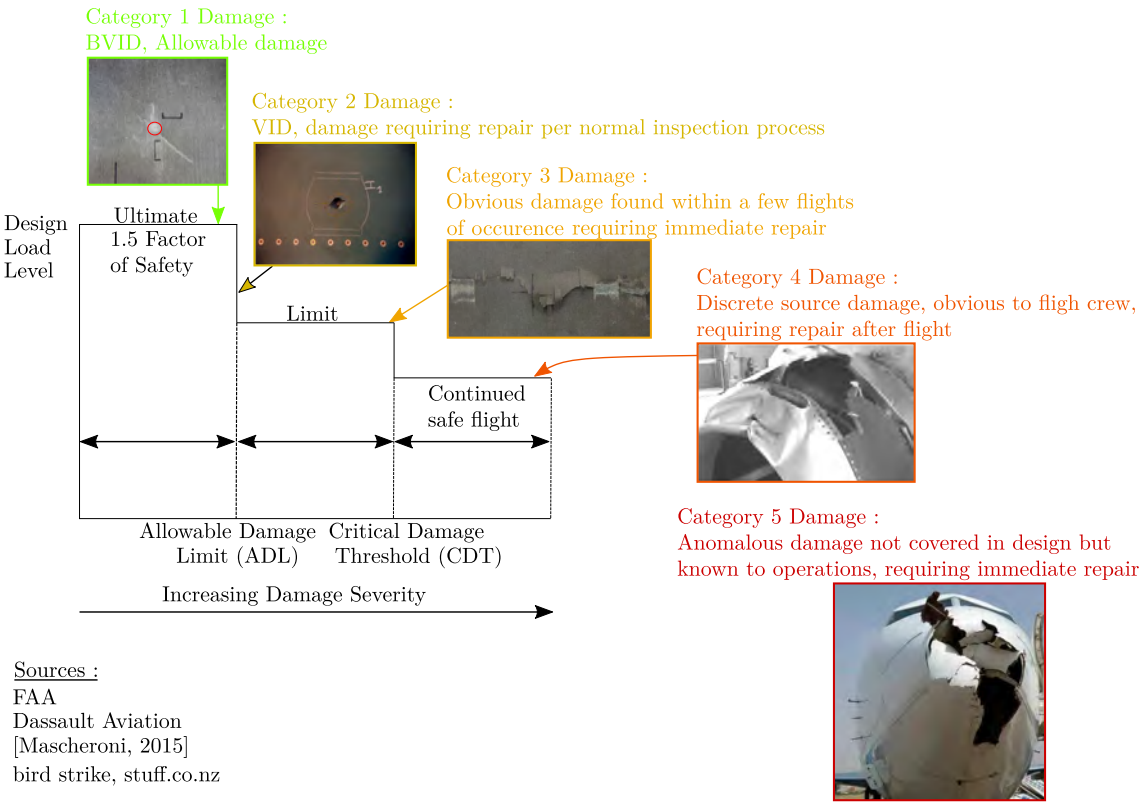

Figure 1.3: Classification of the different damage categories

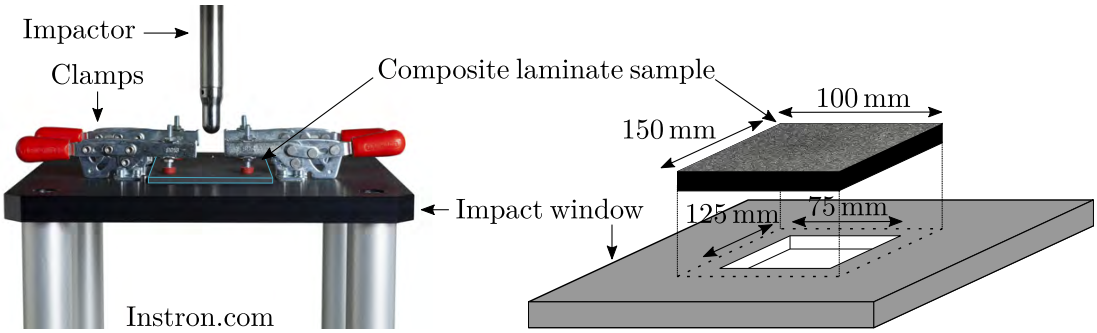

Figure 1.4: Impact configuration according to the standard

global information such as the energy dissipated by the material after the impact (damages and residual elastic energy stored in the laminate), the maximal load peak, the contact duration, and the out-of-plane displacement, as shown in FIGURE 1.5. This information is not enough from design criteria. Indeed, more data is needed concerning the state of damages in the laminate (type of damage mechanisms, damage projected area, distribution through the thickness).
Therefore, industrials perform the inspection using non-destructive solutions such as UI. As it can be observed in FIGURE 1.6, UI are classically performed using a 5 MHz mono-element probe. The probe and the damaged plate are immersed in water. After inspection, the potential damaged area is highlighted, and the projected damaged area is determined. This damaged area is then used to build design criteria. The criteria are defined using large experimental data results with charts, where each projected damaged area gets its residual strength in compression.

Another useful measured quantity considered in the impact test is the residual

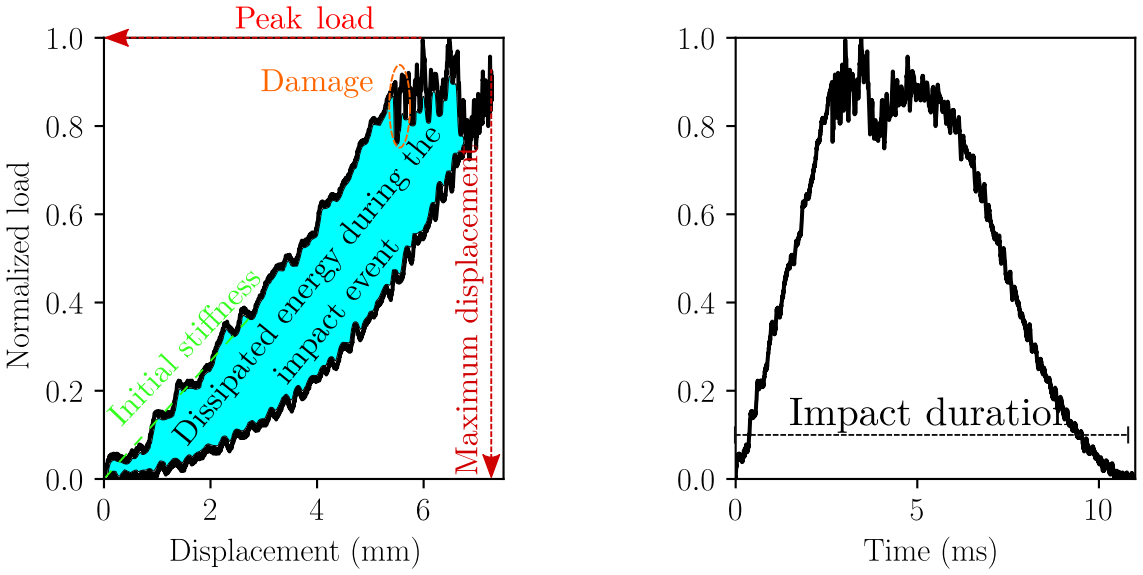

Figure 1.5: Physical response of a carbon/epoxy laminate after a 35 J impact

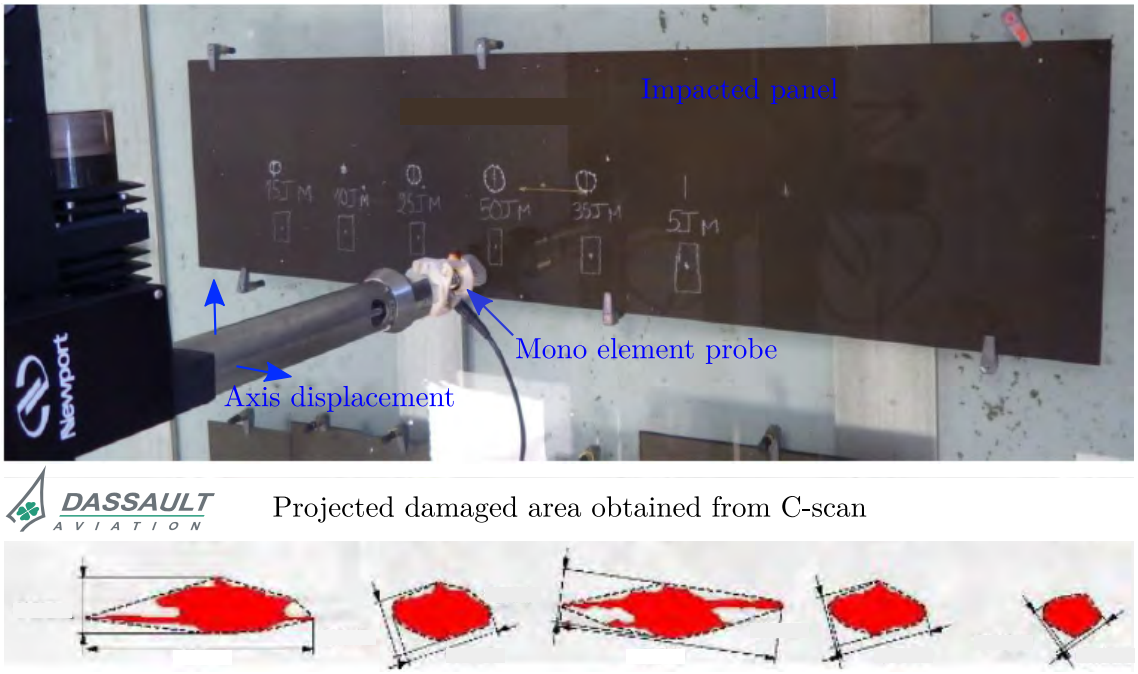

Figure 1.6: Ultrasonic inspection performed on an impacted panel at DASSAULT Aviation. The measurement of the projected damaged area is shown in red

dent measurement. Indeed, as shown in FIGURE 1.3, impact damages with a residual dent lower than BVID are considered category 1. It is therefore important to not bypass the measurement of the residual dent. As illustrated in FIGURE 1.7, the mechanism responsible for a residual dent is the presence of debris inside cracks which prevent them from closure after impact. This residual dent could be measured using a simple mechanical comparator or using an optical profilometer.

Compressive residual strength Once impact tests and inspections are performed, CAI test is carried out to determine the residual compressive strength

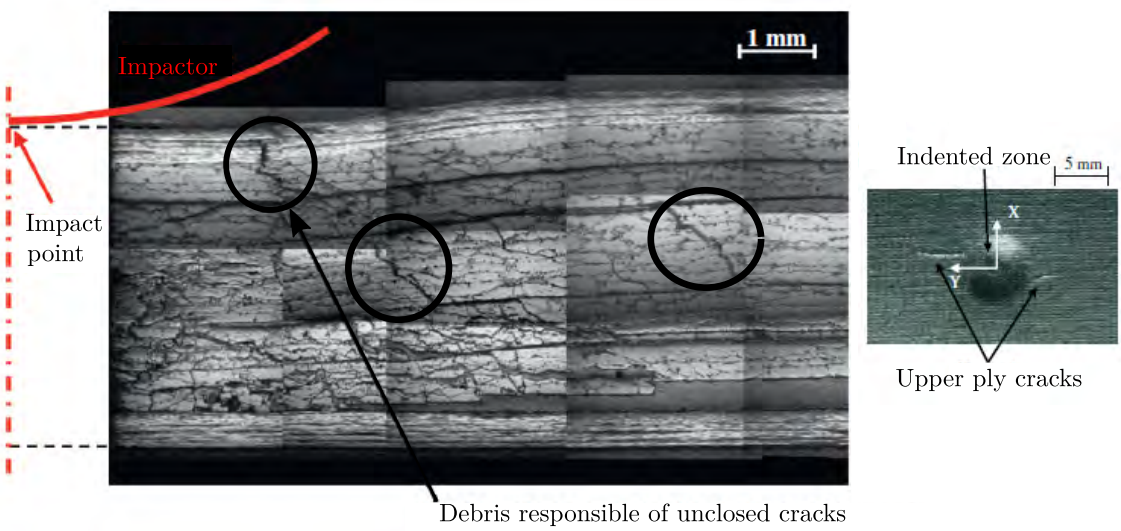

Figure 1.7: Damages responsible for the residual dent [Rivallant et al., 2014a]

according to the standard [AST, 2007a]. Before performing the test, dimensional checks are performed on edges in order to make sure that the edges are parallel. It will guarantee that the compressive load will be carried uniformly through the width and the thickness of the laminate. As shown in FIGURE 1.8, the sample is guided thanks to four grooves that prevent the sample from buckling. Moreover, to accommodate small variations in the specimen thickness, retention plates are adjustable using fixture screws. These screws have to be torqued at 7 Nm. A pre-load has to be carried until 10% of the estimated maximum load, this pre-load removes parasitic displacement due to mechanism slack. Two strain gauges (one at each side) can be fixed on the sample to ensure that the load is carried uniformly through the width and therefore avoiding any spurious bending. The compression load is carried along the top edge, as shown in green in FIGURE 1.8. Once the sample is broken, the maximum compressive stress is calculated by dividing the maximum load at failure by the section where the load is transferred.

Damage tolerance law establishment for category 1 Results obtained from the impact test, and CAI can be crossed to evaluate the impact severity's influence on the residual compressive strength. After that, industrials can establish an abacus, as shown in FIGURE 1.9. The compressive residual strength is plotted as a function of the permanent dent or the projected damaged area obtained in US. This abacus supplies the impact survey needed for the certification phase.

Limitation of standards approach for category 1 damage tolerance One of the advantages of the standard is to allow the repeatability of tests wherever performed. However, the diversity of geometries for composite structures in aircraft engineering with stringers, stiffened panels and open-hole panels imposed on manufacturers to get out the standard. Indeed, the framework defined by the standards is too restrictive for an aircraft manufacturer, especially when the material is a composite laminate where results will highly depend also on stacking sequence, ply thickness...

For impact tests, the standard requires a 125 × 75 mm impact window. This

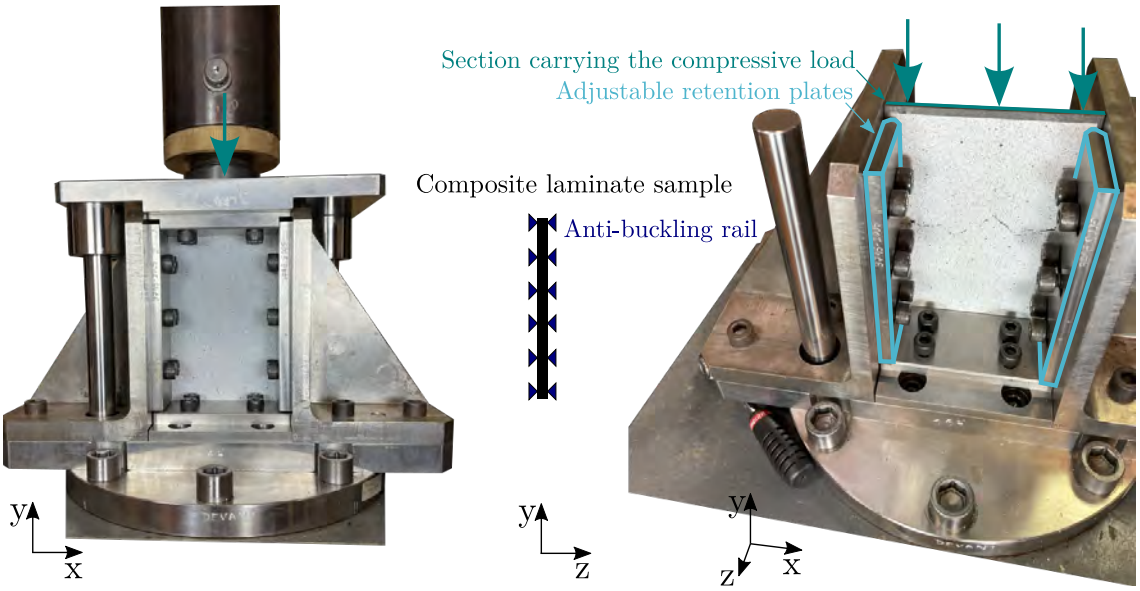

Figure 1.8: Experimental setup for CAI test standard at ONERA

window size could not represent all impact energies and plate thicknesses occurring during operation. Therefore, manufacturers have developed other impact windows (90×90 mm, 230×140 mm). Besides, the standard requires a 16 mm blunt impact that still cannot represent all impacts occurring in reality. Authority regulation required to take into account all impact scenarios that may happen; therefore industrials have to use other impactor geometries in order to define the most detrimental configuration. It leads to lengthy and costly experimental campaigns, especially for composite materials.

Concerning the CAI, the standard presents limitations with the imposed 150×100 mm size of the sample, which is still not representative of all configurations encountered in composite aircraft structures. Moreover, one of the restrictions of this test is the boundary conditions. They are not perfectly mastered as the plate has to be tightened to the fixture, the tightening relies on the operator performing the task, and therefore, it will influence the results. Another point is the lack of instrumentation during the CAI test. The residual strength at failure is the only data used.

Furthermore, the robust approach used by industrial is mainly experimental (a residual compression strength is associated with a permanent dent or a projected damaged area), design criteria are established by crossing results obtained from impact with compression after impact test. An investigation of impact damage mechanisms cannot be performed due to the most significant scale of components. Impact on composite structures has been studied for decades by academics in order to bring new solutions to industries. Experimental testing with more instrumentation and damage characterization using non-destructive and destructive testing has enabled the comprehension of impact damages and their interactions. Understanding the behavior of composite structures subjected to impact will enhance the use of composite materials in aircraft engineering, enrich the methodology of sizing for composite structures and minimize the conservatism introduced in the sizing.

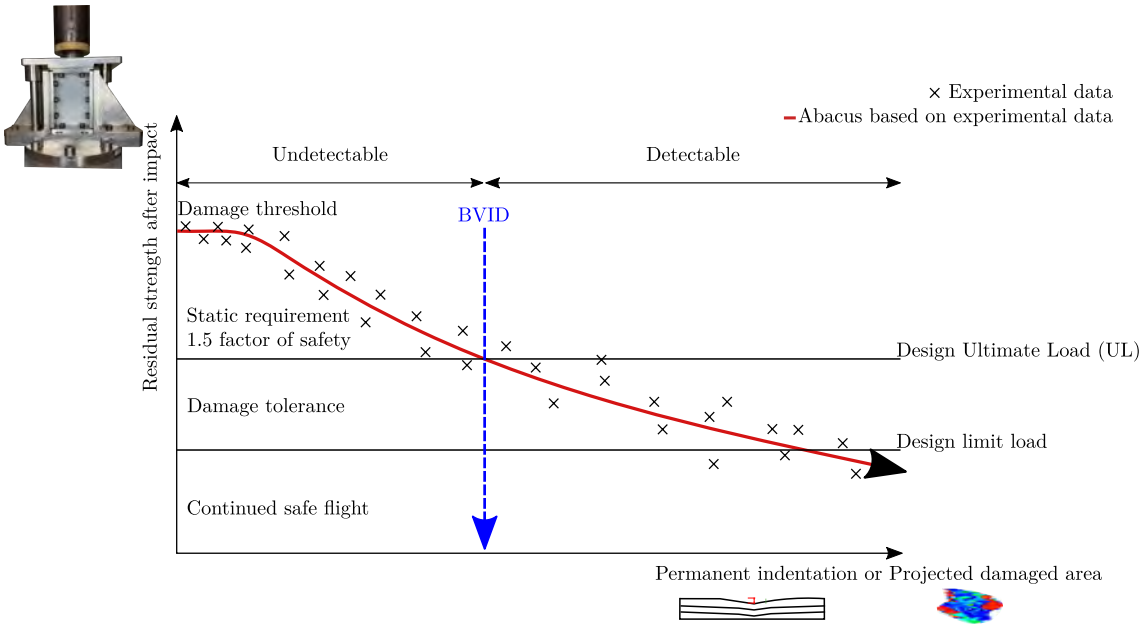

Figure 1.9: Evolution of the residual strength as a function of the damage severity

1.2 Academic experimental methodology for impact damage investigation induced by a LE/LV impact in composite laminates

1.2.1 Experimental setup and inspection methodologies for impact damages characterization

1.2.1.1 Impact experimental setup

In [Olsson, 2000], the author has defined three categories of impact responses as a function of the impact velocity. For very short impact times, the response is dominated by the wave propagation, typically ballistic impact such as in FIGURE 1.10.a The response is initially governed by flexural waves and shear waves for short impact times (FIGURE 1.10.b). The response is influenced by the lowest vibration mode of the impactor-plate for impact times longer than the times required for waves to reach the boundary condition (FIGURE 1.10.c). The impact response induced by a LE/LV impact belongs to the third category. Therefore, the impact damage is highly influenced by the boundary condition. Consequently, many impact configurations have been studied in the literature (experimental configuration close to the standard as in [GarciPerez, 2018], Charpy pendulum impact as studied in [Meola and Boccardi, 2018], circularly clamped or even supported on roller in [Elias, 2015] and [Trousset, 2013]). FIGURE 1.11 resumes some impact experimental testing encountered in the literature.

Impact damages are highly influenced by boundary conditions. For a stiffer configuration, damage mechanisms occur near the top due to higher contact forces (compression-shear matrix damages, fibre damages). In contrast, for a flexible configuration, damages occur near the non-impacted face due to high bending stresses. It is necessary to master the boundary conditions in a LE/LV impact test, especially if the impact test will be modeled using Finite element analysis (FEA).

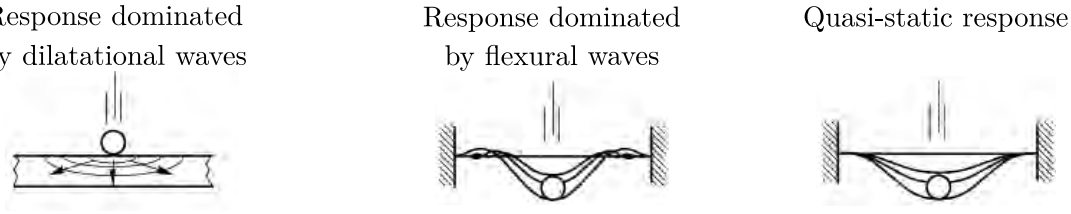

(a) Very short impact times (b) Short impact times (c) Long impact times

Figure 1.10: Effect of the impact velocity on the physical response of a plate [Olsson, 2000]

Supported on rollers Circularly clamped

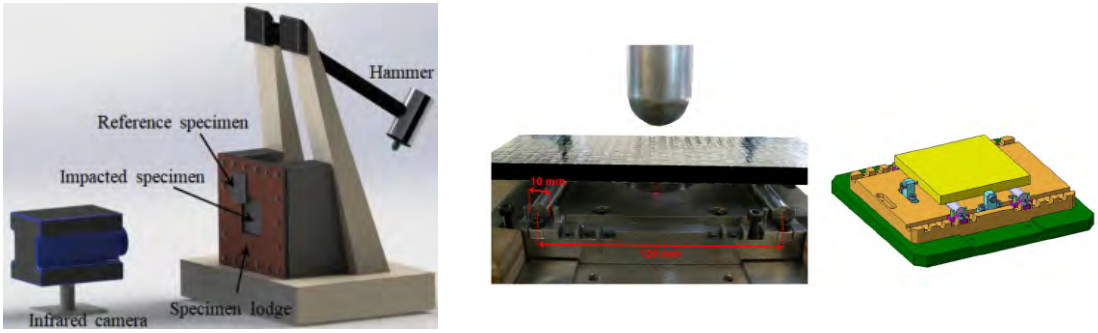

Charpy pendulum Simply supported

Figure 1.11: Experimental impact setup encountered in literature

The impact damage assessment is usually performed using Non-destructive inspection (NDI) and Destructive inspection (DI) as the experimental results provided by the impact machine are not enough to analyze and understand the mechanical behavior of composite laminates subjected to LE/LV impact.

1.2.1.2 Damage assessment using NDI and DI

Different techniques exist which give the overall damage extent (3D) or local damage zone (2D). These techniques could be non-destructive or destructive and are described hereafter.

Micrograph observations Using a microscope with different magnifications allows the observation of the damage topology with a high resolution. In the literature, micrograph observations have revealed the well-known conical shape of impact

damages. FIGURE 1.12 highlights the matrix cracking, the delamination and their interactions. In order to visualize more precisely the damage and their interactions

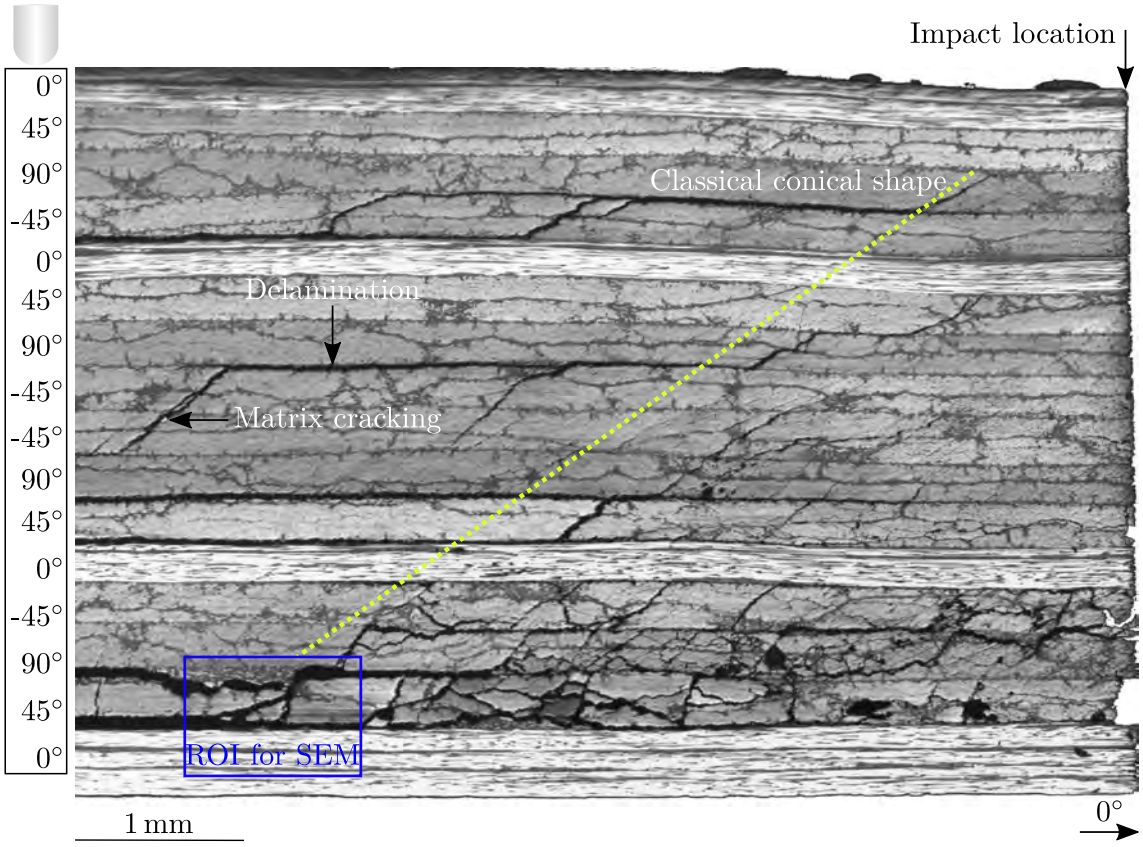

Figure 1.12: Micrograph observation of a T700/M21 composite laminate impacted at 20 J

with a very high resolution, a SEM could be an alternative to an optical microscope. For instance, FIGURE 1.13 shows the Region of interest (ROI) highlighted in blue in FIGURE 1.12. The different damages are observed with a high resolution. However, it requires sample preparation with a carbon deposit on the face wanted to be observed. This deposit allows conduction of the electrons as the epoxy matrix is an electrical insulator. Local information (fibre scale, ply scale) are provided. For a larger scale, it is better to use conventional optical micrographs.

These two means of control can provide good knowledge on local damages occurring on a face. However, they cannot give an overview of impact damages. Besides, it is a destructive means of control, as the specimen is cut and polished to get a ROI for observation.

Active Infrared thermography The inspection of defects or damages in the composites can be performed using AIRT. FIGURE 1.14 presents a classical experimental setup for the inspection. A signal generator defines thermal excitation. A high thermal flux is produced from the heater during a defined time. An IR camera records the thermal evolution of the sample during the test. As the thermal diffusion is modified within the material in the presence of damage or defect, it enables to capture the damaged zone. In [Boccardi, 2017, Maierhofer et al., 2014], NDI using Infrared thermography (IRT) has been used for impact damages characterization.

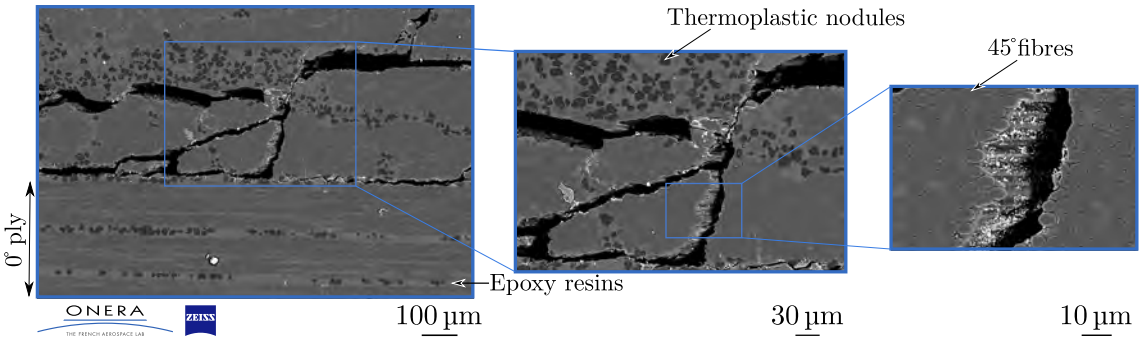

Figure 1.13: Micrographs using SEM of the ROI highlighted in blue in FIGURE 1.12

In [Maierhofer et al., 2014], impact damages have been characterized using AIRT with flash excitation. The authors have tested different configurations in reflection or transmission, as shown in FIGURE 1.14. The authors have excited the impacted sample for a short time using two flash lights. As the thermal flux is intense, the heated time was short to avoid high temperatures which could degrade the material. Thermograms of a composite sample impacted at 14.4 J in transmission and reflection configurations are presented in FIGURE 1.15. The thermal signature is similar for both configurations. It can be noticed that the thermal signature of the damages is well captured for both configurations when the IR camera is placed on the rear face (TB, RB). This technique can quantify the projected damaged area for thin composite laminates moreover, AIRT can enable the inspection of wide areas in a relatively short time. However, AIRT does not provide a faithful value of the damaged extent as it cannot inspect thicker parts due to the thermal dissipation. Therefore, standardized techniques such as UT are for now preferred in aeronautics.

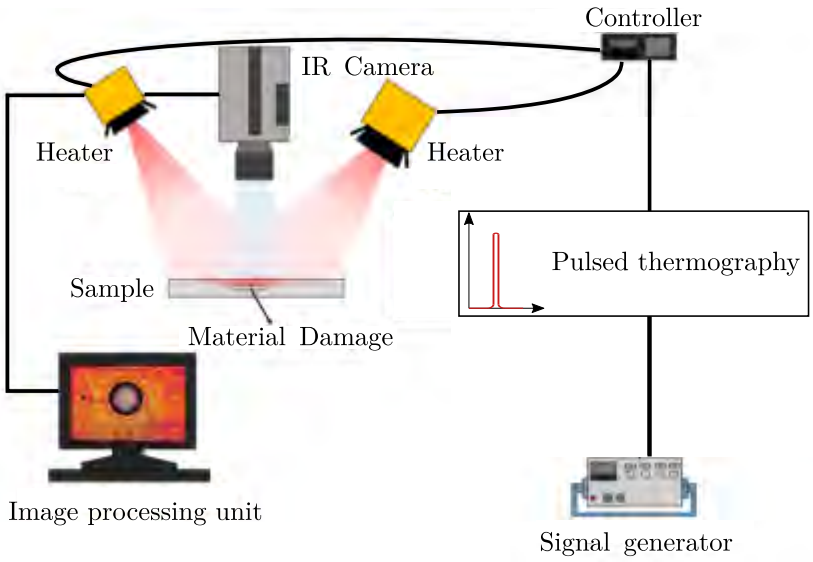

Figure 1.14: Experimental setup for AIRT [Ciampa et al., 2018]

Ultrasonic testing Inspection performed using US has become one of the most used NDT to inspect composite structures. It can allow the detection of defects

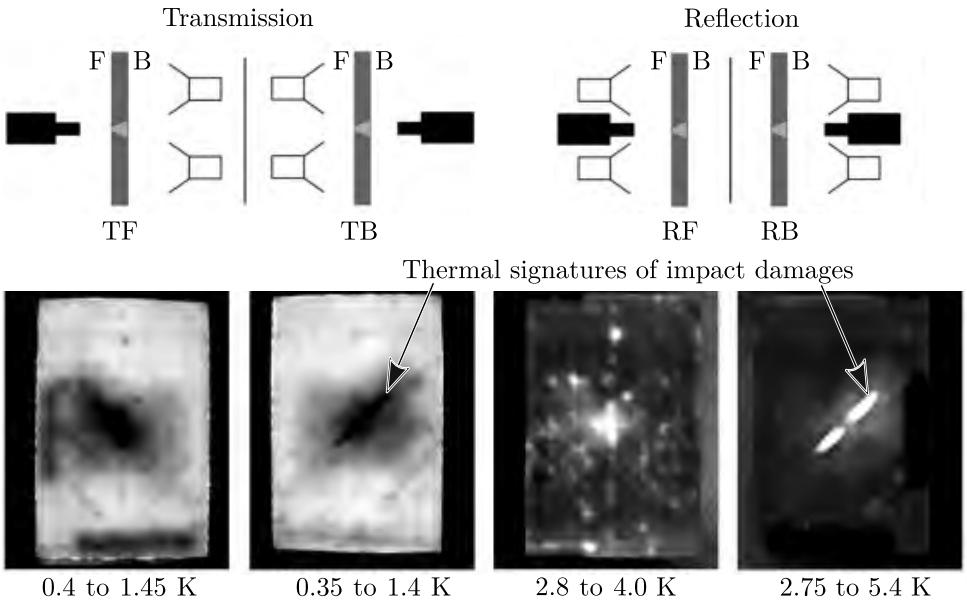

Figure 1.15: Thermograms obtained in reflection and transmission configuration for a composite laminate impacted at 14.4 J [Maierhofer et al., 2014]

or damages and evaluate their positions in depth. The reflection configuration is presented in FIGURE 1.16. A signal is emitted from an ultrasonic probe. Usually, a 5 MHz US probe is used for laminated composite materials to study damage after impact. Once the signal reaches the plate surface, a part of the signal is reflected due to the water and composite material interface. The probe receives the reflected signal and allows the detection of the "gate entrance" in the material. For the signal that has not been reflected at the interface entrance, the wave crosses the laminate thickness and is reflected when exiting the material due to the material/water interface. It defines the way-out gate. However, if damage is present through the thickness, the wave will be reflected toward the probe. The obtained output is an array of ultrasonic wave attenuations in dB. Different treatments of the signal data can be performed. In FIGURE 1.17, the projected damages are observed using a C-scan view, and the signal signatures with A-scan view. The A-scan is shown for two points (one located in the sound material and the other in the damaged zone). It can be seen that for the undamaged point, two peaks are detected, representing the entrance echo and the way-out echo in the composite. Nevertheless, other peak echoes are located between the entrance and way-out signal for the damaged point, which corresponds to the presence of damage. One of the limitations of UT scans is that the signal incidence influences damage detectability. Indeed, only delamination is captured in C-scan as they are perpendicular to the signal propagation direction. Some works, such as [Aymerich and Meili, 2000], studied the signal incidence to detect matrix cracking. Another point is that UT cannot provide a complete 3D damage assessment. Indeed, as presented in FIGURE 1.18, deep delamination cracks are shadowed by shallow delamination cracks. Thus, all the delaminated interfaces are not captured using C-scan. Studies have been performed by the authors, and also in [Wronkowicz-Katunin et al., 2019], to reconstruct the shadowed damages, but it introduces guesses concerning the shadowed damage shapes.

UT scans can provide a good projected damaged area. However, if the aim is to investigate impact damages in each ply/interface with the dissociation of each

damage mechanism, X-ray using μ-computed tomography is preferred.

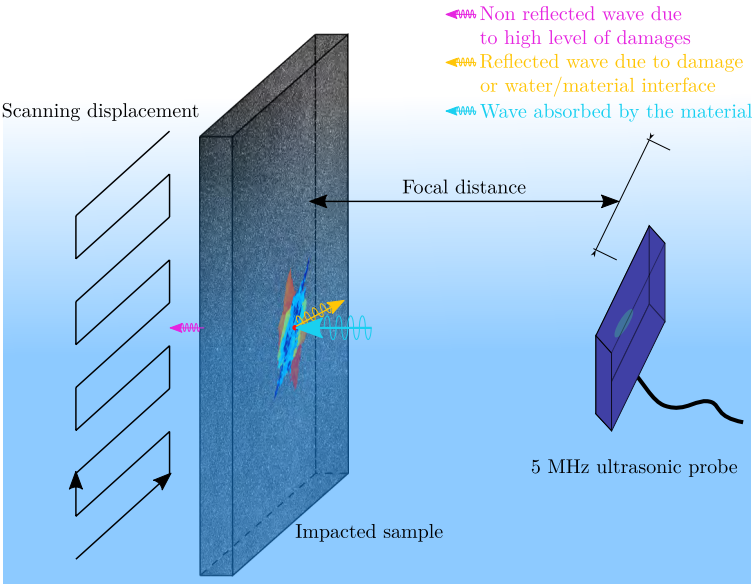

Figure 1.16: UT configuration in a water cistern

X-ray Computed tomography (CT) X-ray has been introduced for impact damage assessment using radiography, as shown in FIGURE 1.19. Each damage is distinguished easily, and the damaged area can be quantified. However, it provides a 2D damage assessment such as C-scan. The μ-CT gives a 3D characterization of impact damages thanks to the scanning configuration. A schematic representation of the inspection using a μ-CT is presented in FIGURE 1.20. An X-ray beam crosses the composite sample lying on a rotating support. The table is gradually rotated step-by-step during the acquisition, and several X-ray 2D radiographs are taken. As the material absorbs X-ray radiation, the presence of damage results in voids inside the laminate. The voids do not absorb the X-ray radiation. Therefore, the X-ray detector capture the X-ray radiation escaped from the material due to damage. Many studies are found on the investigation of impact damage using μ-CT. In [Lin et al., 2020], μ-CT has been used to characterize the overall damage footprint and the internal damage topology (FIGURE 1.21). In [Ellison, 2020] [García-Rodríguez et al., 2018] [Bull et al., 2013] methodologies have been performed to segment impact damages using a ply detection method. The matrix cracking and delamination segmentation for the whole volume has been performed (FIGURE 1.22.1). In [Bull et al., 2013], the authors have performed X-ray inspection using a synchrotron facility. Thereby, in FIGURE 1.22, the same sample has been scanned using classical μ-CT (FIGURE 1.22.2a) and synchrotron CT (SRCT) (FIGURE 1.22.2b). The authors have shown that more damages are captured using SRCT due to a better resolution.

The limiting factor in X-rays is that resolution depends on the sample size. The closer the sample to the beam source, the higher the resolution. Nevertheless, the size of the coupon is defined in order to avoid the collision with the X-ray source when the sample is rotated. Therefore, X-ray CT is destructive as larger samples have to be cut before the inspection. Besides, if the coupon is warped or non-planar, investigating damages or defects can be more difficult.

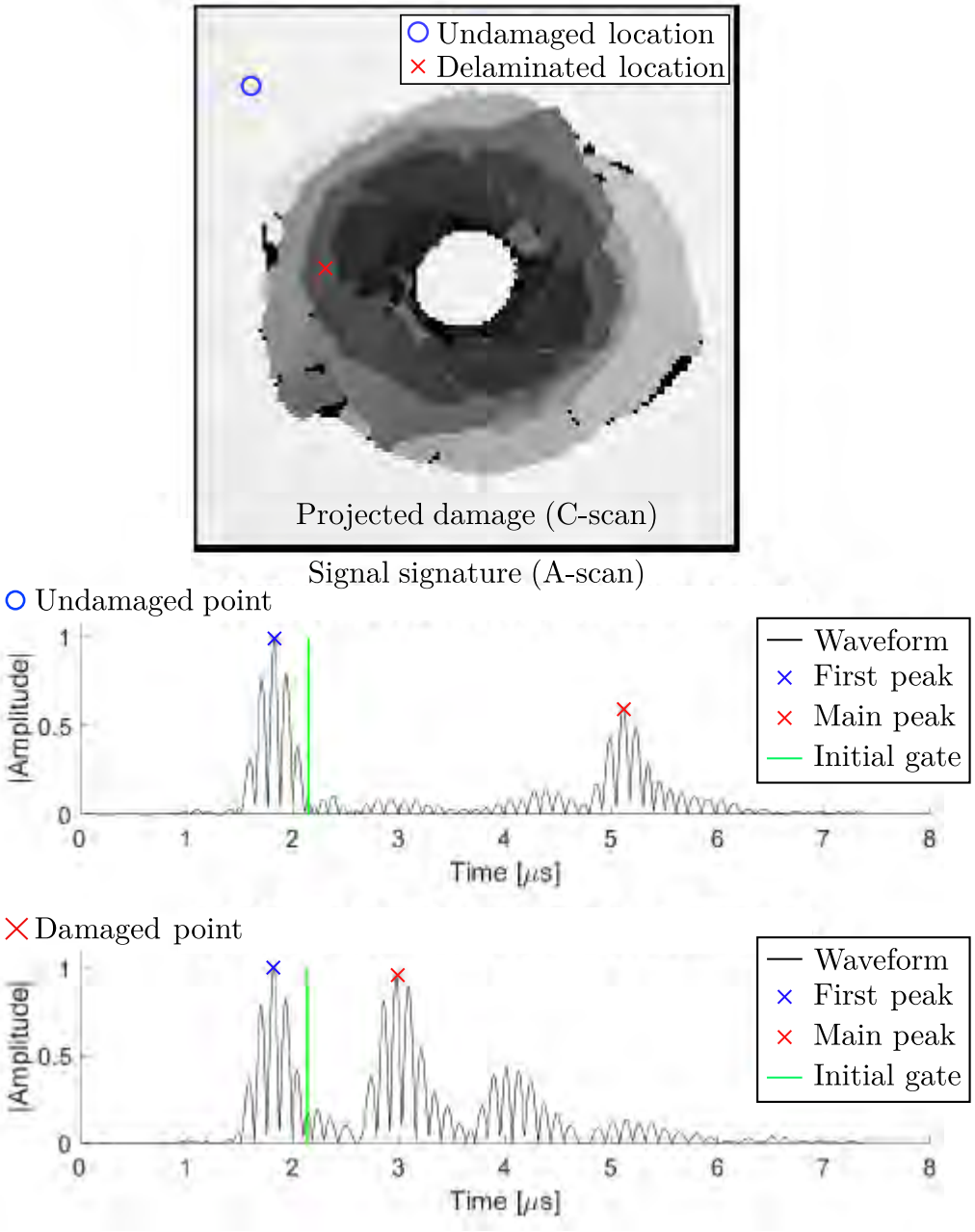

Figure 1.17: UT scan performed on an impacted sample showing the C-scan and A-scan treatments [Ellison, 2020]

Table 1.1 summarizes the different methods for the presented NDI and DI. No specific technique is preferred for impact damage assessment, as each gets its advantages and limitations. Consequently, it is suitable to combine these different techniques to obtain the maximum information on damage topology and perform a complete investigation of impact damages.

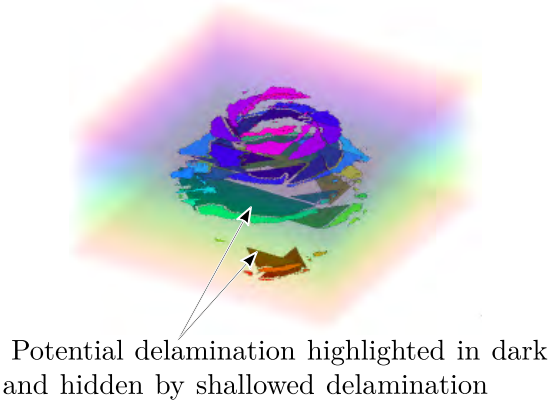

Figure 1.18: 3D rendering of impact damages observed using C-scan and highliting the shadowing effect [Ellison, 2020]

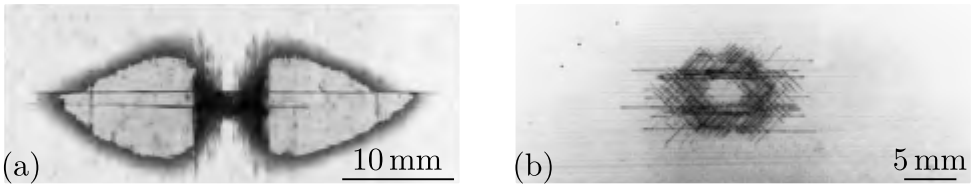

Figure 1.19: X-ray radiographs of impact damages in [Aymerich and Priolo, 2008] (a) and [Hawyes et al., 2001](b)

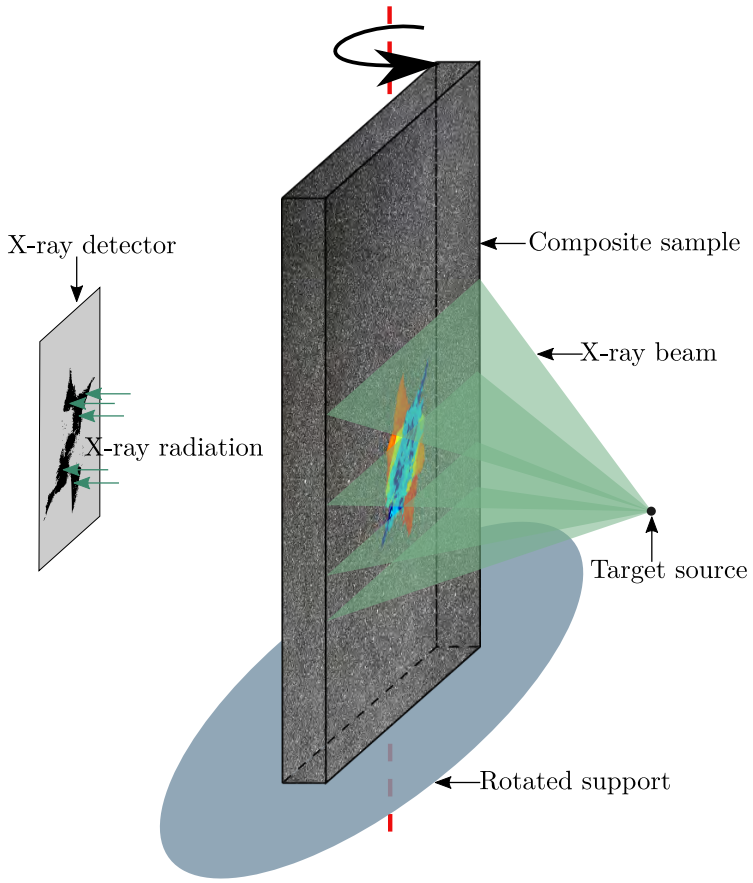

Figure 1.20: X-ray μ-CT testing configuration

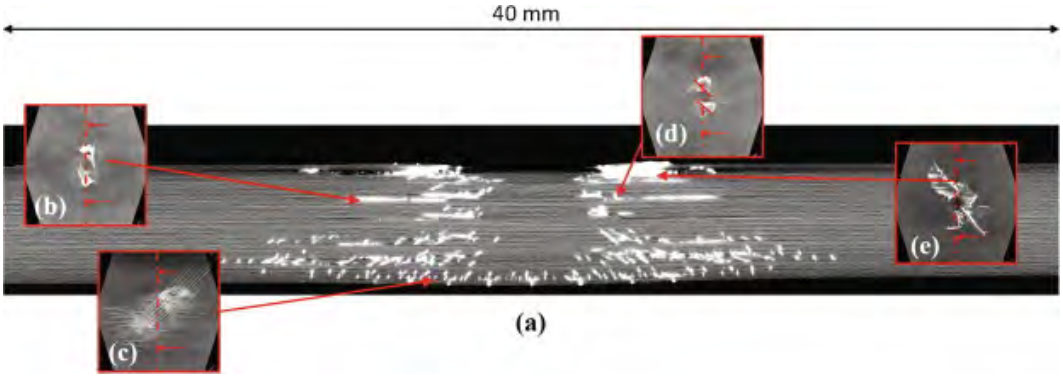

Figure 1.21: Impact damages observed on a μ-CT slice (a) and in different positions in depth (b-d) [Lin et al., 2020]

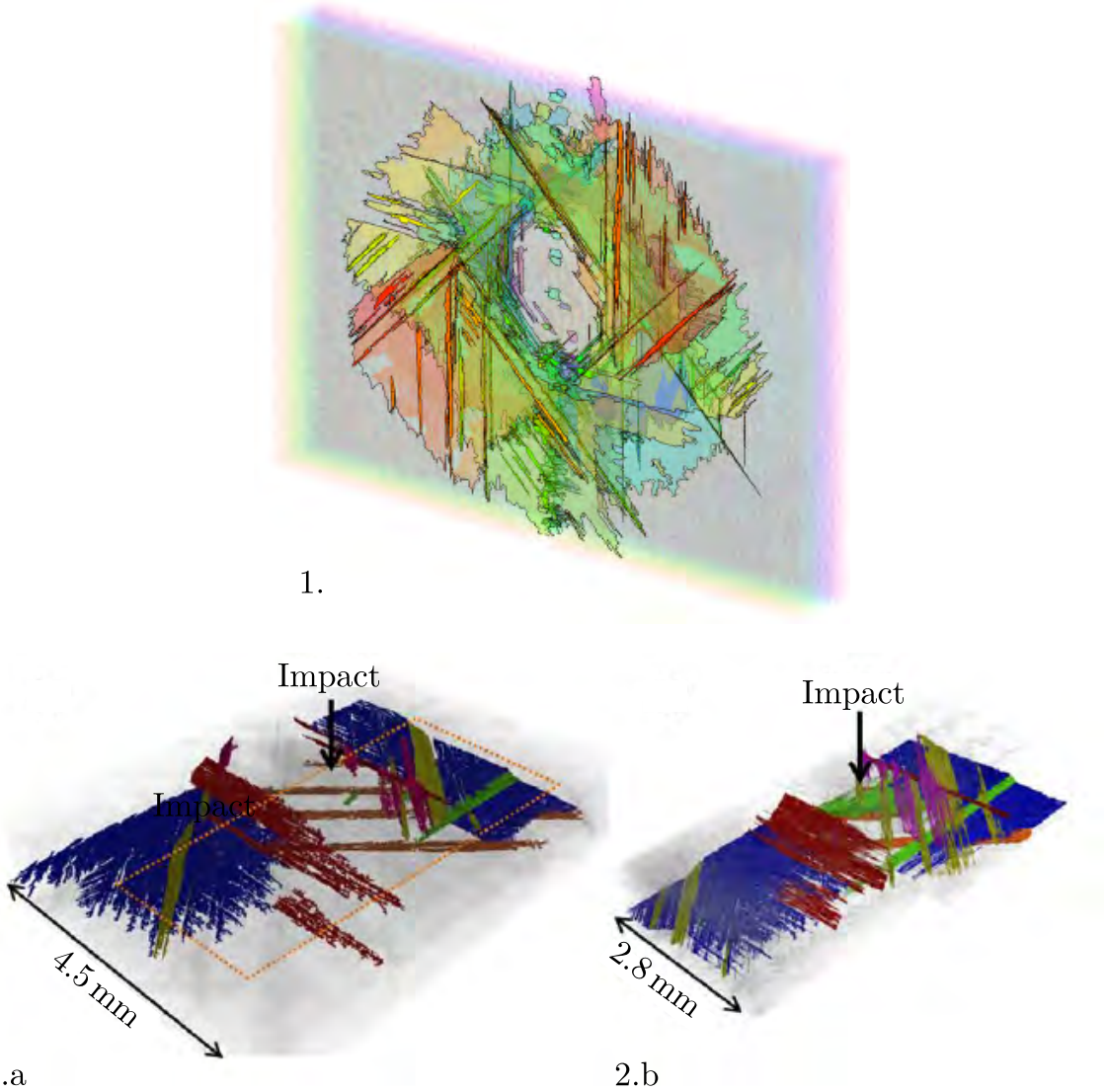

1.

2.a 2.b

Figure 1.22: Impact damages segmentation performed in [Ellison, 2020] (1.) and in [Bull et al., 2013] (2.a using μ-CT, 2.b using SRCT)

Inspection methods	DT	NDT
Micrographs	2D	
AIRT		2D
UT		2.5D
X-ray CT	3D	3D

Table 1.1: Sum-up of the presented inspection methods

1.2.1.3 Comprehension of the mechanical degradation using a damage monitoring

In LE/LV impact as mentioned in Section 1.1, very little interest regarding the instrumentation is considered in the standards:

- A cell load contained in the impactor in order to measure the impact force during the impact test;
- A photocell sensor to measure the initial impact velocity of the striker;

The data acquired during the test allow calculating the impactor displacement and the dissipated energy as explained in Section 1.1. The load-displacement and load-time responses are then plotted to investigate the physical response of the material during the impact event. The damage mechanisms observed using NDT and DT are responsible for the nonlinearity appearing in the global responses (load drop, softening, oscillations). However, it is impossible to link the mechanisms to their designated effects on the global response. Consequently, the temporality of degradation is unknown, and the interactions between damage mechanisms could not be established rigorously.

For damage scenario establishment, two solutions can be found in the literature:

- Damage monitoring during the impact event using adapted instrumentations (fast measurement methods);
- Quasi-static indentation, the test could be interrupted to realize a back and forth between NDI and testing. It allows evaluating the damage extent after each increment loading. It should be highlighted that this method is available only if the loading rate effects are negligible for the studied material;

These two methodologies performed in the literature will be discussed in the following to bring a comprehension of damage mechanisms occurring in composite laminates when subjected to a LE/LV impact.

1.2.1.4 Quasi-static indentation as a substitution of LE/LV impact

A better understanding of the damage appearance is obtained using quasi-static indentation. Indeed, as the test is piloted with the applied displacement, it is possible to interrupt the test, realize NDI and then load again (Figure 1.23). This back and forth between test and NDI allows the control of the damage onset [Wagih

et al., 2016a, Abisset et al., 2016]. In [Wagih et al., 2016a], the authors have performed several indentation tests on a carbon-epoxy laminate with NDI. Four stages have been defined, each stage was associated with the appearance of one damage mechanism.

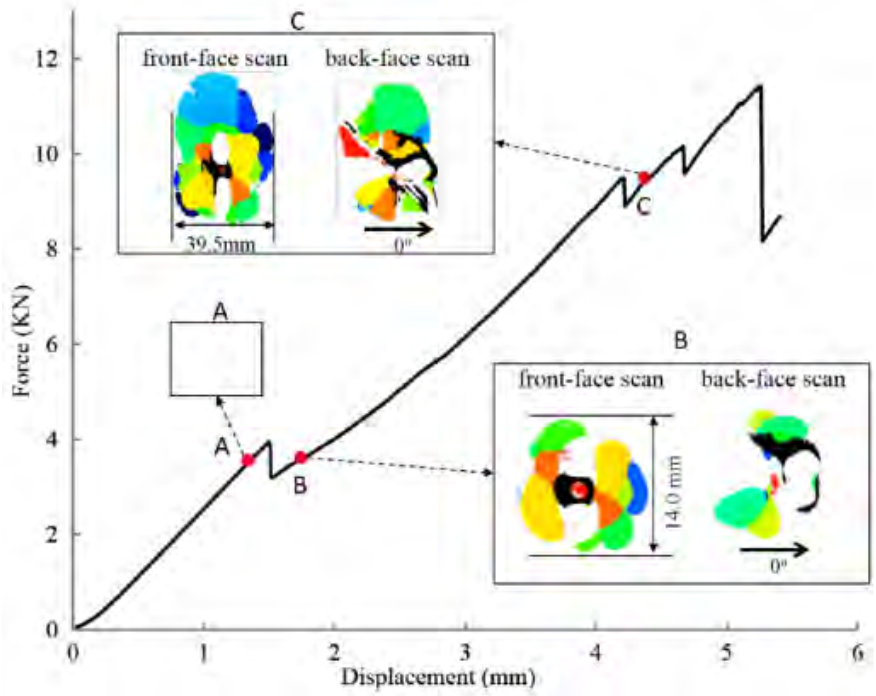

Figure 1.23: Load-displacement response for a QSI test with the different inspections performed using US [Abisset et al., 2016]

Before investigating the damages subjected to indentation, it must be verified that the material behavior is insensitive to the loading rate. Many studies have compared LE/LV impact and quasi-static loading, such as in [Spronk et al., 2018, Aoki et al., 2007, Bull et al., 2015]. In [Spronk et al., 2018] QSI and LE/LV impact have been compared on a carbon/epoxy and an E-glass/polyamide-6 laminates for two different stacking sequences. The authors have shown that similar global responses (load-displacement curves) are obtained for carbon/epoxy laminates. However, the E-glass/polyamide-6 was more sensitive to loading rate effects resulting in different behaviors for the QSI and LE/LV impact. NDI were performed on those laminates. Similar damage mechanisms were observed for the carbon/epoxy laminates with greater damage extent for QSI.

In [Bull et al., 2015] carbon/epoxy laminates have been tested under QSI and LE/LV impact. The specificity of this study was to understand if carbon/epoxy laminate with a reinforced interface using thermoplastic particles is sensitive to strain rate effect. The authors have shown that the projected damaged area obtained from C-scan or X-ray follows a similar linear trend for both QSI and LE/LV impact. The authors concluded that some laminates with different particle sizes had a strain rate effect. Therefore, the equivalence of LE/LV impact and QSI is material-dependent. On the other hand, it is observed that the residual dent is more pronounced for QSI. A possible explanation is a longer contact time between the impactor and the plate.

1.2.1.5 Experimental damage monitoring during a LE/LV impact

An impact is a very short event requiring specific instrumentation with a high-frequency acquisition. In these last decades, technological developments such as the digital image correlation method DIC with high-speed cameras have changed the experimental testing in transient dynamics [JPE, 2019].

High speed DIC performed in impact The impact monitoring using high speed visible cameras has been successfully introduced to measure the evolution of the impact damage within a triaxial braided composite material in [J.Michael Pereira, 2010]. In [Flores et al., 2017], the authors have monitored a LE/LV impact using two 1-megapixel Photron FASTCAM to perform DIC with the acquisition of 20,000 frames per second. The experimental setup is detailed in FIGURE 1.24. A mirror inclined at 45° has been required to capture the images on the rear face. The mirror has been placed below the impact window due to a congestion problem in the experimental device. DIC has provided information such as displacement and deformation fields, and damage events (FIGURE 1.25). Moreover, in [Lin et al., 2020], the authors have compared the out-of-plane (OOP) displacement from DIC, the displacement calculated from the machine, and the maximum height provided by an optical profilometer. They have concluded that the measure provided by DIC was in agreement with the other data.

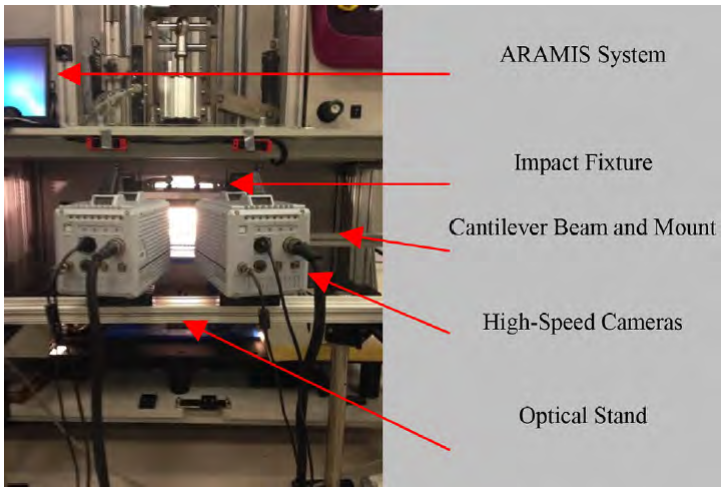

Figure 1.24: Experimental impact setup with high speed cameras [Flores et al., 2017]

High-speed thermography performed during impact As cracks generate a thermal dissipation, it is possible to capture their thermal signature in the infrared range. This heating can be captured using IR thermal cameras. It is another IRT technique called passive IR thermal monitoring. This method has been used in [Joel P Johnston, 2017] to measure the temperature variation on the rear face of triaxially braided composites subjected to ballistic impact. In [Maierhofer et al., 2019], an IR camera has been used to monitor impact damages in glass/epoxy and carbon/epoxy laminates. The authors have carried out several impacts. The IR cameras have been placed in two positions, at the top and at the bottom. The thermal signatures have been captured with an acquisition frequency of 800 Hz. The cameras have captured

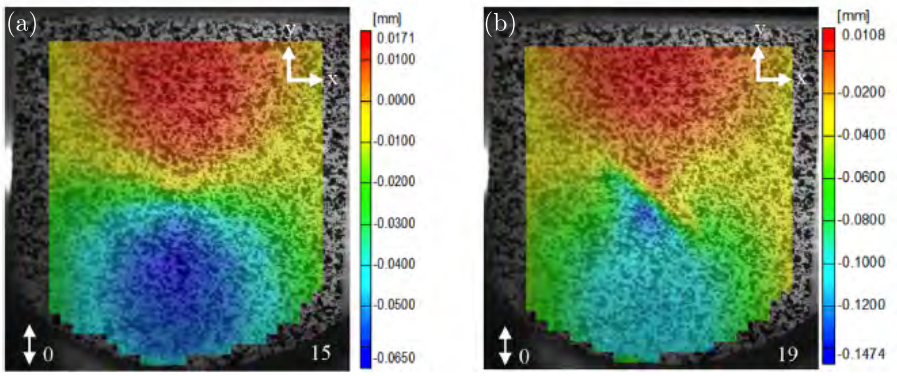

Figure 1.25: Transverse displacement field obtained from DIC before the damage appearance (a) and after the damage outcome (b) [Flores et al., 2017]

thermal signatures related to the different mechanisms. However, the critical limit of the study was that the experimental setup was not containing a load cell. Therefore, the thermal events have not been linked to the nonlinearities occurring in the global response. In [Meola and Boccardi, 2018], a different experimental setup has been considered using a modified Charpy test shown in FIGURE 1.11. An IR FLIR camera with 83 Hz acquisition frequency was used and placed on the rear face. FIGURE 1.26 presents the thermal signatures captured from the IR camera during the impact on a CFRP sample impacted at 18 J. This work focused on developing a methodology to estimate the damaged area by considering the heated area as an input. It can be highlighted that from these two experimental studies classical IR cameras have been used with poor frequency acquisitions (< 800 Hz). Moreover, no links have been established between the thermal signatures and the global responses. A more advanced analysis as performed in [Joel P Johnston, 2017] has not been found on LE/LV.

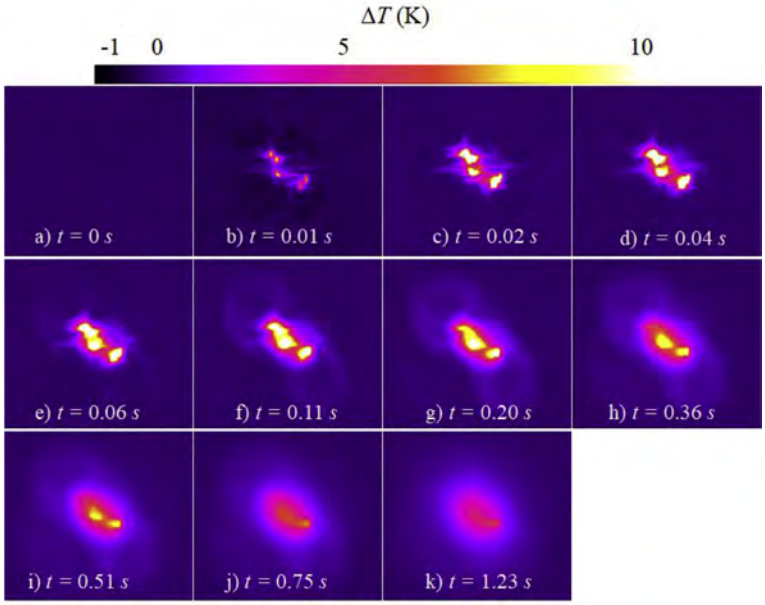

Figure 1.26: Thermal signature of impact damages occurring on a CFRP sample impacted at 18 J [Meola and Boccardi, 2018]

1.2.2 Damage mechanisms in composite laminates induced by a LE/LV impact for composite laminates

This subsection presents an overview of the classical damage mechanisms encountered in composite laminates made of Unidirectional laminate UD plies. The specificity of impact damages is then treated. Finally, the latest advancement in composite materials strengthening and how the composite laminates can be more damage tolerant are presented.

1.2.2.1 Classical damage mechanisms occurring in composite laminates

Damage mechanisms in composite laminates can be divided into two families (intraply and interply damages). These damages are presented in FIGURE 1.27.

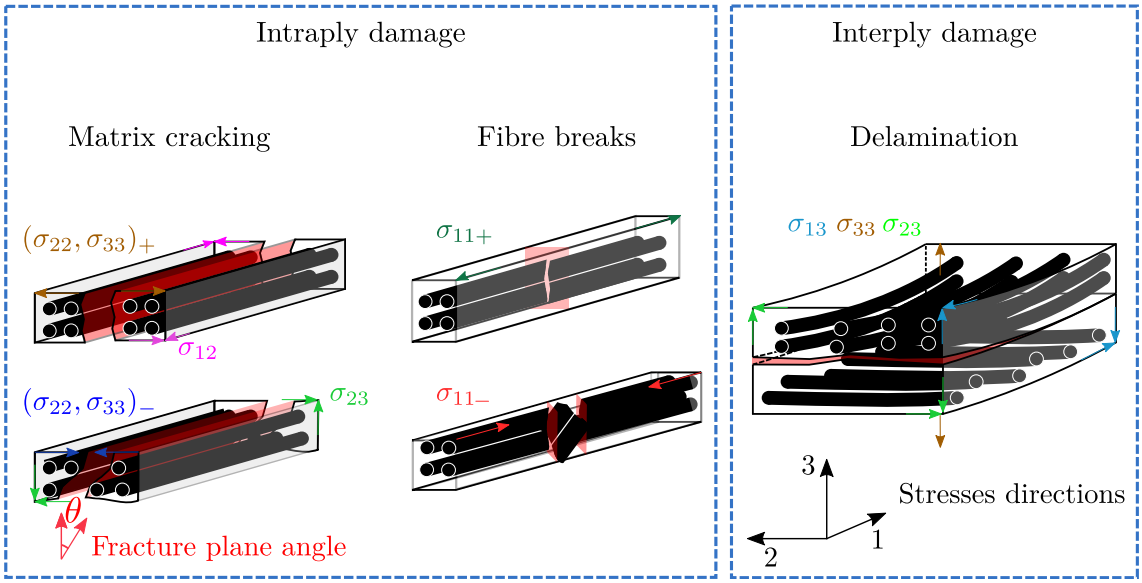

Figure 1.27: Damages mechanisms occurring in UD composite laminates

Matrix cracking Matrix cracking is a mesoscopic intraply damage. It is induced by the coalescence of fibre-matrix debonding at the microscopic scale (FIGURE 1.28.a). In [Puck and Schürmann, 2002], the authors have shown that the fracture plane angle depends on the loading axes.

For a positive transversal loading (in direction 2 or 3) or an in-plane shearing (plane 1-2), the fracture plane is perpendicular to direction 2 ($\theta = 90°$).

For combined compressive transverse loading (in directions 2 or 3) and in-plane or out-of-plane shearing, the fracture plane angle is higher than 0°. The higher the transverse compressive loading, the higher $\theta°$ with a maximum angle of 53°. Matrix cracking is highly influenced by the ply thickness, as discussed in [Chang and Chen, 1987]. For thicker plies, the matrix cracking appears earlier and has an important effect on the delamination (FIGURE 1.28.a).

Delamination The interface localized between two adjacent plies is characterized by its adhesion. The adhesion can be weakened during the life cycle of the laminate due to the presence of defects (void, resin river) or due to high out-of-plane

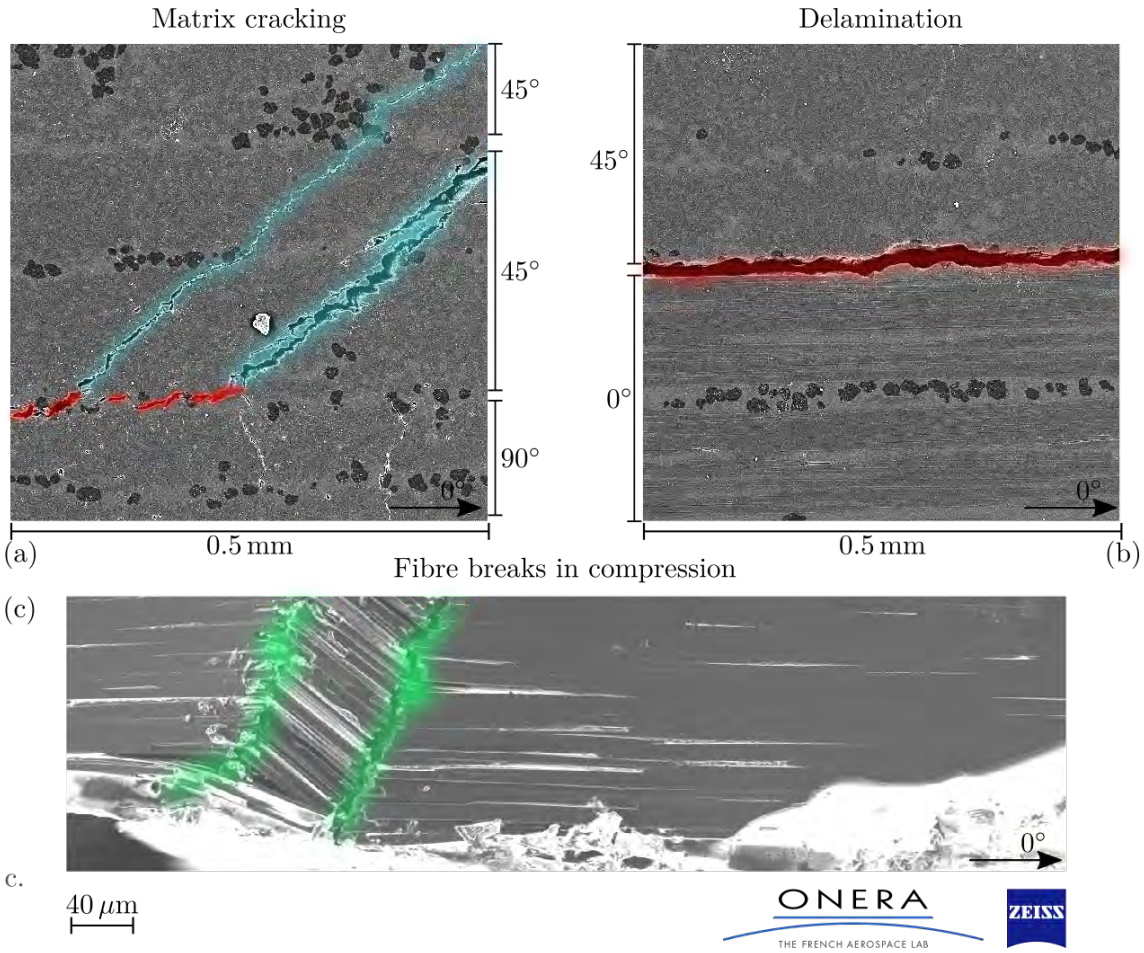

Figure 1.28: SEM micrographs showing the three different damage mechanisms encountered in composite laminates [ONERA]

loading. The delamination is initiated once the interface fails (FIGURE 1.28.b). The mechanical loading does not impose the delamination orientation. In the presence of no fibre breaks, the delamination is clustered between the matrix cracking from the upper and lower plies.

The delamination cracks can induce a catastrophic failure of the laminate when subjected to bending or in-plane compression. Indeed, the laminate will be subdivided into sublaminates resulting in the drop of the inertia moment $I_{2,3}$, and therefore, a decrease of the buckling strength onset.

Fibre breaks The fibre breaks are a highly energetic degradation mechanism. They occur when fibres have reached their maximum bearing capability. When fibres break, the loading is transferred violently to the neighborhood. This induces a succession of failures leading to an unstable phenomenon. The fibre failure dissipates 10-100× more energy than delamination. Therefore, it represents the critical dissipative mechanism. The mechanism responsible for the failure in a UD ply subjected to longitudinal tension or compression is different. In tension, the maximum deformation of fibres induces ply failure in fibre mode. However, in compression, the mechanisms are more complex. Indeed, the failure depends on the local state of the neighboring matrix but also on how the fibres undergo the local buckling (FIGURE 1.28.c).

1.2.2.2 Interaction of damages occurring in impact

During an impact event, the kinetic energy is converted to internal energy. An amount of this energy is stored as elastic energy, and another part is dissipated by the creation of damage. Three stages are usually encountered in impact damages, as shown in FIGURE 1.29. The first one is the coalescence of matrix cracking within the ply. These cracks are induced by high transverse and shear out-of-plane stresses. The second stage is the initiation of the delamination due to high shear stresses at the interface. The delamination can also be triggered when the matrix cracks reach the interface. Indeed, in the literature several authors have studied the interaction between matrix cracking and delamination [McElroy et al., 2017]. The third stage is the apparition of fibre breaks when fibres reach their maximum bearing capabilities. At this stage, it is pretty challenging to establish in a precise manner the damage scenario as the damages interact together. In FIGURE 1.29, the well-known "pine tree" shape of impact damage is shown. An undamaged zone under the impact is highlighted in yellow. The material exhibits a shear reinforcement preventing matrix cracking and delamination under the impactor. Therefore, no damage is observed below the impact zone, explaining the damage's conical shape. The introduction of Zinc iodure penetrant in FIGURE 1.29 highlights the damage connectivity, especially for matrix cracking/delamination.

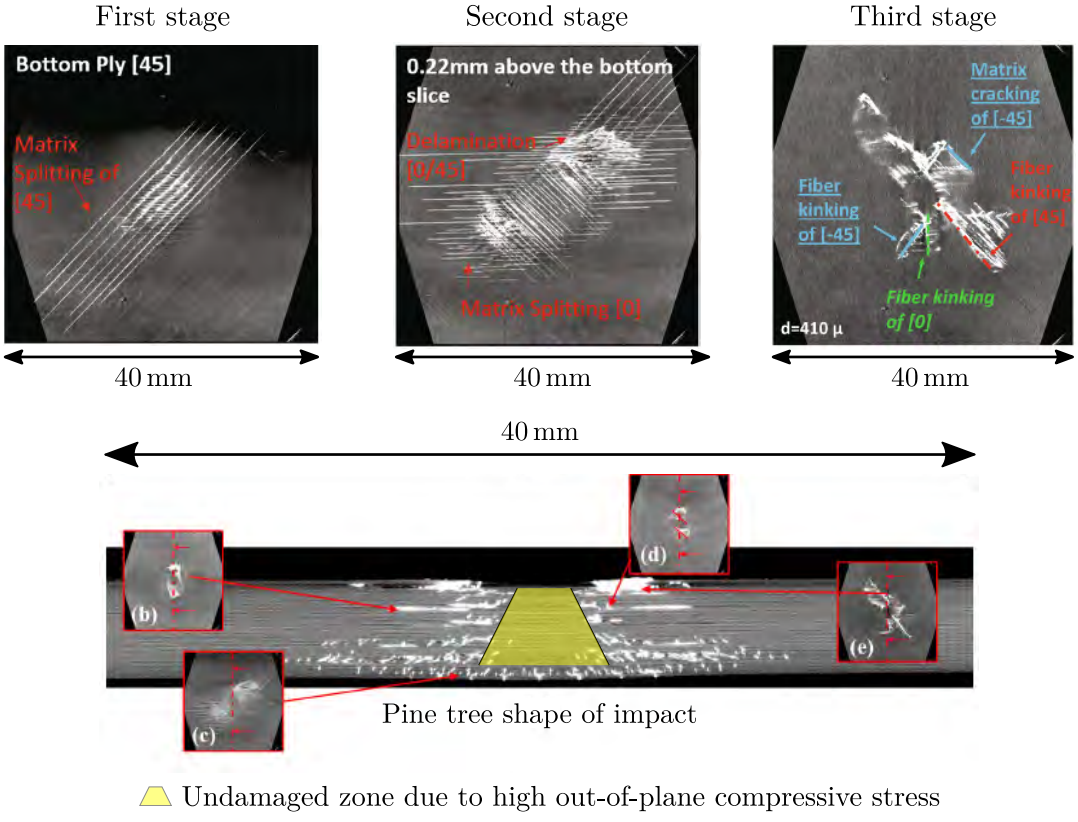

Figure 1.29: Impact damages observed in a μ-CT slices [Lin et al., 2020]

1.2.2.3 How to increase the impact resistance in composite laminates ?

Designing differently with unconventional rules Infinite possibilities of designing composite laminates exist, and different leverages have been introduced :

- In [Wagih et al., 2019], the authors have compared three different laminates with different mismatch angles under quasi-static indentation. They have shown that the higher the mismatch angle, the higher the damage resistance. Nevertheless, the higher the mismatch angle, the lower the maximum load capability;

- In [Wagih et al., 2016b], the authors have compared ultra thin-ply (UTP) (80 gsm, 0.08 mm thick) and thin-ply (TP) laminates (160 gsm, 0.16 mm thick) under quasi-static indentation. The authors have shown that UTP enhances the damage resistance. However, this laminate exhibits a brittle failure. Using TP, laminates have shown a better maximum load capability;

- In [Sasikumar et al., 2019], the authors have used unconventional laminates with unsymmetrical stacking sequences and ply clustering. The authors have shown that clustering the plies near the impacted side have enhanced the damage resistance and have reduced the delamination at low impact energy;

All of these parameters have an effect on either damage resistance or the load capacity. The potential of composite laminates can be improved using new design thinking.

During LE/LV impact, the interfacial toughness in mode II (G_{IIc}) is a material parameter of concern. Indeed, the delamination propagates mainly in mode II. Therefore, material manufacturers and scientists have studied new material architectures to improve the interfacial toughness and reduce the delaminated area after impact. Two research studies on damage resistances using interleaved composite laminates or thermoplastic resins are discussed below.

Interleaving composite laminates In the literature, several researchers have studied the toughening of epoxy resins. The fracture and toughening mechanisms have been studied when a different phase is introduced into the epoxy (silica nanoparticle or rubber particle). In [Hsieh et al., 2010], the authors have introduced different volume fractions of silica nanoparticles. They have observed that the fracture toughness increases with the volume fraction of silica nanoparticle. Interleaving composite laminates with thermoplastic particles has also been studied in [Gao et al., 2007, Bull et al., 2014, Priasso, 2017]. Thermoplastic particles are located at the interface between plies, and different sizes of particles are possible. The higher the size, the thicker the interface. Thus, the microstructure of the laminate is no more conventional. The interface thickness is equivalent to 1/5 of the ply thickness, while for classical material, the interface thickness is 1/10 of the ply thickness. In [Gao et al., 2007], the authors have studied the toughening effect on the interface toughness in mode II G_{IIc} using quasi-static indentation. By comparing the studied material to a conventional carbon-epoxy laminate, interleaving allows better performance by delaying damage onset, and increasing the peak load. The same conclusions have been dressed in [Bull et al., 2014]. Moreover, the two studies have highlighted the toughening mechanisms responsible for better performance. In FIGURE 1.30, the toughening mechanisms are presented in the absence of particles, the crack propagation is straight. However, when the crack tip faces a particle, either enough energy is available and the crack breaks the particle or, the crack skirts the particle. Another phenomenon, such as crack bridging, allows carrying the load through the

ligament and reduces stress concentrations in the crack tip. Consequently, more energy is required to propagate a crack resulting in less delamination.

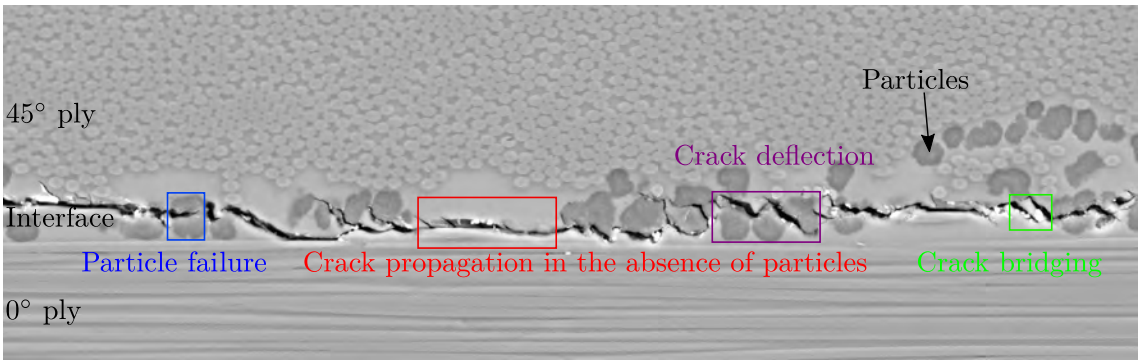

Figure 1.30: Toughening mechanisms responsible for G_{IIc} enhancement [ONERA]

Thermoplastic based composite laminates Some thermoplastic resins have a better fracture toughness than thermoset resins. As delamination can lead to catastrophic failure of composite structures. Using carbon/thermoplastic materials may enhance the damage resistance of composite laminates. In [Liu et al., 2020], the authors have compared two cross-ply laminates made of UD plies. The first cross-ply was made of carbon-thermoplastic and the second one with carbon-epoxy toughened UD ply. The experiment reveals that carbon-thermoplastic shows better impact response than carbon-epoxy toughened with a higher damage resistance. However, a limiting factor highlighted in [Bouvet et al., 2020] is the sensitivity to strain rate effect in carbon-thermoplastic materials. The authors have developed a measurement methodology based on IR to measure the G_{IIc} during an unstable propagation (FIGURE 1.31). The experiment reveals that G_{IIc} drops during unstable crack propagation. The actual comprehension of the damage mechanisms of carbon-thermoplastic is currently at an early stage, and more studies are needed to understand clearly the damage mechanisms of those alternative materials.

1.2.3 Summary of the academic experimental characterization of impact damages induced by a LE/LV impact

This section presents an overview of the work performed by academics on LE/LV on composites. In these last decades, researchers have enabled the understanding of physical phenomena occurring after an impact and the damage assessment within composites. The overview has presented the testing procedure, inspection methods, and damage mechanisms for composite laminates. It has revealed a lack in damage scenario establishment as inspection means are mainly performed after the impact.

Some academics have proposed solutions using *in situ* damage monitoring. Those studies show the high potential of damage assessment thanks to the real-time information provided during the test. Unfortunately, as the impact is a short event (a few milliseconds), it requires specific instrumentation dealing with high-frequency acquisition, and, therefore, costly means. Another solution is the quasi-static indentation, which allows a step-by-step understanding of damage mechanisms occurring

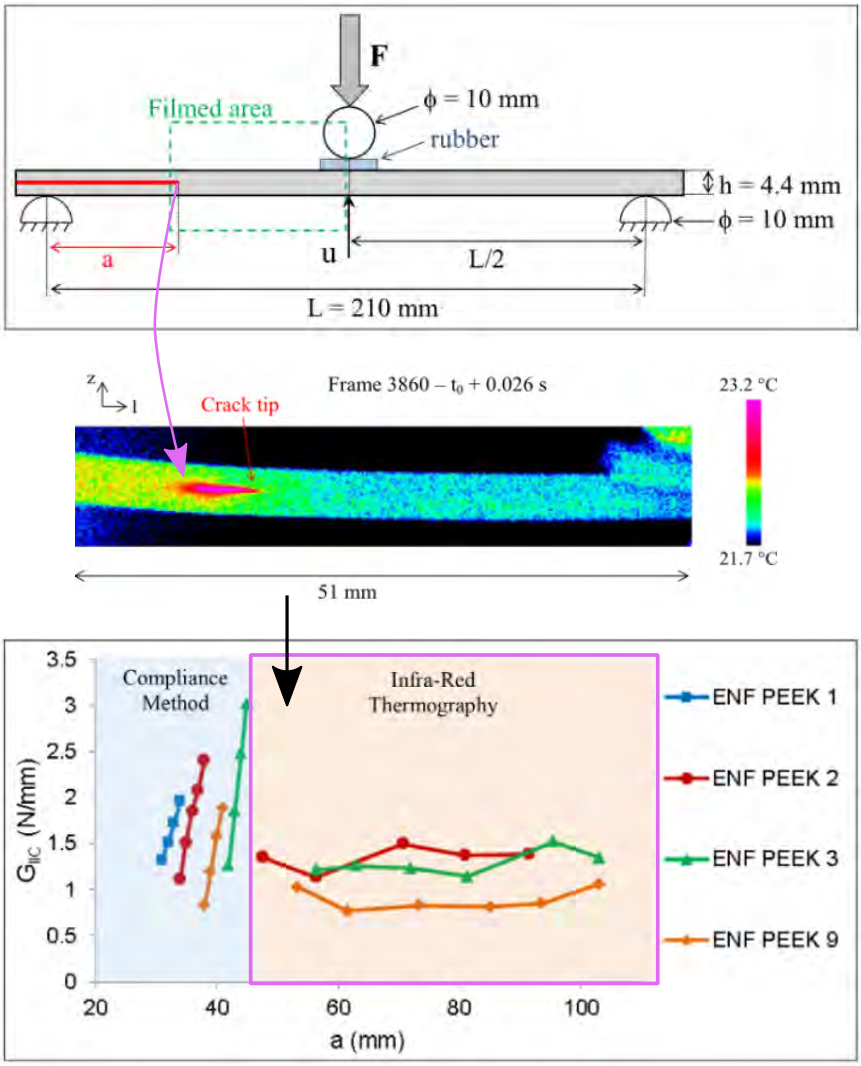

Figure 1.31: Experimental procedure performed in [Bouvet et al., 2020] for R curve reconstruction using IR thermography during an unstable crack propagation

in composite laminates, as it is possible to interrupt the test and perform inspections. Nevertheless, lots of care should be used by approximating an impact as a quasi-static indentation since materials could be sensitive to the loading rate effect.

Another solution to determine the damage scenario is the resort to numerical models using FEA. Indeed, these last decades several damage models have been developed by academics in order to predict the impact damages within a composite structure subjected to a LE/LV. Moreover, some models are capable of evaluating the residual strength by simulating a CAI test. Thus, in the next sections, an overview of the different damage modeling strategies and the simulation of LE/LV and CAI using FEA is presented.

1.3 Damage modeling and simulation of a LE/LV impact using FEA

1.3.1 Finite element model of a LE/LV impact

The modeling of a LE/LV test is usually performed using a FEM as shown in FIGURE 1.32. The components of the experimental setup (impactor, impact window and eventually rigid clamps or fixture) are modeled using rigid elements as they are supposed to be undeformable regarding the composite plate. Concerning the laminate, two strategies are feasible. The first one is a full 3D constitutive behavior with a solid element (C3D8) and the second solution is the use of conventional shell elements (S4).

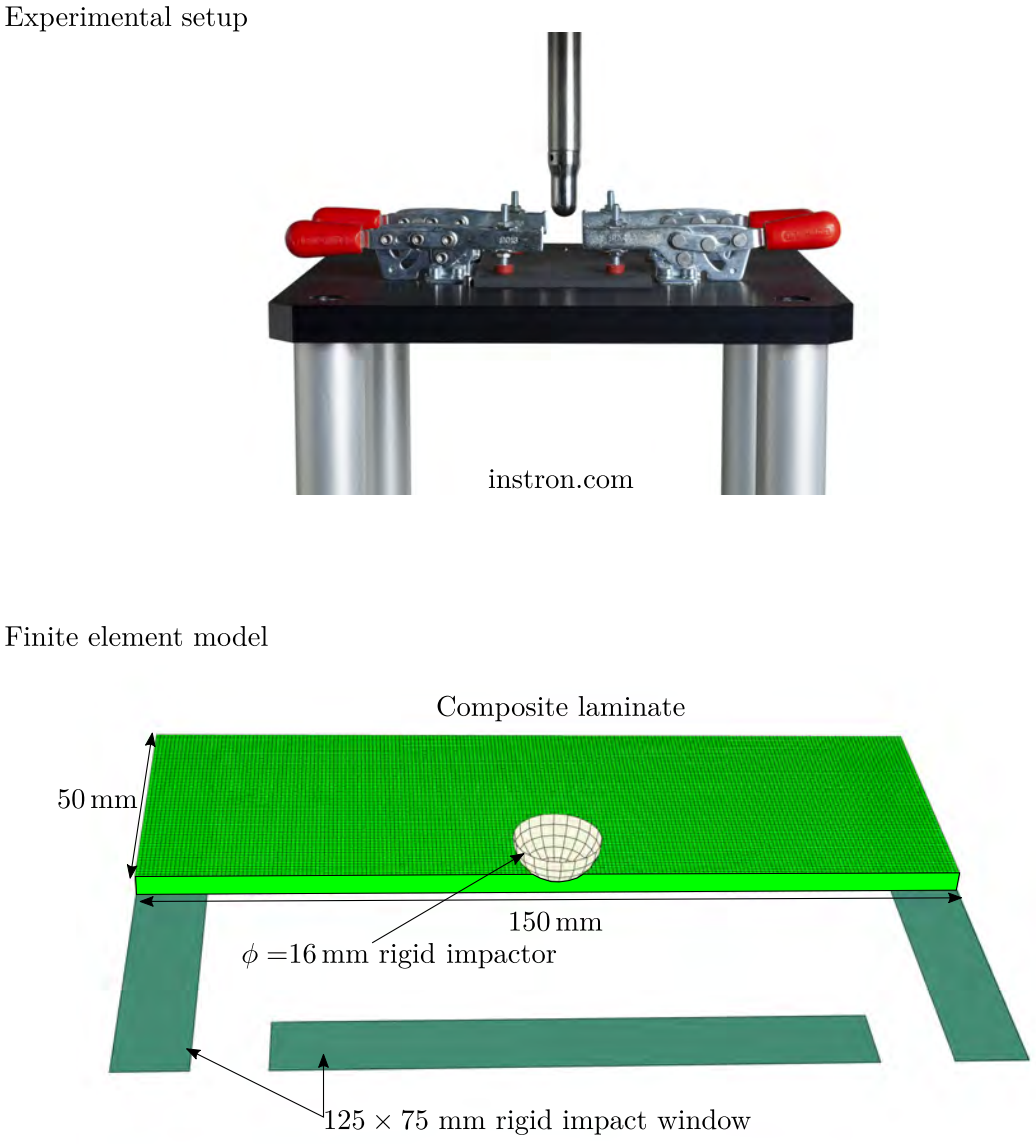

Figure 1.32: Classical FEM of a LE/LV impact test

1.3.1.1 Impact model using solid element

Using a 3D formulation for the element (with 3 degrees of freedom per node) allows the computation of all stress components, which is essential to model the matrix damage as in impact, the stress σ_{23} is mainly responsible for matrix damage. Impact damages are located near the impact zone. Mesh strategies are therefore adopted in the literature to save computational time. In [Abir et al., 2017], refinement near the damaged zone has been performed using regular and unstructured mesh. In [Bouvet et al., 2009], oriented mesh has been used to represent matrix cracking occurring in the laminate. As the plate undergoes bending during the impact loading, small mesh size is required to describe the deflection and avoid shear locking. Moreover, simulating laminates with numerous plies can lead to a costly computational problem. Consequently, a trade-off between the computational times and the modeling strategies is considered. Mesoscopic approach is commonly adopted in LE/LV simulations where each ply is meshed using one element in the thickness. However, it can require significant computational resources as the size of the FEM is large and the simulations are highly nonlinear. A solution adopted in some studies consists in using reduced integration [Feng and Aymerich, 2014, Lopes et al., 2016]. However, care must be taken when using reduced integration as high stress gradients are encountered in the thickness.

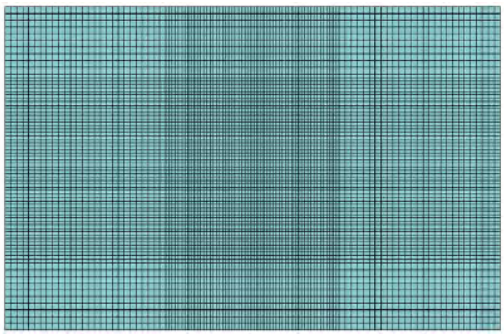

Regular mesh

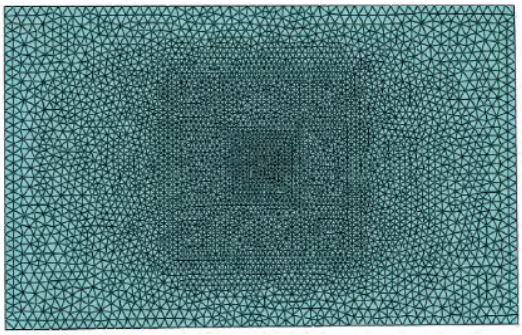

Unstructured mesh

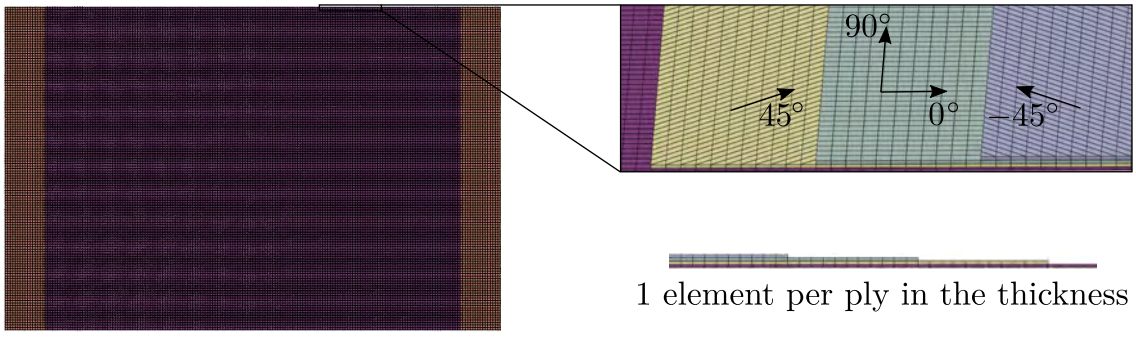

Oriented mesh

Figure 1.33: FEM strategies used in the literature for impact simulations, regular and unstructured mesh used in [Abir et al., 2017], oriented mesh used in DPM [Hongkarnjanakul et al., 2013]

1.3.1.2 Impact model using shell element

Although 3D FEM predicts a good impact response and damage shapes, it requires important computational means to simulate laminates with numerous plies or large panels. Thus, as industrials demonstrate an interest in having predictive tools to simulate damages within composite structures, in reasonable calculation times, authors have taken the plunge to simulate LE/LV impact using shell elements [González et al., 2018, Soto et al., 2018a, Thorsson et al., 2018, Baluch et al., 2019]. In [González et al., 2018], the authors have proposed a modeling strategy to simulate impact damages in thin plies using shell elements (S4R) in Abaqus. The authors have shown that the model captured the initial elastic stiffness; moreover, the peak load for each configuration was reproduced accurately. However, the model underestimated the prediction of damages (delamination). In [Thorsson et al., 2018, Baluch et al., 2019], the authors have chosen continuum shell elements (SC8R) in Abaqus. These elements are similar to 3D elements but with a shell formulation. They are more suitable for contact as they have eight nodes and defined top/bottom surfaces. In [Thorsson et al., 2018], despite an underestimated dissipated energy, the peak load was remarkably predicted. The authors have compared the out-of-plane displacement profile of the rear face at different times during the loading; they have shown that the simulated deformed shape was in good agreement with the experiment. The authors concluded with a comparison using inspection means and shown that the damaged shapes captured by the model were consistent with the information provided by inspections.

Thus, the main advantages of the shell are enriched kinematics which describes rotations $\Theta_{x,y}$ and the computational time saving regarding a 3D FEM. However, classical shell elements in commercial codes do not compute the out-of-plane stresses (Kirchoff-Love theory). However in impact, out-of-plane stresses (normal and shears) are responsible for the matrix and interlaminar damages. To overcome this issue, some authors have developed shell formulations with enriched kinematic assumptions (higher-order shear formulations) [Tabiei and Tanov, 2000] or a stress-based formulation [Bouteiller, 2022] but are not currently available in commercial codes.

1.3.1.3 Temporal discretization algorithm

During a dynamic analysis, the inertial effect is no longer neglected, the resolution of the hyperbolic problem is performed using the semi-discretized equation shown in Equation (1.4).

$$\mathbf{M}\ddot{\mathbf{d}} + \mathbf{C}\dot{\mathbf{d}} + \mathbf{K}\mathbf{d} = \mathbf{F}(t) \tag{1.4}$$

where $\mathbf{M}$ is the mass matrix, $\mathbf{C}$ is the viscous damping matrix, $\mathbf{K}$ is the stiffness matrix, $\mathbf{F}$ is the applied forces vector and $\mathbf{d}$, $\dot{\mathbf{d}}$ and $\ddot{\mathbf{d}}$ are respectively the displacement, velocity, and acceleration vectors. Equation (1.5) gives the initial conditions that have to be satisfied.

$$\begin{cases} d(t_0) = d_0 \\ \dot{d}(t_0) = \dot{d}_0 \end{cases} \tag{1.5}$$

Newmark family scheme The resolution of the dynamic problem is performed using a numerical scheme called time integration. It requires to discretize the

time $(t_{n-1}, t_n, t_{n+1}, \ldots)$. In a Newmark scheme EQUATION (1.4) is discretized using EQUATION (1.6).

$$\mathbf{M}a_{n+1} + \mathbf{C}v_{n+1} + \mathbf{K}d_{n+1} = F_{n+1} \tag{1.6}$$

Using the finite difference the displacement and velocity fields are calculated according to Equations (1.7) to (1.8)

$$d_{n+1} = d_n + \delta t v_n + \frac{\delta t^2}{2}[(1-2\beta)a_n + 2\beta a_{n+1}] \tag{1.7}$$

$$v_{n+1} = v_n + \delta t[(1-\gamma)a_n + \gamma a_{n+1}] \tag{1.8}$$

where $\mathbf{d_n}$, $\mathbf{v_n}$ and $\mathbf{a_n}$ are the approximations of $\mathbf{d}(t_n)$, $\dot{\mathbf{d}}(t_n)$, and $\ddot{\mathbf{d}}(t_n)$. The parameters (β, γ) determine the stability and accuracy properties of the algorithm under consideration. Different algorithms are possible as a function of the parameters (β, γ) [Hughes, 2012].

Parameter choices Unconditional stability is obtained when γ is chosen according EQUATION (1.9). It leads to an implicit resolution requiring a Newton-Raphson algorithm to obtain the solution. Convergence is ensured for linear problem. However, for highly nonlinear problems, especially if the problem is rough (contacts, damage mechanics), numerous iterations are required to obtain a possible convergence.

$$2\beta \geq \gamma \geq \frac{1}{2} \tag{1.9}$$

One of the limitation of such algorithms is that high-frequency dissipation is introduced for $\gamma \neq \frac{1}{2}$. However, a loss of first-order accuracy is obtained for $\gamma \neq \frac{1}{2}$. High frequencies can make parasitic artifacts undesirable; damping in this bandwidth can alleviate the problem.

The central difference scheme (Explicit dynamics) The well known explicit solver is a special case of the Newmark method. This time integration is classically used for short-time events such as crashes and high-velocity impact due to the rough nature of the problem. Therefore, by choosing in the Newmark framework $(\beta, \alpha) = (0, \frac{1}{2})$ and using a diagonalized mass matrix it allows an explicit resolution. The drawback is that the problem becomes conditionally stable, and there is no confirmation that the dynamic equilibrium path is computed accurately. The stability is ensured by satisfying the Courant–Friedrichs–Lewy (CFL) criterion as shown in the EQUATION (1.10)

$$\delta t = \frac{2}{\omega_{\text{crit}}} \tag{1.10}$$

where δt is the time step, ω_{crit} is the maximal natural frequency of the FEM. ω_{crit} is expensive to compute. It can be proved that $\omega_{\text{crit}} \geq \omega^e_{\text{crit}}$ where ω^e_{crit} is the maximal natural frequency of the critical element. In practice, it is preferred to use ω^e_{crit}. This condition introduces a dependency of the time step to the element size. The smaller the element size, the lower the time step and the higher the computational cost of the finite element problem.

α-Method (Hilber-Hugues-Taylor Method) As highlighted for Newmark schemes, a trade-off between second order accuracy and high-frequency dissipations is needed. The α method allows conserving the second order accuracy while introducing damping for high-frequency. The EQUATION (1.6) is modified by introducing a parameter α as shown in the EQUATION (1.11).

$$\mathbf{M}a_{n+1} + (1+\alpha)\mathbf{C}v_{n+1} - \alpha\mathbf{C}v_n + (1+\alpha)\mathbf{K}d_{n+1} - \alpha\mathbf{K}d_n = F(t_{n+1} + \alpha\delta t) \quad (1.11)$$

By choosing $\alpha = 0$ the classical Newmark scheme is found. An unconditionally stable and second-order accurate is found using the parameter in EQUATIONS (1.12–1.14). Moreover, high frequency dissipation is introduced ($\gamma > \frac{1}{2}$) for $\alpha < 0$.

$$\alpha \in \left[-\frac{1}{2}, 0\right] \quad (1.12)$$

$$\gamma = \frac{1}{2}(1 - 2\alpha) \quad (1.13)$$

$$\beta = \frac{1}{4}(1 - \alpha)^2 \quad (1.14)$$

1.3.2 Damage modeling

The modeling of each damage mechanism (matrix cracking, delamination, fibre breaks) is implemented using damage laws. These damage laws are first established at the Gauss point scale before being implemented in a finite element code. The first step ensures that :

- The thermodynamical framework is fulfilled (irreversible nature of the damage);
- The different stages of the law are respected (elastic phase before the onset of damage, post-peak softening stage);

Two sorts of formalism can be found. The first one is continuum damage mechanics (which does not introduce any discontinuity in the mesh). The second one is discrete damage modeling (failure creates a discontinuity in the mesh). The FIGURE 1.34 presents the two different frameworks for discrete and continuum damage. An overview of the different damage modelings encountered in composite laminates is presented in the following.

1.3.2.1 Delamination modeling

As explained in the previous part, the delamination is a crucial damage mechanism; it characterizes the damage of the interface that bonds two plies. Thus, the fracture path is commonly known. Two modeling strategies exist, The first one is based on fracture mechanics and the second is based on damage mechanics.

Fracture mechanics approach For instance, the Virtual Crack Closure Technique (VCCT) allows calculating the energy release rate. It has been used in [Bouvet et al., 2009] to determine the critical energy release rate for a double cantilever beam test (DCB). However, as far as we know, this method has not been extended

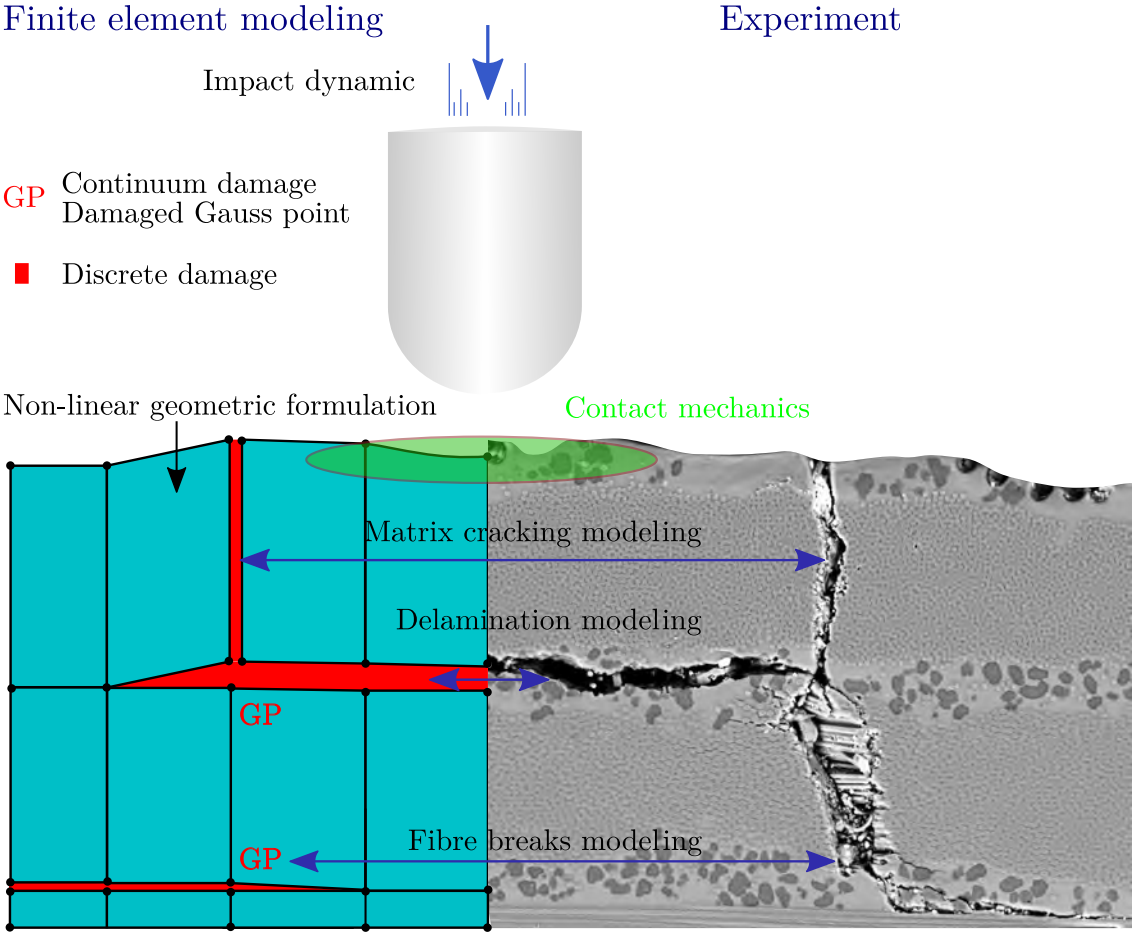

Figure 1.34: Modeling strategies for the different damages and nonlinearities occurring in LE/LV impact

to LE/LV impact simulations. Indeed, the first drawback is that a crack has to be inserted for this methodology. In impact, not all the interfaces are delaminated; therefore, it is impossible to guess where cracks must be positioned. Besides, oscillatory singularity exists for a crack located at the interface between two different materials. The calculated strain energy release rate in modes I and II depend on the mesh size near the crack tip. [Krueger et al., 2013] have proposed some practical rules to overcome this problem by restricting the element size in front of the crack tip regarding the thickness. The authors have shown that minimal variation of the mode mixity is observed by respecting the criterion presented in EQUATION (1.15). Nevertheless, it introduces a mesh size condition:

$$\frac{1}{20} < \frac{\delta a}{h} < 1 \tag{1.15}$$

where δa is the element size ahead from the crack tip, h is the thickness of the ply.

Damage mechanics approach The other delamination modeling strategy is based on damage mechanics using CZM. Cohesive elements of a defined thickness are inserted at the interface between two plies, as shown in FIGURE 1.35. Usually, the element uses zero thickness. The element technology is eight nodes with four integration points. CZM allows the onset and the propagation of the delamination

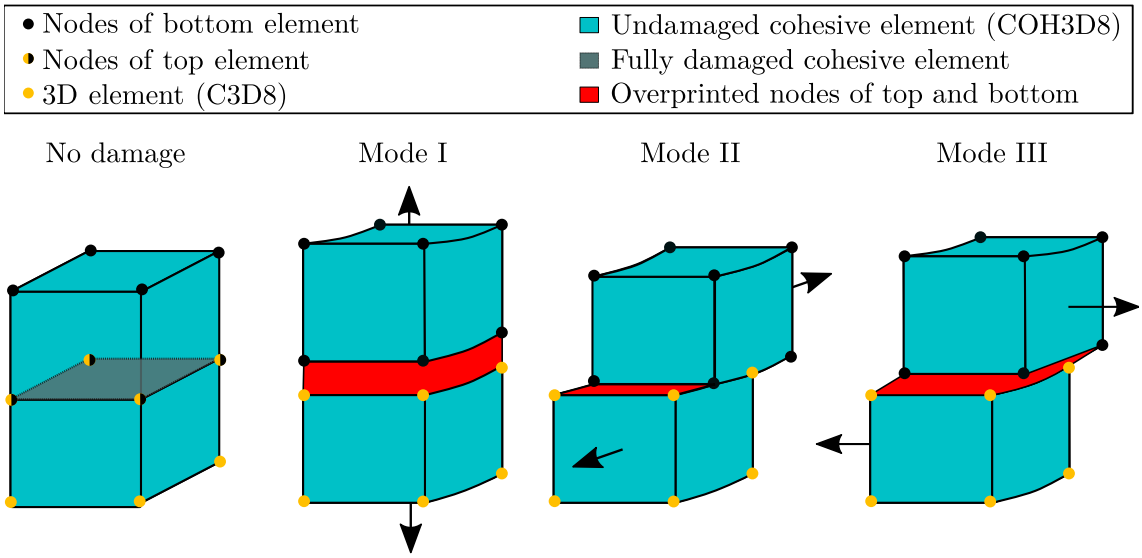

Figure 1.35: Cohesive element schematization and failure modes encountered in CZM

to be modelled. A traction separation law [Hillerborg et al., 1976] is used with two criteria, one defining the damage onset at σ_c, and one governing the energetic dissipation G during the post-peak softening stage, as illustrated in FIGURE 1.36. The formulation is different from classical damage mechanics laws [Hou et al., 2001] as it is expressed in stress-displacement jumps ($\sigma - \Delta u$). Consequently, the integration of this law provides a surface energy density ($\mathrm{J\,mm^{-2}}$), which allows the clinging to fracture mechanics with the concept of energy release rate G_c. A damage variable d characterizes the interface state. The damage variable affects the numerical stiffness K^{eff} linearly. When d=0 the interface is sound, $d = 1$, the interface is fully damaged, and a surface energy equal to $\mathrm{G_c}$ has been dissipated. FIGURE 1.35 presents the different modes. When the modes are combined (mixed-mode loading), the CZM shows its powerful interest as the mixed-mode law parameter (σ_c, G_c) shown in gray in FIGURE 1.36 are computed using mixed-mode initiation and propagation criteria [Camanho and Dávila, 2002] [Turon et al., 2010].

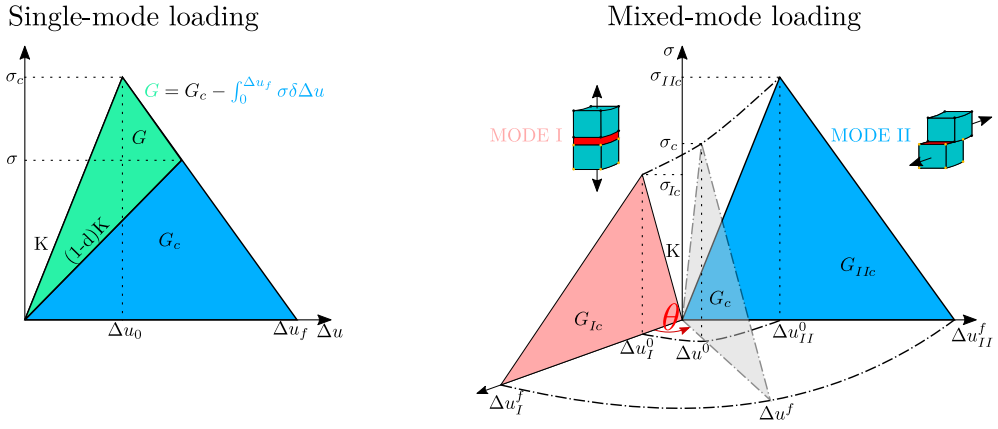

Figure 1.36: Traction-separation law defined for single and mixed-mode loadings

Drawback of the CZM The first disadvantageous factor of CZM is the mesh requirement. A process zone is required to capture the softening ahead of the crack tip accurately. The process zone corresponds to the area where $d \in [0, 1]$. The damage gradient in the process zone is characterized by a cohesive zone length l_{cz} where $l_{cz} \propto G_c/\sigma_c^2$. The process zone needs a sufficient number of elements to capture the gradient accurately. In [Turon et al., 2007], empirical rules have been established to estimate accurately the process zone with an element size $h < \frac{l_{cz}}{3}$. It leads to a dependence of the process zone on the interfacial properties. The second drawback of the CZM is the numerical convergence difficulties encountered with this model. In [Germain, 2020], the author has studied the convergence rate for classical DCB and mixed-mode bending tests (MMB) simulated in an in-house FE code. It has been shown that a high amount of iterations is required to obtain the convergence of the increment using a Newton-Raphson algorithm. Indeed, by analyzing the convergence rate at each iteration, the author concluded that the delamination progress bounds the convergence. In other words, the delamination cannot propagate more than one element between two iterations. Besides, he proposed a practical recommendation to deal with unstable delamination propagation using an implicit solver. Classical snap-backs are shown when delamination becomes unstable, making the convergence unlikely. Thus, inertial effects are introduced by switching the analysis from static to dynamic, reducing the instability's roughness at the cost of very low time increments.

Another possibility consists in introducing viscosity in the traction-separation law; the problem becomes rate-dependent by bounding the damage variable [Chaboche et al., 2001]. The critical limits of this method are that viscosity induces energy dissipation, and the mechanical solution must not be degraded when a viscous parameter is introduced.

1.3.2.2 Matrix cracking modeling

The modeling strategy of intraply matrix cracking is more divided within the scientific community than the delamination modeling. Two methodologies exist, the first is discrete damage modeling, and the second uses continuum damage mechanics. Hereafter, we will discuss the capabilities of these models to predict matrix damages in composite laminates.

Discrete damage approach One of the specificities of UD composite laminates is that the topology of the matrix cracks is parallel to the fibres. Thus, it is an advantage to model this damage using discrete cracks. In [Hongkarnjanakul et al., 2013], an oriented mesh parallel to the fibre direction in each ply has been developed. Cohesive elements parallel to the element longitudinal 1-direction are then inserted between the elements. A schematic of the strategy adopted is presented in FIGURE 1.37. The cohesive element integrity is verified thanks to a failure criterion applied on the integration point of the volume element neighboring the cohesive element. The failure criterion is a classical Hashin criterion presented in EQUATION (1.16). By satisfying this criterion, it leads to the brittle failure of the cohesive

element leading to the matrix crack.

$$f_2 = \left(\frac{\langle \sigma_{22} \rangle_+}{Y^R}\right)^2 + \left(\frac{\sigma_{12}}{S^R}\right)^2 + \left(\frac{\sigma_{23}}{S^R}\right)^2 \tag{1.16}$$

where $\langle \cdot \rangle_+$ is the Macaulay brackets. In [Sun et al., 2016], quasi-static indentations

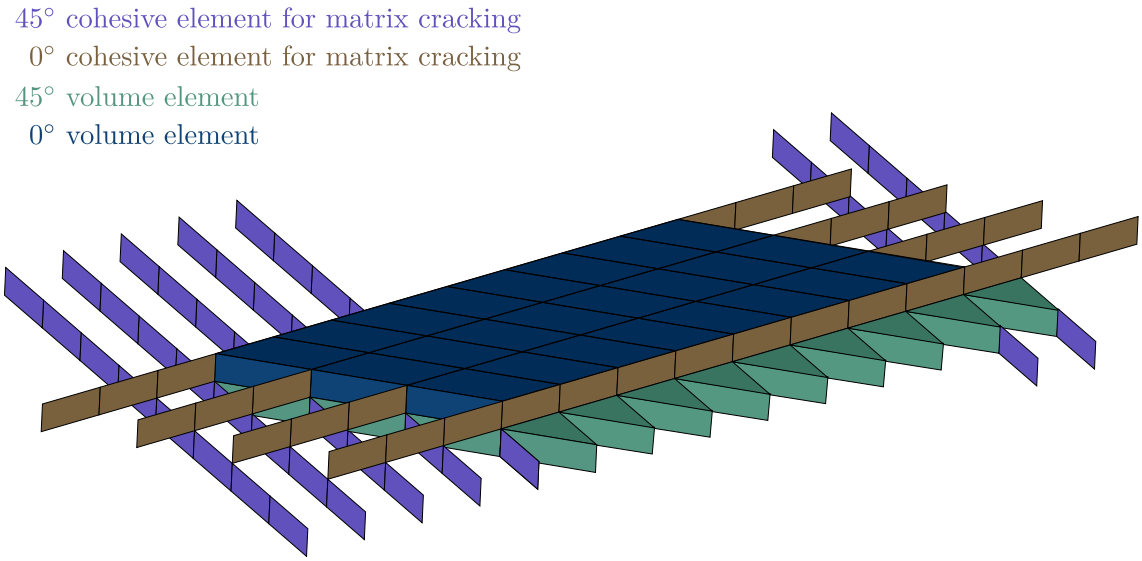

Figure 1.37: Matrix cracking modeling in DPM

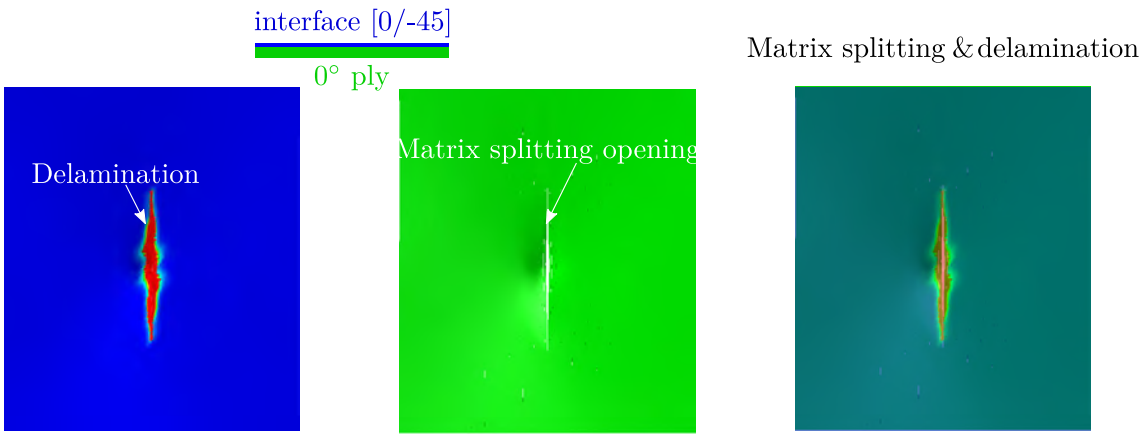

Figure 1.38: Interaction between matrix splitting occurring on the lower 0° ply with the delamination of the 0°/45° interface above. Image generated using DPM

have been simulated with different models. The models have been defined in function of the number of intralaminar cohesive elements inserted to model the matrix splitting occurring (from 0 to 6-splits). In this study, the authors used a traction-separation law presented previously with a mixed-mode quadratic criterion for the onset of damage and a mixed-mode power-law criterion for the damage propagation. The authors have shown that the model using 6-splits obtained the best results; it allows capturing accurately the delamination induced by matrix cracks. In impact or QSI, there is a strong coupling between matrix cracking and delamination. In FIGURE 1.38, matrix splitting occurring in the lower ply of a laminate is modeled using discrete elements. The delamination follows the matrix splitting by superposing

the upper cohesive interface [0°/45°], the delamination follows the matrix splitting. Indeed, the use of discrete damage for matrix cracking modeling with CZM allows representing the strong coupling between the two mechanisms.

Another method to simulate matrix cracking while guaranteeing the mesh continuity is X-FEM family. The latest improvement of X-FEM method (RX-FEM) developed in [Iarve et al., 2011] has been used in [Mollenhauer et al., 2020]. The authors have simulated Compact tension (CT) test with an arbitrary mesh, RX-FEM modeled the matrix cracking. The authors have considered the LaRC04 failure criterion for matrix cracking onset; once satisfied, a crack is inserted while conserving the mesh continuity. This method is based on an enrichment of the degrees of freedom of the displacement node. A gradient zone replaces the surface of each crack; the fracture surface energy is computed using cohesive energy in the gradient zone. The propagation is controlled by a traction-separation law using node displacement jumps. The authors have shown a striking correlation with the μ-CT as shown in FIGURE 1.39.

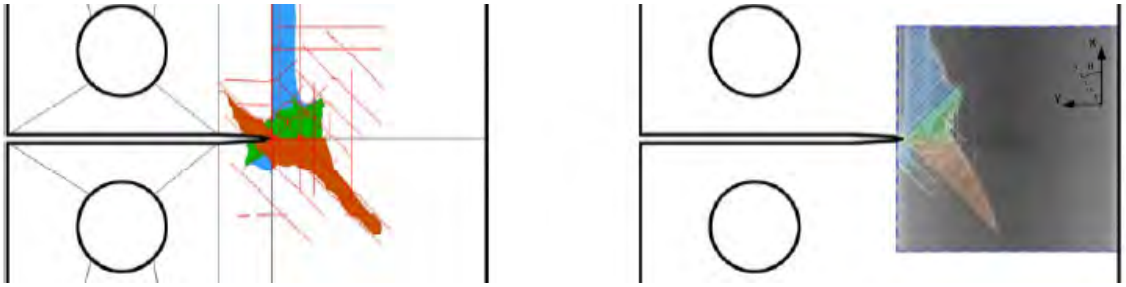

Figure 1.39: Comparison of damages obtained using RX-FEM on the left and X-ray on the right [Mollenhauer et al., 2020]

To summarize, discrete matrix cracking represents the topology of a matrix crack very well. However, it has a cost, heavy computational times are required as the matrix crack strips are inserted between two neighboring volume elements, and nodes are doubled. Another drawback is a strong hypothesis on the crack fracture plane. In the literature the angle of the crack plane depends on the loading state, as shown in [Puck and Schürmann, 2002]. The cohesive elements are inserted parallel to the longitudinal direction of the element with presupposed 90° fracture crack plane, which allows for making a not complex meshing. Of course, RX-FEM solves the two previously exposed problems with the use of LaRC04 criterion, enabling to determine the crack angle plane and mesh continuity without nodes doubling. However, its implementation in commercial codes is not available. The continuum damage framework provides the flexibility of damage laws without shape's restriction. At the same time, it is more suitable for diffuse damages as no guess on the crack location is needed.

Continuum damage approach By conserving the mesh continuity, Continuum damage model (CDM) is used to predict the failure and the post-peak softening due to a crack. The damage model is composed of a failure criterion as presented for the discrete model. Once the criterion is fulfilled, the failure is initiated, and the softening is obtained using a damage law evolution; this law controls the growth of the damage variable. Then, the damage variable affects the stiffness/compliance

components to express the damaging effect. Different scales for CDM exist (microscopic, mesoscopic, and macroscopic scale). The better compromise found in the literature is CDM using the mesoscopic scale, as it describes the damage mechanisms accurately at the ply scale. Therefore, two frameworks will be discussed. The first is a mesoscopic framework (at the ply scale), and the second is a multiscale framework.

Mesoscopic CDM In the mesoscopic damage model, the ply is homogenized. A failure criterion at the ply scale is considered. Several failure criteria have been developed to predict the transverse cracking for combined loadings [Puck and Schürmann, 2002, Camanho et al., 2013, Maimí et al., 2007]. In [Camanho et al., 2013], the authors have used two different transverse cracking criteria depending on the sign of the transverse stress. They used a modified formulation from [Puck and Schürmann, 2002] ϕ_{2-} for combined shear and transverse compressive stresses. Indeed, rather than using the strength measured in the UD test (S_L, S_T), they have adopted the *in situ* strengths (Y_c, S_T), which depend on the ply thickness and are calculated numerically. For combined shear and transverse tensile stresses, the criterion proposed in [Catalanotti et al., 2013] has been adopted ϕ_{2+}. In [Maimi et al., 2008], the LaRC04 criterion has been considered for the prevision of the failure and the fracture ply angle. The damage model finds its foundation in the irreversible thermodynamics framework. The positiveness of the damage rate $\dot{d} > 0$ ensures the thermodynamic framework (damage could only grow). Two different fracture plane angles are considered (0° for transverse tensile stress or shear stress combined with minor transverse compressive stress and 53° for uniaxial transverse compressive stress). For the softening regime, the author used an exponential damage law with a crack band formulation to ensure the correct energy dissipation within the element.

Multiscale CDM Multiscale approaches represent the behavior of composite materials at the scales where the damage mechanisms are observed [Ladevèze et al., 2017, Laurin et al., 2013]. It links the damaged behavior at mesoscopic (transverse crack) and microscopic (fibre/matrix debonding) scales. In [Ladevèze et al., 2017], the mesoscopic damage model is formulated using the free energy per unit volume E_d. Two mechanisms, diffuse damage and transverse cracking damage, are modeled. Their driving forces are calculated by deriving the free energy according to their damage variables, as shown in Equation (1.17). Diffuse damage represents the failure occurring at microscale in the matrix. Three damage variables define this mechanism (d for in-plane transverse shear, d' for transverse tensile stress, and d_{23} for out-of-plane shear). The damage variables are calculated using an evolution law, as presented in Equation (1.18), where Y_0, Y_c are material parameters. Moreover, inelastic strain is modeled using a plasticity model with isotropic hardening.

$$Y_d = \frac{\partial E_\mathrm{d}}{\partial d} \tag{1.17}$$

$$d = \frac{\sqrt{Y} - \sqrt{Y_0}}{\sqrt{Y_\mathrm{c}} - \sqrt{Y_0}} \tag{1.18}$$

Multiscale modeling takes part in transverse cracking damage. Indeed, the authors have developed a micro-meso bridge to represents the mechanical degradations occurring at the microscale in the mesoscale modeling. The idea is reported

in FIGURE 1.40. Two cells are considered. Discrete cracks (transverse cracking and delamination) are considered on the left. A mesoscopic approach is considered (homogenization at the ply scale) on the right. The same loading is applied for both cells. The goal is to establish the equivalence between these two modeling by moving-up damage effects occurring with the discrete vision toward the mesoscopic diffuse one. Three additional mesodamage variables are introduced for the degradation due to transverse cracking occurring at the microscopic cell. These three damage variables ($\bar{d}_{12}$, $\bar{d}_{22}$, $\bar{d}_{23}$) depend on functions defining the microcracking rate ρ. These functions are obtained numerically thanks to the micro/meso bridge. This micro-meso bridge introduces a physical meaning by introducing the transverse cracking rate. An opening of this model has been performed toward quasi-static indentation in [Abisset, 2012] and [Priasso, 2017].

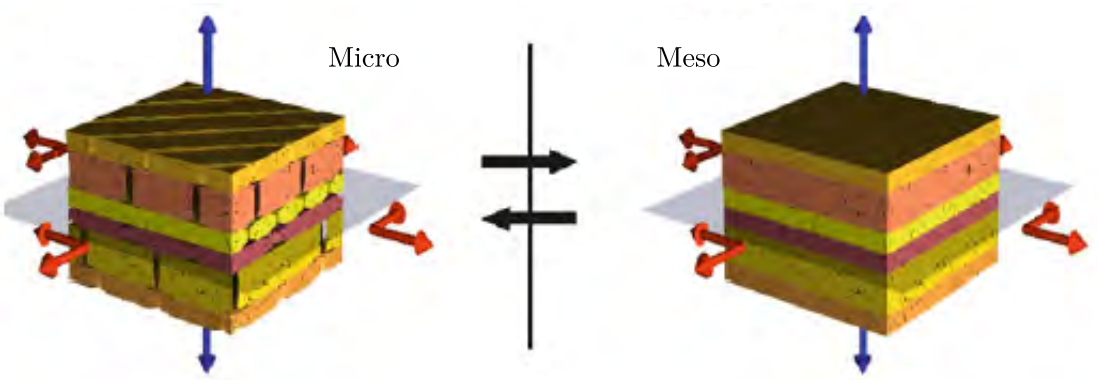

Figure 1.40: Two different scales presented for the micro-meso bridge establishment [Ladevèze et al., 2017]

Another multiscale model developed at ONERA within World Wide Failure Exercise III (WWFE) [Laurin et al., 2013] is presented. The proposed approach defined by the authors considers a 3D progressive damage model based on observable physical variables. These two variables are the normalized crack density $\bar{\rho}$ and the local delamination induced by matrix crack $\bar{\mu}$. The authors have considered a nonlinear visco-elastic model to simulate the viscous behavior of UD ply during off-axis loading occurring before damage. The nonlinear nature of the law is explained firstly by the inherent behavior of the matrix. The second source of nonlinearity describes the effect on the viscous compliance tensor of the micro-damage occurring at the microscale (fibre-matrix debonding, matrix cracks). Moreover, a permanent strain is introduced in the model to express the residual strain induced by that micro-damage. The damage model considers four inter-fibre failure (IFF) modes. There are characterized by their failure criteria (f_2^-, f_3^+, f_3^-, f_2^+). The criterion f_2^+ for transverse tensile strength, or combined low compressive and high shear stresses, involve the use of $\bar{\rho}$ and $\bar{\mu}$, which are represented in FIGURE 1.41. These two damage variables are strongly connected. The local delamination is initiated only at the tips of transverse cracks. Besides, local delamination tends to slow down the evolution of the transverse matrix crack density. The authors have considered three thermodynamic forces (y_I, y_{II}, y_{III}), which depend respectively on the transverse stress σ_{22}, the in-plane shear stress σ_{12}, and the out-of-plane shear stress σ_{23}. The damage is onset if the thermodynamical forces exceed the thermodynamical force

thresholds. The threshold depends on the ply thickness h as mentioned previously. Once the failure criterion is fulfilled, $\bar{\rho}$ and $\bar{\mu}$ are calculated using an implicit formulation. Then, the softening is performed by increasing the compliance tensor components. The damage effect on the compliance components is quantified using a Finite element (FE) numerical approach. A representative periodic cell is defined for a given crack density and the associated local delamination rate.

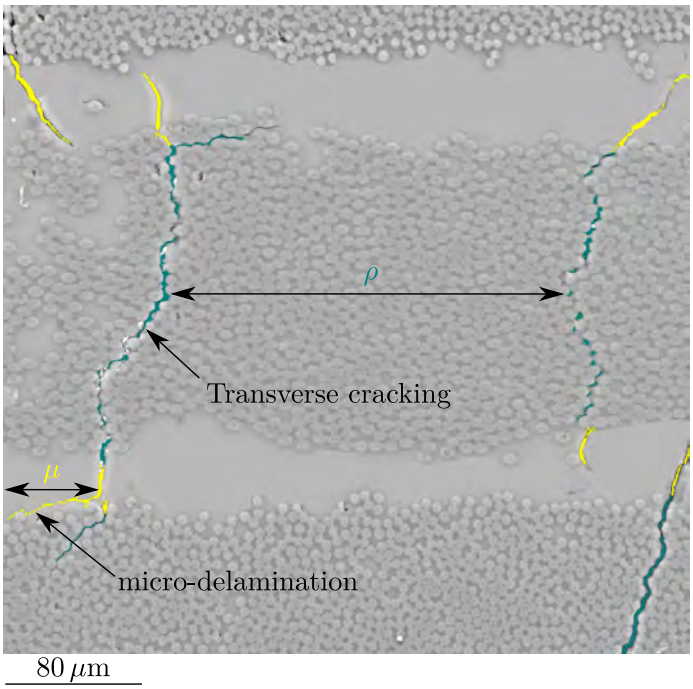

Figure 1.41: Matrix cracking density and micro-delamination described in a micrograph observation using a SEM [ONERA]

Reflection on the different matrix cracking modeling approaches Two damage modeling approaches have been presented for matrix cracking, showing their strength and limitation. Discrete damage allows capturing with high fidelity the matrix cracking. Moreover, the discontinuity created after the failure reproduces the load transfer observed experimentally. However, it requires critical algorithmic means as cohesive elements are inserted between two neighboring elements.

The CDM allows freedom in defining the architecture of the damage model. The continuum mechanics framework is available as no discontinuity is introduced in the mesh. For diffusive damage, the CDM shows a particular interest, no guess on the damage location is needed. However, CDM faces some issues. The first is the localization problem during strain-softening. Indeed, if the damage model considers strain-softening constitutive behavior, it will lead to damage localization in an element strip. The problem introduces a spurious mesh-size dependence which can lead to null dissipated energy if the element size tends to zero. In the next section, more details will be given on this pathology and how to overcome this issue. The second drawback of CDM is the material parameters identification. The higher the number of parameters, the more complex the identification, and the farthest the implementation in commercial codes and its utility for industrials. A primary focus in damage models establishment with a reasonable complexity is necessary. Finally,

for complex loading, where interactions between damages will occur as for impact, CDM suffers from a lack of information exchanges between the different damages. Indeed, the interaction observed experimentally between matrix cracking and delamination is not reproduced when intraply damage mechanisms are modeled using CDM and delamination with discrete damage (cohesive element). Strategies exist to overcome this situation, such as those developed in [Ladevèze et al., 2017] and applied in [Le et al., 2018]. The authors have performed a methodology mixing CDM and discrete damage to predict the failure of a composite plate with a geometrical accident (open hole plate or double-edge notched laminates). Large splittings occur around the critical zone, and CDM cannot capture the discrete crack due to splitting resulting in no accurate interaction with delamination. Therefore, the authors have used a criterion to identify each point where transverse microcracking density is due to shear. Once the points are determined, the simulation is restarted with discrete cohesive cracks inserted at the location where the criterion was fulfilled. The drawback of that methodology is that possible re-meshing is required to be compatible with the split growth. Another possibility that will be discussed later is to use an artificial coupling between intraply CDM and CZM by reducing the mechanical interface property when the volume element above or under the interface is damaged.

1.3.2.3 Fibre breaks modeling

The fibre breaks are a considerable dissipative mechanism. The non-inclusion of their modeling in simulations will lead to incorrect failure scenario establishment. As failure mechanisms differ in traction and compression, academics use different laws to describe the behavior.

Fibre breaks in traction Different approaches exist to treat the fibre failure, in [Hallett et al., 2009] the authors have used a Weibull statistical framework. The theory proposed by Weibull supposed that statistically distributed flaws govern the strength of fibres. The failure criterion is expressed according to a probability density law where the assumption of equal probability of survival at σ_{failure} is assumed. The criterion is evaluated at post-processing at the centroid of each element. Another approach is based on CDM [Laurin et al., 2013, Hongkarnjanakul et al., 2013, Pinho et al., 2006, Maimí et al., 2007] for instance. In [Pinho et al., 2006], the authors have considered a simple maximum stress criterion for the onset, whereas in [Maimí et al., 2007, Hongkarnjanakul et al., 2013], a maximum strain criterion was considered for the onset. The approach adopted in [Laurin et al., 2013] is more enriched, a strain criterion is considered, and microdamages occurring in the matrix are degrading the failure strain. Concerning the softening part of the model, crack band theory governs the softening, which allows dissipating the right amount of energy in [Maimi et al., 2008, Hongkarnjanakul et al., 2013, Pinho et al., 2006]. In [Laurin et al., 2013], a damage variable is calculated using a damage kinetic function. The softening is taken into account by increasing the compliance component tensor in direction 1.

Fibre breaks in compression The approach used for longitudinal compressive failure is more complicated. The neighboring state of the matrix strongly influences fibre behavior. Moreover, fibre is susceptible to buckle in the plane 1-2 (red) or 1-3

(yellow) as illustrated in FIGURE 1.42. In [Laurin et al., 2013], the failure criterion f_{1-} determines the failure plane using the EQUATION (1.19).

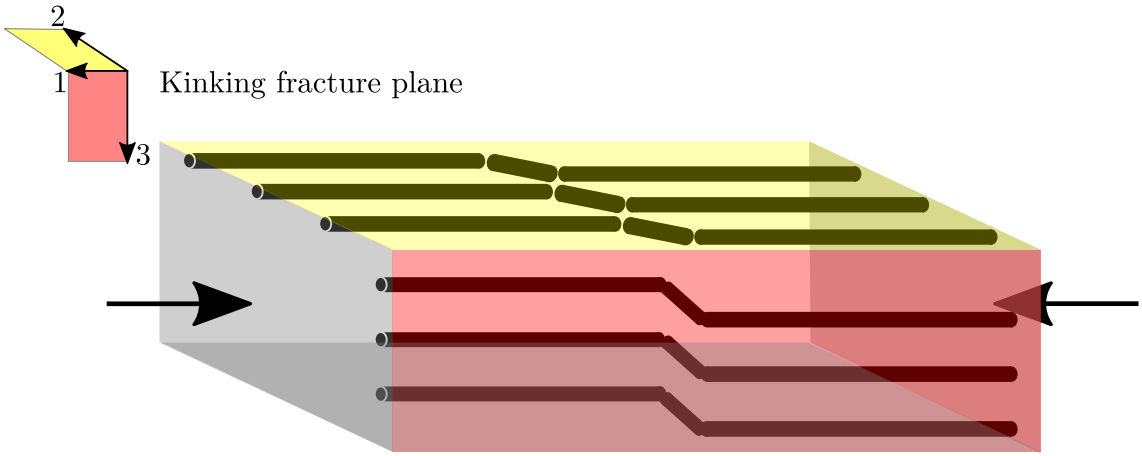

Figure 1.42: Possible fracture planes occurring during fibre kinking

$$\max_{i=2,3}\left(\sqrt{g_n^{1-}(\sigma_{11}-\sigma_{ii})^2+g_t^{1-}\tau_{1i}^2}\right) \tag{1.19}$$

The originality of this criterion is the awareness of transverse compressive normal stresses which prevent fibre from buckling using the material parameter g_n^{1-}, g_t^{1-} is a material parameter expressing the influence of shear on the kinking.

The presence of debris after failure has conducted some authors to introduce a residual strain to underline the inelastic character of the fibre kinking. In [Rivallant et al., 2013a], the damage law is illustrated in FIGURE 1.43. Once the strain reaches ε_C^R, the softening is initiated. The residual strain ε_{res} starts to increase. When the stress reaches the critical crushing stress σ^{cru}, the residual deformation is increased at each increment by $\delta\langle\varepsilon\rangle_-$. The residual strain accounts for the debris induced by the fibre kinking.

1.3.2.4 Regularization in presence of material instability

As presented previously, one of the main drawbacks of CDM is the damage localization which results in spurious mesh dependency when the mechanical problem is discretized using FEM. Before introducing the regularization methods to overcome this material instability, a first focus on how the mechanical problem becomes ill-posed is discussed.

The linear rate boundary value problem The mechanical problem formulated in velocity is presented in EQUATIONS (1.20–1.22).

$$\dot{\boldsymbol{\varepsilon}} = \frac{1}{2}\left(\nabla\mathbf{v}+\nabla^T\mathbf{v}\right) \tag{1.20}$$

$$\rho\dot{\boldsymbol{\gamma}} = \boldsymbol{\nabla}\cdot(\dot{\boldsymbol{\sigma}})+\rho\dot{\boldsymbol{f}} \tag{1.21}$$

$$\dot{\boldsymbol{\sigma}} = \mathbb{C}:\dot{\boldsymbol{\varepsilon}} \tag{1.22}$$

where $\dot{[\cdot]} = \dfrac{\partial[\cdot]}{\partial t}$, $\boldsymbol{\varepsilon}$ is the strain, $\boldsymbol{\sigma}$ is the stress, ρ is the density, $\boldsymbol{f}$ is the volume force and $\mathbb{C}$ is the fourth-order stiffness tensor. The stability of the problem is guaranteed

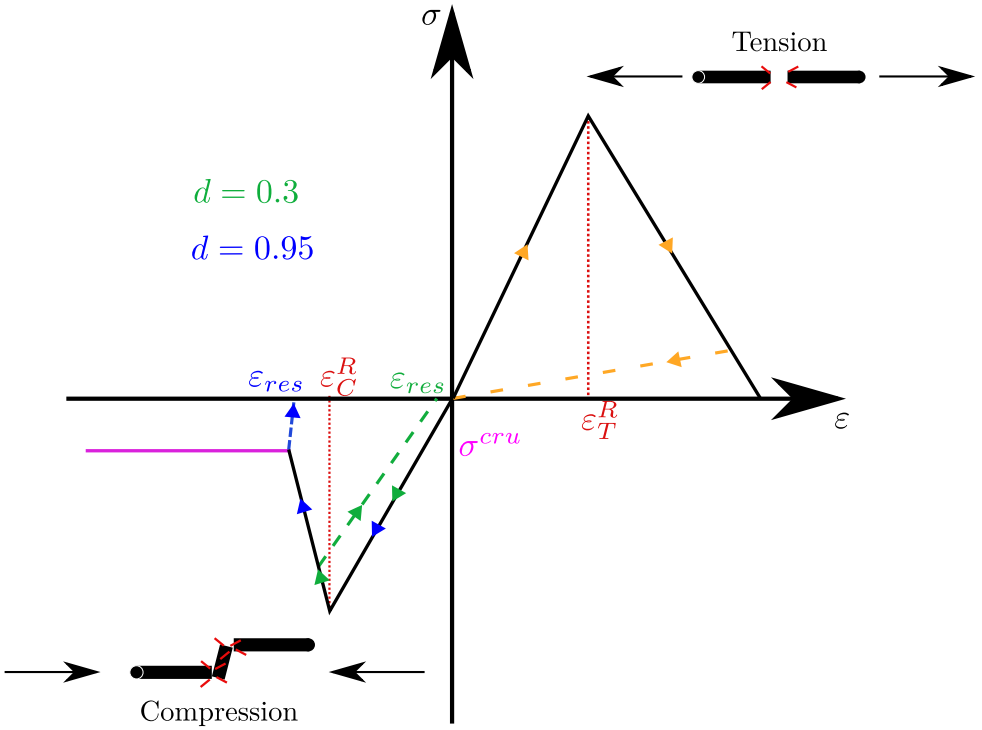

Figure 1.43: Damage law for fibre breaks in traction and compression in DPM

by the HILL local condition defined in EQUATION (1.23)

$$\dot{\boldsymbol{\sigma}} : \dot{\boldsymbol{\varepsilon}} > 0. \tag{1.23}$$

Using EQUATION (1.22), it leads to EQUATION (1.24) which ensures the uniqueness of the solution if and only if for whatever values of $\dot{\boldsymbol{\varepsilon}}$, the positive-definiteness of the material stiffness tensor is fulfilled:

$$\dot{\boldsymbol{\varepsilon}}^T : \mathbb{C} : \dot{\boldsymbol{\varepsilon}} > 0. \tag{1.24}$$

In general, EQUATION (1.24) is satisfied for a linear elastic problem, the uniqueness of the solution is ensured. However, the uniqueness is not guaranteed when the problem includes strain-softening or a material constitutive model leading to a non-symmetric stiffness tensor. EQUATION (1.24) is violated, which leads to material instability with bifurcation modes.

The nonlinear rate boundary value problem The framework of CDM with a damage variable d which affects the stiffness tensor components is now considered. Let's call $\mathbb{H}$ the damaged stiffness tensor for now with $\mathbb{H} = \mathbb{C}(d)$.

$$\dot{\boldsymbol{\sigma}} = \mathbb{H} : \dot{\boldsymbol{\varepsilon}} \tag{1.25}$$

Let's consider a plate in traction at t_0 with a homogeneous state (σ_0, ϵ_0, $\dot{\sigma_0}$, $\dot{\epsilon}_0$) as shown in FIGURE 1.44. At time t_1 a bifurcation occurs, resulting in the creation of a discontinuity band characterized by the state (σ_0, ϵ_0, $\dot{\sigma_1}$, $\dot{\epsilon}_1$) and its normal $\mathbf{n}$. At the two interfaces $\Gamma_1(t)$ and $\Gamma_2(t)$, the continuity has to be controlled using EQUATION (1.26). Hadamard's conditions which define the conditions for jumping

across a discontinuity surface, are used for $\boldsymbol{\gamma}$, $\dot{\boldsymbol{\varepsilon}}$ and $\dot{\boldsymbol{\sigma}}$ in EQUATION 1.27. Then, by linking the two last EQUATIONS of 1.27, it leads to EQUATION (1.28).

$$\dot{\boldsymbol{\sigma}}_1 \boldsymbol{n} = \dot{\boldsymbol{\sigma}}_0 \boldsymbol{n} \iff [\![\dot{\boldsymbol{\sigma}} \boldsymbol{n}]\!] = 0 \tag{1.26}$$

$$\begin{cases} [\![\dot{\varepsilon}_{ij}]\!] = \frac{1}{2}(g_i n_j + g_j n_i) \\ [\![\boldsymbol{\gamma}]\!] = -c\boldsymbol{g} \\ [\![\dot{\boldsymbol{\sigma}}_{ij,k}]\!] = \alpha_{ij} n_j \\ [\![\dot{\boldsymbol{\sigma}}_{ij}]\!] = -c\alpha_{ij} \end{cases} \tag{1.27}$$

$$c[\![\boldsymbol{\nabla} \cdot (\dot{\boldsymbol{\sigma}})]\!] = -[\![\dot{\boldsymbol{\sigma}} \boldsymbol{n}]\!] \tag{1.28}$$

where $[\![\cdot]\!] = (\cdot)_{\text{left}} - (\cdot)_{\text{right}}$ is the jump of the quantity under the bracket, $\boldsymbol{g}$ is a vector defining the bifurcation mode, c is a scalar parameter, and $\boldsymbol{\alpha}$ is a tensor composed of constants.

EQUATION (1.29) is then obtained using EQUATION (1.28), and the two first EQUATIONS of (1.27) in EQUATION (1.29), the volume force is omitted. Assuming the mass conservation across the discontinuity surface using $[\![\rho c]\!] = 0$ leads to EQUATION (1.30) which its solutions are given by solving EQUATION (1.31). It defines the localization condition, where the bifurcation modes $\mathbf{g}$ are found when the tensor $[\mathbf{n} \cdot \mathbb{H} \cdot \mathbf{n}]$ is singular. This condition is called loss of the ellipticity of the equilibrium equation in velocity. Physically, it corresponds to the presence of stationary acceleration waves. The tensor $\mathbf{n} \cdot \mathbb{H} \cdot \mathbf{n}$ is called acoustic tensor as ρc^2 corresponds to the eigenvalue of the acoustic tensor in the direction $\mathbf{n}$.

$$[\mathbf{n} \cdot \mathbb{H} \cdot \mathbf{n}] \cdot \mathbf{g} = \rho c^2 \mathbf{g} \tag{1.29}$$

$$[\mathbf{n} \cdot \mathbb{H} \cdot \mathbf{n}] \cdot \mathbf{g} = 0 \tag{1.30}$$

$$\det[\mathbf{n} \cdot \mathbb{H} \cdot \mathbf{n}] = 0 \tag{1.31}$$

EQUATION (1.31) characterizes the presence of instability. The discontinuous band localization occurs when EQUATION (1.31) becomes negative. When the problem is discretized using finite elements, the damage will localize in a strip band of one element width. It leads to incorrect energy dissipation as the smaller the element size, the smaller the dissipated energy. Indeed, the dissipated energy depends on the element volume ($\mathcal{E}_{\text{d}} = f(V_{\text{elem}})$).
The analysis leading to material instability has shown that the positive definiteness of the material stiffness is violated in the presence of strain-softening constitutive behavior. Two criteria have been established in [Lemaitre et al., 2020, Benallal et al., 1993, DE BORST et al., 2022], which define the localization conditions. These criteria allow identifying the critical requirements of localization occurrence. To overcome this difficulty and keep the well-posed mathematical problem, different methods can be found in the literature.

1.3.2.5 Damage regularization in presence of strain-softening constitutive behavior

In this subsection, we will review the different regularization methods in order to avoid material instability and recover the uniqueness of the solution. Two families exist, considering either a temporal or a spatial regularization of the damage.

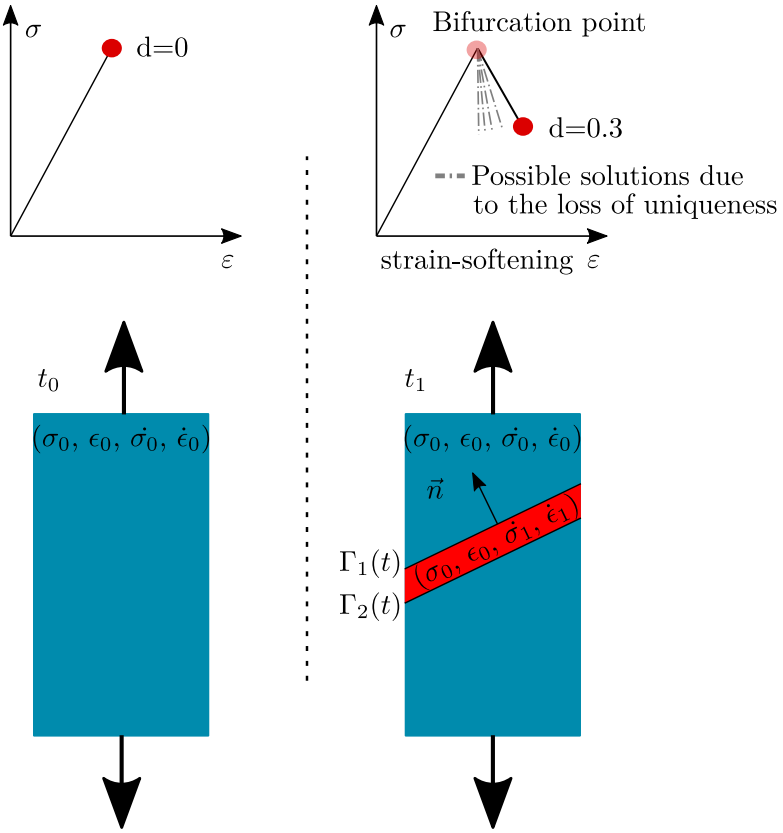

Figure 1.44: Band discontinuity occurring during the softening. Loss of uniqueness of the solution after strain-softening onset

Viscous characteristic time In a damaged material, the propagation of the elastic waves slows down in the presence of flaws or cracks. Thus, it has motivated [Ladeveze, 1992] to limit the damage rate evolution using a delay effect on the damage variable. In [Deü, 1997], the author has shown the limits of the damage rate evolution shape proposed in [Ladeveze, 1992]. Indeed, if a sudden failure occurs, the damage rate will be increased without limitation due to the increase of the driving force, which will lead to damage localization. Thus, in [Allix, 2013], the authors proposed limiting the damage rate using a new law, as presented in EQUATION (1.32). It can be seen that if the driving force grows suddenly, the evolution of the damage rate will be bounded by a characteristic time τ_c^{-1}. The advantage of this method is that even in the presence of sudden failure, ellipticity or hyperbolicity problem is recovered, avoiding these bifurcation modes and damage localization.

$$\dot{d} = \frac{1}{\tau_c}(1 - \exp(-a\langle d_s - d\rangle_+)) \tag{1.32}$$

where τ_c is a characteristic time, a is a material parameter to identify, d_s is the computed damage variable for a designated driving force Y_d, and d is the damage variable. The disadvantages of using viscous regularization are:

- The viscous parameter bounds the damage evolution resulting in a rate-dependent mechanical problem;
- The parameter τ_c has to be as small as possible to not distort the solution while regularizing the problem (additional viscous energy);

- The validity framework is more arguable in quasi-static loading, resulting in important characteristic time;

An alternative to maintaining the problem rate-independent while regularizing the solution consists of using internal spatial lengths. Two different methods used in the literature will be presented. The first one is based on crack band theory, and the second corresponds to introducing gradient damage models.

Crack band theory The first solution is the resort of crack band theory developed in [Bažant and Oh, 1983]. This method does not allow for retrieving the ellipticity/hyperbolicity of the mechanical problem. On the contrary, it uses the fact that damage is localized on an element strip to link the fracture toughness G_c to the energy density stored in the Gauss point W_d by introducing an internal length L_e. By choosing the internal length to be equal to the element size related to the fracture width L_e (FIGURE 1.45), the damaged stiffness slope has to be adjusted to ensure that the dissipated energy equals G_c. The authors have shown that simulations performed with different mesh sizes (therefore different values of L_e) yield to identical results. This method was introduced in [Rivallant et al., 2013a, Ebina et al., 2018, Lin et al., 2020] to predict the fibre failure of composite laminates subjected to impact.

The disadvantages of using crack band method are :

- The crack band does not solve the material instability due to strain-softening, it deals with it. Therefore, care must be taken with the choice of the internal length to dissipate the right amount of energy;

- The theory proposed by Bazant has been established with structured mesh without bias. If oriented mesh will is used, it will localize the damage into a strip of element-oriented by the mesh;

- The internal length choice have to be perpendicular to the fracture plane. In composites, thanks to the anisotropy of the material, the fracture path is supposed to be known;

- When cracks are oriented at $\theta°$ according to the mesh line, the crack shape will follow a zig-zag path. It can therefore be difficult to guess the internal length that has to be chosen. Moreover, the damage tends to be trapped by the local orientation;

Gradient damage models An internal spatial length is introduced into the gradient damage model. However, unlike the crack band, this internal length restores the well-posed mathematical framework. Damage is smoothed around a zone controlled by the internal length, which avoids a sharp gradient. Two different gradient damage models are prevalent in the literature, the non-local damage model and the phase-field approach. These two methods will be exposed in the following.

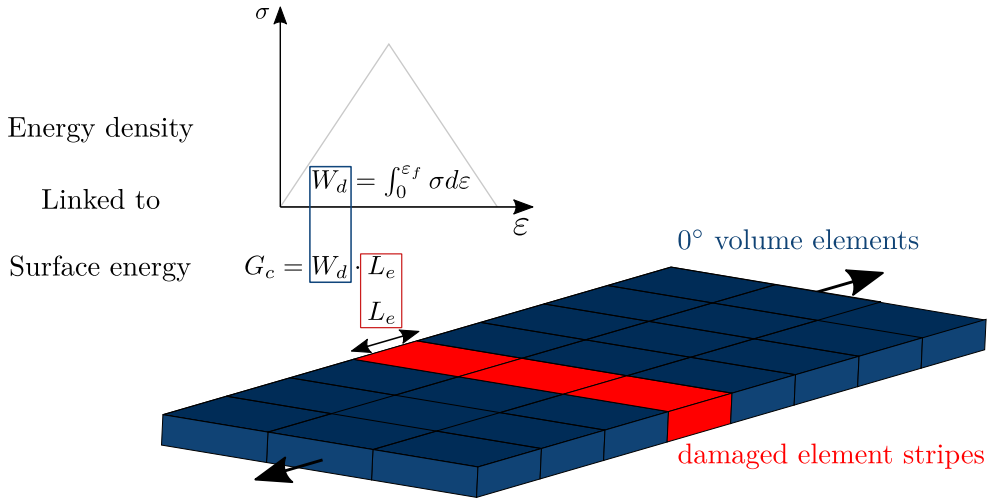

Figure 1.45: Internal length chosen to link the fracture toughness with the elastic energy density

Non-local damage Different formulations of non-local damage have been proposed in the literature. This theory aims to smooth the sharp gradient of a localized quantity thanks to an internal length. This internal length allows an averaging over a volume of the localized quantity. In [Pijaudier-Cabot and Bažant, 1987, Bazant and Pijaudier-Cabot, 1988] the authors have proposed to delocalize the variables responsible for strain-softening while keeping the local character of the constitutive behavior (Hooke's law). In other words, the damage variable responsible for the softening is averaged in a volume defined by the internal length. Equation (1.33) defines the averaged quantity:

$$\overline{d} = \frac{1}{V_r} \int_V \alpha(s-x) d(s)\, \mathrm{d}V(s) \tag{1.33}$$

where d is the localized damage variable, V_r defines the volume of material inhomogeneities. The variable $\overline{d}$ will be spread only within the boundary of V_r. The spatial averaging operator α characterizes this spreading. An adaptation of Equation (1.33) performed in [Peerlings et al., 1996] makes the concept of delocalization more understandable and more suitable for FE. Indeed, as proposed in Equation (1.34), c defines the internal length squared. The higher c, the more the quantity $\overline{X}$ is spread out. This formulation allows a simpler discretization in FE since it involves only gradients that can be held by FE, whereas the initial formulation requires a convolution operation.

$$\overline{X} = X + c\nabla^2 \overline{X} \tag{1.34}$$

The internal length squared c finds its justification as a material property. It defines the surrounding zone where material inhomogeneities such as micro-cracks are found. In [Médeau, 2019], the author tried identifying this material parameter for 3D woven composites using compact tension tests. The advantage of non-local damage is that its combination with a CDM is straightforward. However, the main drawbacks of non-local damage are :

- No control on the damage spreading is performed, resulting in an oversized damaged zone; thus, describing sharp cracks as fibre failures remains very difficult;
- As the damage extends, the value of the damage variable increases with difficulty and does not reach its maximum value. It results in high residual stresses after failure that inaccurately describes the failure of some mechanisms;
- The control of the dissipated energy is difficult as CDM provides a volume energy density which is not correlated to the fracture toughness G_c;
- The choice of the variable to be delocalized can influence the damage threshold. Indeed, if the driving force is delocalized, the driving force will reach the damage threshold more lately. Thus, we must reflect on what variable we should have to delocalize;

In order to limit the damage spreading, some authors have studied the possibility of introducing a decreasing internal length [Geers et al., 1998, Poh and Sun, 2017, Desmorat et al., 2015]. For quasi-brittle material, diffuse damages precede the localized macro-failure such as fibre or matrix failure. It justifies the approach used in [Poh and Sun, 2017], where the internal length is weighted by an interaction function. This interaction function decreases when the damage variable increases. In [Geers et al., 1998], Equation (4.2) has been modified by replacing the parameter c with a variable ξ which defines the gradient activity. The finite element formulation has been enriched by one degree of freedom which describes the state of ξ. The evolution of the variable ξ is a function of a strain threshold. ξ evolves until the strain reaches the strain threshold. Once reached, ξ is fixed.

Phase-field damage gradient Another gradient damage family introduced by [Francfort and Marigo, 1998, Bourdin et al., 2008] is based on the variational approach of the fracture mechanics theory introduced by Griffith and presented in Equation (1.35). The total energy $\mathfrak{E}(u,\phi)$ takes the contribution of the elastic bulk energy $\mathfrak{E}_{\text{bulk}}$, the fracture energy $\mathfrak{E}_{\text{frac}}$ and the external potential energy $\mathfrak{P}(u)$.

$$\mathfrak{E}(u,\phi) = \overbrace{\int_\Omega g(\phi)\psi_0(\varepsilon(u))\,\mathrm{d}V}^{\mathfrak{E}_{\text{bulk}}} + \overbrace{\int_\Omega G_c\gamma(\phi,\nabla\phi)\,\mathrm{d}V}^{\mathfrak{E}_{\text{frac}}} - \mathfrak{P}(\mathfrak{u}) \tag{1.35}$$

where $g(\boldsymbol{\phi})$ is the degradation function, ψ_0 is the elastic potential energy density, u is the displacement and ϕ the damage variable. A sharp crack defined by a crack surface Γ is approximated by a regularized crack surface Γ_ℓ using a diffuse damage variable ϕ. ϕ is diffused in the neighborhood thanks to an internal length ℓ_0. Figure 1.46 illustrates the concept. The phase-field attenuates the strong gradient by stretching the Dirac-like discontinuity into a bell characterized by an inner length. This approximation is performed using Equation (1.36).

$$\Psi_c(\Gamma) = \int_\Gamma G_c\,\mathrm{d}S \approx \int_\Omega G_c\gamma(\phi,\nabla\phi)\,\mathrm{d}V \tag{1.36}$$

The fracture energy $\Psi_c(\Gamma)$ defined by a surface integral is approximated using a volume integral. A function γ is introduced depending on the damage ϕ and its

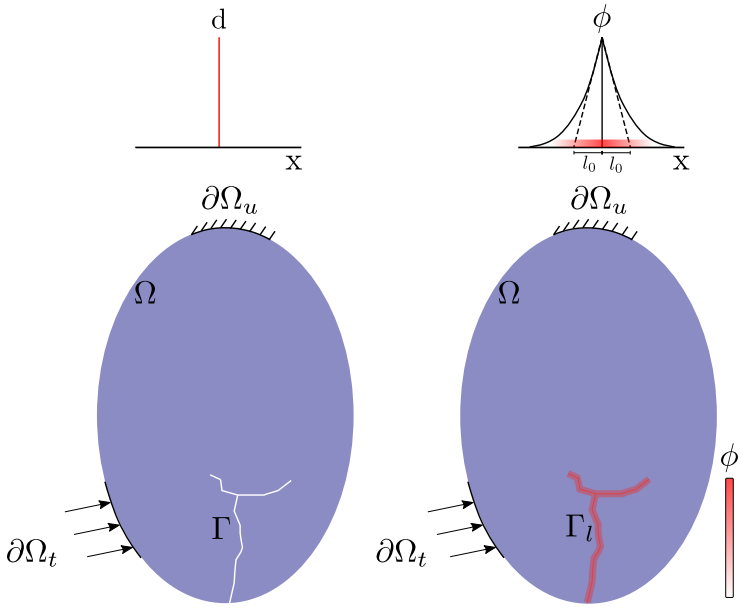

Figure 1.46: Solid body Ω subjected to a discrete sharp crack on the left and a diffuse crack using the phase-field framework on the right

gradient. Different choices of the gamma function exist (AT1, AT2) as presented in EQUATION (1.37). These formulations are presented in [Wu and Nguyen, 2018] and satisfy the Γ-convergence (the regularized crack surface Γ_ℓ converges to a sharp crack when $\ell_0 \to 0$)

$$\begin{cases} \gamma(\phi, \nabla\phi) & = \frac{3}{8}\left(\phi + \ell_0^2(\nabla\phi \cdot \nabla\phi)\right) \text{ for AT1} \\ \gamma(\phi, \nabla\phi) & = \frac{1}{2}\left(\phi^2 + \ell_0^2(\nabla\phi \cdot \nabla\phi)\right) \text{ for AT2} \end{cases} \tag{1.37}$$

The internal length ℓ_0 governs the width of the diffuse crack by controlling the spatial operator. Thus, the higher ℓ_0, the more important the spatial operator $\nabla\phi$ acts.

The formulation is sophisticated as the fracture toughness G_c is introduced. It links the damages occurring in the volume with G_c thanks to the internal length ℓ_0. As the formulation was developed for isotropic material, $g(\phi)$ degrades all the stiffness tensor components. More recently, the phase-field has been used to model the failure for composite materials [Bleyer and Alessi, 2018, Quintanas-Corominas et al., 2019]. In [Bleyer and Alessi, 2018], the authors developed an anisotropic phase-field formulation. Different damage mechanisms such as fibre failure and matrix cracking are modeled with two phase-field damage variables.

The disadvantage of the phase-field is the strong interdependence between the peak stress σ_c, G_c and ℓ_0. The choice of two parameters affects the third one. In [Wu and Nguyen, 2018], a modification of the degradation function $g(\phi)$ has revealed an insensitivity to the length scale. However, the resolution of the phase-field problem becomes nonlinear.

Which regularization method should be chosen ? The different presented methods have shown their strengths and their weaknesses. Implementing a regu-

larization method in a finite element code must be the least intrusive for easier implementation in commercial codes. Viscous damage and the crack band are good candidates for efficient implementation in commercial FE codes. Non-local damage and phase-field have shown strength in avoiding material instabilities while staying rate independent. Non-local damage allows freedom in the local damage law establishment; however, the local damage kinetics is no more ensured due to the delocalization. The phase-field uses a variational approach to the brittle failure, which is not a damage law, the framework is therefore imposed. The implementation of the gradient damage is performed using two algorithm resolution strategies. In [Médeau, 2019], the author has shown that solving the global problem by minimizing the functional energy for the couple (u, ϕ) is difficult using a monolithic resolution. The author has used another resolution method called the alternate scheme. This resolution method has revealed robustness, a key parameter for use in the industrial context. However, it is intrusive and difficult to implement in a commercial code.

To conclude, using the crack band and viscous damage are not intrusive and allow a fast implementation with freedom in stress-strain behavior law. The gradient damage models are perfect candidates for regularizing the solution. However, their implementations in commercial codes are "pretty heavy".

1.3.3 Simulation of LE/LV impact using FEA

The previous sections have described the FEM and the damage laws used to model each damage mechanism. The simulations using FEA of a LE/LV impact will be presented now. Several studies can be found in the literature. Almost all of the works are considering an explicit solver [Hongkarnjanakul et al., 2013, Falcó et al., 2022, González et al., 2018, Sun and Hallett, 2017]. However, in [Abir et al., 2017], impact simulations using an implicit solver have been performed. It is interesting to notice that implicit solvers avoid using significant loading rate or mass scaling to perform compression after impact simulations as required in an explicit framework. The predictive capabilities of the different models are evaluated by comparing the numerical macroscopic responses (load-displacement, load-contact time, dissipated energy) with the experiment results. The projected damaged area obtained from simulations is usually compared with a classical C-scan image (Figure 1.48). However, in some studies [Sun and Hallett, 2017, Song et al., 2018, Manseri, 2020], advanced comparisons with CT images have been performed. Indeed, in [Sun and Hallett, 2017] the simulated interface damages have been compared with CT-scan slices for a 16 plies laminated composite impacted at 10 J.

To conclude this part, advanced comparison with X-ray and other experimental data (advanced instrumentation) are needed to evaluate the predictive capabilities of impact models. Few studies have shown deep comparisons where the interply and intraply damages are confronted with the experimental results. Moreover, [Abir et al., 2017] have shown that simulations using implicit solvers can be carried out despite the rough impact problem. Studies need to be continued on the simulation using implicit dynamics, which guarantees the reliability of the results as the convergence is fulfilled.

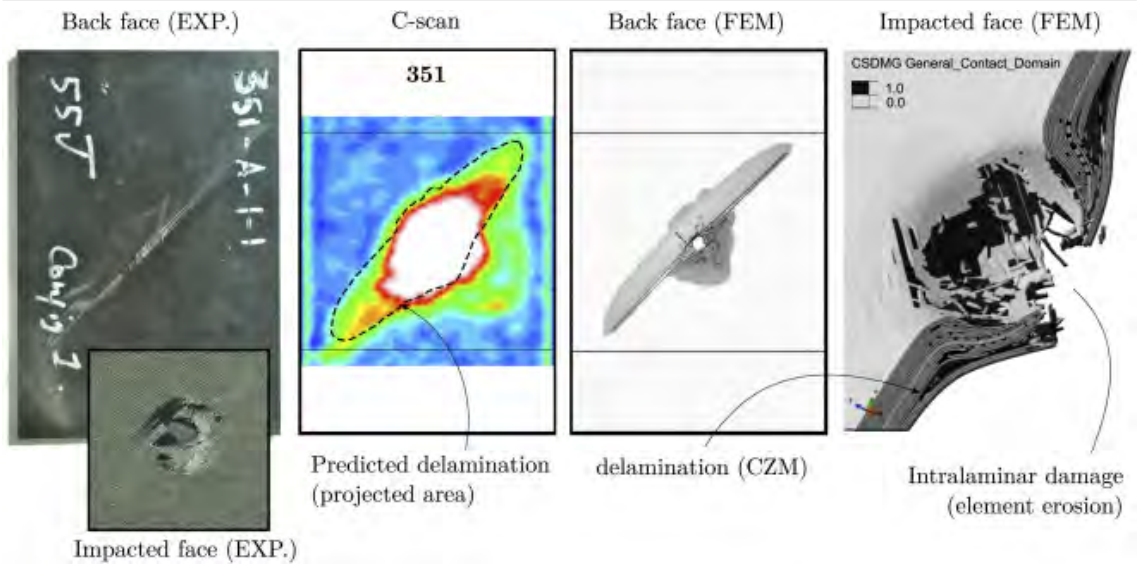

Figure 1.47: Comparison of the projected delamination area between C-scan image and FE simulation on a 24 plies laminated composite material impacted at 55 J [Falcó et al., 2022]

1.4 Behavior of composite laminates subjected to CAI

As detailed previously, LE/LV impact induces different damages presenting a strong coupling between intra and inter-ply mechanisms. The multi-delamination occurring in wide interfaces is the most critical damage resulting in the drop of the flexural modulus. If an impacted sample is loaded in compression for composite laminate, catastrophic failure may occur as the laminate is subdivided into sublaminates which favors the local buckling possibility. Therefore, compression after impact is the critical reference test to estimate the residual performance of composite laminates after impact. In the literature, authors classically use the [AST, 2007a] to evaluate the residual strength of composite laminates with a more or less enriched instrumentation (fibre failure tracking using IRT or detection of buckling initiation using DIC). Once performed, academics model the CAI test using FEA to estimate the simulated residual strength. The following sections will discuss the experimental and numerical academic methodology to evaluate the residual compressive strength after impact.

1.4.0.1 Experimental analysis of CAI performed by academics

As the residual compression strength is the most concerning data for category 1 substantiation, the comprehension of the damage mechanisms occurring during a CAI test is essential for designing criteria from an industrial point of view. In the literature, many studies have considered CAI tests using the classical experimental setup [Rivallant et al., 2014b, Ranatunga et al., 2019, Liv et al., 2017, Liu et al., 2018, Flores, 2016, Sun and Hallett, 2018]. Numerous additional tools can be added to the experimental setup to prevent buckling, these tools could generate additional compliance and parasitic displacements. To ensure that the loading is well distributed along the plate, strain gauges can be used during the test as in [Rivallant

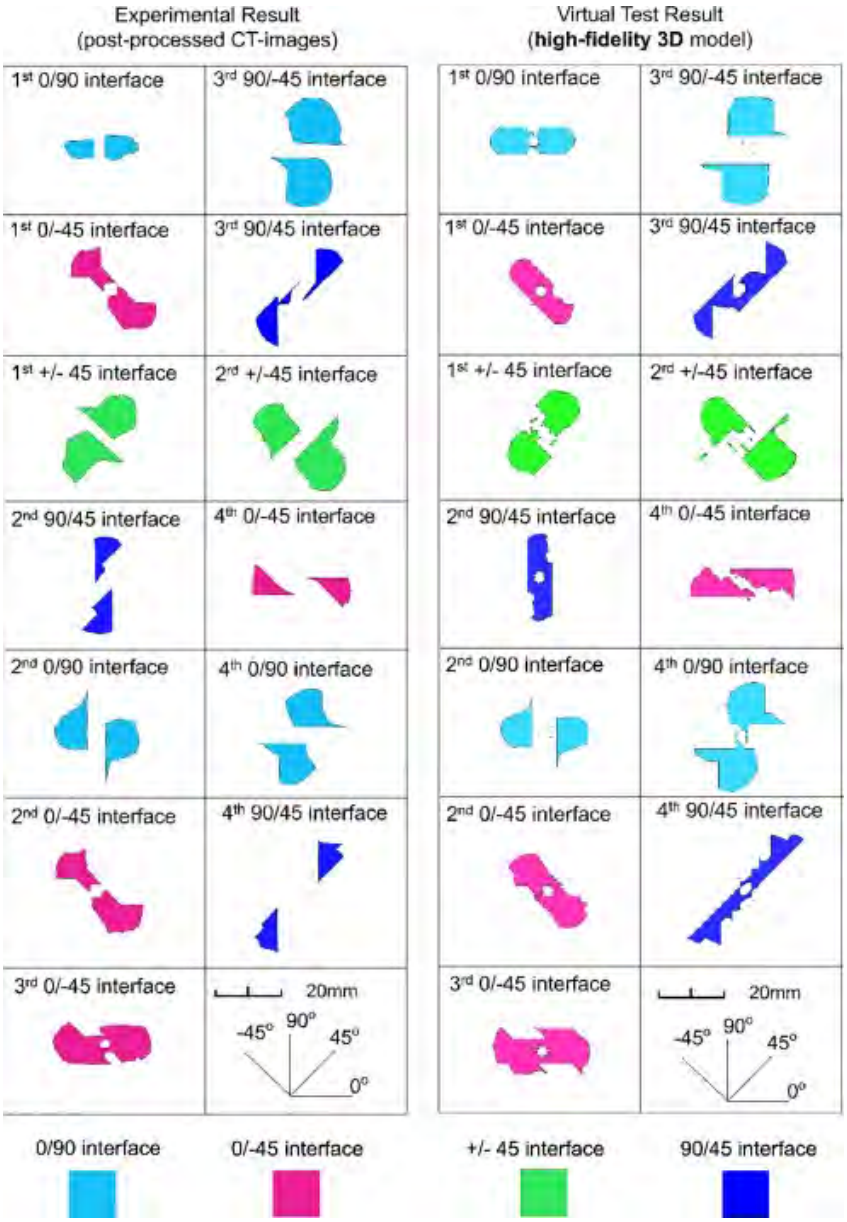

Figure 1.48: Comparison of the delamination between CT-scan images and FE predictions on a 16 plies laminated composite material impacted at 10 J [Sun and Hallett, 2017]

et al., 2014b] [Flores, 2016]. As shown in FIGURE 1.8, the sample is guided with anti-buckling rails and clamped using the retention plate. This arrangement allows a large free area where instrumentations such as DIC and IRT can be used. Thus, in [Rivallant et al., 2014b, Sun and Hallett, 2018, Flores, 2016], the authors have placed cameras on both sides to perform DIC enabling to provide precious information such as the knee-point where the local buckling is triggered. Three stages shown in FIGURE 1.49 occur during a CAI test. The first one is a linear loading until local buckling occur(A), then the local buckling is more pronounced (B-C). Finally, the fibre break in compression is triggered until it reaches the plate's edges (D). The higher the impact energy, the earlier the buckling stress threshold. To minimize the coupling between compression and buckling failure, it can be interesting to investigate the CAI with more realistic structures such as aircraft stiffened panels [Soto et al., 2018b] or wide panels [Action and Flores, 2018]. In [Action and Flores, 2018], another experimental setting device was presented to estimate the residual compression strength of 330 × 280 mm panels. A compression fixture blocking the out-of-plane displacement while allowing a free window to perform DIC has been considered. This method allows controlling boundary conditions while instrumenting the experimental test. It is interesting to notice that the plate was not undergoing buckling thanks to its considerable thickness and wide dimensions. From an industrial point of view, it is essential to separate a pure compression material failure mode from a combined compression-buckling failure as the failure mechanisms are different. The failure induced by a combined compressive and buckling loading will occur prematurely to a pure compression failure. That is why industrials treat these two problems in two different manners (for a pure compression failure mode, anti-buckling tools are introduced in the two different faces).

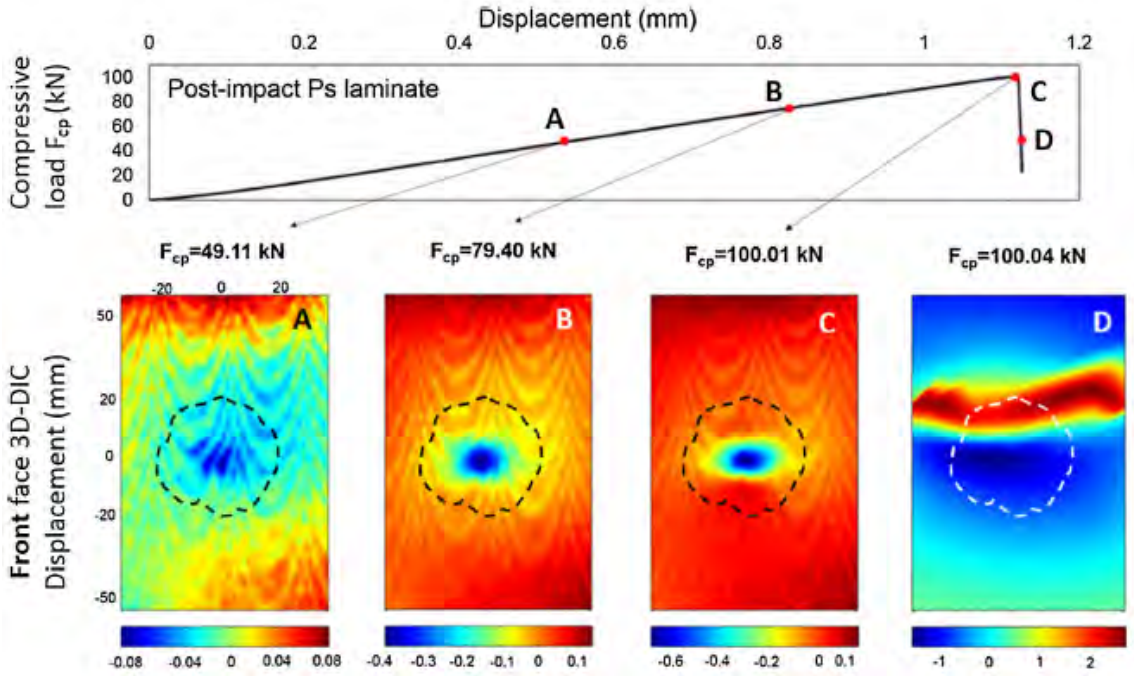

Figure 1.49: Out-of-plane displacement field on the impacted face obtained from DIC, and showing the local buckling occurring during the loading [Sun and Hallett, 2018]

1.4.0.2 Simulation of the residual compression strength using FEA

The comprehension of damage mechanisms occurring during CAI is hardly understandable as sudden failure occurs. One solution consists of performing simulations of CAI to understand the damage mechanisms occurring during the test. Simulating CAI test involves already a robust simulation of impact damages which is challenging to achieve. Thus, few damage models can perform impact and compression after impact [Rivallant et al., 2013b, Abir et al., 2017, McQuien et al., 2020, Liu et al., 2018, Soto et al., 2018a, Sun and Hallett, 2018]. The CAI step is performed after the LE/LV impact, the boundary conditions are shown in FIGURE 1.50, the rigid surface in green defines the anti-buckling system, a straight contact with the plate is defined. A compressive displacement is applied at the top of the plate while the bottom remains fixed. The residual compression strength test is quasi-static. Performing such simulation in an explicit framework needs some strategies such as, mass scaling or high loading rate to save computational times. If the material is sensitive to the rate effect, leverage on the loading rate is impossible. Another solution using implicit dynamics as performed in [Abir et al., 2017] is possible. In [Abir et al., 2017], the authors have performed a sensitivity analysis on material parameters during the CAI test. It has shown that G_{IIc} has a considerable influence on the buckling onset, the higher the delamination fracture toughness G_{IIc}, the lower the delamination, and the later buckling occur. Besides the authors have shown that the higher the material parameters describing the fibre break in compression (the fibre fracture toughness G_{Ic} and the compressive strength X_c), the higher the residual strength. It underlines the necessity to identify carefully these material parameters, which can play an essential role in the results. In [Rivallant et al., 2013b] the CAI simulation was performed using an explicit solver, the authors have shown interesting results capturing the correct damage shape at impact and CAI. During the loading, the compressive stress increases linearly with the strain. At a certain point, the laminates buckle, which triggers fibre breaks in compression. Sudden failure occurs when the damages (delamination and fibre breaks) reach the plate edges (FIGURE 1.50). The numerical simulations allow understanding that the failure is explained by these two mechanisms (delamination and fibre breaks).

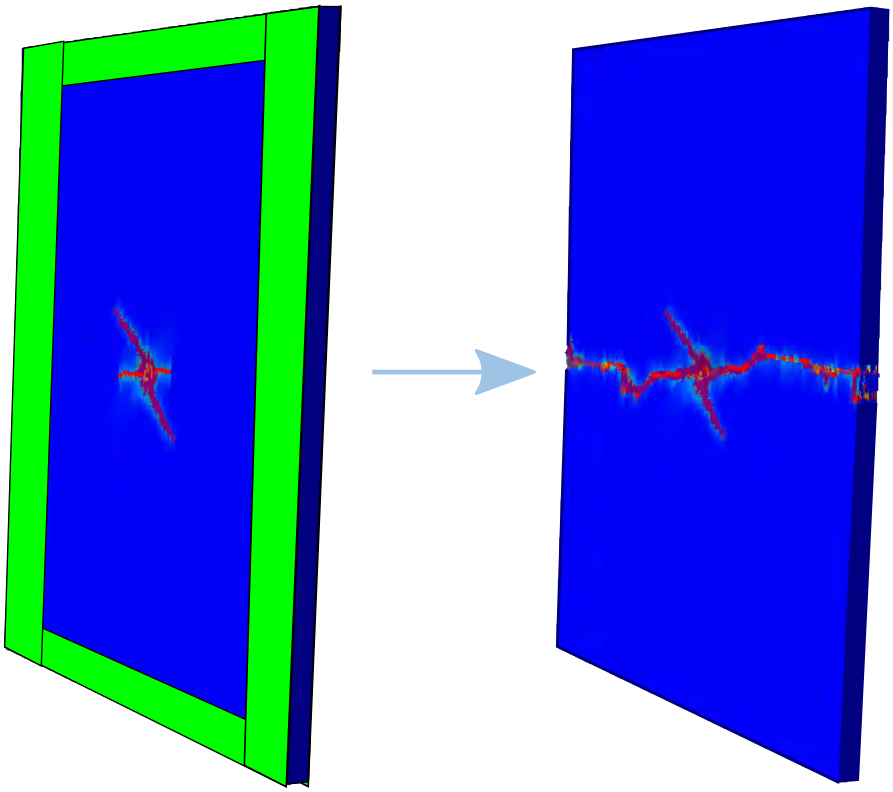

Figure 1.50: CAI simulation performed using DPM, fibre damages growth during the compression loading

1.5 Conclusion on the state of the art about impact on composite laminates

In this chapter, an overview on impact damages in laminated composite materials has been presented. Four foundations in the field of impact damage tolerance have been presented. The first corresponds to the industrial approach which must meet safety requirements defined by regulation authorities. It has been shown how difficult the substantiation is with lengthy and expensive experimental campaigns. The approach defined by the standard is suitable for coupons. However, in aeronautics, the scale is not limited to coupons. Substantiation must be proved that components, structures have to be damage tolerant. Thus, aircraft manufacturers use a pragmatic approach where the studying of impact damage at the mesoscopic scale is not possible.

The second foundation is how the impact on composite structures has been placed in the heart of concerns these last decades. Indeed, several experimental setup are found in the literature with different means to inspect the structure and investigate impact damages. Lastly, the progress on high-frequency monitoring with IR and DIC has shown its strength in comprehension of impact physics on composite structures. The awareness of the different types of damage and the interactions between the different damage mechanisms have enabled enhancing the damage resistance of composite laminates with new material architectures.

The third foundation is numerical modeling. Numerical simulations can enable a complementary with experimental testing with simulating configurations that have

not been tested. Moreover, numerical models will allow understanding the damage scenario occurring during impact tests. Several models exist, but few of them simulate the impact damages with a good accuracy. Indeed, the complexity of impact damages induces an inherent difficulty in modeling the damage mechanisms accurately.

The last foundation, which is the main concern for the industrial, is the residual compression strength of composite laminates. To substantiate category 1 impact damage the residual strength must not be lower than the UL. Few numerical models are simulating the CAI, as the accurate prevision of impact damages is a necessary step. The prevision of residual strength will establish the entire virtual testing process for damage tolerance evaluation.

Based on the analysis of the literature, the proposed work will characterize in chapter 2 the behavior of recent generation of carbon-epoxy toughened composite laminates after a LE/LV impact. In chapter 3, real-time damage monitoring has been performed using high-speed cameras (IR and visible cameras) besides, a study of loading rate effect will be presented for this material with QSI test. Then in chapter 4, the FEM and the damage models developed at ONERA and ICA will be presented for the prediction of impact damages.

Chapter 2

Investigation of impact damages using classical inspection methods

Contents

2.1 Physical responses of last generation composite laminates under low energy/low velocity impact

2.1.1 Studied laminated composite material

Dassault Aviation has provided the composite material. Composite laminates with "industrial" stacking sequences are considered in this work. Due to the material's confidential character, the datasheet will not be shared in the present manuscript. The material is a carbon/epoxy UD ply proposed by HEXCEL. A ply weight of 200 gsm and a 0.192 mm ply cured thickness are considered. The prepreg is composed of ultra-high modulus and strength carbon fibres and a very tough epoxy resin for aerospace structural applications. According to conventional composite laminates, the specificity of this material is that interfaces are thicker as they are charged

with particles. Indeed, the interface thickness is 1/5 of the ply thickness, whereas usually, it is 1/20 of the ply thickness. This material is called in this study last generation composite laminate. FIGURE 2.1 illustrates the microstructure of the material. This material has been already characterized for in-plane loadings in [Priasso, 2017, Germain, 2020], showing a diminution of delamination as the interface toughness has been increased. For impact loading, an experimental study has been carried out in [Bull et al., 2014] for similar material. The authors have concluded that delamination is reduced due to toughening mechanisms.

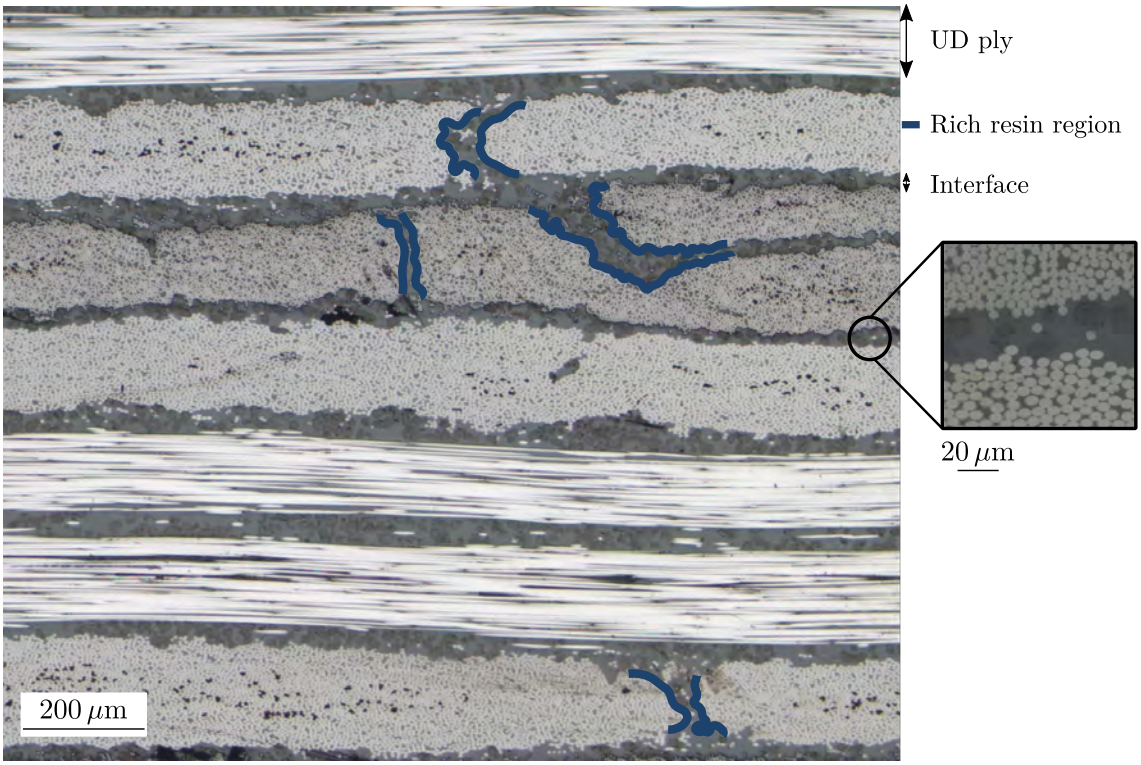

Figure 2.1: Microstructure of the Q16 laminate made of carbon/epoxy UD plies

At the beginning of the work, this material was not characterized under out-of-plane loadings, especially for impact cases. Therefore, the scope of this work is the material characterization under LE/LV impact loading (drop tools case). Two industrial composite laminates have been investigated.

- A 3.07 mm-thick quasi-isotropic laminate made of 16 plies, called Q16 $[(0/45/90/-45)_2]_s$
- A 3.84 mm-thick highly oriented laminate made of 20 plies, called C20 $[0/-45/0/45/0/90/45/0/-45/0]_s$

2.1.2 Impact testing experimental configuration

Experimental configuration LE/LV impacts were performed at ONERA using an 8250 Dynatup impact machine. FIGURE 2.2 presents the experimental setup. Drop height imposes the impact velocity. Once fallen, the impactor is guided toward the plate. Standard guidelines have been used for the experiments with a 150 × 100 mm sample size supported on a 125 × 75 mm impact window and impacted

with a 16 mm diameter impactor. However, it has been chosen to impact with a heavier mass than recommended by the standard [AST, 2007b] (13.01 kg than 5 kg). No rubber clamp has been used to maintain the sample in order to control the boundary conditions in the FEM. The impact machine is instrumented with a load cell in the impactor and a photodiode sensor. The impact velocity is calculated when the metal stripe crosses the sensor's split (in green). The impact table is supported on four blue steel beams, which transmit the loading to the ground. It can be shown that the impact window is not directly embedded in the impact table; many tools are used that are likely to introduce clearance and flexibility during impact. An anti-rebound system is used with a pneumatic system to avoid multi-impact on the sample. The cylinder rod automatically goes up during the rebound phase. When the impactor goes down a second time; it crushes the cylinder rod, which prevents double impacts on the plate.

Samples preparation Dassault Aviation has provided 2 different material batches. For the first batch (Batch A), a cutting plane has been defined to obtain the 150 × 100 mm samples for Q16 and C20. The cuts have been performed at ONERA using a diamond saw machine with a 2.5 mm blade thickness. The second batch (Batch B) provides 150 × 100 mm machined specimens using water jet cutting performed by Dassault Aviation. Scattering between the two batches has been evaluated. Due to similar results, it has been decided to not distinguish the results between these two batches.

Experimental campaign The impact tests have been performed on the two laminate stacking sequences with different impact energies levels. Several impact energy levels have been considered to identify each damage mechanism occurrence. Indeed, the damage mechanisms encountered in composite laminates are generated as a function of the amount of energy stored in the composite plate. For lower energy impact levels, classical matrix cracking and delamination occur. For higher energy impact levels, fibre breaks will appear. The defined range for the impact energy levels evolves from 6.5 J to 35 J, which will allow crossing the apparition of each kind of damage. The experimental campaign is summarized in Table 2.1.

Laminate	Impact energy					
	6.5 J	11 J	20 J	25.9 J	31.15 J	35 J
Q16	1	1	2	1	1	3
C20	1	1	1			2

Table 2.1: Sum-up of the experimental impact tests performed during the MARCOS II project

For each energy level and stacking sequence, the number of tests is mentioned.

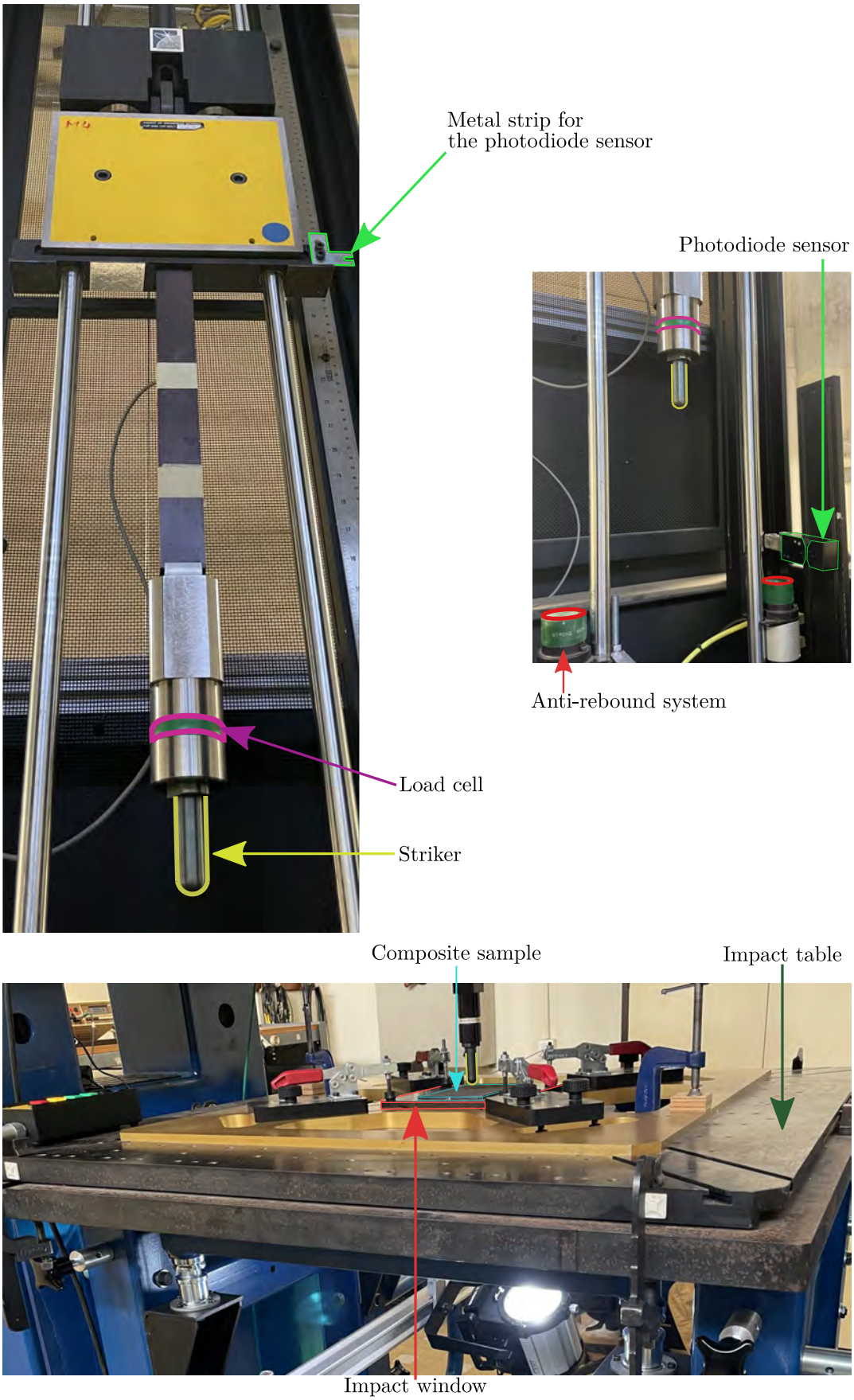

Figure 2.2: ONERA's drop weight impact machine

2.1.3 Analysis of the Q16 & C20 physical responses under LE/LV impact

In this subsection, a first analysis will be performed based on the experimental data obtained from the machine acquisition during the LE/LV impacts.

2.1.3.1 Quasi-isotropic laminate Q16 results

Load-displacement responses The load-displacement curves are presented for the Q16 in FIGURE 2.3. First of all, it can be shown in FIGURE 2.3 that :

- For each impact energy, low scattering is observed during the loading stage;
- The higher the energy, the higher the hysteresis. The occurrence of impact damages induces the presence of hysteresis;
- At almost 4 mm, the knee point marks the stiffness shifting. The structure seems stiffer. The knee point appears after 4 mm of deflection for a plate thickness of 3.07 mm. The geometrical non-linearity could explain the stiffening;
- Strong oscillations are observed for higher impact energies. An energetic phenomenon such as fibre failures can explain the instability observed;

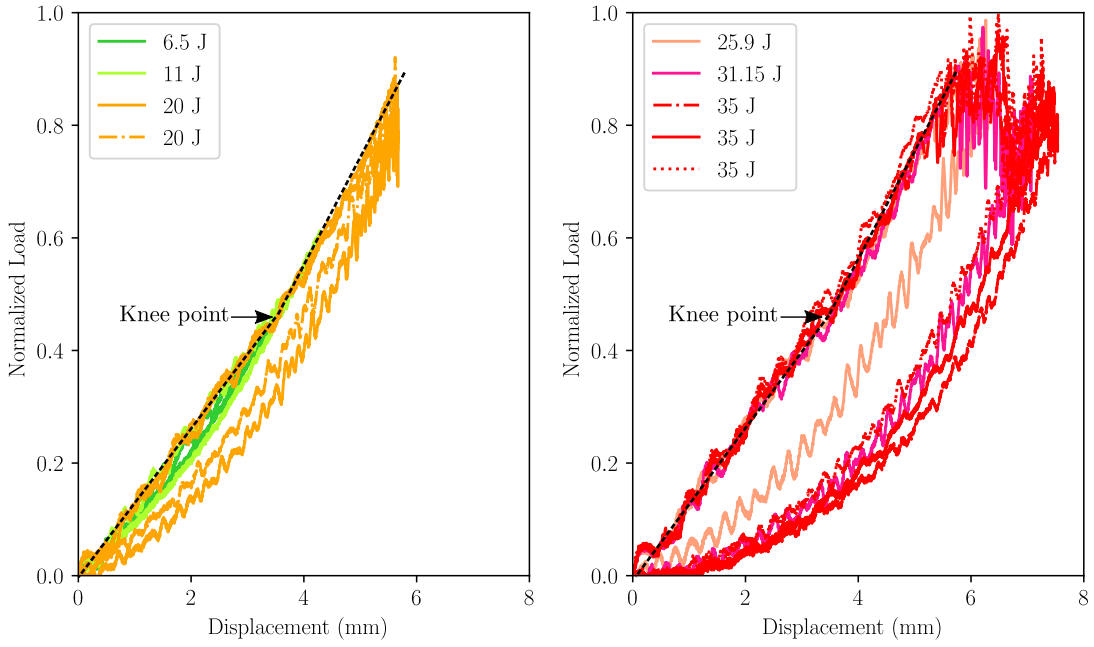

Figure 2.3: Load-displacement curves for the quasi-isotropic laminate Q16 at different impact energy levels

If we analyze the responses for each energy level as proposed in FIGURE 2.4:

- Lower impact energies (6.5 J, 11 J) show few energy dissipation;

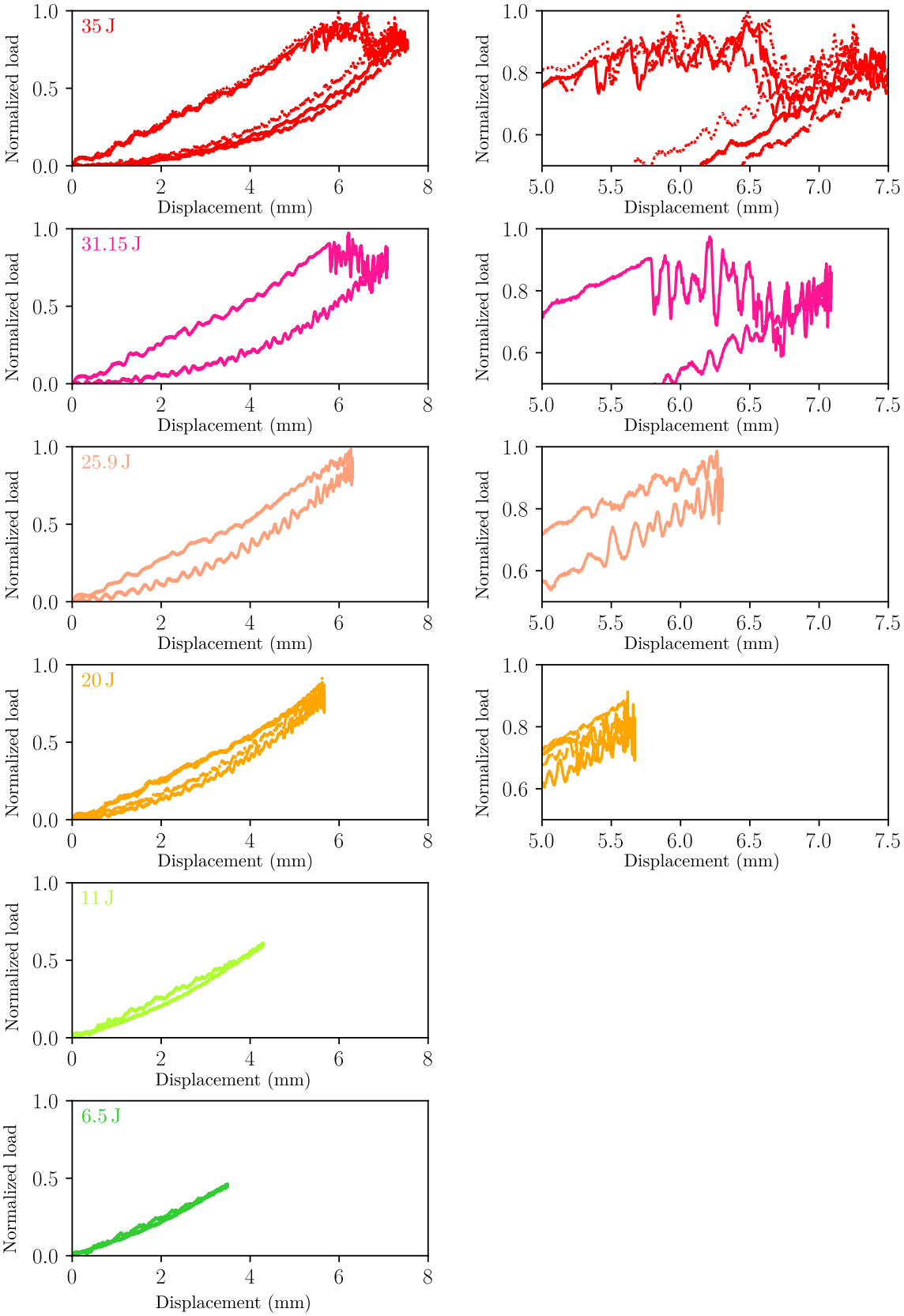

Figure 2.4: Load-displacement curves for the quasi-isotropic laminate Q16 at different impact energy levels

- At 20 J, load drops with oscillations occur. Severe damages may occur, showing that the laminate's bearing capability has been affected. It is interesting to notice that this phenomenon arises around 5.5 mm;
- At 25.9 J, a load drop occurs around 6.2 mm, which is later than observed at 20 J;
- At 31.15 J, after the first impact load drop, the load is increased again, showing that the laminate presents a residual stiffness;
- At 35 J, low scattering is shown. As observed at 31.15 J, even after the load drop, the laminate is able to reload;

Energetic assessment FIGURE 2.5 presents the kinetic energy evolution and the energetic assessment. The impactor impacts the plate with the defined kinetic energy at time $t = 0$ ms. During the impact, the kinetic energy is converted into internal energy. This internal energy is composed of elastic deformation energy recovered integrally after the impact, dissipative energy due to impact damages, and residual kinetic energy stored in the material after the impact event.

The impactor's kinetic energy decreases during the impact event as it is converted into the plate's internal energy. Once the kinetic energy is null, the impactor velocity equals zero, and the rebound phase is initiated. The plate starts to recover its initial shape by converting its internal energy into the impactor's kinetic energy. The impactor moves back up. In the end, the initial kinetic energy will not be integrally recovered since damage mechanisms have dissipated an amount. Indeed, from FIGURE 2.5, it is observed that the higher the impact energy, the lower the kinetic energy recovery. It should be noted, that an amount of the unrecovered kinetic energy have been dissipated due to friction during the contact and the stored residual kinetic energy within the plate.

An energy assessment has been performed in FIGURE 2.5. The dissipated energy has been calculated numerically by integrating the area under the load-displacement curve. Once computed, the dissipated energy, the recovered kinetic energy, and the total energy have been plotted. The total energy was obtained by summing the recovered kinetic and dissipated energy. It can be noted, as expected, that around 100% of the energy is obtained after summation.

2.1.3.2 Physical responses for the highly oriented laminate C20

Load-displacement responses The load-displacement curves for the C20 laminate are presented on the left of FIGURE 2.6. The same assessment can be dressed for this laminate:

- Monotonous loading is observed from 6.5–20 J with low scattering during the loading stage;
- The hysteresis is increased with impact energy, especially for the highest impact energy level 35 J;
- The highest impact energy shows that a threshold is reached after 80 % of the maximum load where two load drops of the same magnitude have occurred (around 20% of the maximum load), resulting in strong oscillations;

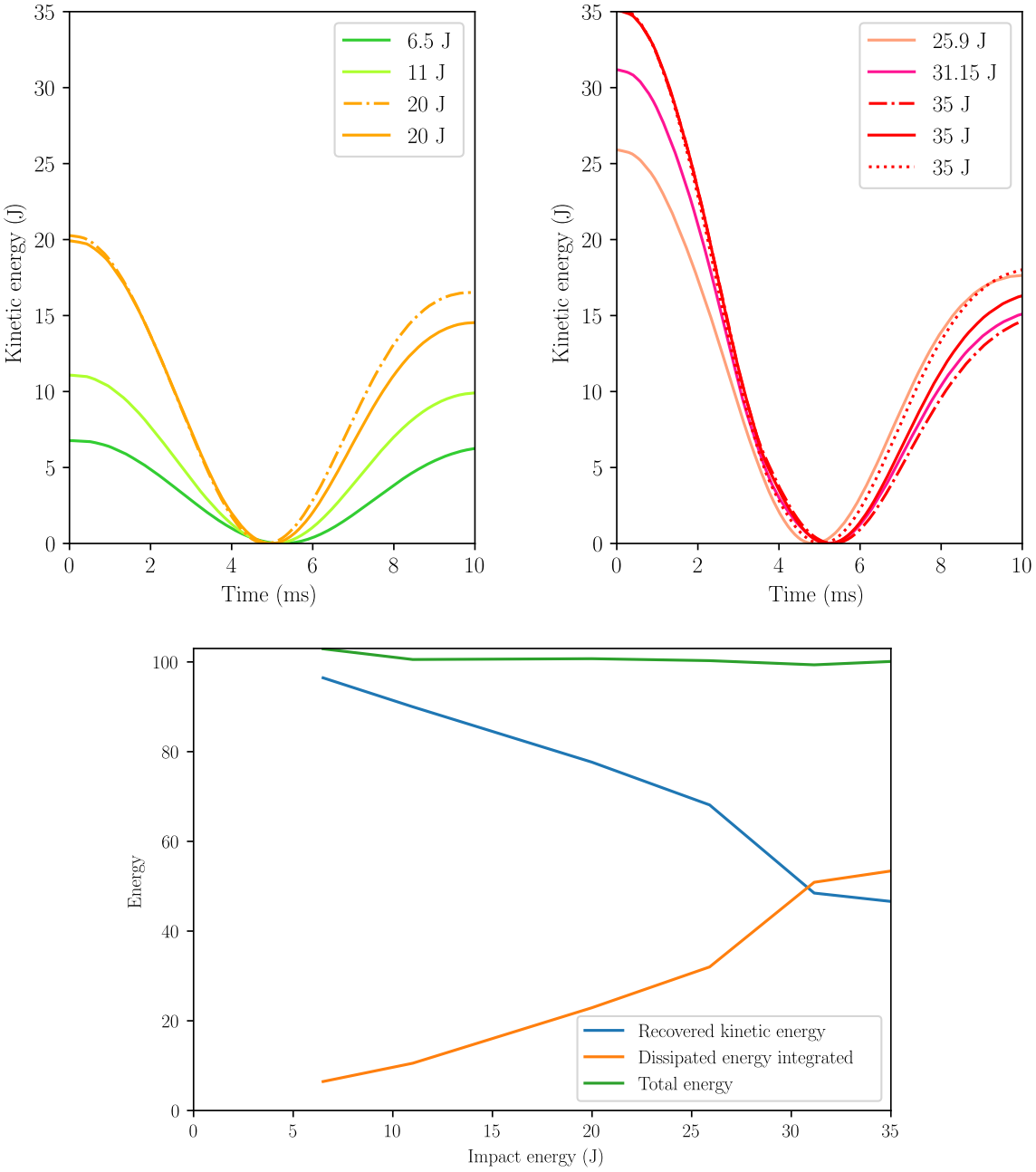

Figure 2.5: Energy assessment for the quasi-isotropic laminate Q16 for different energy levels

Energetic assessment The energetic assessment for the C20 laminate is performed on the right of FIGURE 2.7. Similar trends are observed for the C20 laminate as for Q16 laminate. The higher the impact energy, the higher the dissipated energy, and the lower the recovered kinetic energy. It is also observed that the total energy varies around 100% showing that the critical dissipative mechanism responsible for the non-full recovery of the kinetic energy is due to damage creations in the laminate.

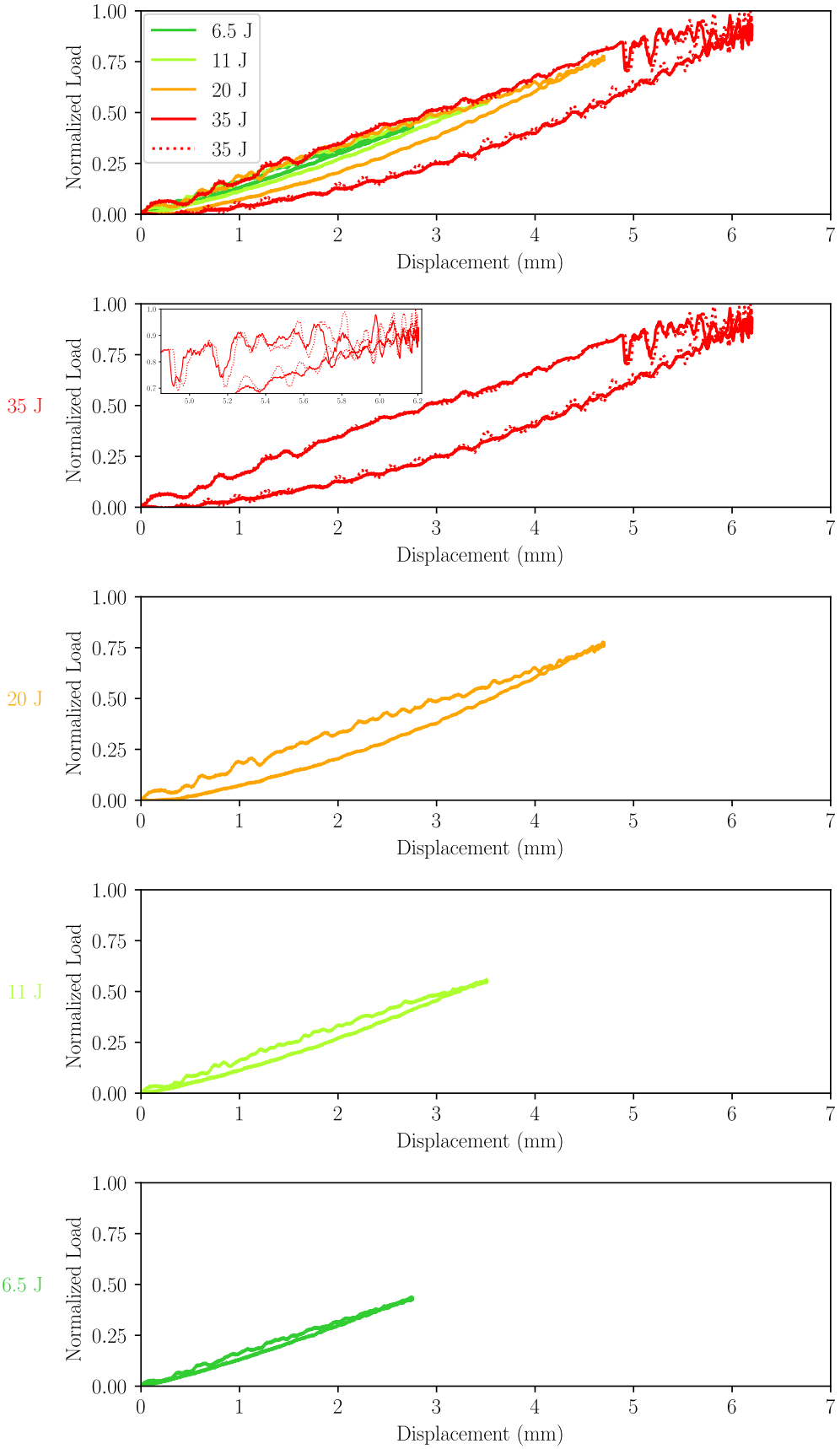

Figure 2.6: Load-displacement responses presented for the highly oriented laminate C20

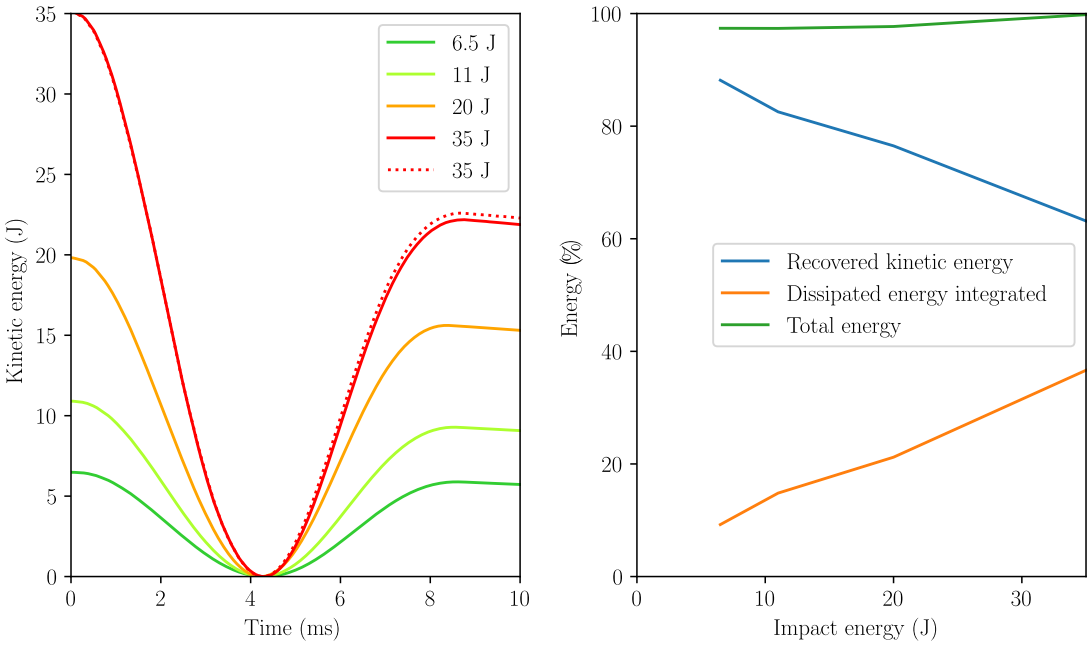

Figure 2.7: Energetic curves presented for the highly oriented laminate C20

2.1.3.3 Influence of the stacking sequence on macroscopic behavior and impact damage resistance

The two laminates are compared firstly using the load-displacement response on the top of FIGURE 2.8. All results that have been doubled or tripled have been averaged. As C20 laminates are stiffer than Q16, the global responses present a higher tangent modulus. The maximum load reached is 20% higher for the C20 laminate. The Q16 laminate is more compliant and the out-of-plane displacement is almost 20% greater than for C20 laminate. For lower impact energy, similar hystereses are found for Q16 and C20 laminates. However, after 20 J, dissipation increases for the Q16 laminates as the hysteresis is more important than that observed on C20 laminates.

At the bottom of FIGURE 2.8, the kinetic energy evolutions have been compared on the left. Firstly, the contact times are different between the two laminates. Indeed, the contact time is a function of $\sqrt{m/k}$, where m is the mass of the impactor and k is the stiffness of the plate and impactor. Thus, the stiffer the plate, the shorter the contact time.

For the C20 laminates, the kinetic energy is rapidly converted to strain energy. After impact, a similar amount of kinetic energy is recovered from 6.5–20 J for both laminates. Nevertheless, at 35 J, the Q16 dissipates 20% more than C20 laminates. On the right, the energetic assessment is presented for both laminates. The dissipated energy increases linearly for the C20. For the Q16, the dissipated energy increases linearly until 20 J. A significant hike is shown after 25.9 J for the Q16, highlighting an important dissipation due to additional failure mechanisms.

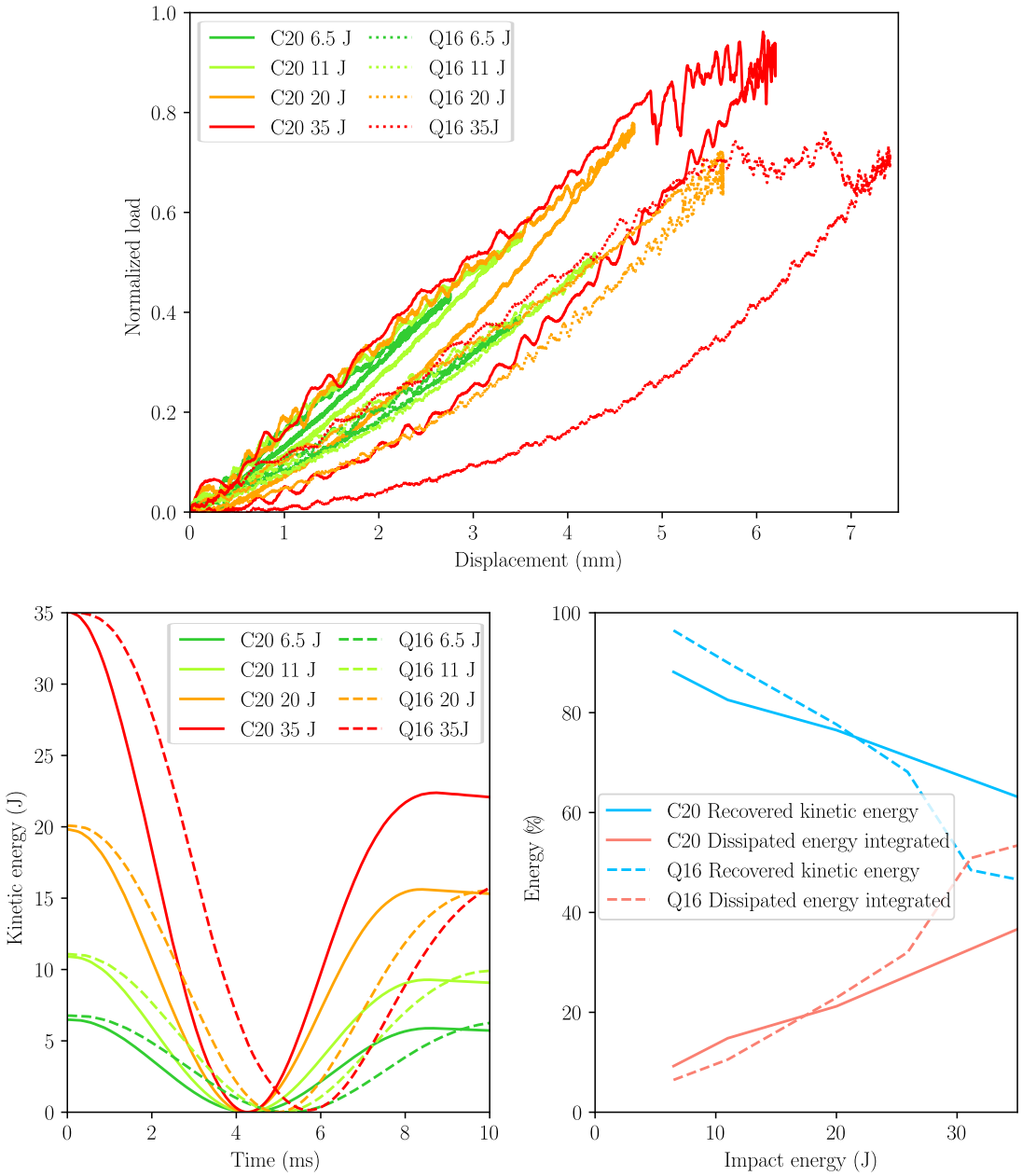

Figure 2.8: Comparison of the global responses between Q16 & C20 laminates

2.1.3.4 First understanding of the degradation induced by a low-velocity impact

A first analysis has been conducted based on the results obtained for LE/LV impact tests performed on the last generation of composite laminates. The analysis has given essential information on the different studied laminates (Q16 and C20). It has also highlighted the different behaviors of the two laminates. Several non-linearities have been observed during the loading stage. For the quasi-isotropic laminate Q16, a knee point marking a stiffness shifting has been observed. Indeed, the structure undergoes stiffening for displacement higher than that value (about 4 mm), which could be explained by non-linear geometrics. At a certain point, load drops with successive oscillations occur, since 20 J for the Q16 laminate and 35 J for the C20 laminate.

The presence of oscillations is caused by a high amount of energy release induced by damage, which is responsible for structural instability. The damage mechanism responsible for this severe non-linearity or its location through the thickness is unknown for now. After the unloading, load-displacement curves present hystereses, highlighting that irreversible phenomena (impact damages) occurred during the impact test. An indicator of the damage severity is the calculated dissipated energy. However, it does not provide further information about the nature of the damage mechanisms responsible for this total dissipation.

Thus, it is essential to introduce the NDT and the DT methods to inspect and control the damage state in the two different laminates. The following section will detail the investigation of impact damages using classical inspection means.

2.2 Investigation of impact damages using NDT and DT methods

Once the impact has been performed, NDI and DI have been carried out with two objectives. The first consists of visualizing the different damage patterns for this specific material and bringing qualitative comprehension of the damage mechanisms. The second objective analyzes the damage quantitatively (calculating the damaged area and measuring the residual dent). Different means have been selected to fulfill these objectives and allow a clear damage assessment for this specific material. The tables 2.2 and 2.3 summarize the techniques used for impact damage investigation.

NDI & DI	Impact energy					
	6.5 J	11 J	20 J	25.9 J	31.15 J	35 J
Dent measurement	✓	✓	✓	✓	✓	✓
UT	✓	✓	✓	✓	✓	✓
Micrographs	✗	✗	✓	✗	✗	✗
CT	✓	✓	1 ✓ 1 ✗	✗	✓	1 ✓ 2 ✗

Table 2.2: Sum-up of the controls performed on the Q16 laminate

NDI are firstly carried out :

- The residual dent has been measured using a mechanical comparator, which evaluates the dent depth as a function of the impact energy;
- UT provides information about the projected damaged area and the location through the thickness of the damage (mainly delamination);

Once these inspections are carried out, DI takes place. The sample is cut and prepared for :

- Micrograph observations to evaluate qualitatively the damage shapes and the different kinds of damage encountered in this specific material;

NDI & DI	Impact energy			
	6.5 J	11 J	20 J	35 J
Dent measurement	✓	✓	✓	✓
UT	✓	✓	✓	✓
Micrographs	✗	✗	✓	✗
CT	✓	✓	✓	1A ✓ 1A ✗

Table 2.3: Sum-up of the controls performed on the C20 laminate

- X-ray CT to provide a deep understanding of the damage mechanisms through the laminate thanks to 3D volume information;

All of these controls are complementary for a full assessment of impact damages and will provide answering tools on the mechanical behavior of this material when subjected to impact loading.

2.2.1 Presentation of the different NDT and DT methods associated to the experimental campaign

2.2.1.1 Residual dent measurement

Once impact tests were performed, the residual dent was measured 24 hours after the impact. A Mitutoyo mechanical comparator has been used for the measurement, as shown in FIGURE 2.9. The sample is supported on the impact window, and the comparator is calibrated to zero on edge. The measurement precision is equal to 1/100 mm.

Figure 2.9: Mechanical comparator used for the measurement of the residual dent

2.2.1.2 Ultrasonic inspection

Two different systems have been considered, as shown in FIGURE 2.10. The first one uses a mono-element ultrasonic probe with a Sofranel signal generation and a Picoscope device for data acquisition. High resolutions are obtained using this probe. However, it requires long-time acquisitions. The second system recently acquired is a complete system provided by TPAC. The Pioneer line comprises phased array hardware, a 5 MHz multi-element probe with 128 cells, and in-house software for data acquisition. Fast controls are obtained using multi-element cells. Nevertheless, the main drawback is a lower resolution than obtained with mono-element cells. Different scan techniques are allowable for the multi-element probe. A focalization of the signal toward the sample with a 25 mm focal distance has been chosen.

The sample is immersed in a water tank. The sample is fixed to a motorized arm with 2 degrees of freedom. The arm is piloted using a Newport controller. Different possibilities can be used to define the scan trajectory, an automated zig-zag path, or a displacement controlled by the operator. Once the acquisition is finished, the data

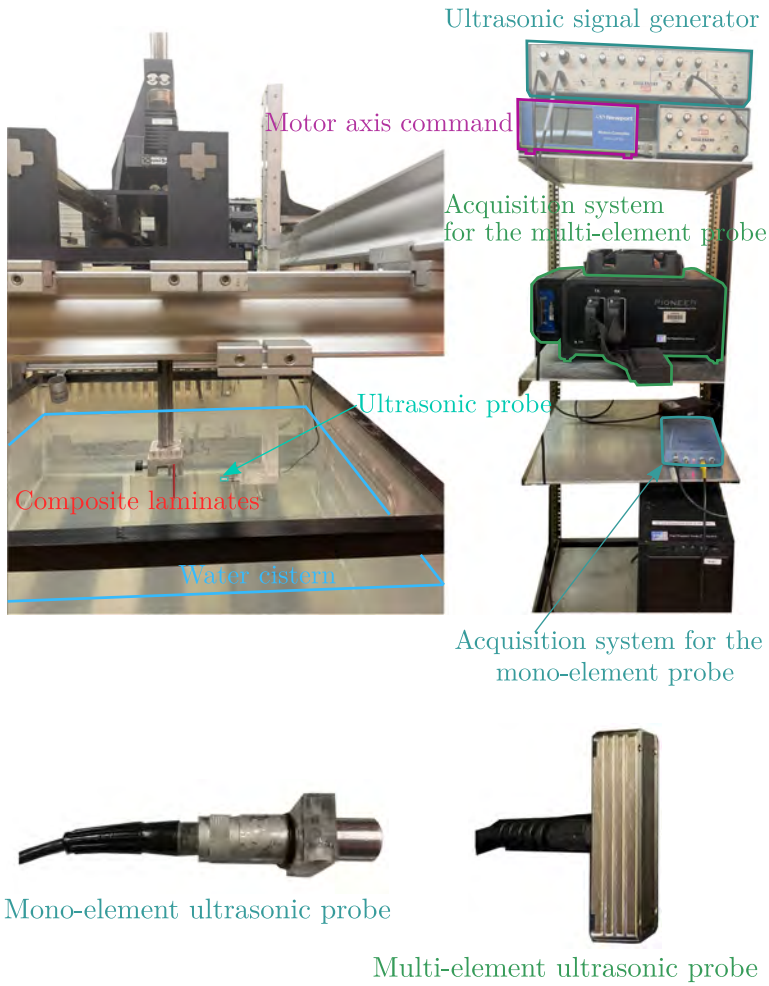

Figure 2.10: Ultrasonic devices at ONERA

is loaded into a non-destructive evaluation software CIVA provided by EXTENDE. First, the data is processed by creating gates to remove all the parasitic signals reflected between the water and the material at the interface entrance. Then, the echo for each point is recalled toward the entrance gate. Finally, the data are

analyzed (A-scan, C-scan) as shown in FIGURE 2.11. Importance is given to the C-scan in-depth as it provides the projected damaged area, which is crucial information for industrials. Moreover, the C-scan in-depth determines the delamination location through the thickness.

- Signal of the designated point in black

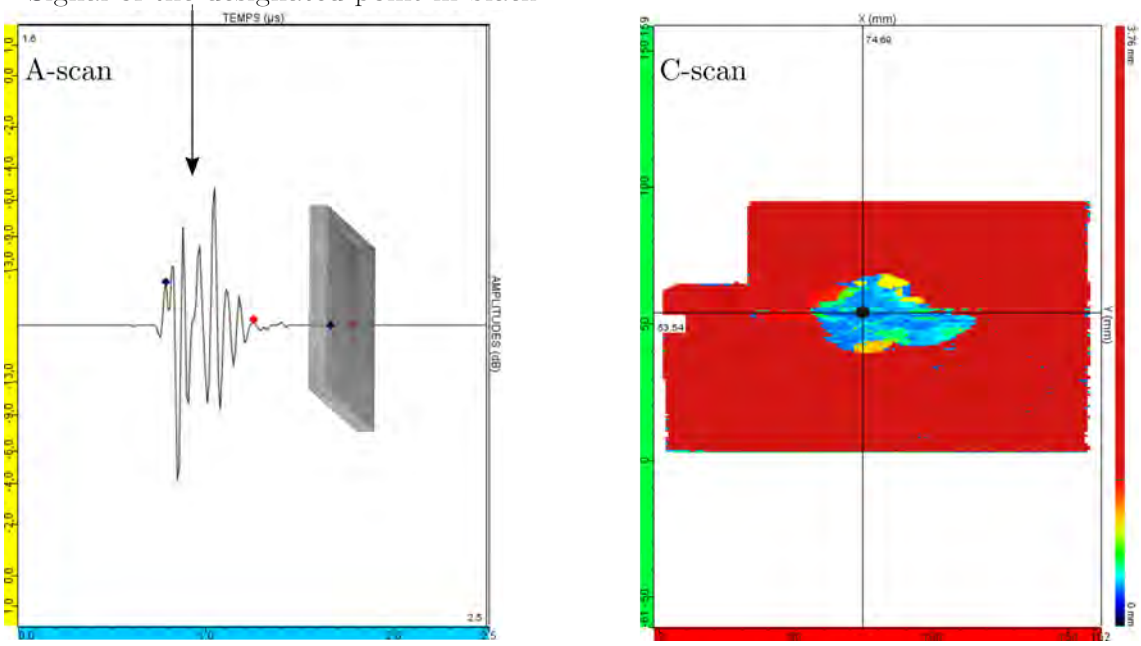

Figure 2.11: Signal outputs obtained after the UI for A-scan and C-scan

2.2.1.3 Micrograph observations

Observations of the impact damages have been carried out using optical microscopes and SEM at ONERA, as presented in FIGURE 2.12. Before observations, samples were cut using a diamond saw at 0° and 90° to visualize in these two planes the damaged topology, as reported in FIGURE 2.13. Once cut, the samples have been polished before observations using different Silicon carbide (SiC) sanding papers until (0.25 μm). The finish has been performed with a diamond-coated suspension.

Optical observations Two different microscopes have been used in the presented work (An Olympus and a Zeiss) with different magnifications to observe the damages ($\times 5$, $\times 10$).

SEM In order to study more locally the damage topology with higher resolution and depth of field, SEM observations have also been carried out on the samples already cut for optical observations. The observation was performed using a ZEISS Merlin with a field emission gun. A tension of 5 kV and an amperage of 5 nA were applied to the sample. Different visualizations were performed:

- A topography contrast to visualize the depth;
- A chemical contrast to distinguish the different materials within the composite material;

Optical microscopes SEM

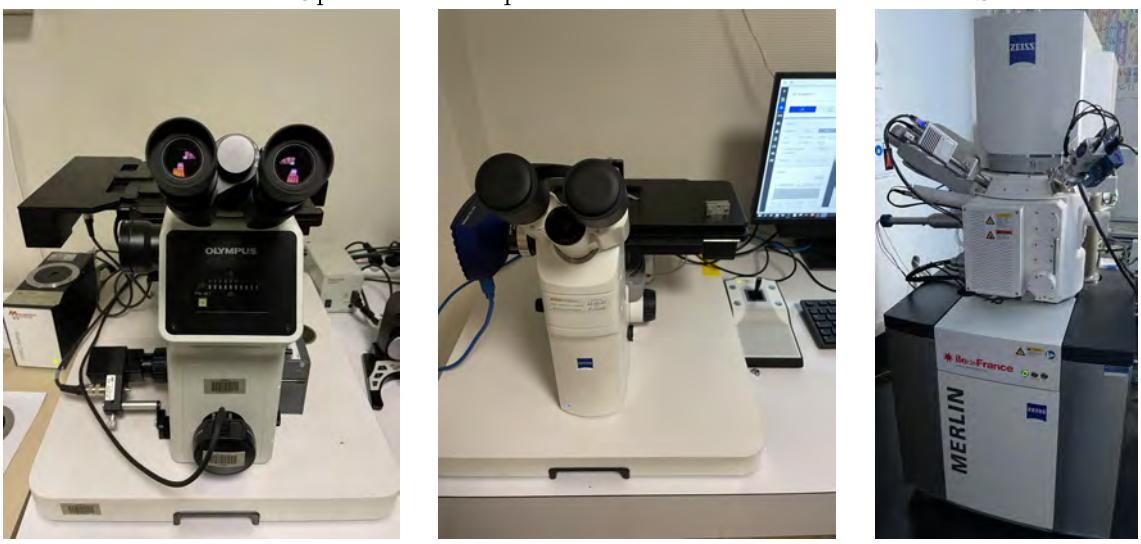

Figure 2.12: ONERA's microscopes for the inspection of impacted samples

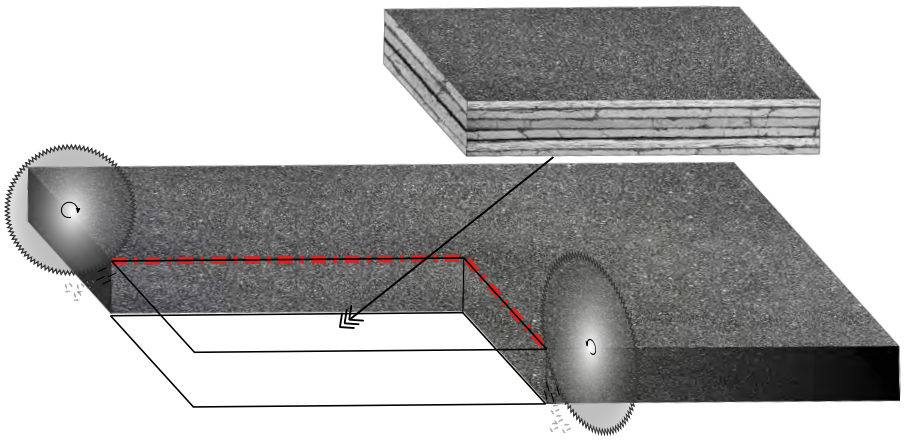

Figure 2.13: Cutting plane showing the cut path orientation at 0° and 90° for the micrograph observations

2.2.1.4 CT tomography

CT scans have been performed to obtain a deep understanding of impact damages thanks to the volume character of the inspection. It allows recognition of the different damages and their location through the thickness of the sample.

Sample preparations As exposed in chapter 1, the higher the distance from the X-ray beam, the lower the resolution. Thus, in order to obtain good resolution for CT scans, it is necessary to avoid wide samples. Thanks to the previous UI (especially C-scan), the boundaries of the damaged zone have been determined to remove the undamaged material from the samples. Samples have then been cut, as reported in FIGURE 2.14. Finally, the impacted samples have been split into five bundles as a function of the damage width. A damage width defines each bundle. The resolution obtained for each bundle is presented in TABLE 2.4. As the ply is 0.192 mm thick, the number of slices through the thickness evolves from 10 slices

(18 μm resolution) to 14 slices (13 μm resolution) for each ply.

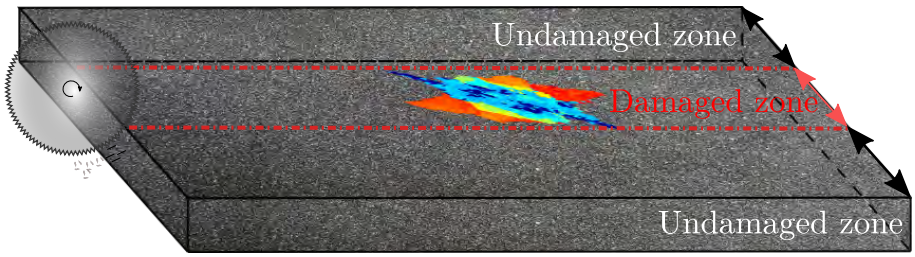

Figure 2.14: Cutting plane for CT control

Bundle (damage width)	< 25 mm	< 30 mm	< 35 mm	< 38 mm	< 45 mm
Resolution (μm)	13	14	16	16	18

Table 2.4: Resolution obtained for each bundle after CT scans

CT scans The inspection by CT scans has been realized at LMPS (FIGURE 2.15) using a North Star Imaging (NSI) X50 250 kV computed tomography device. The system is equipped with a detector of 3072×3888 pixels, 14 bits with a cesium scintillator. X-rays were generated using a high-power focal spot (120kV and 150 μA). The data acquisition was carried out with a time exposure of 500 ms, a number of projections of about 2000, and the number of frames per projection was 20. Finally, the acquisition time for each sample was about 105 minutes. The reconstruction of the 3D volume has been performed by LMPS using the NSI software.

Image processing After reconstruction, image processing has been performed:

- Rotation in the three axes performed with ImageJ [Schneider et al., 2012];
- Contrast enhancement using the Scikit-image library in python [van der Walt et al., 2014]. Contrast Limited Adaptive Histogram Equalization (CLAHE) algorithm has been used to stretch the histogram of each slice, as shown in FIGURE 2.16;
- Substantial brightness variation through the thickness has been observed for some CT scans. Histogram matching has been performed on each slice to get the same histogram repartition through the width. Consequently, brightness gradients are minimized in width;

All of these treatments make damage segmentation easier.

Impact damage segmentation using deep learning Once image processing is completed, impact damage segmentations are performed. A first attempt has been used in this work using the Otsu threshold ([Otsu, 1979]). Interesting results were obtained, but damaged pixels greater than the Otsu threshold value were not captured. Moreover, as the external environment pixel value is similar to the damaged

Figure 2.15: X-ray tomograph device at LMPS laboratory

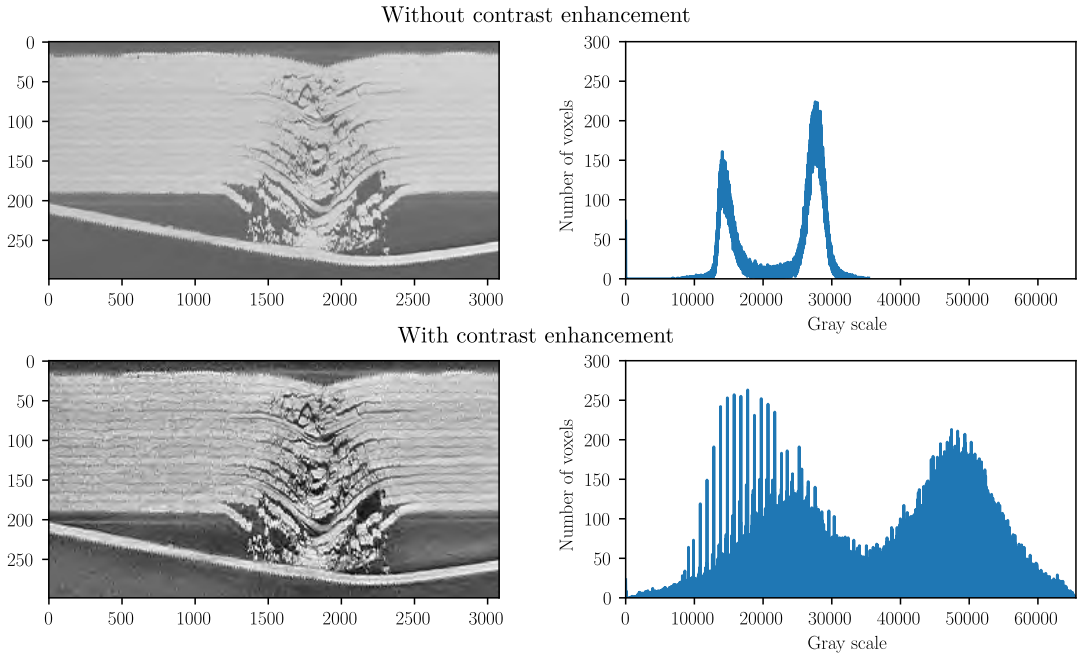

Figure 2.16: Influence of contrast enhancement on through the thickness impact damage observation

pixels, the segmentation also captured the pixels belonging to the external environment. In [Ellison, 2020], a strategy based on detecting the laminate boundaries

allows for removing the exterior air. However, based on the excellent results obtained in [Badran et al., 2020] for the segmentation of cracks in ceramic composites using deep learning, it has been chosen to investigate this segmentation methodology.

Thus, the segmentation has been performed in Dragonfly [Dragonfly, 2021], a free-of-charge software for non-commercial research use. The Deep-learning toolbox integrates the TensorFlow and Keras libraries from Google. The training and inference data are performed using the deep-learning toolbox. A conventional neural networks (CNNs) U-NET algorithm has been chosen for performing the damage segmentation. Indeed, this algorithm has been suitable for performing reliable segmentation for medical images ([Ronneberger et al., 2015]). The neural network architecture has obtained relevant results with three hidden layers. Several parameters were needed to be defined for the model training :

- Patch size defines the size of 2D square patches. The image is subdivided into patches that contain local image information;
- Stride-to-input ratio defines the location of the nearby patch. A stride-to-input ratio of 0.5 will overlap half of the two adjacent patches;
- Batch size contains several patches. The neural network weights are updated between two training batches;
- Epochs correspond to the number of iterations during the training. An epoch involves the training of all batches in one iteration;

Training data The objective is to segment the different impact damage mechanisms. The main issue is that the impact damage pixel gray value is similar to the exterior environment. Therefore, as shown in FIGURE 2.17, three labels have been defined. The first label in green is for the external environment, the second in red for the sound material, and the last in purple for the impact damages. The training data has been performed on 2D slices containing the entire thickness. It has been motivated to distinguish the three different labels easily.

For lower impact energy, the impact damages were contained within the laminate. However, for higher impact energy levels, a network between the impact damages and the external environment was observed on the top and bottom surfaces, which has made the training more complex. In consequence, 10–15 transverse images were needed to train the samples impacted at lower energies. For higher energies, the training data need 15–20 transverse images. 80% of the patches were used for training, and 20% were used to evaluate the predictive capability of the trained model. After a few epochs (typically between 40 and 50), the trained model reaches fast convergence with a 98-99 % accurate score.

Several trials have been performed to obtain the optimal training parameters. Based on the final inference quality performed on untrained data, it has been decided to select a patch size of (32×32 pixels), a stride-to-input ratio of 50%, and a batch size of (64×64 pixels), $2\times$ the patch-size. The loss and the validation loss functions are plotted for each iteration during the training, as presented in FIGURE 2.18. The lower these functions are, the higher the model's accuracy. 28 iterations have been performed (epochs) in a total of one hour and a half for this model. It can be shown that fast convergence is obtained for the two functions highlighting a suitable model architecture (hidden layers, cost functions) for this segmentation problem.

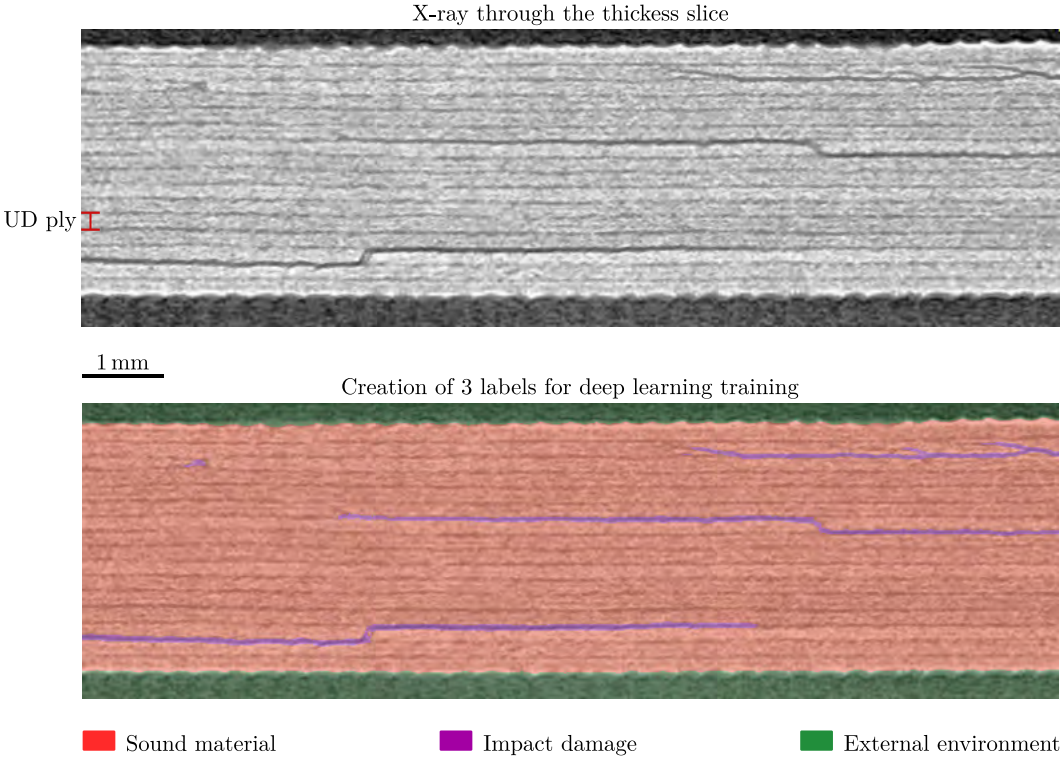

Figure 2.17: Labelling process for deep learning training

Moreover, it can be noted that the two functions are almost overlapping, resulting in a quasi-perfect fitting. In other words, the model fits the training data very nicely.

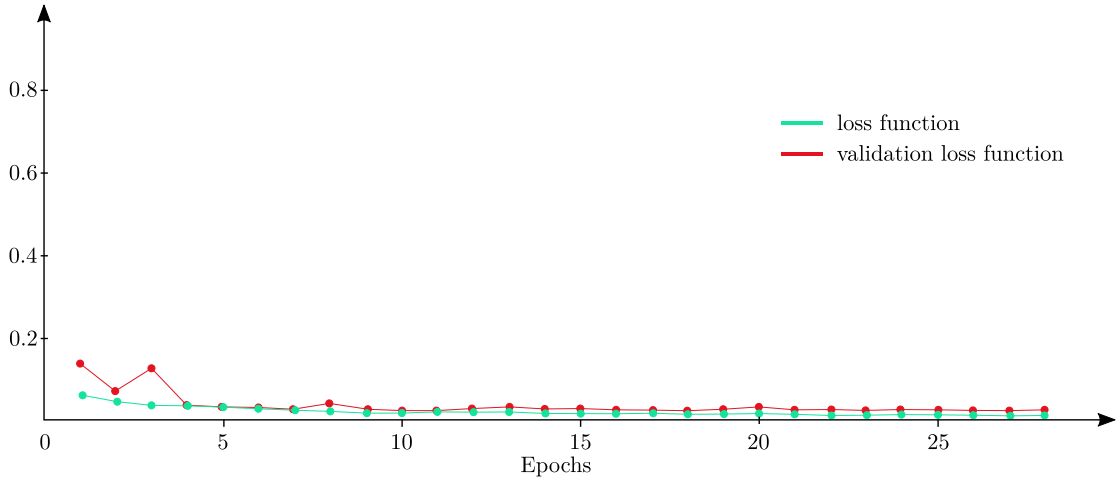

Figure 2.18: Convergence analysis of the trained U-net algorithm

Segmentation results Once the model is trained, the segmentation has been performed on the untrained CT images of the composite plate. Complete segmentation of the impact damages for the entire X-ray tomography volume was performed in 90 minutes. Visual inspection confirmed the result's reliability. The prediction results are presented for three slices in different planes for the specimen impacted at

31.15 J in FIGURE 2.19. It can be observed that the segmentation of the three labels was performed accurately. Despite the similar grayscale levels, the impact damage is dissociated from the external environment, confirming the algorithm's reliability. The complex damage pattern was straightforwardly captured.

It should be noted that the segmentation performed for higher impact energy levels was quite challenging as the material no more bounds impact damages. In some regions, no explicit boundaries are present between the impact damage and the exterior air. Thus, the U-net algorithm makes it difficult to predict the accurate label in these regions. Nevertheless, it can be shown that excellent results are obtained using DL U-net. The overall damage (especially delamination) is captured accurately through the thickness.

Impact damage segmentation rendering The visualization of damages has been performed using Paraview, an open-source software ([Ahrens et al., 2005]). The segmentation of impact damages is presented in FIGURE 2.19 for a Q16 laminate impacted at 31.15 J. A color-coding has been used to visualize the damage within the thickness. It can be seen that a clear visualization of impact damages is obtained with very few noises thanks to deep learning.

2.2.2 Analysis of impact damages

In this subsection, the investigation of impact damages for this specific material is carried out. Firstly, an introduction to the different damages encountered in this material is presented. Then, the damage state as a function of the impact energy is studied.

2.2.2.1 Qualitative understanding of impact damages

Delamination The delamination is first introduced as it represents critical damage that can lead to the catastrophic failure of the composite plate. The delamination extends is easily detectable using UI or CT. FIGURE 2.20 shows the damage extent obtained from the X-ray in a shaded 3D and coded color through the thickness (top right image). The delamination extent is easily observed for each interface, thanks to the high resolution of X-ray CT scans. If we study more locally the damage using X-ray (Plane 3), the delamination extent is observed for the third interface [0/-45] starting from the bottom. It can be observed that the delamination is classically clustered between the 0° bottom ply matrix crack and the 45° upper ply matrix crack. Planes 1 and 2 show the delamination cracks through the thickness, which highlights the strong connection between the delamination and matrix cracking with delamination migration phenomenon as studied in [McElroy et al., 2017].

Matrix cracking Two kinds of matrix cracking are observed for this material, as presented in FIGURE 2.21. The first one is matrix cracking due to high out-of-plane stresses (σ_{23} and σ_{13}) highlighted in orange squares. These cracks are mainly oriented at 45°. The second is matrix cracking induced by high bending stresses σ_{22} for the bottom plies (near the non-impacted face) highlighted in blue squares. As shown from the plane 2 in FIGURE 2.20, no matrix cracking are observed directly under the impact.

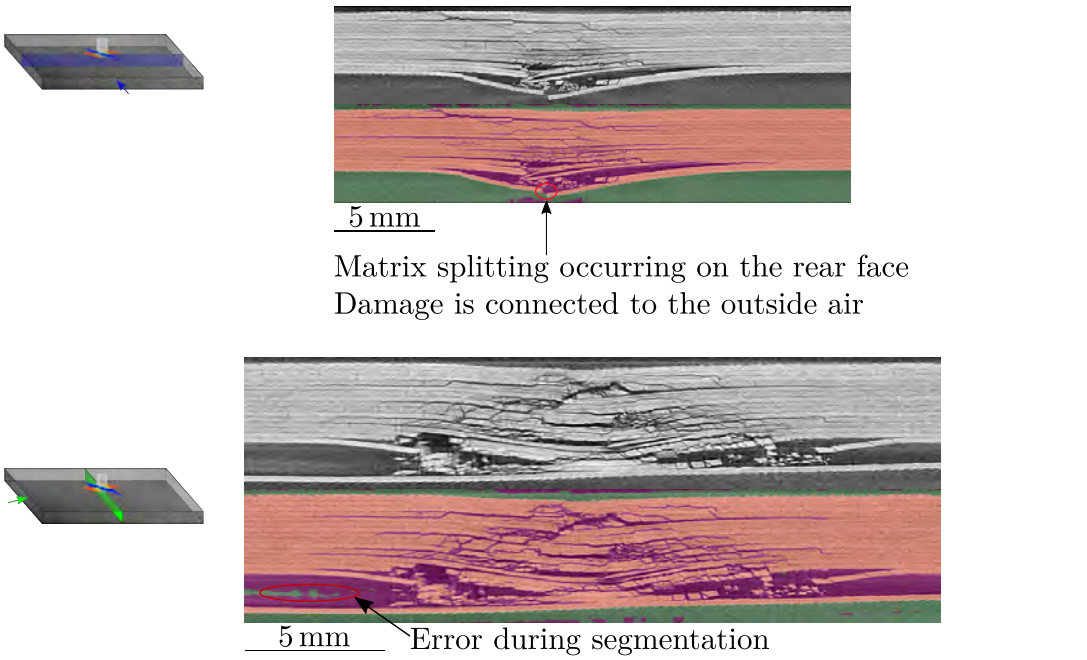

Figure 2.19: Segmentation results obtained using the U-net trained algorithm for the Q16 laminate impacted at 31.15 J

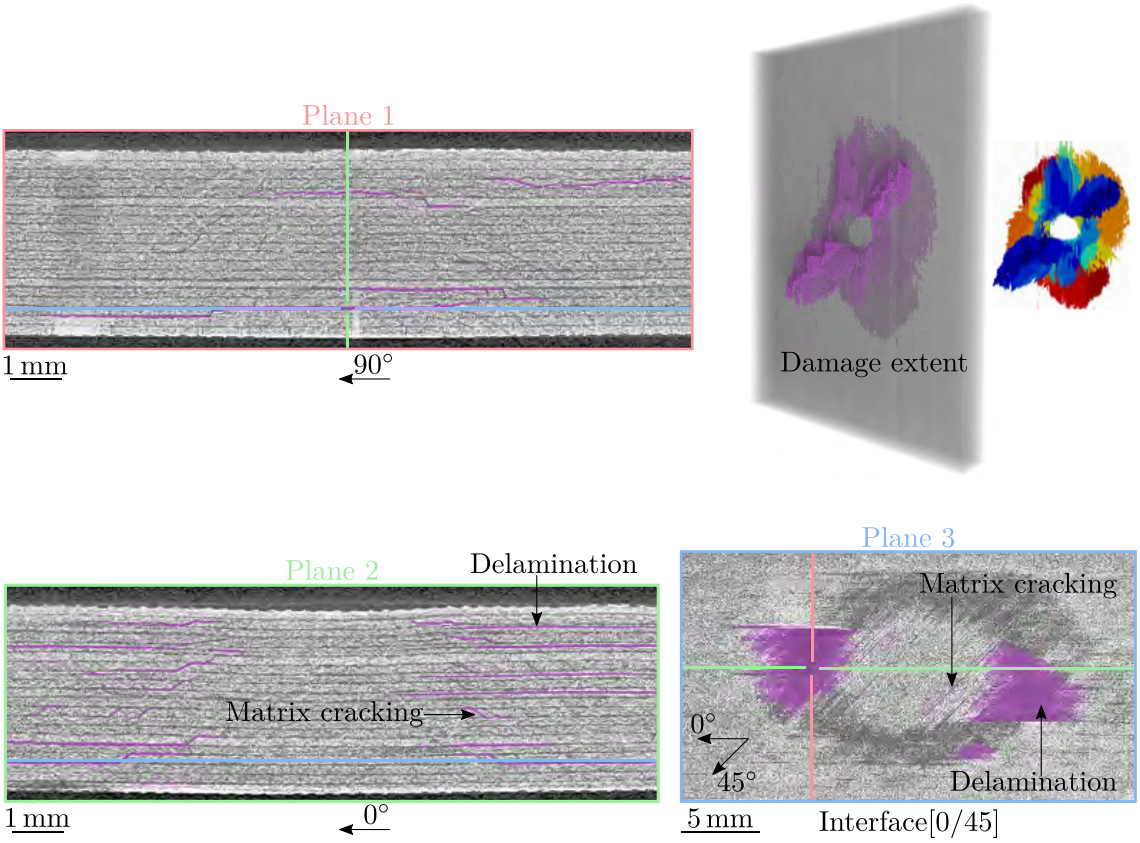

Figure 2.20: Delamination highlighted in X-ray according to the different planes for the C20 laminate impacted at 20 J

Fibre breaks in compression One of the specificities of this composite material is the strong presence of fibre breaks in compression for the top plies. The fibre breaks in compression arise early (since 6.5 J) for both laminates. The higher the impact energy, the deeper the fibre breaks in compression occur. In FIGURE 2.22, the fibre kinking mechanism is presented. Micrographs obtained from SEM show the failure of 0° plies in FIGURE 2.22.a and (b), the kink band is straightforwardly observable. It can be noted that the fibre kinking induces the failure of the interface. In FIGURE 2.22.c and (d), the fibre kinking for the second ply from the impact surface using X-ray CT is presented. The fibre kinking illustrated in FIGURE 2.22.c is characterized by a sharp crack oriented at -45° and perpendicular to the ply orientation (45°). No fibre break is observed below the impact zone. Indeed, the material undergoes reinforcement thanks to the local hydrostatic pressure. In other words, the principal stresses are all negative which prevent failure. In FIGURE 2.22.d, the slice highlighted in red is shown, it can be observed a 45° oriented kink-band regarding the normal of the slice.

Fibre breaks in tension The fibre breaks in tension occur for higher energy impact levels for the lower plies. Besides, it has been observed that the fibre breaks depend on the laminate stacking sequence. Indeed, for the Q16 it appears at 20 J, whereas for C20 laminates, fibre breaks in tension occur at 35 J. FIGURE 2.23 illustrates the fibre breaks observed using SEM and X-ray. On the left, fibre breaks in the 45° ply are observed using a SEM. X-ray slice shows the sharp crack induced

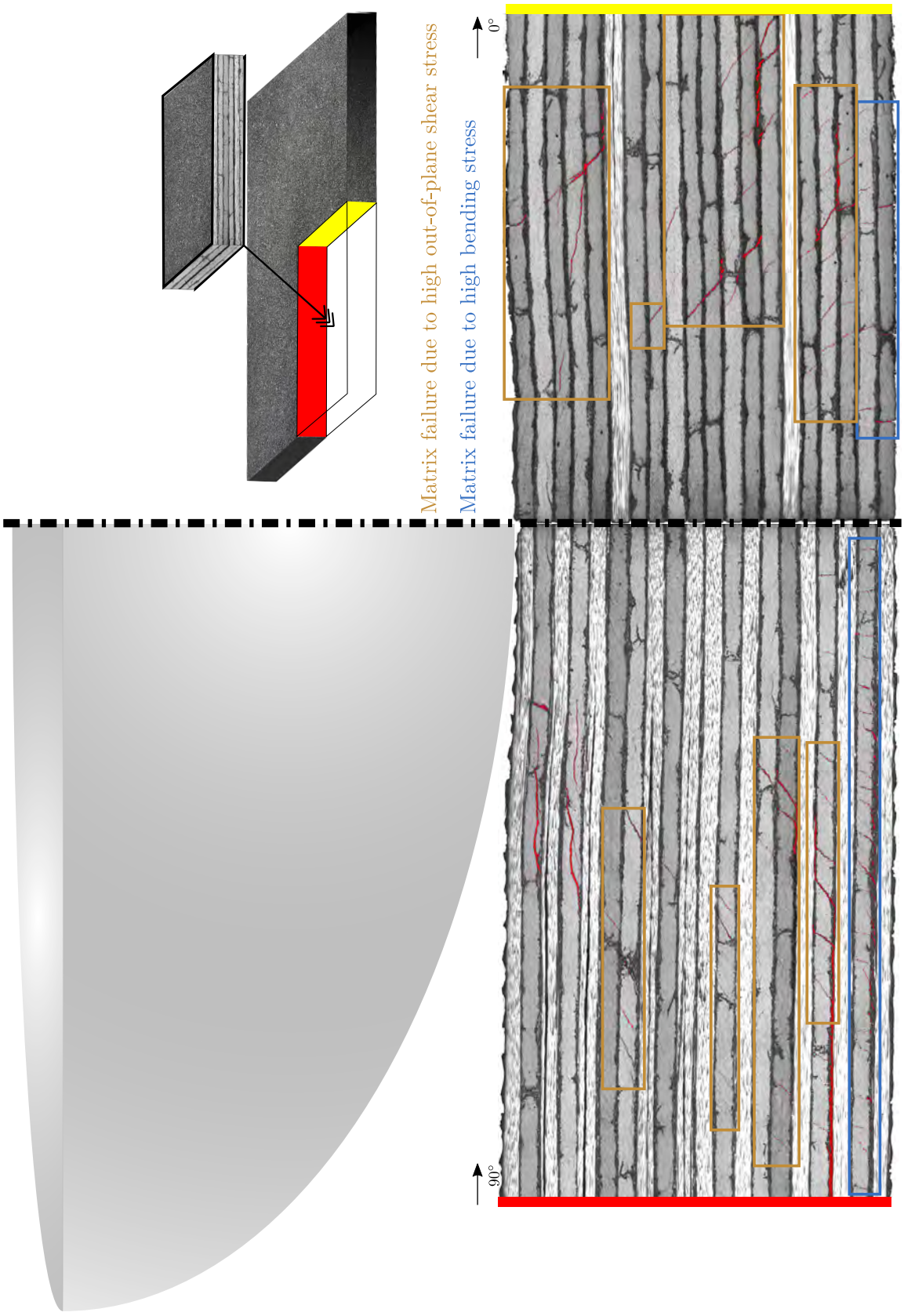

Figure 2.21: Matrix cracking observed using micrograph observations for two different cuts of the C20 laminate impacted at 20 J

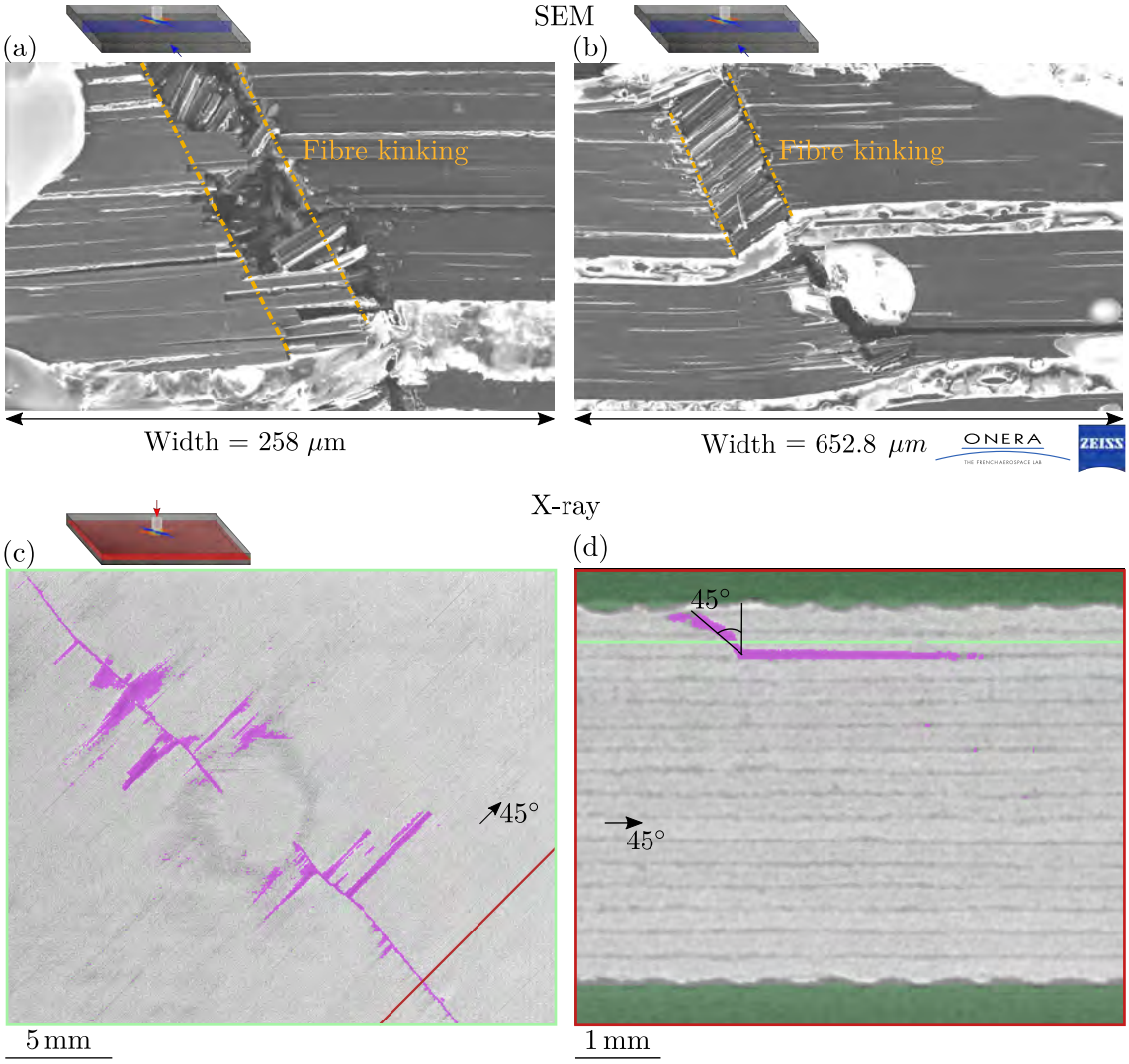

Figure 2.22: Fibre breaks in compression occurring in a $[0_{16}]$ laminate during an ILSS test (SEM) and in the Q16 laminate impacted at 20 J (CT scans)

by fibre failure on the right. Once fibre breaks occur, the laminate stiffness is highly affected and the sample is warped. Thus, the X-ray slice contains multiple pieces of information, making the understanding difficult for correct damage assessment. For instance the X-ray slice in FIGURE 2.23 contains the matrix cracking occurring in the 45 ply, the delamination located at the interface [45/90] and the fibre breaks occurring in the 90° ply.

Intraply macroscopic cracks It has been observed for this specific material that the fibre failure triggers intraply delamination. Usually, for conventional laminates, the fibre failure triggers the delamination at the interface. Nevertheless, more energy is required for this material to propagate within the interface due to the specific interlaminar toughening. Thus, the crack tends to propagate within the ply, requiring less propagation energy. FIGURE 2.24 shows the intraply delamination observed using SEM and X-ray. As observed on the left, this mechanism subdivides the ply into two parts. From the CT scan, it can be observed that the intraply delamination is triggered at the edge of fibre breaks in compression.

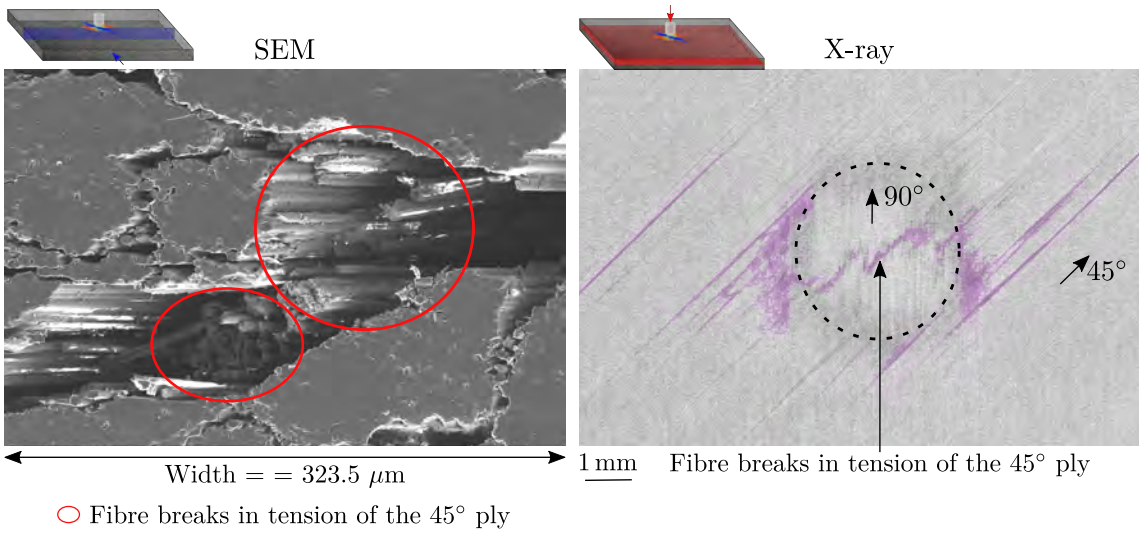

Figure 2.23: Fibre breaks in tension occurring on the 45° ply of the Q16 laminate impacted at 20 J

2.2.2.2 Damage state evaluation

This section is dedicated firstly to the evaluation of impact damage severity. Figure 2.25 and Figure 2.26 show that similar results are obtained between C-scan and X-ray for the two stacking sequences. However, the damaged area obtained from X-ray is systematically lower than obtained with C-scan. Same observations have been found in [Ellison, 2020]. It can be explained that damages, mainly delamination will be detected using UT due to the acoustic impedance created by the damage. For X-ray, damage sizes below the resolution will not be captured. Two remarks can be established based on the projected damaged surfaces obtained from the X-ray:

- Firstly, many damages occur near the impacted side (in blue) for both laminates. For the Q16 laminate, these damages are mainly oriented at -45°, whereas for C20 laminate the damages are oriented at 45°. This orientation is defined by the second ply below the impacted face. Indeed, as illustrated in Figure 2.27, the fracture orientation of the second ply below the impacted face (in cerulean) imposes the top ply 0° fracture orientation (in red). Moreover, Figure 2.27 shows that the intraply delamination is triggered at the edge of fibre kinking, highlighting the strong coupling between these two mechanisms. As fibre breaks in compression occur since 6.5 J (very soon compared to other materials), it explains the high amount of damage near the impacted face;

- Secondly, analyzing the different energy levels, it can be noted that the delamination cracks propagate firstly at the lower interfaces (near the rear face) for both laminates. This is explained by the high amount of matrix cracks at the rear face, which triggers the delamination. Besides, for lower impact energy levels, a non-damaged zone is observed. This non-damaged zone vanishes once fibre failures in tension occur (20 J for the Q16 laminate and at 35 J for the C20 laminate), it causes the failure of interfaces and thus delamination;

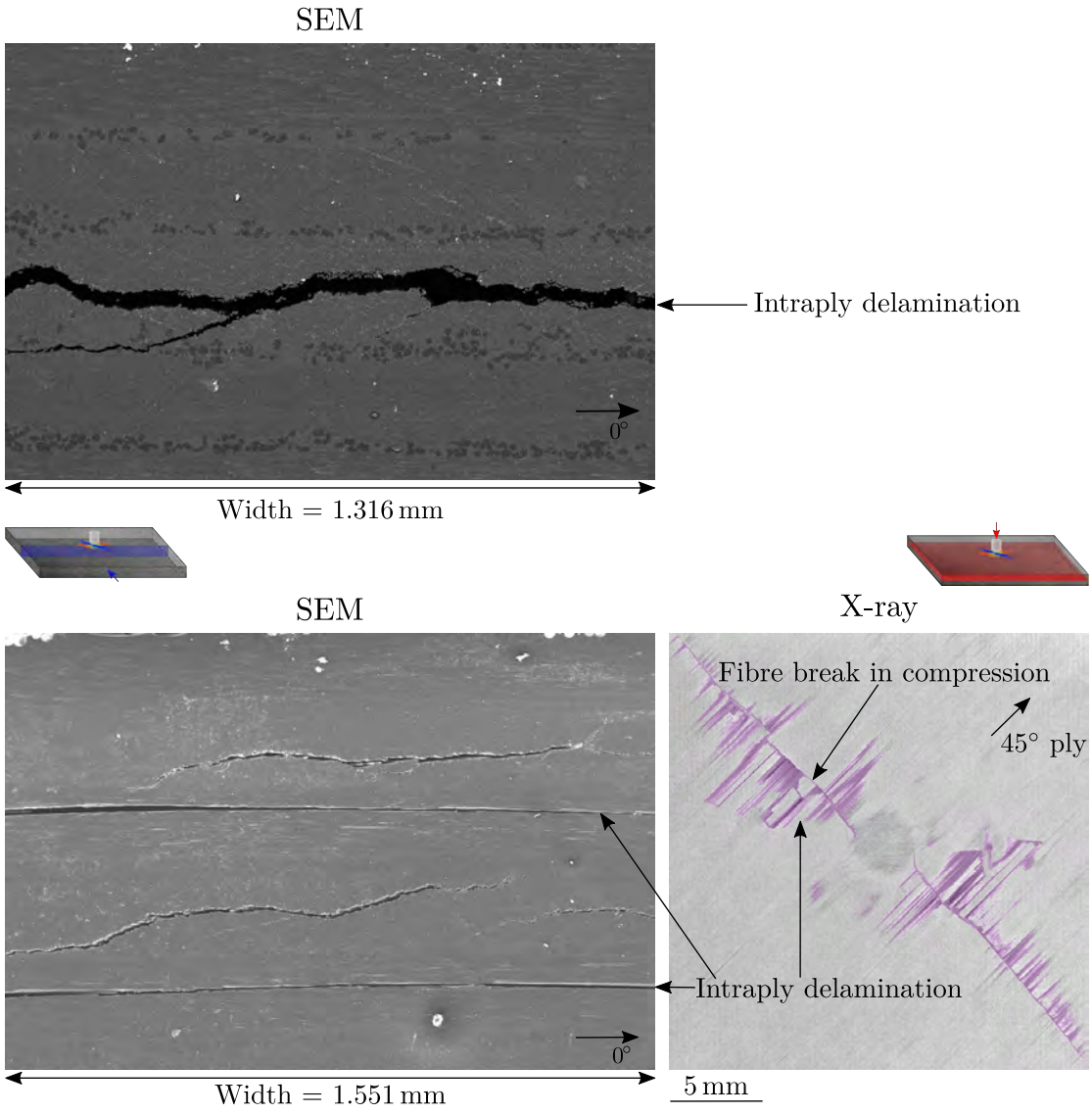

Figure 2.24: Intraply delamination mechanisms

In FIGURE 2.28, the evolution of the projected damaged area and the dent depth is presented for the two laminates. Similar results between C-scan and X-ray for the lower impact energies are observed for both laminates. However, for the higher impact energy levels, the difference is higher. At 20 J, the damaged area is more significant for the Q16 laminate. Concerning the dent depth, the mechanical comparator measurements show a linear trend for the Q16 laminate until 25.9 J and a significant increase in dent depth after 30 J. For the C20 laminate, a linear trend is also observed but for all impact energy levels. For the highest energy level, the Q16 laminate shows a residual dent equivalent to the thickness of three plies, whereas, for the C20 laminate, the residual dent depth is slightly more significant than the ply thickness. From these curves, it can be dressed that the damage is more pronounced for the Q16 laminate than the C20 laminate after 20 J. Based on the analysis obtained from controls, four stages can be defined:

- The first stage corresponds to the presence of fibre breaks in compression and matrix cracking through the laminate. The LE/LV impact performed at 6.5 J

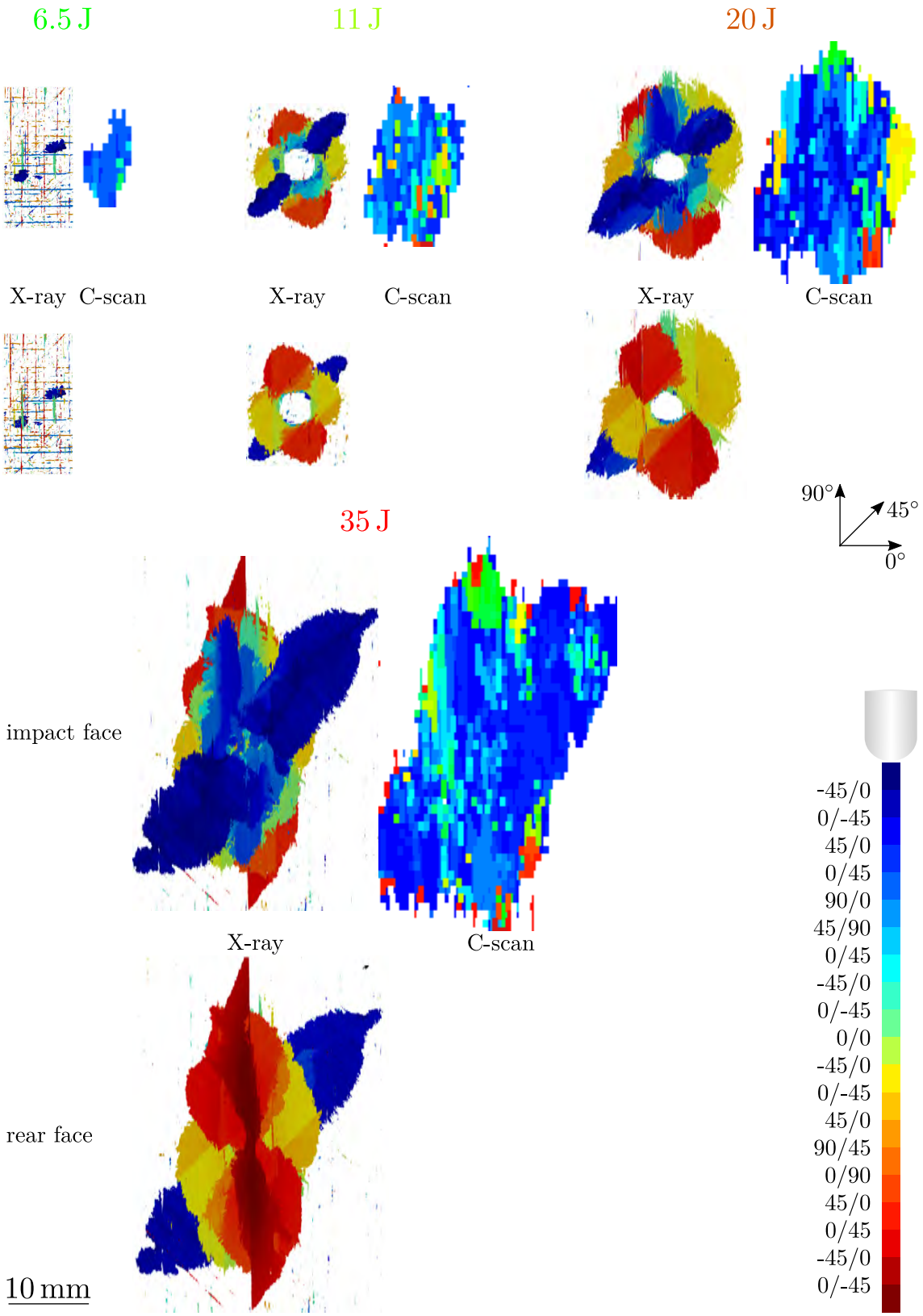

Figure 2.25: Projected damaged area obtained from C-scan and X-ray for the C20 laminate at different energy levels

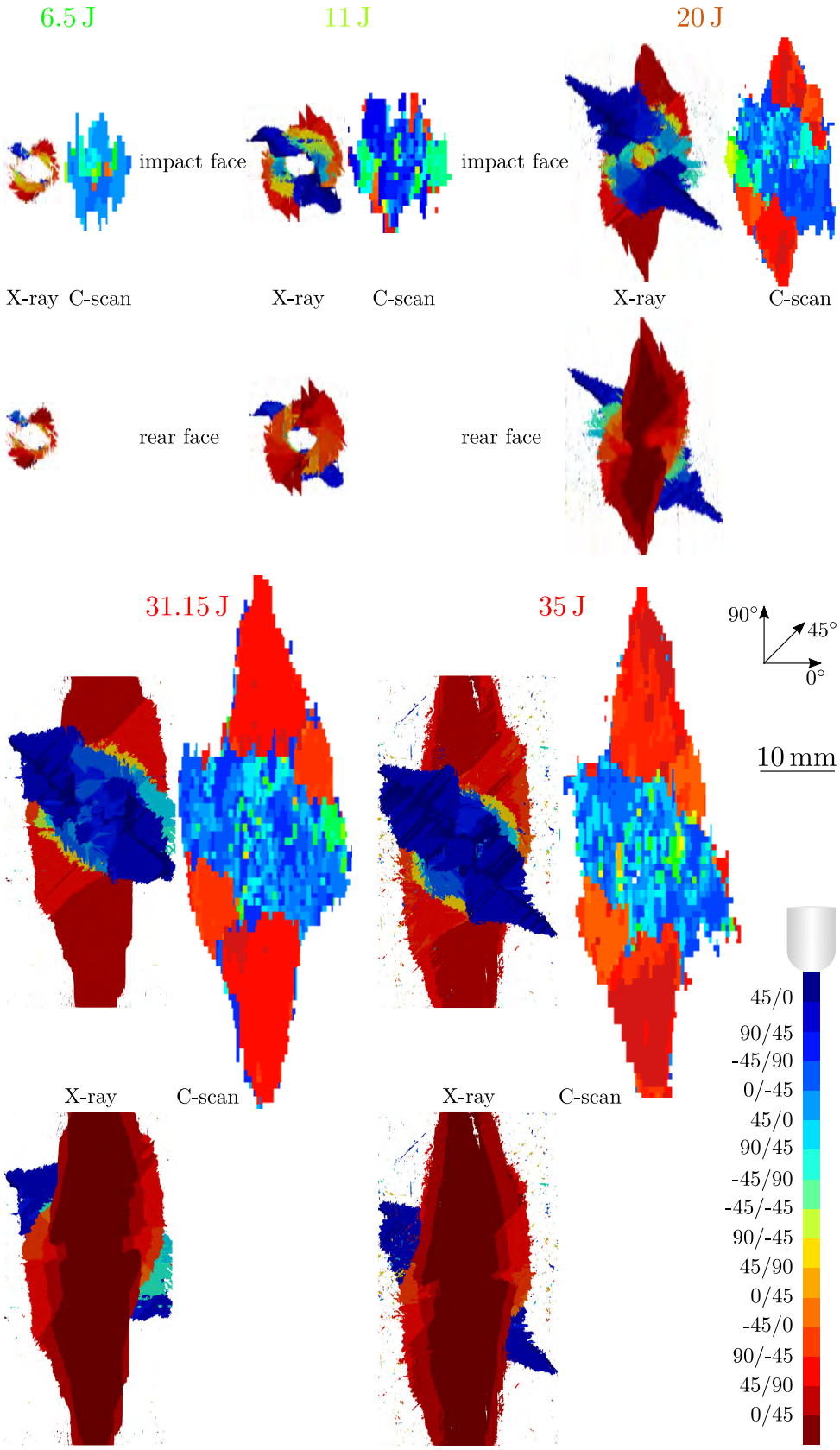

Figure 2.26: Projected damaged area obtained from C-scan and X-ray for the Q16 laminate

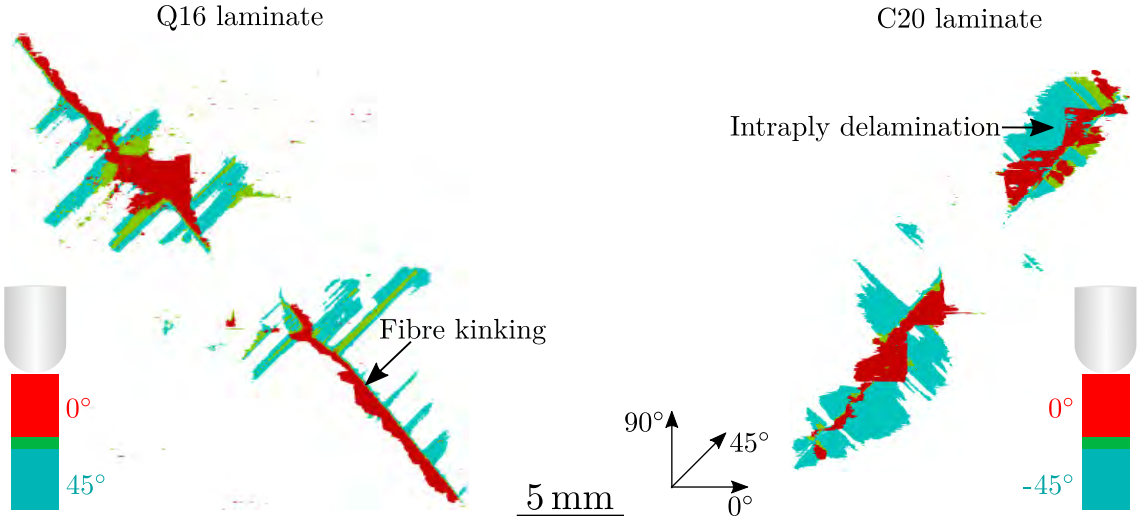

Figure 2.27: Projected damage for the top two plies in the Q16 and C20 laminates impacted at 20 J

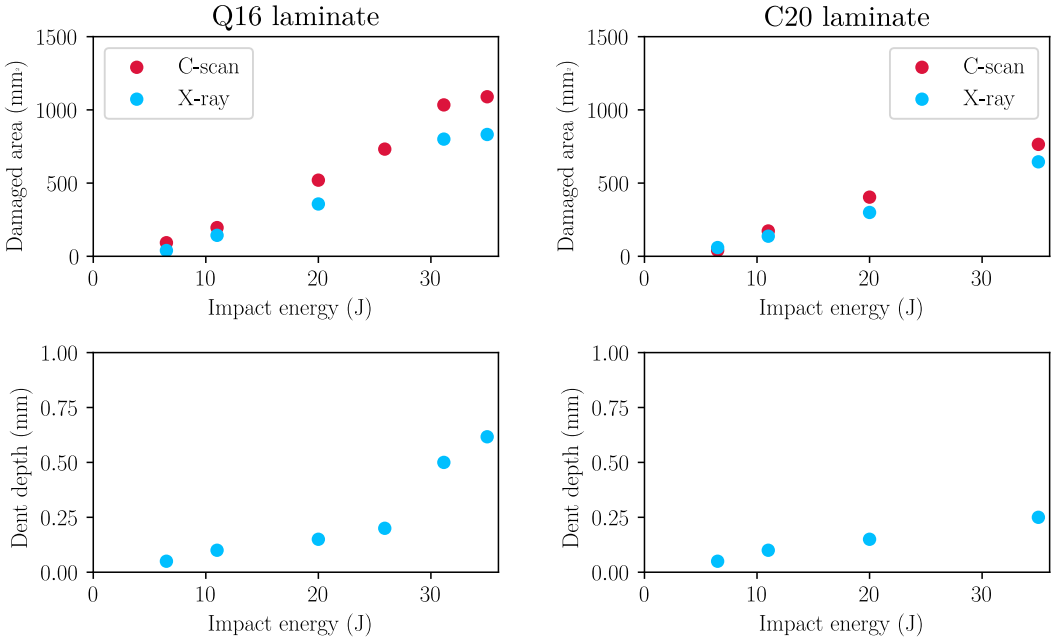

Figure 2.28: Evolution of the damaged area and dent depth as a function of the impact energy for the Q16 and C20 laminates

for the laminate C20 belongs to this category;

- The second stage is the presence of fibre breaks in compression, matrix cracking, and delamination for the lower interfaces. The laminate Q16 impacted at 6.5 J belongs to this category where the delamination is occurring in the lower interfaces;
- The third stage is multi-delamination occurring in several interfaces from the bottom to the top. It concerns the Q16 laminate and C20 laminate at 11 J and the C20 laminate at 20 J;
- The fourth stage indicates the presence of fibre breaks in tension. It occurs

for higher impact energy. It can be noted that for the C20 laminate, it occurs at 35 J whereas, for the Q16 laminate, it arises at 20 J. At this stage, it is challenging to analyze the X-ray tomography slices as the sample is highly warped due to fibre breaks in tension;

2.2.3 Lack of temporal events for damage scenario establishment

The analysis presented in this chapter has enabled understanding the mechanical behavior of a new generation of composite material with charged interfaces when subjected to impact loadings. The investigation of impact damages has shown classical impact damages such as matrix cracks, delamination, and fibre breaks (in compression and tension for high energy levels). However, it has highlighted different damage mechanisms than those observed on classical carbon/epoxy laminated composite materials. Indeed, intraply delamination and significant fibre failure in compression are observed. Moreover, strong interaction between the different kinds of damage has been observed. Similar damage mechanisms have been retrieved for two different laminate stacking sequences. However, the analysis shows that damage mechanisms are not arising simultaneously, especially for fibre breaks in tension that occur earlier for Q16 laminate.

One drawback of such analysis, highlighted in the previous chapter, is the non-confrontation of the macroscopic results obtained with the analysis of impact damages. No link could be established on which kind of damages have caused the different load drops or stiffness shifts. The damage occurrences need to be related to the time to identify each damage mechanism's effect on the global response analysis. It would enable the damage scenario reconstitution. The current *post mortem* analysis has to be enriched with time events providing information about the evolution of damages and their interactions during the impact event. Thus, in the next chapter, an in-situ damage monitoring methodology is presented to enrich the comprehension of the damage mechanisms in such material.

Chapter 3

Impact damage assessment using damage monitoring

Contents

This chapter aims to complete the understanding of the damage mechanisms occurring in the material under study. Firstly, the enriched experimental setup using high-speed Infrared cameras (IRC) and Visible cameras (VC) is presented.

Secondly, QSI is performed to evaluate the strain-rate effect compared to impact and to establish the damage chronology. Finally, the advantages and limitations of these two methods (impact vs indentation) are discussed and evaluated.

3.1 Experimental configuration for *in situ* monitoring of LE/LV impact on composite material

3.1.1 Modification of the actual impact machine

In situ monitoring was impossible due to a very crowded and confined space to monitor the rear side. Therefore, as presented in FIGURE 3.1, the impact machine has been lifted to allow positioning instrumentation to monitor the rear side.

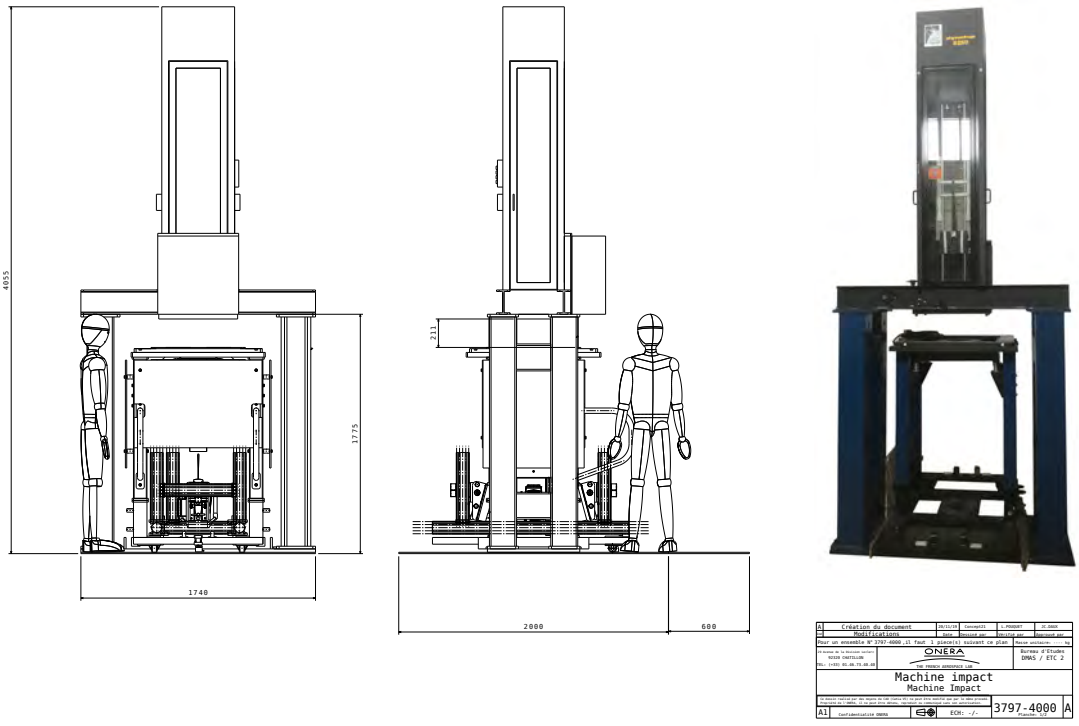

Figure 3.1: Impact machine modification

3.1.2 Presentation of the cameras for impact test monitoring

The experimental setup presented in the previous chapter is still considered. Nevertheless, four high-speed cameras have been introduced to complete the instrumentation of the impact test. FIGURE 3.2 presents the experimental setup considered in this study.

Two FASTCAM SA-X2 high-speed cameras are positioned under the sample to perform stereo DIC on the sample's rear face. The highest spatial resolution captured by the cameras is defined by the Frame size (FS). For a FS of 1024×1024

pixels, the Frequency (FQ) and the Shutter speed (SS) are limited to 12 500 Hz and 1 ms. The frame rate of the camera (FQ) can be increased up to 900 000 fps by reducing the spatial resolution. A black and white speckle pattern was applied on the rear face of the specimen. The rear face is lightened with two high power LED projectors (150 W). A special care on the selection of LED projector has been considered to reduce the exposure time in order to limit blurred area in the images, while ensuring that the thermal field measurement is not disturbed.

Two different IRC have been considered to capture the occurrence and evolution of the damage mechanisms likely to occur near the impacted and rear faces. The first one is a CEDIP JADE III LWIR camera oriented at 60° from the impact surface because of the experimental device and the presence of the impactor. This camera can capture 320×254 pixels images at 300 Hz. As the emissivity is a function of the angle of observation, the temperature could not be calculated because of the angle of observation introduced. This camera is therefore used for damage observation and the results will be presented on the mean measurement from the camera expressed in digital levels. The objective of this camera is to monitor the damage mechanisms (especially fibre kinking occurring close to the impactor).

The second one is a TELOPS FAST M3k MWIR camera. This camera can capture 320×254 pixels images at 3000 Hz. As presented in the previous chapter, matrix cracking and delamination initiates first for the bottom plies/interfaces. Thus, numerous events are likely to occur near the rear face, and it requires higher frequency acquisition to capture it. Thanks to the modification of the impact machine, the TELOPS camera has been placed perpendicularly to the rear face. As no angle of observation is introduced between the sample and the camera, and by considering the composite plate as a gray body with a high value of emissivity (≥ 0.95), the temperature fields are obtained using the manufacturer's integrated calibration for the different lens and parameters of the camera.

Table 3.1 summarises the different parameters chosen for the different cameras. These parameters choices allow the best compromise between the spatial and temporal resolution with the highest noise to signal ratio that can be achieved for this impact configuration. A DEWESOFT acquisition system was used to synchronize the time between the recorded data from the impact machine (load, displacement) and the images captured by the IR and visible cameras.

3.2 Kinematic fields obtained from DIC

3.2.1 Transverse in-plane displacement analysis

The two PHOTRON cameras have been used to perform DIC using ARAMIS software provided by GOM. As the upper ply is oriented according to the longitudinal x direction (0°), the transverse field u_y provide information about the damage state due to matrix failure. Thus, the transverse in-plane displacement u_y is presented in Figure 3.3. A virtual extensometer of 6 mm has been used to calculate the strain ε_{22} plotted in sky blue. Four different times (2, 3.8, 4.72 and 5.12 ms) for the Q16 laminate impacted at 20 J have been chosen according to the discontinuities highlighted by the strain plot (ε_{22} in sky blue). For the first times (2 ms, 3.8 ms), the field is continuous with smooth gradients. However, at 4.72 ms, after the first discontinuity, the displacement field is marked by a sharp gradient. This sharp gradient

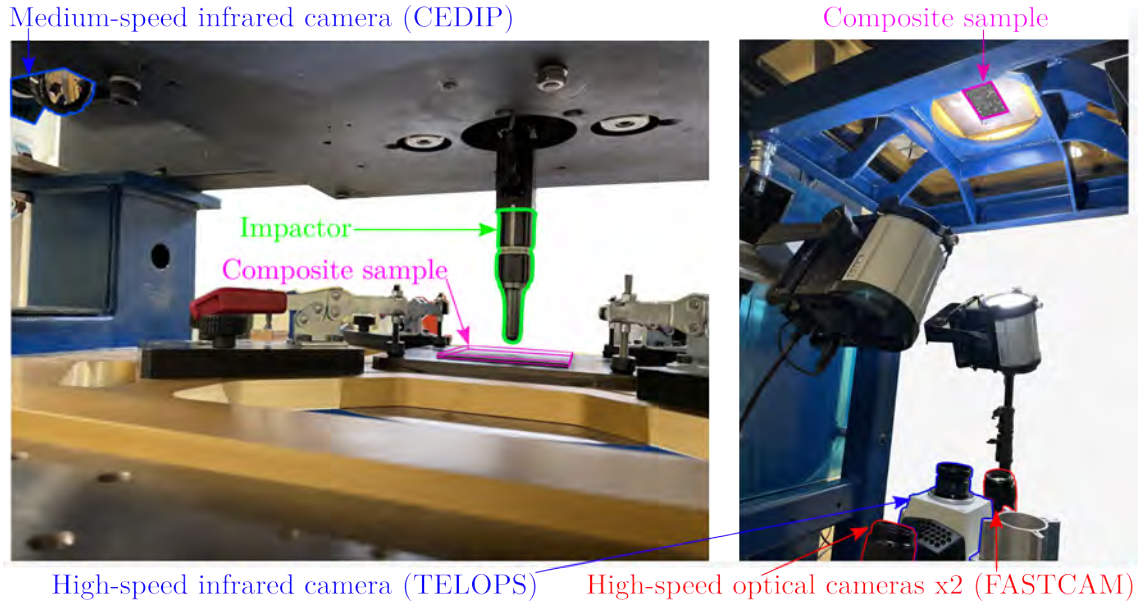

Figure 3.2: Experimental setup showing the different cameras

Cameras		6.5 J	11 J	20 J	35 J
OC	FS	896 × 520	896 × 520	896 × 520	896 × 520
FASTCAM	FQ	25 000 Hz	25 000 Hz	25 000 Hz	25 000 Hz
	SS	12.5 µs	12.5 µs	12.5 µs	12.5 µs
IRC	FS	80 × 59	80 × 59	80 × 60	80 × 59
CEDIP	FQ	3050 Hz	3050 Hz	3050 Hz	3050 Hz
	IT	70 µs	70 µs	70 µs	70 µs
IRC	FS	128 × 100	128 × 100	128 × 100	128 × 100
TELOPS	FQ	12 500 Hz	12 500 Hz	12 500 Hz	12 500 Hz
	IT	9.96 µs	9.96 µs	9.96 µs	9.96 µs

Table 3.1: Specifications of the different cameras

can be associated to matrix splitting in the lower ply. At 5.12 ms, the displacement gradient has increased with an unloaded zone bounded by the two lobes (in red and blue). It is interesting to highlight that the discontinuities occurring in the strain curve (in sky blue) are appearing after the significant load drops. Thus, the load drops may have intensified the matrix splitting.

3.2.2 Out-of-plane displacement analysis

As presented in [Flores et al., 2017, Lin et al., 2020], the out-of-plane displacement cartography is presented in FIGURE 3.4 at 2, 4, 6 and 8 ms for the Q16 laminate

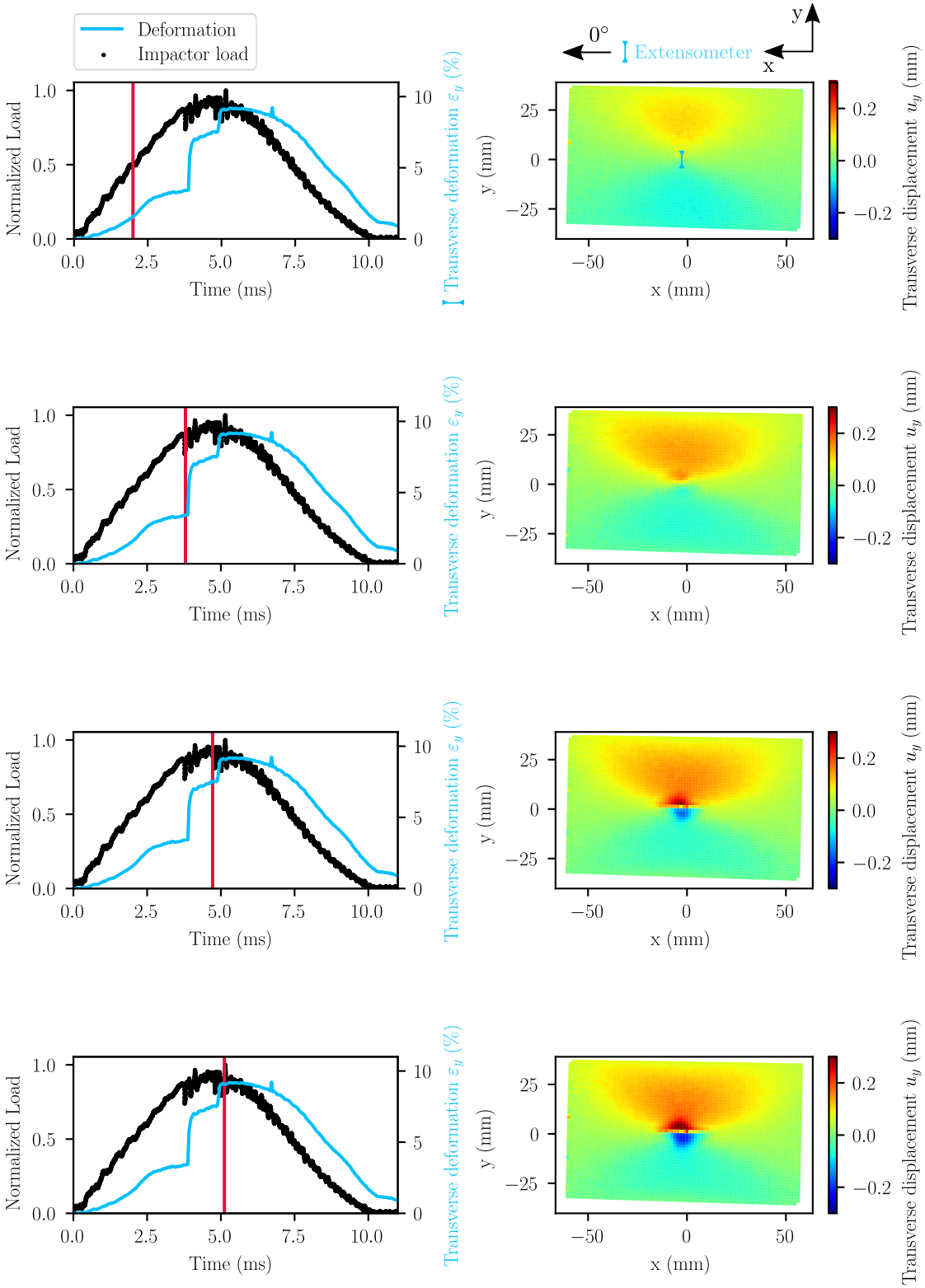

Figure 3.3: Transverse displacement u_y cartography at different times highlighting matrix damage on the rear face for the Q16 laminate impacted at 20 J

impacted at 20 J. The impactor load and displacement are plotted over the contact time. Moreover, the DIC out-of-plane displacement (u_z) for the point of interest (POI) represented by the black cross centered on the right hand side is plotted. A delay of 0.25 ms is observed before the displacement provided by DIC starts to increase. The gap between the two displacement curves increases until reaching 0.2 mm at the load peak. This difference could be explained by the residual dent depth, which is equal to 0.15 mm and by the crushing according to the z axis. After the load peak, unusual behavior is observed with DIC. Whereas the impactor goes up during the rebound stage, the plate seems to stay around 5 mm. This global response of the plate is also present for lower impact energies. Therefore, the damage was not responsible for this phenomenon. As briefly mentioned previously, the impact window is not fixed to the impact machine. The impact window is fitted in different tools, which are likely to introduce clearances. Therefore, in the following, a more advanced study of the behavior of the impact machine is presented to acknowledge the comprehension of the results.

Concerning the out-of-plane displacement cartography, the displacement field over the correlated area is presented. It can be observed that the higher the load, the higher the displacement gradient. This cartography will be confronted with the numerical results obtained from FEA to see if this trend is also observed numerically, especially for low impact levels, where few damages are observed.

3.2.3 Investigation of the impact machine response during impact

During the unloading stage, the out-of-plane displacement obtained from DIC exhibits a different response than that measured on the impactor. It seems that the plate does not return to a null displacement. Therefore, five aluminum plates of 150 × 100 mm have been impacted at (6.5, 11, 20, 35 and 50 J) to investigate this issue. In Figure 3.5, two laser displacement sensors from Keyence (in blue) have been used to measure the out-of-plane displacement of the impact window (in green). The two Keyence sensors have been fixed and isolated from the impact table.

Figure 3.6 presents the impactor and the Keyence out-of-plane displacements plotted over time. Moreover, the load/Keyence displacement curve is plotted to analyze the stiffness fixture evolution with the different energy levels. First of all, the Keyence displacement is plotted for the two points (highlighted by the red laser beam in Figure 3.5). Similar deflections are obtained for these two points in Figure 3.6, which are at the same distance of the impactor. The Keyence displacements and the impactor displacement show similar trends, with an increase of the displacement until reaching the peak and then a decrease of the displacement until 0. However, the Keyence displacement curves do not show a perfect ring bell. The Keyence highlights the presence of spurious displacement which varies from 0.8 mm to 1.28 mm at the load peak. The load versus the Keyence displacement has been plotted to evaluate the stiffness of the fixture. As expected due to the dynamic character of the impact event, the two Keyence sensors highlight a nonlinear stiffness for each impact energy. Moreover, a sensitivity to the impact velocity is shown, as different paths are observed for each impact energy level. The spurious displacement obtained at the different load peaks of each impact energy levels is inferior to the out-of-plane displacement obtained after the impact event in Figure 3.4 (almost

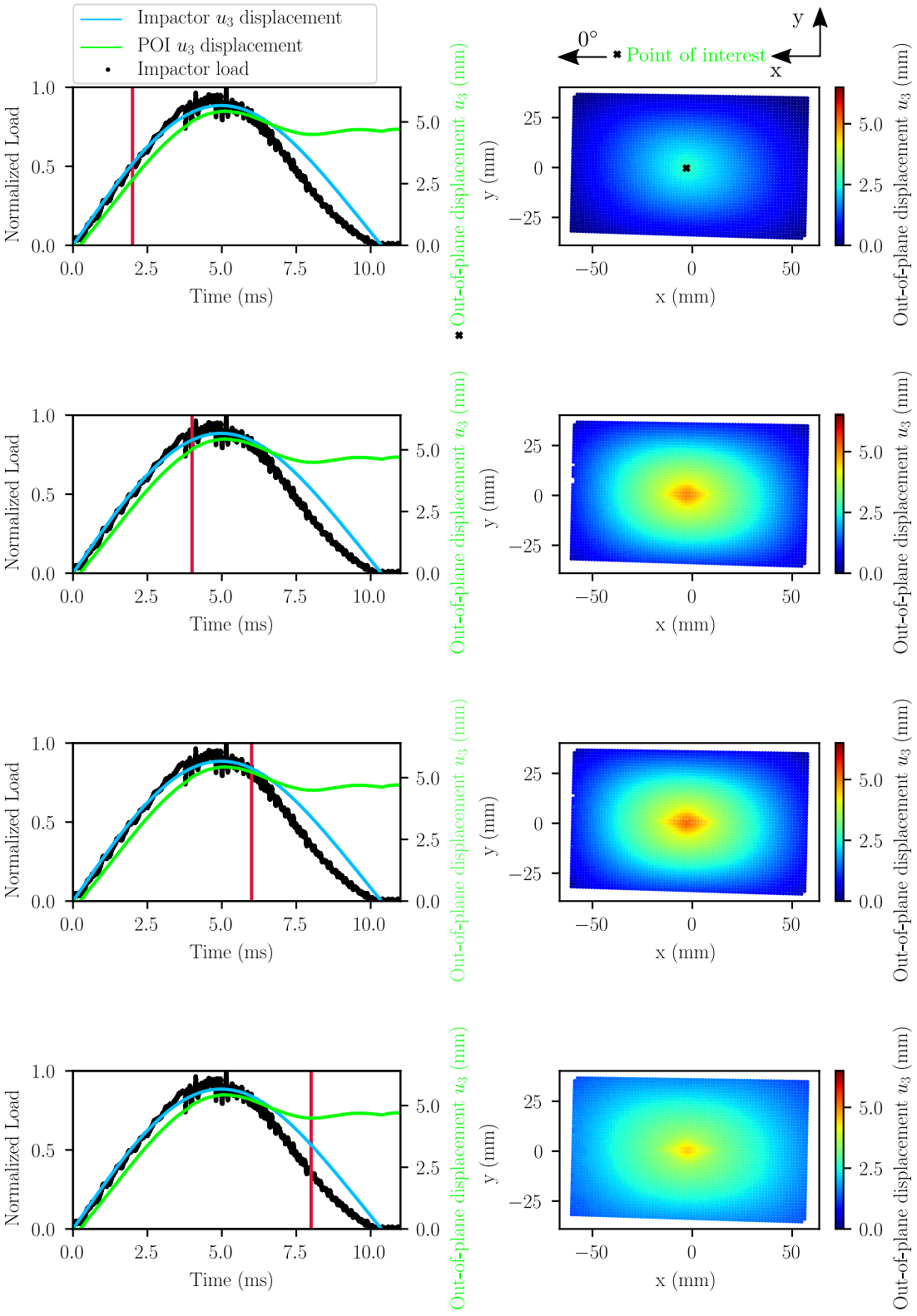

Figure 3.4: Out-of-plane displacement field obtained from DIC for different times during the 20 J impact test on Q16 laminate

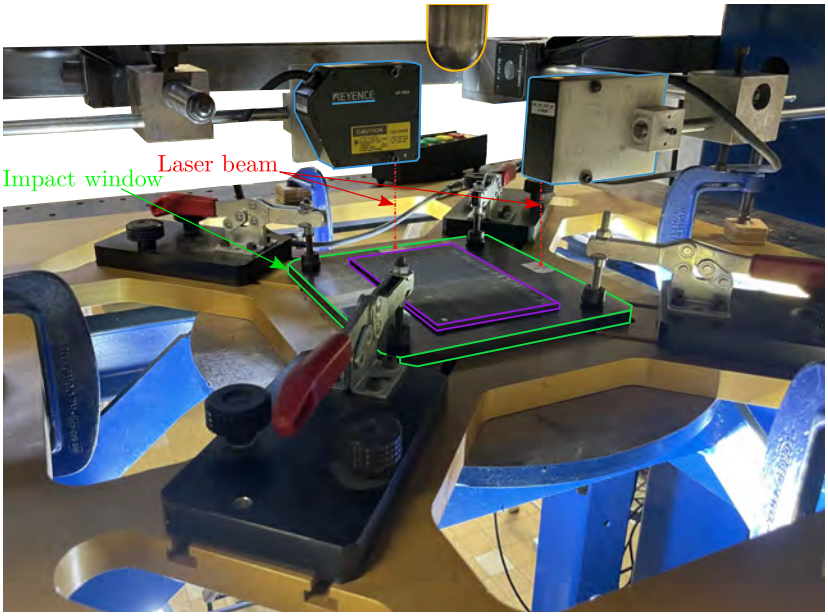

Figure 3.5: Experimental setup introducing the two Keyence displacement sensors

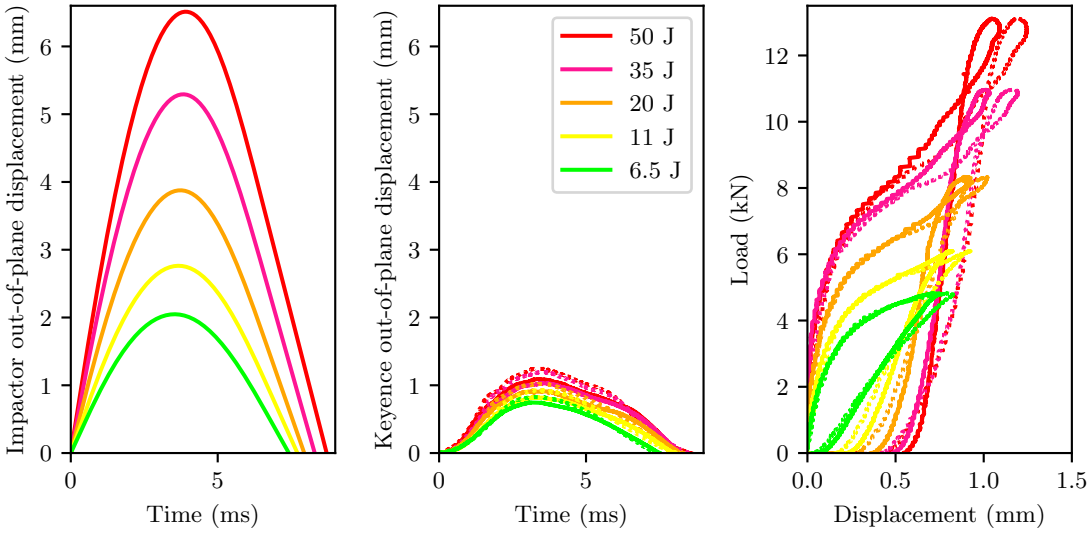

Figure 3.6: Influence of the impact energy on the machine displacement

5 mm). Thus, the clearance introduced in the experimental setup does not explain the entire residual displacement obtained at the end of the test. Indeed, another point to underline is that the cameras are not isolated from the impact machine, and therefore during the unloading stage, the stress waves could disrupt the cameras. Consequently, care must be taken before comparing the out-of-plane displacement field measured by DIC with those obtained by FEA, since the impact window is assumed to be fixed for the definition of the boundary conditions in FEM. A solution to deal with these spurious displacements which is a perspective of this work, will be to speckle not only the rear face but also the impact window to perform DIC. Indeed, it will allow determining accurately the boundary conditions. Therefore, because of the presented issues encountered with DIC, the obtained measurements have not been further analyzed, the effort being put on the analysis of the IR cameras data.

3.3 In situ damage monitoring using high-speed infrared thermography

In this section, the analysis of the IR signals obtained during the impact event is carried out. Then, the different thermal signatures are linked to the global response for the Q16 laminate at each impact energy level in order to reconstruct the damage scenario. Finally, the thermal signatures for the Q16 and C20 laminates are compared for the highest energy level (35 J).

3.3.1 Data treatment and time synchronization of the IR signals with the impact response

The first step consists in removing the ambient temperature to highlight the thermal variations induced by the impact test. Thus, the thermal field at time t_0 (before the impact event) is substracted of the thermal field at time t ($\Delta T = T(t) - T(t_0)$). Then, the time synchronization of the IR signals according to the load/time response is performed. In absence of damage, when a material is stretched, the material undergoes cooling due to thermo-elasticity. However, when the material is compressed, the material undergoes warming. Thus, as shown in FIGURE 3.7, the thermogram of a designated pixel obtained from the two cameras (CEDIP on the left and TELOPS on the right) are synchronized according to the load/time response. Due to the high frequency, the integration time of the IR cameras are small, which induce noisy signals. Therefore, a Hendrick-Prescott filter was used to simplify the detection of the warming/cooling initiation. Another possibility is to average pixel values in a zone close to the center of the impact event. Concerning the CEDIP, the temperature is not calculated because of the angle between the camera and the sample surface. The data will be presented as a variation of digits (Δ digits).

3.3.2 Analysis of the thermal signatures

After the synchronization, different images obtained from the two cameras have been selected to analyze the thermal events for each impact energy on the Q16 laminate. The thermal images are presented in FIGURES 3.8–3.9 and the thermal events are analyzed for each impact energy below:

- **6.5 J**. From the FIGURE 3.8, the images obtained from the CEDIP camera are presented. During the impact event, the impactor (in black) penetrates the composite plate. As the impacted surface is compressed, the material is warmed (4.66 ms). Few thermal signatures are visualized as the impactor hides the zone under the impact. However, the last image (at 14 ms) highlights a warmed area when the impactor goes up. This area shows that damages have occurred which could be linked to the high contact stresses.

  From the FIGURE 3.9, the images captured on the rear face using the TELOPS camera are presented. A cooling is observed near the center of the plate due to thermoelasticity (the lower ply is stretched). Then at 2 ms, the first splitting parallel to the ply orientation (0° ply) is observed. During the loading, this crack growths, and other matrix cracks appear. At 5.04 ms and 5.84 ms, it is interesting to notice that two half circles are observed. These lobes highlight

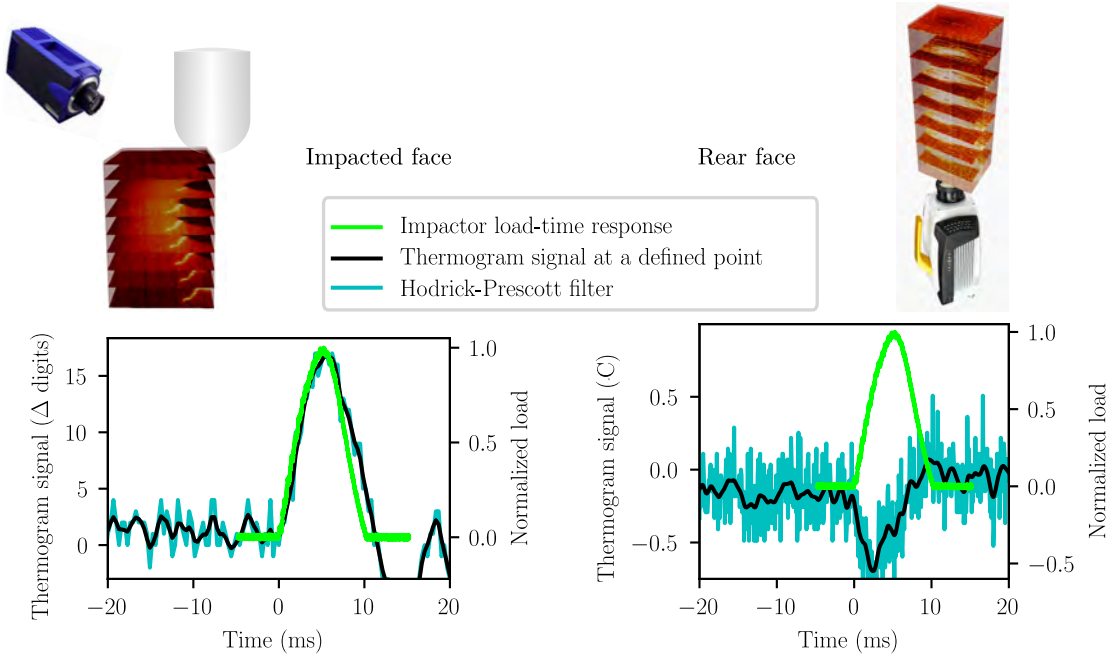

Figure 3.7: Synchronization of the thermal signals with the load-time curves for the CEDIP camera on the left and for the TELOPS camera on the right

the delamination crack tip which is moving during the impact event. Finally, during the unloading, the images become warmer as shown at 11.84 ms, it is explained by the thermal diffusion induced by the damage dissipation.

- **11 J**. Contrarily to the 6.5 J impact test, a bright -45° crack is observed at 3.93 ms in FIGURE 3.8. After the impact event, the bright warmed area is clearly observable.

  From the TELOPS camera (FIGURE 3.9), similar thermal signatures are observed. Moreover, as the impact velocity is 1.3× faster than at 6.5 J, the matrix cracking appears earlier (at 0.88 ms). The delamination growth is easily observed thanks to the crack tip warming;

- **20 J**. The evolution of the -45° crack is easily observed on the impacted face (FIGURE 3.8). Moreover, the warmed area related to the fibre breaks in compression is observed at the end of the impact event.

  Again from the TELOPS camera (FIGURE 3.9), similar thermal signatures are observed. However at 4.13 ms a highly energetic phenomenon has occurred. It is difficult to guess which kind of damage mechanism is related to this phenomenon as the thermal signal is oversaturated.

3.3.3 Damage scenario establishment

The thermal events have been linked to the load-time responses for the 6.5, 11 and 20 J tests. FIGURE 3.10 presents the different events for each impact energy level. The thermal images related to the impacted surface are plotted on the left, it can be highlighted that the higher the impact velocity the earlier the fibre breaks in compression occur. The thermal images related to the rear face are shown on the

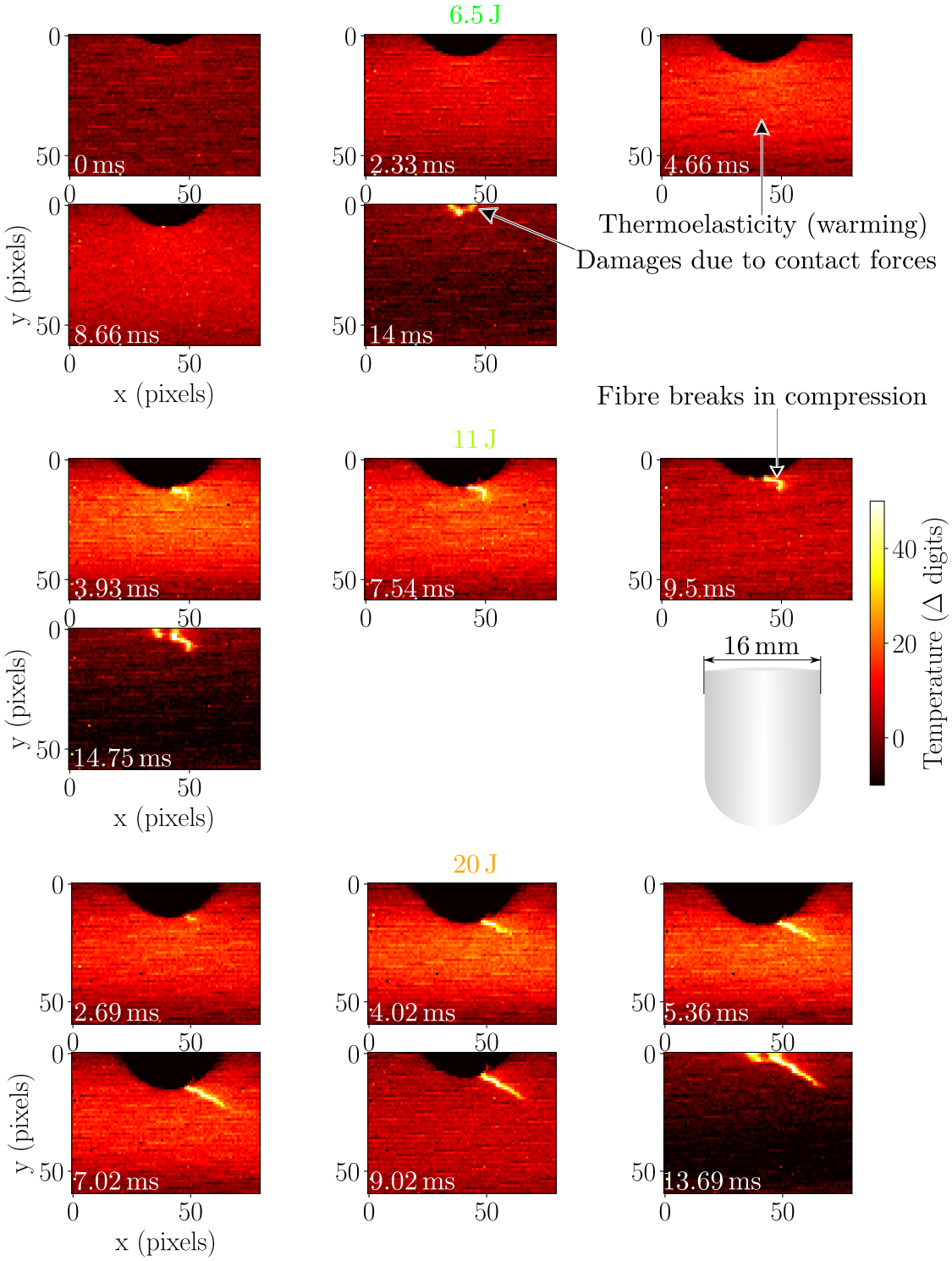

Figure 3.8: Thermal signatures obtained from the two IR cameras for the Q16 laminate

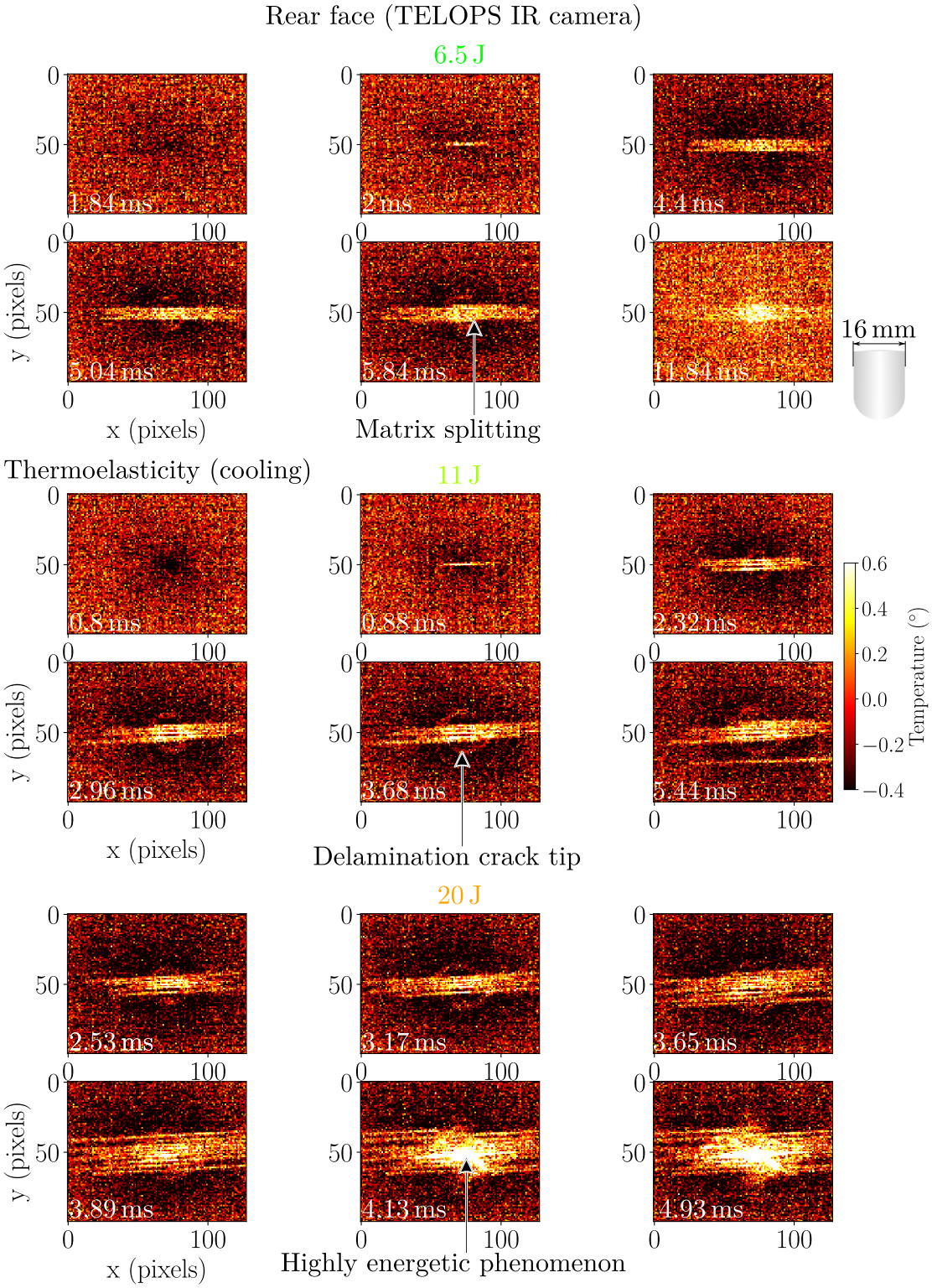

Figure 3.9: Thermal signatures obtained from the two IR cameras for the Q16 laminate

right. It is interesting to notice that the matrix splitting and the delamination occurring on the rear face does not induce a load drop for the lower impact energy levels (6.5 and 11 J). Moreover, since 20 J, the thermal bright events and the load drops arise at the same time. In the chapter 2, fibre breaks in tension happen since 20 J. Thus, the bright thermal signatures could be linked to the fibre breaks in tension which occur near the rear face.

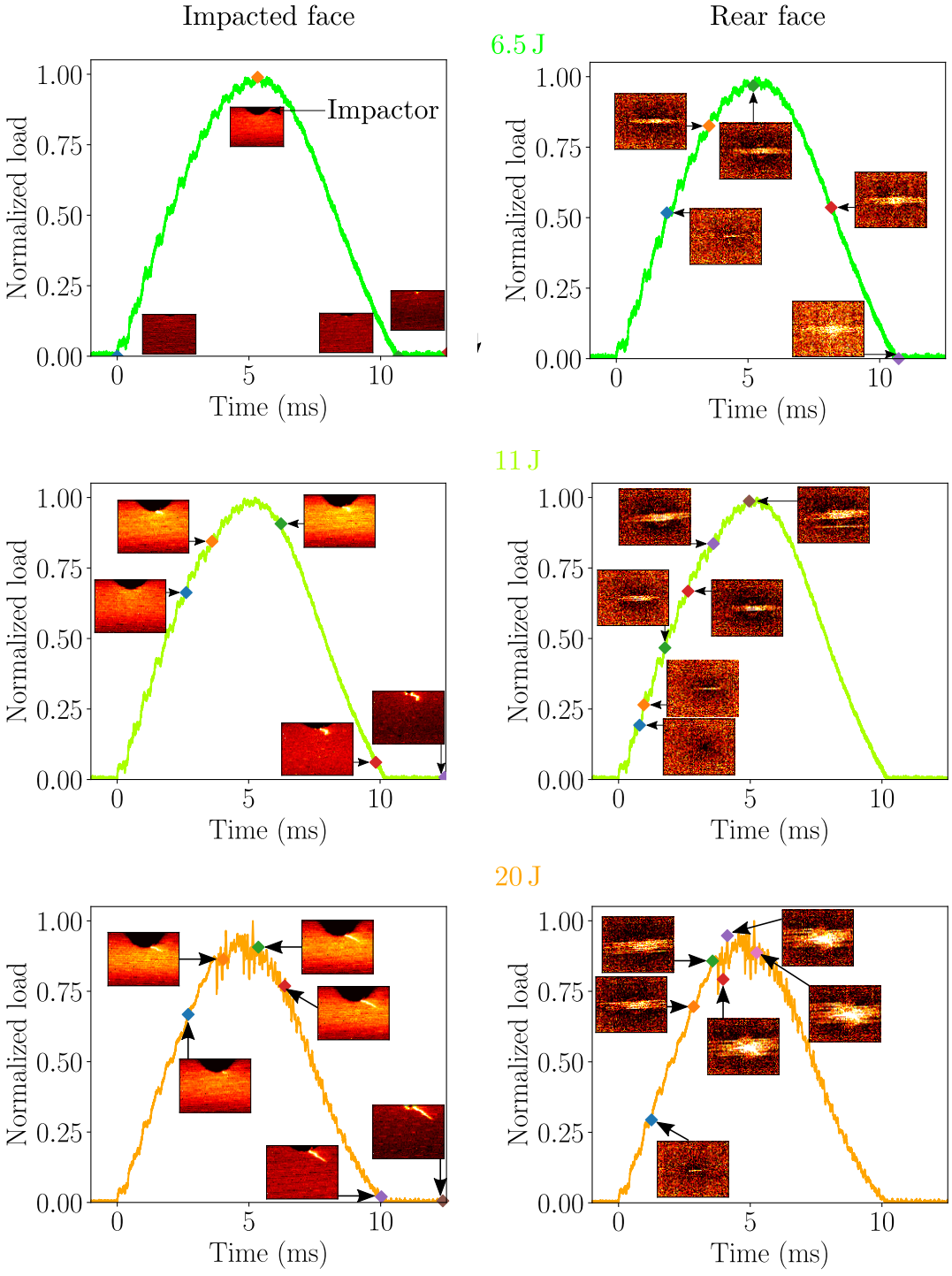

Figure 3.10: Damage scenario for the Q16 laminate for each impact energy level

Based on the FIGURE 3.10, the damage temporality can be established for lower

impact energies:

- ✓ The matrix splitting occur first;
- ✓ The delamination is then triggered by the matrix splitting;
- ✓ The fibre breaks in compression appear since 6.5 J.

At 20 J, for the rear face, the damage scenario is understandable until the apparition of the bright thermal event captured by the TELOPS camera at 4.13 ms. Indeed, the thermal field saturates, making the understanding challenging. It is therefore, difficult to confirm that this event is linked to the fibre breaks in tension, and therefore, to validate the damage scenario. An advanced data treatment of the thermogram is required to identify the damage mechanism responsible for this thermal signature.

3.3.4 Advanced IR data treatment based on diffusion time

In [Berthe and Ragonet, 2018], the authors have shown that the thermal diffusion of a crack below a sound ply is about 45 ms. As the ply in this work is thinner than the ply thickness used in [Berthe and Ragonet, 2018], a lower time diffusion can be postulated, as the resins are quite similar. Based on the thickness ratio, a postulated time diffusion of 37 ms will be used in the sequel. As presented in Equation (3.1), the new thermal fields have been calculated by subtracting the thermogram at a designated time (one, two or three times the postulated diffusion time) with the thermogram at the end of the impact event to highlight the damaged area. The time at the end of the impact event has been chosen to avoid thermal event induced by the thermoelasticity as the laminate is unloaded.

$$T(i \cdot t_{\text{diff}} + t_{\text{end}}) - T(t_{\text{end}}) \tag{3.1}$$

with $i \in [1, 3]$ and t_{diff} the postulated thermal diffusion time (equal to 37 ms) and t_{end} the end time of the impact event (about 10 ms for the Q16 laminate). The results have been plotted for the Q16 laminates in Figure 3.11 using this treatment. For each impact energy level, three thermograms at different times have been plotted on the left. The first one is at 37 ms (the diffusion time) after the end of the impact event. The second and the third thermogram are respectively at 2 and 3× the diffusion time. It can be shown that the higher the time, the brighter the thermal signature. Indeed, for the images at 121.6 ms, the thermal diffusion of the neighbor plies are caught. This treatment gives a good understanding of the damaged shape, close to those obtained with X-rays. At 20 J, the treatment of the thermogram using Equation (3.1) highlights two highly bright shapes. These shapes are oriented at 45° and -45°, which could be associated with the fibre breaks in tension occurring in the 45° ply.

3.3.5 Comparison between the Q16 and the C20 laminates at 35 J

The two different laminates have been compared for the highest impact energy. The load has been normalized according the maximum load value obtained from the

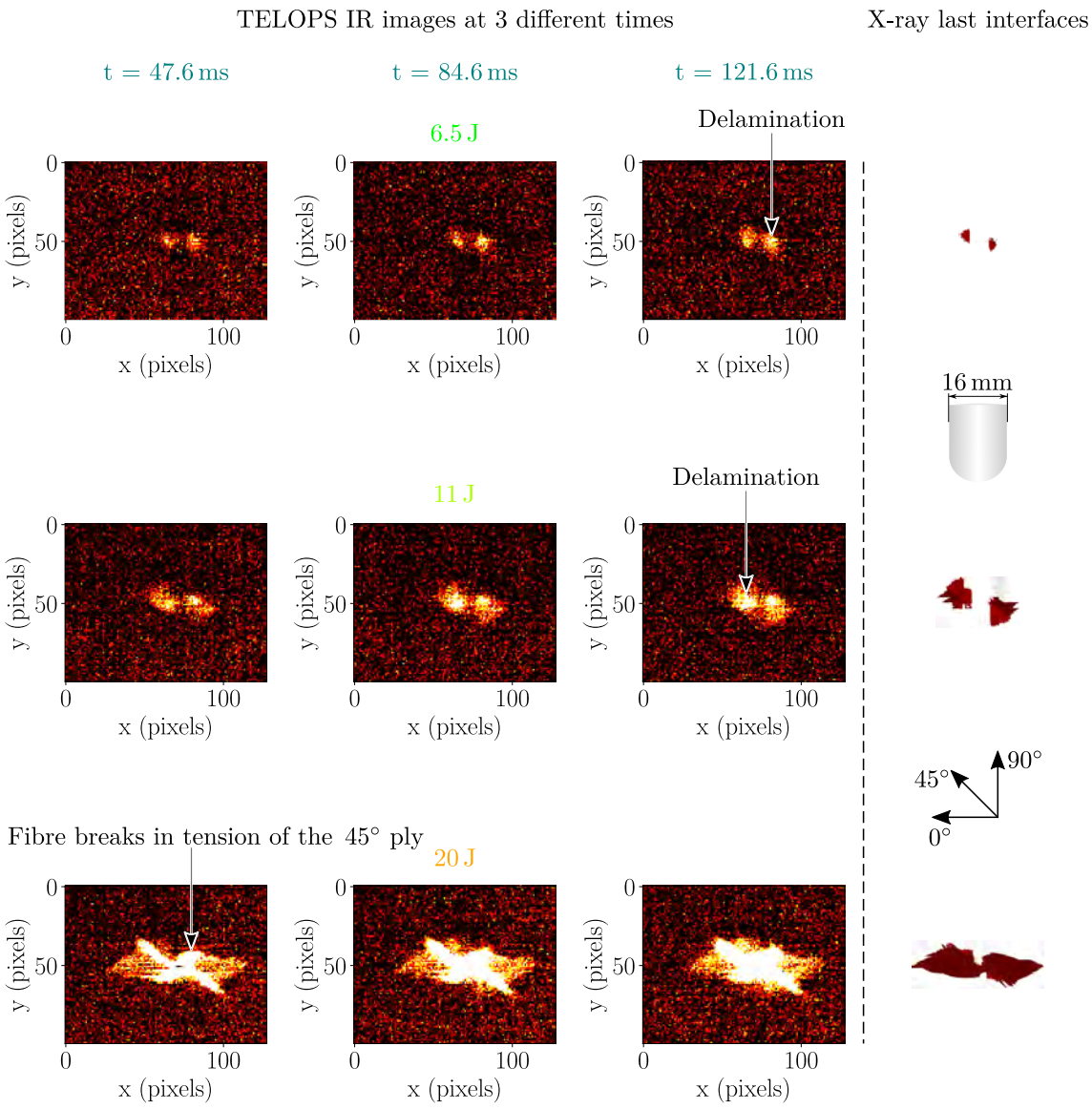

Figure 3.11: Comparison of the delaminated area of the lowest interfaces obtained from X-ray with the thermal signatures obtained at three different times

response of the C20 laminate. Firstly the damage events occurring during the impact have been plotted for the two cameras in FIGURE 3.12. The thermograms obtained from the CEDIP camera show similar thermal signatures for both laminates. Indeed, fibre breaks in compression occur for the two laminates. As explained in the previous chapter, the fibre breaks in the upper surface ply (0°) are triggered by the fibre kinking occurring in the ply below. As the second ply is oriented at 45° for the Q16 laminate, the fibre kinking is oriented at -45°. However, for the C20 laminate, the second ply is oriented at -45°, it induces a fibre kinking orientation at 45°. The fibre kinking occurs around 2 ms for both laminates. However, it occurs for lower impact load for the Q16 laminate than for the C20 laminate (around 40% of the max load obtained for the C20 impact test). For the thermogram obtained from the TELOPS cameras, similar damage mechanisms are observed, mainly matrix splitting. The matrix splitting occurs near 1 ms for both laminates. However, for the Q16 laminate, it arises for a lower load than for the C20 laminate. As the

load increases, more splitting cracks occur, which seems to be triggered by the delamination. Indeed, the delamination cracks are tracked thanks to the crack tip thermal signature. Again, a bright thermal signature occurs for both laminates around 2.5 ms. For the Q16 it arises sooner. This bright event occurs just after the load drop and could be associated to fibre breaks in tension. Based on the impact event and thermal images, the C20 laminate is more damage tolerant than the Q16 laminate. In FIGURE 3.13, the thermograms with the specific procedure defined in

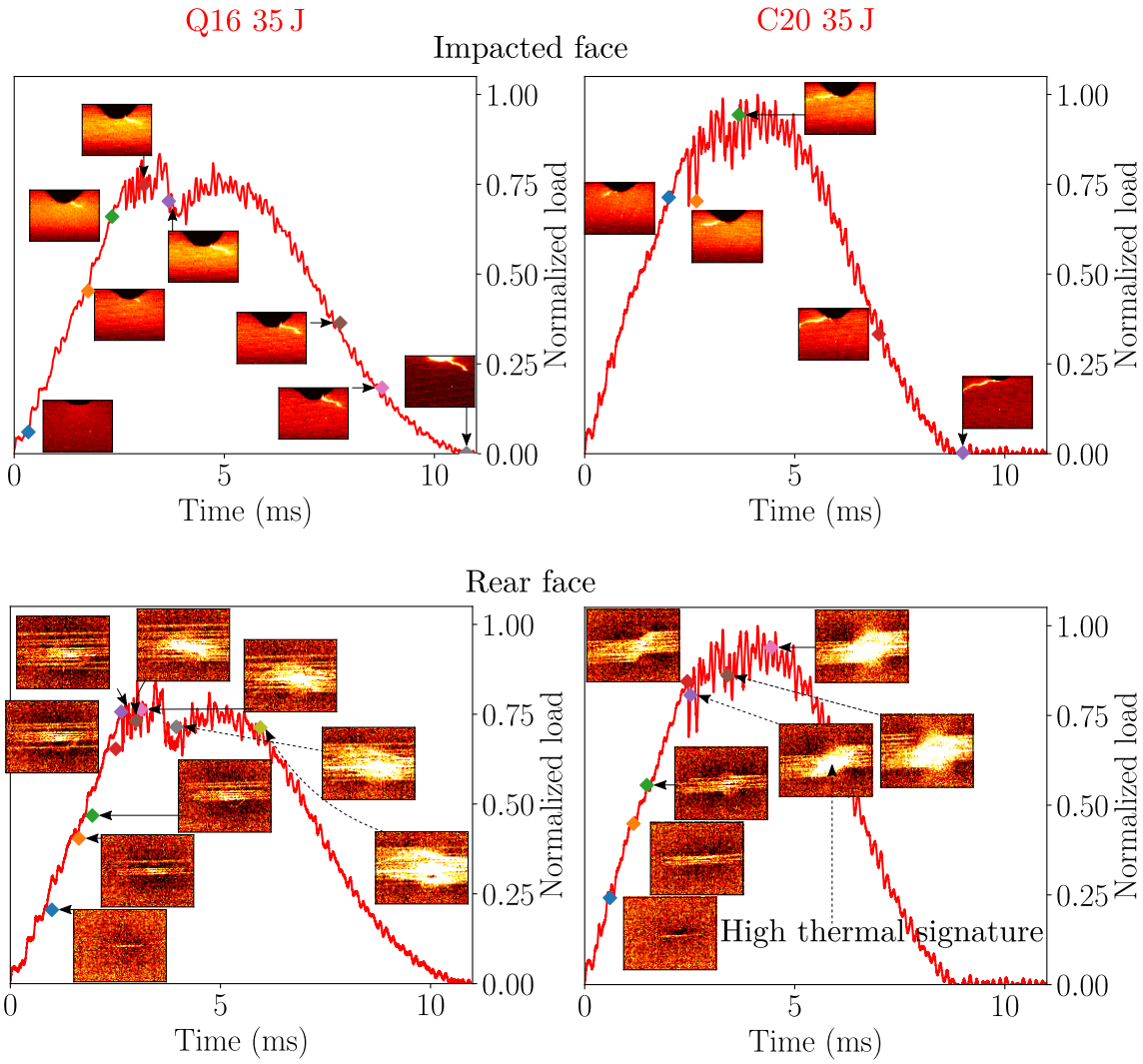

Figure 3.12: Thermal signatures occurring during the impact event for the two different laminates during an impact at 35 J

EQUATION (3.1) of both laminates are compared to the damaged lower interfaces detected by CT-scan. A clear warmed area is captured, which is quite similar to the projected damage obtained from the X-ray. Moreover, as shown formerly, the higher the time, the warmer the area. Indeed, using higher times enables the thermal diffusion to reach the rear surface. The shape of the bright zone is understandable for the Q16 laminate and can be associated with fibre breaks in tension. However, for the C20 laminate, it is difficult to understand what have been occurred since the thermal diffusion of the different damage mechanisms interact.

The IR thermography has brought precious information for the establishment of the damage scenario. The thermal signatures have been linked to the different

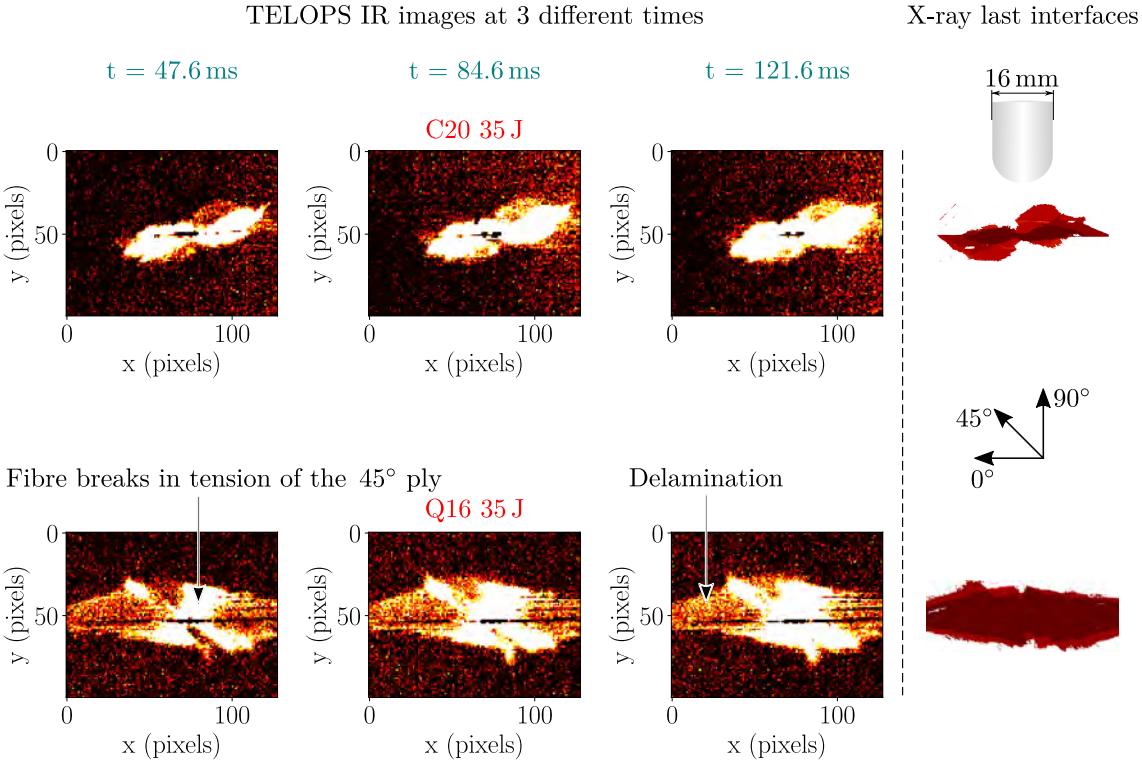

Figure 3.13: Comparison at 35 J of the delaminated area of the lowest interfaces obtained from the X-ray with the thermal signatures at three different times

damage mechanisms as the different crack topologies have been recognized (matrix splitting for instance). The damage temporality have been built thanks to the link with the global responses. For lower impact energy levels, matrix splitting, delamination of the lowest interface and fibre breaks in compression have been observed. For higher impact energy levels, fibre breaks in tension have been observed thanks to an advanced treatment of the thermal signals. The IR thermography highlights the strong damage coupling between the matrix splitting and the delamination on the rear face. Moreover, it allows the detection of the delamination for the lowest interface, which is the largest damaged interface for the Q16. The comprehension of the damage degradation has been clearly improved. To complete the investigation, the results obtained from quasi-static indentation tests will be presented in the following section with the study of the strain-rate effect and the analysis of the different damage mechanisms.

3.4 Quasi-static indentation

3.4.1 Experimental configuration and methodology

QSI tests have been carried out to confirm the damage scenario considering no strain-rate effect on damage growth. It has been decided to select five displacements from the load-displacement curves obtained during impact tests. As the QSI tests have been performed before the *in situ* experimental campaign, the different points have been selected according to previous impact test results performed at the beginning of the Ph.D. thesis. FIGURE 3.14.a presents the five displacements selected for each

indentation test. The experimental setup is presented in FIGURE 3.14.b. An MTS electromechanical uniaxial testing device with a 20 kN load cell has been considered. The imposed displacement rate is 0.5 mm/min. The QSI test has been monitored with one displacement sensor (LVDT) to measure the maximal displacement on the opposite face. An acoustic sensor has also been considered to identify the damage threshold and monitor the evolution of acoustic events during QSI loading using the cumulated acoustic energy. A MISTRAS acquisition software was used for the acoustic emission, a threshold of 40 dB was defined for the acoustic threshold with a frequency of 100 kHz.

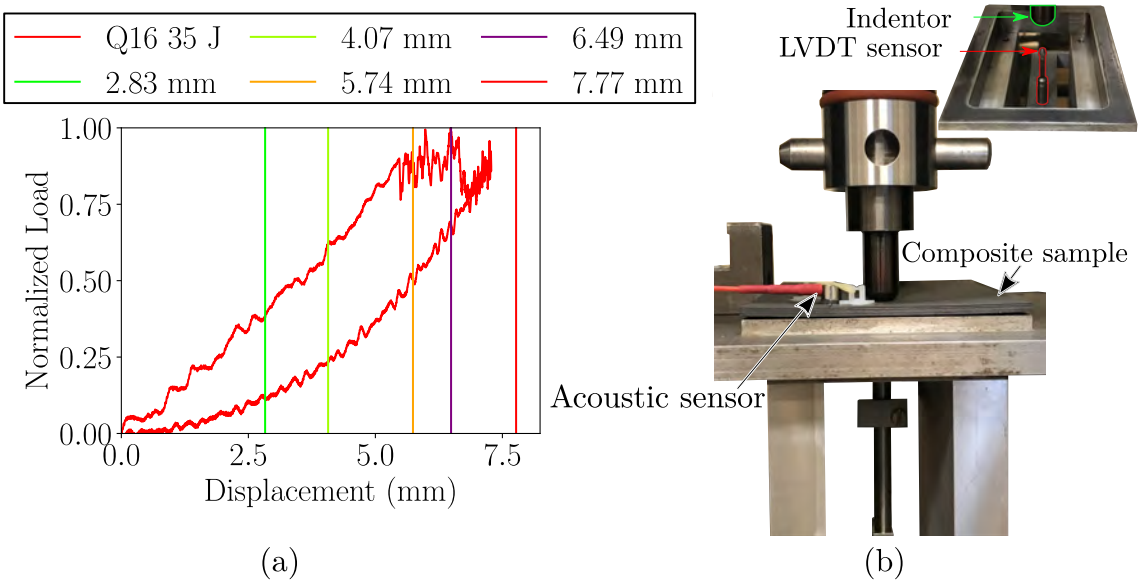

Figure 3.14: Definition of the different displacements for the Q16 QSI tests (a) and presentation of the experimental setup (b)

3.4.2 Macroscopic behavior of the Q16 laminate subjected to QSI

FIGURE 3.15.1 shows the load-displacement responses for the five QSI tests.

- It can be highlighted that the same loading path is observed for each test.
- The higher the displacement, the higher the dissipated energy;
- The response exhibits a nonlinearity for each test after 2.83 mm;
- The two highest applied displacement tests (6.49 mm, 7.77 mm) exhibit load drops after 5.5 mm. It seems that the material has reached its maximum bearing capability without severe damage occurrence. At almost 7 mm, a high drop arises, followed by a stiffness recovery;

FIGURE 3.15.2 introduces the results obtained from acoustic emission. The cumulated acoustic energy, which could be defined by the acoustic events occurring above the defined threshold (40 dB) is plotted as a function of the displacement. For each test, the acoustic events arise at almost 1.3 mm, which can be used at a "damage

threshold". The acoustic events associated to the test with a maximal displacement equal to 4.07 mm have not been plotted as the sensor have lost the contact with the composite plate. The evolution trend of the acoustic events is similar for all tests except for the highest one (red in FIGURE 3.15.2) where the cumulated energy is lower than in the other tests.

3.4.3 Study of potential strain-rate effect

3.4.3.1 Macroscopic results

In order to investigate damages induced by QSI tests and understand the damage scenario, the first comparison between QSI and impact tests has been performed to ensure that the material is not sensitive to the strain-rate effect. The comparison is performed on the global responses, the damage shapes provided by X-ray and C-scan, and on the residual dent depth. In FIGURE 3.15.3, the load-displacement responses obtained from impact and QSI are compared. The imposed displacement in QSI is not equal to the maximum displacement observed from impact results as QSI tests were performed earlier to the *in situ* experimental campaign. In any case, similar responses between QSI and LE/LV impact. Three different stages can be defined for the comparison.

- For lower displacements (2.83 and 4.07 mm), the QSI results are compared to the 6.5 and 11 J equal test results. The results are quite similar. The unloading stage for the QSI tests is a little bit softer than those observed for impact results;
- At 5.74 mm, the QSI test is compared with the 20 J impact test response. It can be shown that the loading response up to 4 mm is almost the same. However, for higher displacement, the QSI response is stiffer than that obtained with impact. Care must be taken as the experimental dispersion has not been evaluated;
- For the two higher displacements (6.49 and 7.77 mm), the QSI results are compared to the 25.9 and 35 J. The same stiffness is observed for the two plots. The load drops occur slightly earlier for the impact results (for a lower load). Load drops without oscillations are observed for the QSI. For the red curve, it is interesting to notice that the load drop for impact and QSI are captured at the same displacement level.

Based on the macroscopic results, it can be dressed that the same initial behavior is captured for each test. QSI requires a slightly higher load for the appearance of load drops than that observed for impact test.

3.4.3.2 *Post mortem* analysis

The macroscopic study is enriched here with the analysis of the damage shape using X-ray and C-scan projected damages. As presented in FIGURE 3.16, the projected damaged areas are compared for QSI and impact tests.

- The projected damaged area obtained for the 4.07 mm displacement test is very similar between QSI and impact tests. It can be highlighted that the fibre

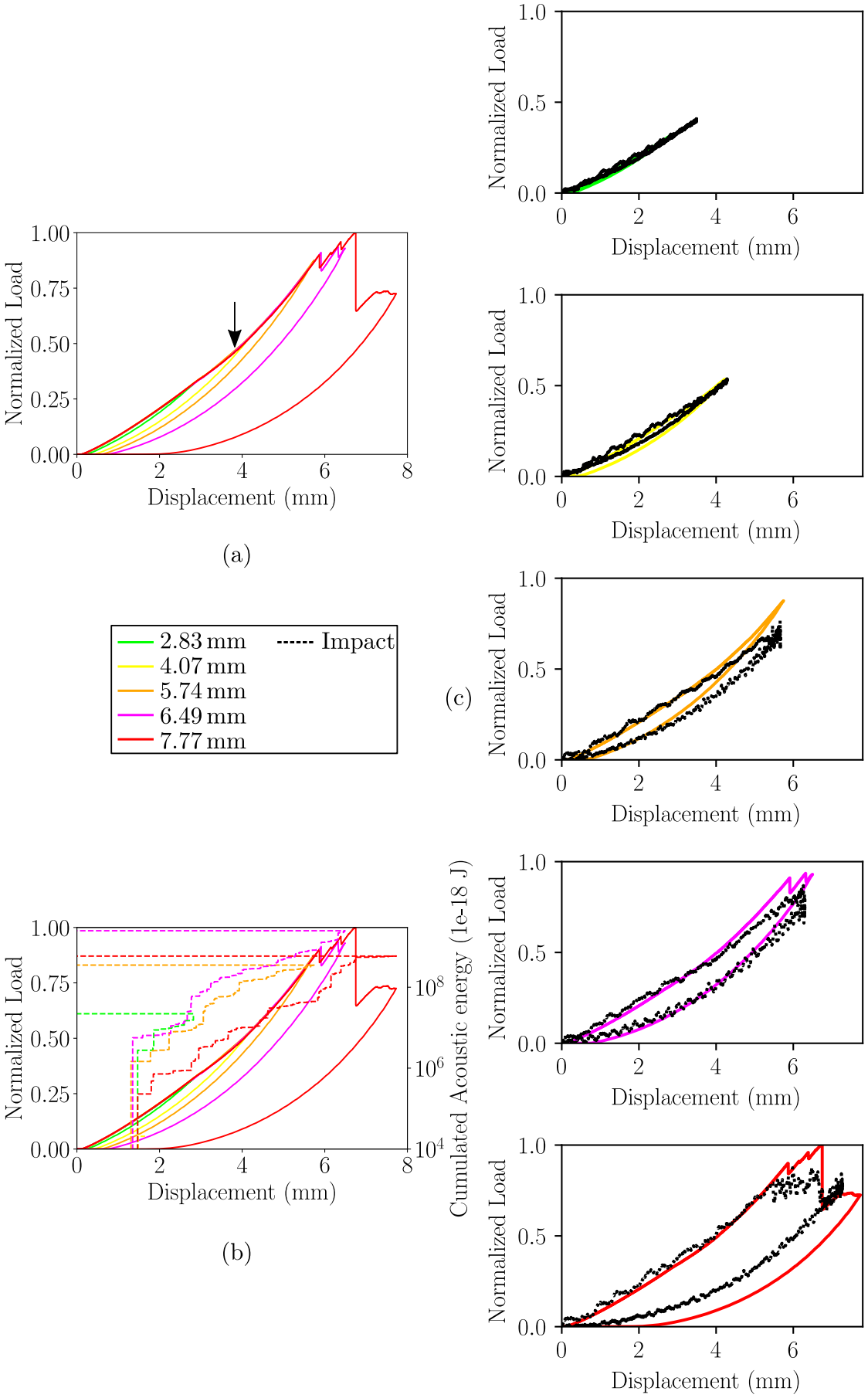

Figure 3.15: QSI load-displacement responses (a), with acoustic emission (b) and comparison with impact responses (c)

breaks in compression occurring near the impacted face is more pronounced for QSI. It can be explained by the fact that the contact time between the plate and the indentor is higher, which results in higher damage states occurring near the impacted surface. An undamaged zone below the indentation/impact zone is observed for both tests;

- For 5.74 mm QSI test, the damage shapes are different. Fibre breaks in compression are more pronounced for QSI than impact, especially the fibre breaks in the 90° ply. The undamaged zone is observed through all the thickness for the QSI test, which highlights the fact that no fibre breaks in tension have occurred. Indeed, the fibre breaks in tension occur near the center of the plate where the strain reaches its maximum value. The presence of fibre breaks in tension has been demonstrated in impact, and is present until the seven interface ([90/-45]). When fibre breaks in tension occur, the neighbor interface fail. Thus, it explains why there is no undamaged zone as observed in QSI. Moreover, the fibre breaks in tension modify the curvature of the sample and seem to influence the delamination of the lowest interfaces in red, which is more pronounced for the impact test;

- For the two highest displacements (6.49 and 7.77 mm), similar damages between QSI and impact are observed with a high amount of damage on the loaded surface. A strong interaction is observed between the fibre breaks in compression and the delamination. As explained previously, the fibre kinking triggers the delamination. At these load levels, fibre breaks in tension occur for QSI, and it can be noted that the largest delamination is observed for the lower interface as obtained in impact. Thus, it can be confirmed that the fibre breaks in tension have an influence on the delamination of the lower interface in red ([0/45]).

3.4.3.3 Trend of the measurable quantity

The dissipated energy, the projected damaged area, and the residual dent depth have been compared for each test in FIGURE 3.17. For lower applied displacements, the QSI dissipates a little more energy than impact which could be associated with the higher amount of fibre breaks in compression. For the tests with a displacement of 6 mm, the impact result dissipates a slightly higher energy than QSI due to the occurrence of fibre breaks in tension. QSI tests result in a slightly more pronounced projected damaged area than impact. In any case, the trends are very similar for the dissipated energy and the damaged area. An interesting point to notice is the residual dent depth. Indeed, as the contact time is higher for QSI, the residual dent depth is more important in QSI tests. From an industrial point of view, the substantiation of category 1 impact damages where the BVID is a concern will result in a conservative sizing if the QSI tests are used instead of impact tests for the substantiation. Indeed, the residual dent is more noticeable using QSI tests. To summarize the investigation of the strain-rate effect for this specific material:

- Similar trends are obtained from the macroscopic responses (load/displacement curves, dissipated energies). The material sustains higher loading without load drop in case of QSI;

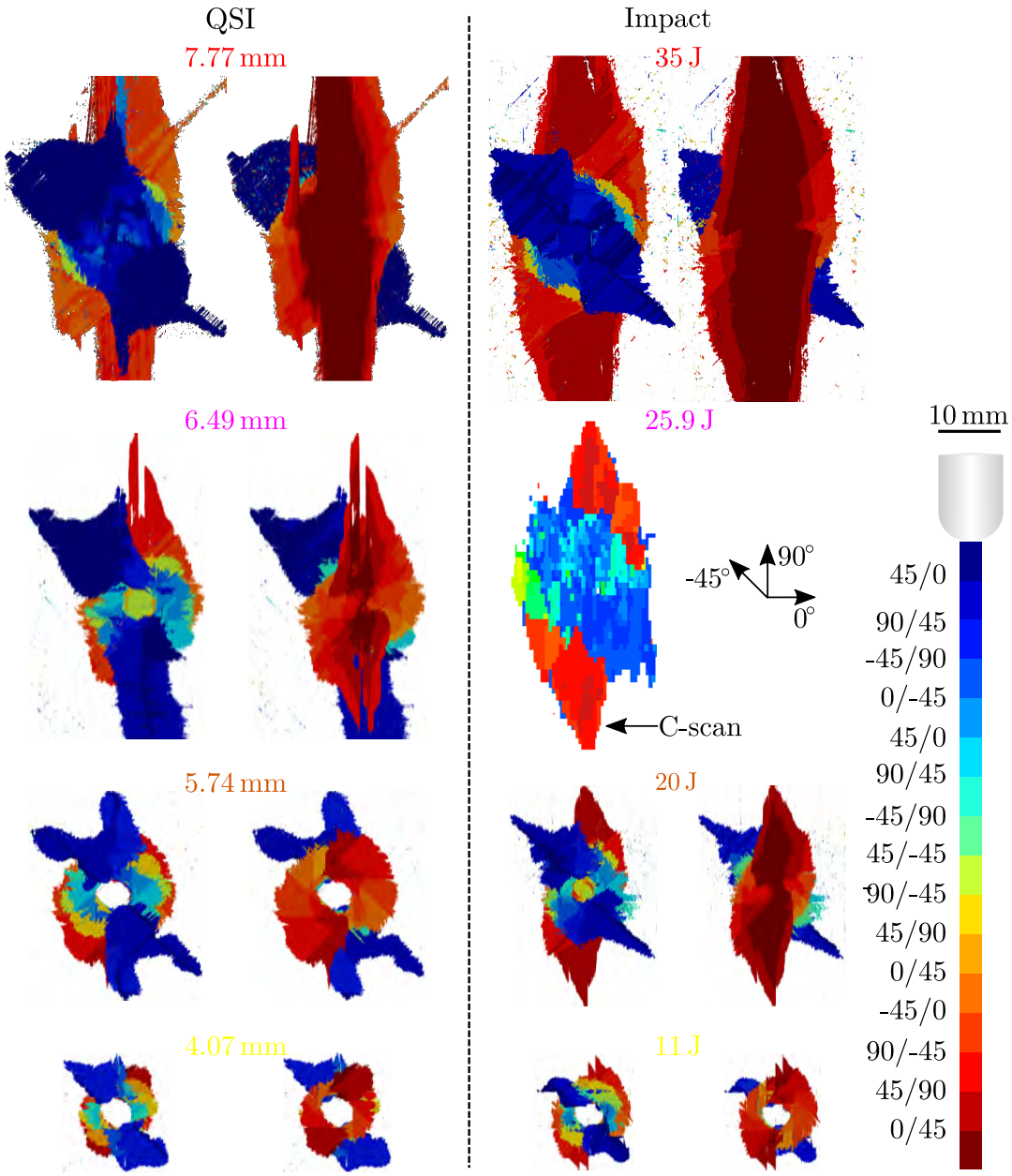

Figure 3.16: Comparison of the projected damaged area obtained from QSI and LEI/LVI

- Comparing the projected damage mechanisms observed from CT-scans and C-scan controls, the same damage mechanisms are encountered in QSI and impact tests. However, the fibre breaks in compression are more pronounced in QSI, resulting in a little higher level of damage near the loaded surface. The fibre breaks in tension are delayed in the case of QSI. Once occurred, the fibre breaks in tension modify the shape of the laminates by warping it. The generated curvature seems to trigger the delamination of the lowest interface [0/45];

- The residual dent depth is more pronounced for QSI tests. It can invalidate the approximation of LEI/LVI by QSI if the principal purpose of the comparison is the BVID.

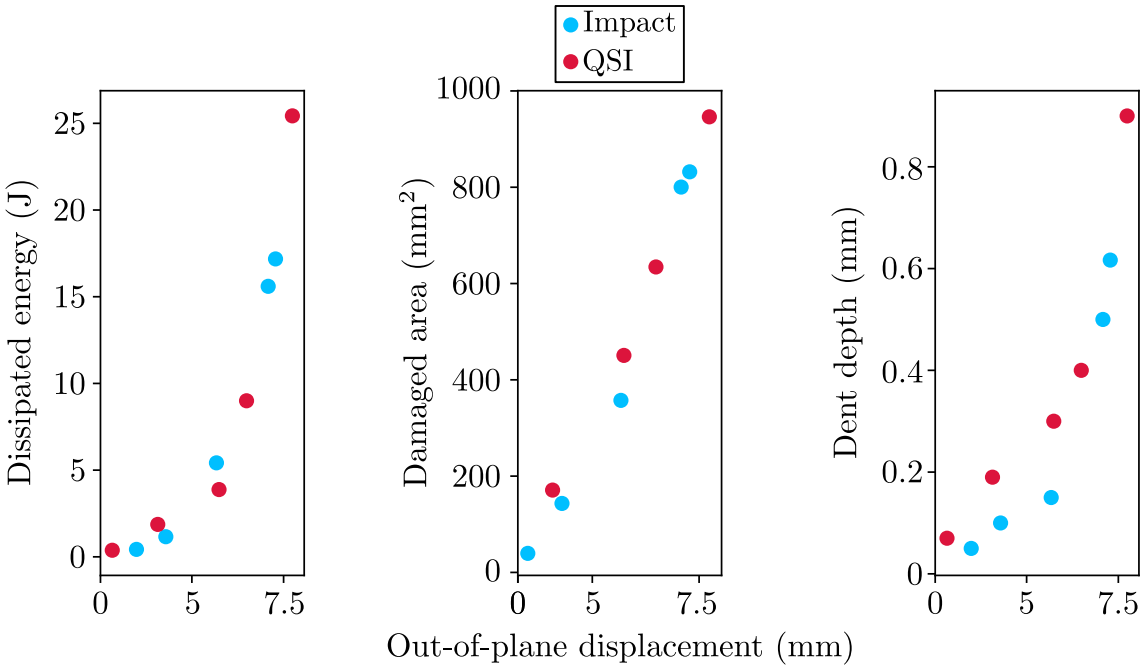

Figure 3.17: Comparison of the dissipated energy, projected damaged area and residual dent between QSI and impact tests

3.4.4 Influence of the fibre breaks in tension on the crushing in QSI

In order to evaluate the effect of the fibre breaks through the thickness, the displacements obtained from the machine and from LVDT are compared in FIGURE 3.18. The two displacements are plotted as a function of the machine displacement. The linear trend corresponds, therefore, to the machine displacement. Moreover, the crushing which is defined by

$$\text{Crushing} = \text{Machine}_{\text{disp}} - \text{LVDT}_{\text{disp}} \tag{3.2}$$

is also plotted on the right axis. It can be shown that the displacement on the opposite face obtained from the LVDT starts later to increase. It results in a higher initial crushing. Once the sample starts to bend, the crushing is linear until 3 mm. After 3 mm, it is observed for all tests an inflection point, the damages occurring on the rear face seem to increase the value obtained from the LVDT. For the two last plots (purple and red), a drop of the crushing is observed. This drop is explained by the increase in the displacement measured from LVDT. The matrix splitting aperture and the delamination could explain this trend. To lean on this assumption, the LVDT displacement and the normalized load for the 7.77 mm test have been plotted in FIGURE 3.19. It can be shown that discontinuities of the measured LVDT displacement arise at the load drop occurrences. In other words, the load drops are responsible for an increase of the LVDT displacement. The load drops are related to fibre breaks in tension, once the fibres are broken, the laminate stiffness is highly reduced. Therefore, the out-of-plane displacement in the center of the laminate increase. The fibre breaks in tension push the matrix splitting apertures on the rear face, which trigger the delamination of the lowest interfaces.

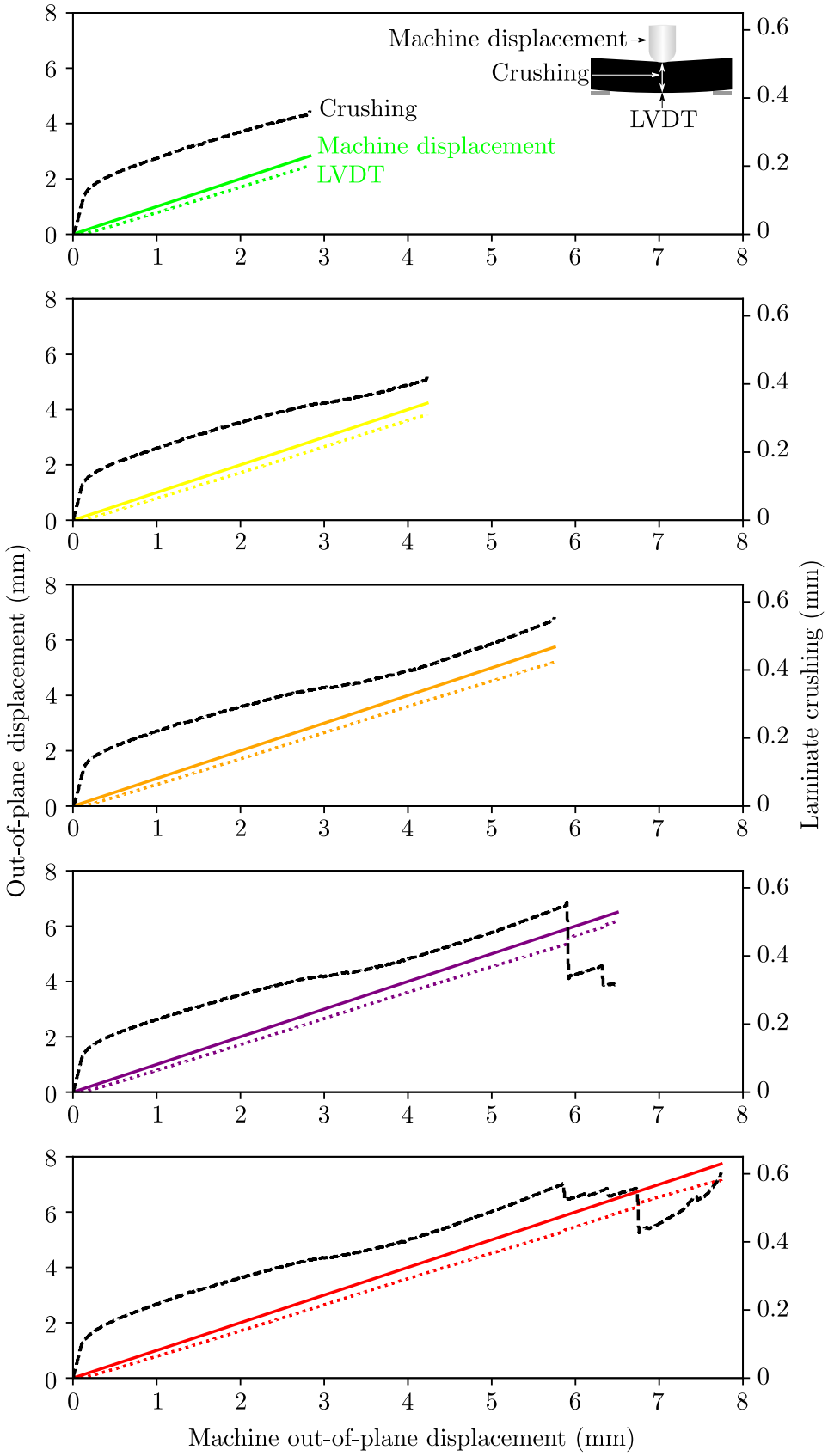

Figure 3.18: Evolution of the Q16 laminate's crushing as a function of the machine displacement

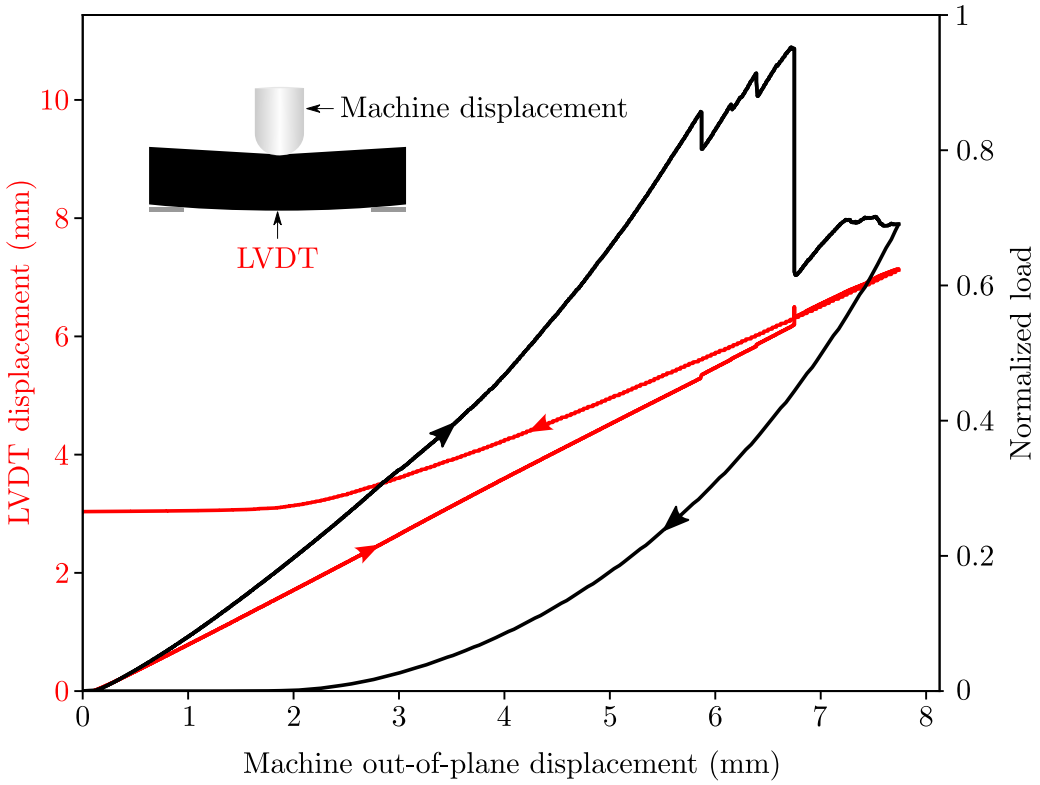

Figure 3.19: Influence of the load drops on the displacement measured by the LVDT sensor

3.5 Conclusion

In this chapter, two different approaches based on the literature state-of-the-art have been presented to establish the damage scenario. Considering the poor monitoring usually used in impact, the first methodology was based on the enrichment of the LEI/LVI tests using high-speed cameras. Four high-speed cameras have been used, two high-speed visible cameras to perform DIC on the rear face and two high-speed thermal cameras (one near the impacted face and one on the rear face). As presented in the literature, the displacement fields obtained from DIC on the rear face were analyzed. It has highlighted that care should be taken before any comparison with FE simulation as the experimental setup gets some compliance. This compliance has induced spurious displacement, which invalidates the out-of-plane comparison with FEA. However, comparison of other displacement fields, such as u_y is an aperture in damage detection. Advanced treatments which are beyond the scope of this thesis will enable us to detect more easily the delamination and matrix damages.

An originality of this work is the introduction of high-speed thermal cameras. Such experimental configurations have not been introduced in the literature. Thus, it has been chosen to detail the entire process of data handling and treatment in order to associate the thermal signature events with the damage mechanisms. Several events occur during an impact test, which lead the understanding and the explanation of the results quite difficult. A novel methodology has been developed, which allows for visualizing the damaged shapes by taking advantage of the thermal diffusion. The results obtained from this methodology have been confronted with the damages occurring in the last interfaces obtained from X-rays. A great similarity

has been shown, which validates the proposed approach.

Finally, a QSI study has been performed on this material with two objectives. The first one was to study if the material was sensitive to strain-rate. Secondly, an investigation of QSI damages has been performed in order to enrich the comprehension of the damage creations, evolutions and interactions. This study reveals that the material behaves similarly in QSI and impact. Nevertheless, some differences have been pointed out, such as the high amount of damage occurring near the loaded surface with a deeper residual dent (major difference between QSI and impact tests). Thanks to the enriched instrumentation using the LVDT sensor, the fibre breaks in tension have highlighted an increase in the displacement captured by the LVDT. This displacement increase was associated with the opening of matrix splitting and delamination.

The QSI can allow a better understanding of damages occurring in insensitive strain-rate composite materials. However, it requires several tests to perform. In contrast, the *in situ* monitoring requires one test to visualize each damage mechanism and to quantify the damaged area occurring near the impacted and rear faces.

At this stage, the mechanical behavior of this material has been understood. Thus based on the physical relevant observations, the modeling of the different damage mechanisms will now be performed using damage mechanics. These damage laws will be presented and implemented in a FE software in order to predict the impact damages occurring in such material in the next chapter.

Chapter 4

Material degradation modeling and FE simulation of impact damages

Contents

This chapter aims to describe the damage modeling at the ply scale of the studied material. Thus, a brief review of the considered damage models is introduced for ONERA Progressive Failure Model (OPFM) and DPM to identify the current advantages and limitations. Then, the further development of OPFM is detailed. Finally, the simulation of impact damages using both models is presented and a comparison is performed with the previously presented experimental data.

4.1 Current damage models and FE discretization

In this work, two different models have been considered. The first one is OPFM. This model includes matrix cracking modeling developed in [Germain, 2020] and delamination modeling in [Vandellos, 2011]. The second damage model is the Discrete Ply Model (DPM) developed over a decade [Bouvet et al., 2009], DPM models transverse cracking, delamination and fibre breaks in tension and in compression. The presentation of the two FE impact models (with respectively a continuous and diffuse representation of damage or with a discrete description of damage) is discussed first. Then, the two damage models will be presented as they were at the beginning of this work.

4.1.1 ONERA progressive failure model

4.1.1.1 FE discretization of the impact experimental configuration

The FEM of the impact configuration is presented in FIGURE 4.1. The composite sample is shown in green. Each ply is meshed using 3D elements. A defined rectangle of 30 × 20 mm is meshed using 3D 8-node linear brick with full integration (C3D8). The local quantities (stresses, strains) have converged with a 0.6 mm element size. The element size accurately captures the gradients occurring in this area due to the high contact stresses. In order to reduce the computational problem, a 6-node linear triangular prism has been considered outside the "impact area", the mesh size decreases until reaching the border of the impact window (in blue). Each ply is meshed explicitly with an orthotropic non-linear behavior. Zero-thickness cohesive elements highlighted in cyan are inserted between each ply with different orientations.

The impactor is colored in crimson, using a 4-nodes linear tetrahedron. An isotropic steel elastic behavior is assigned to this part. The volume density has been modified to meet the experimental mass since just a part of the impactor is modeled. An initial velocity on the striker is applied. For the impact window shown in blue, a 6-node linear triangular prism has been used for the mesh. An isotropic steel elastic behavior is assigned to that part (same as the impactor).

Impact modeling is a rough problem due to the presence of strong nonlinearities:

- Contact mechanics is introduced between the striker/plate and the plate/impact window;
- The composite laminate is modeled using a nonlinear damage law to predict the failure of each damage and failure mechanism.

The time is discretized using a **dynamic implicit scheme**, the α-method algorithm is considered for the semi-discretized problem as presented in chapter 1. The parameters considered are (α, β, γ), γ and β are calculated as a function of α which is chosen equal to 0.3. It can be noticed that α has been chosen to be relatively high. Indeed, as explained in chapter 1, α introduces damping for high-frequencies which can enhance the convergence rate. The number of degrees of freedom for the Q16 and C20 laminates are respectively 484 000 and 584 000.

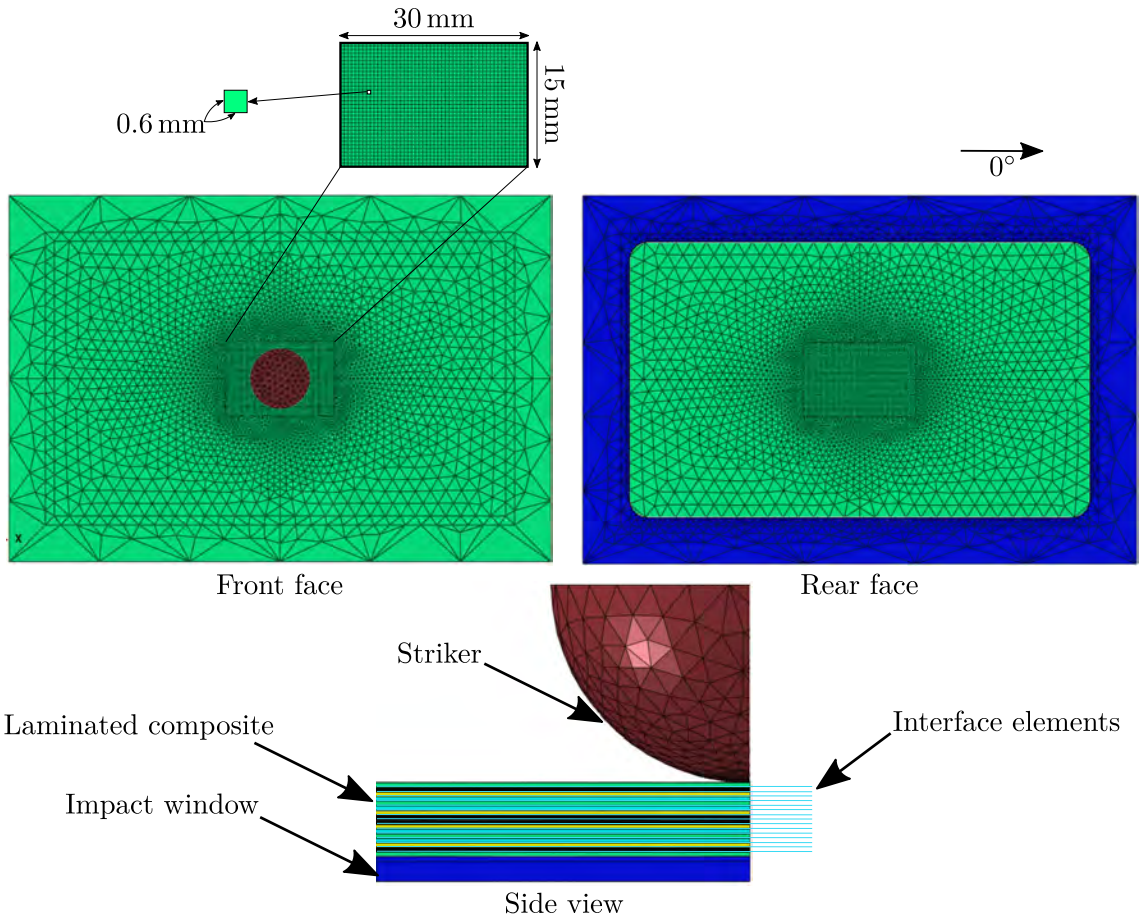

Figure 4.1: FEM of the impact experimental test for OPFM

4.1.1.2 Effect of nonlinear geometric formulation on impact results

As the composite laminate undergoes high displacement, the assumption of small displacement/small rotation is no longer fulfilled. A Jaumann-rate corotational formulation has been considered to calculate accurately the strains during the impact simulation. From FIGURE 4.2, the composite plate is compared with and without the nonlinear geometric formulation at the same time (when the load peak is reached for the cyan curve). A strong indentation can be highlighted when NLGEOM (Nonlinear geometric formulation is not activated). This is due to the fact that the local material rotation (fibre orientation) are not considered in the small displacement assumption. This rotation is emphasized when delamination occurs. The two load-displacement responses are similar until 2 kN. Once exceeded, the delamination spreads below the striker, intensifying the local indentation for the simulation performed without NLGEOM formulation. A stress plateau is then reached. When NLGEOM is activated, the gradient transformation tensor $\boldsymbol{F}$ is calculated taking into account the rotations, and the phenomenon of the striker breaking into the composite plate is avoided.

In conclusion, to obtain relevant results in accordance with the observations, NLGEOM formulation is activated in the impact simulations.

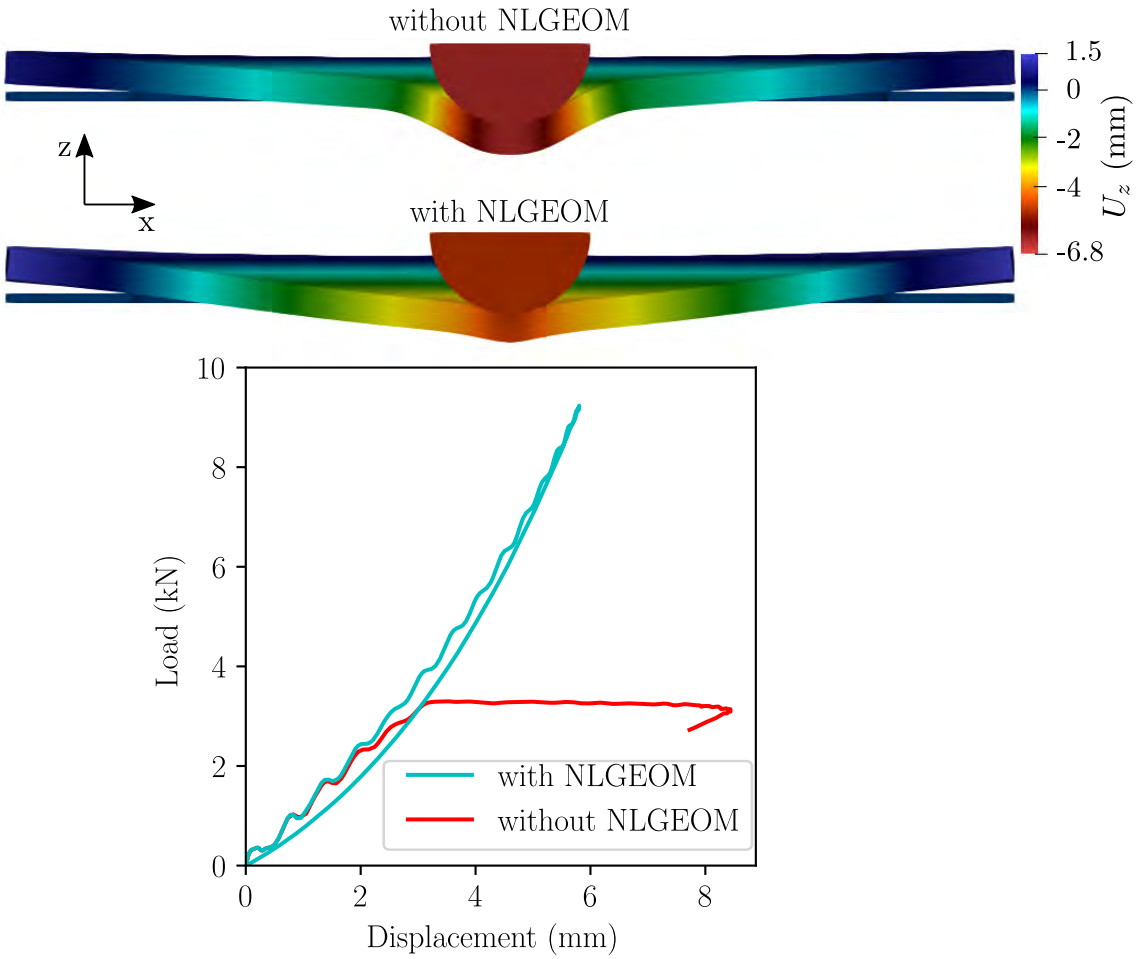

Figure 4.2: Effect of the nonlinear geometric formulation on the deformed shape of the composite plate and on the macroscopic load-displacement responses

4.1.1.3 Overview of the ONERA damage model

OPFM is a multiscale model where the behavior of the fibre and the matrix are taken into account at the mesoscopic scale. The model has been detailed in [Germain, 2006], however, the model is summarized to identify the lacks.

Nonlinear longitudinal elastic behavior In [Germain, 2020], the material under study has been characterized for in-plane loadings. Tensile tests have been performed on $[0^\circ_n]$ laminates. The experimental results reveal a nonlinearity in the macroscopic load-displacement response. Indeed, as the loading was increased, the material behavior underwent stiffening. This phenomenon has also been observed for longitudinal compression tests. However, the material behavior underwent softening. In the literature, this behavior has already been marked for composite laminates. An assumption made in [Allix et al., 1994] is that potential initial waviness is likely to occur during manufacturing. Thus, when the material is subjected to tensile loading, the fibres are stretched, enhancing the longitudinal elastic modulus. However, when the material is subjected to compressive loading, the initial waviness are exacerbated, reducing the longitudinal elastic modulus. In [Abisset, 2012], this phenomenon was modeled using a nonlinear elastic behavior. The concept was an evolution of the stiffness as a function of the longitudinal strain value. In other

words, for tensile loading the higher the longitudinal strain, the higher the stiffness value. For compressive loading, the lower the longitudinal strainNon, the lower the stiffness value.

As this formulation is elegant, a similar framework has been adopted in [Germain, 2020]. To help understanding the physical meaning of the law, FIGURE 4.3 presents the numerical longitudinal response. The five material parameters are highlighted in the plot. E_{1C}, E_{1T} are respectively the tangential asymptotical modulus in compression and in traction. E_1 is the initial elastic stiffness modulus. ε_{10C} resp. ε_{10T} are the longitudinal strain at which the stiffness tangent line crosses the strain axis. The effective stiffness $E_{1,\text{eff}}$ is calculated using EQUATION (4.1). An activation indice η_1 determines if $E_{1,\text{eff}}$ is a compression resp. traction modulus. η_1 takes 0 or 1 as a function of the sign of the stress σ_{11}. The computation of the effective stiffness in compression $E_{1C,\text{eff}}$ resp. traction $E_{1T,\text{eff}}$ will not be presented here. For a complete description, the reader is prayed to refer to [Germain, 2020].

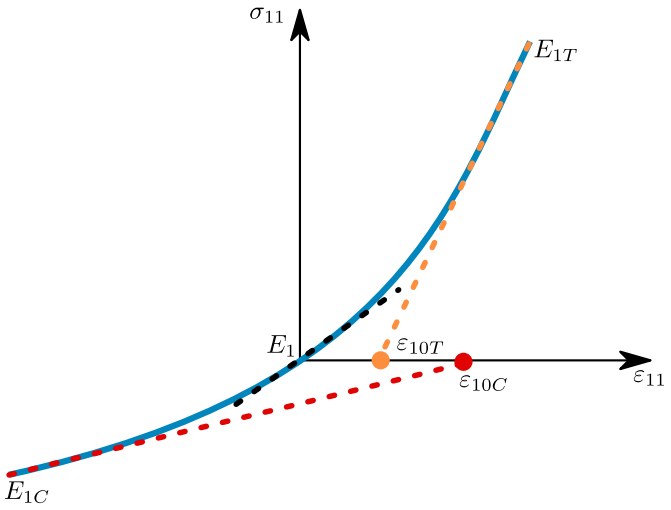

Figure 4.3: Nonlinear longitudinal stress-strain response highlighting the evolution of the longitudinal modulus [Germain, 2020]

$$E_{1,\text{eff}} = \eta_1 E_{1T,\text{eff}} + (1-\eta_1) E_{1C,\text{eff}} \text{ where } \eta_1 = \begin{cases} 1 \text{ if } \sigma_{11} > 0 \\ 0 \text{ if } \sigma_{11} < 0 \end{cases} \tag{4.1}$$

Once the effective stiffness is computed, it has been chosen to not update the compliance component ($S^0_{11} = 1/E_1$) with $E_{1,\text{eff}}$ for numerical efficiency. The longitudinal nonlinearity is rather expressed using a nonlinear elastic strain $\boldsymbol{\varepsilon^{nl}}$ allowing to not update the stiffness tensor $\mathbb{C}^0 = \mathbb{S}^{0-1}$ for each Newton-Raphson iteration. EQUATION (4.2) presents the calculation of the nonlinear longitudinal strain. The calculation of $\boldsymbol{\varepsilon^{nl}}$ is performed using the double contraction of an effect tensor $\mathbb{H}^{nl}$ with the stress tensor $\boldsymbol{\sigma}$. The presence of the effect tensor $\mathbb{H}^{nl}$ allows choosing which components of the nonlinear elastic vector are non-null. Thus, as shown in EQUATION (4.3), the longitudinal component is affected by this nonlinearity. Moreover, the non diagonal components in the fibre-matrix planes (1-2, 1-3) are also affected.

Indeed, the longitudinal strain is coupled to the transverse strain by Poisson effect.

$$\boldsymbol{\varepsilon}^{nl} = \left(\frac{E_1}{E_{1,\text{eff}}} - 1 \right) \mathbb{H}^{nl} : \boldsymbol{\sigma} \tag{4.2}$$

$$\mathbb{H}^{nl} = \begin{pmatrix} S_{11}^0 & S_{12}^0 & S_{13}^0 & 0 & \cdots & 0 \\ & 0 & & & & \vdots \\ & & \ddots & & & \vdots \\ & \text{SYM.} & & \ddots & & \vdots \\ & & & & \ddots & \vdots \\ & & & & & 0 \end{pmatrix} \tag{4.3}$$

Viscous behavior of the ply The elastic behavior in the longitudinal direction has been described. However, when the ply is loaded in the off-axis direction (transverse or in-plane shear directions), the matrix behavior governs the ply behavior. The entire response observed during a tensile test on a $[45°/-45°]_{2s}$ T700/M21 laminates is shown in FIGURE 4.4. Three different stages can be observed. The first one is a linear viscoelastic stage. Then, the behavior starts being nonlinear prior to the ply failure. Therefore, a classical viscoelastic model will not accurately predict the behavior of such laminates for higher strain levels. Based on previous work

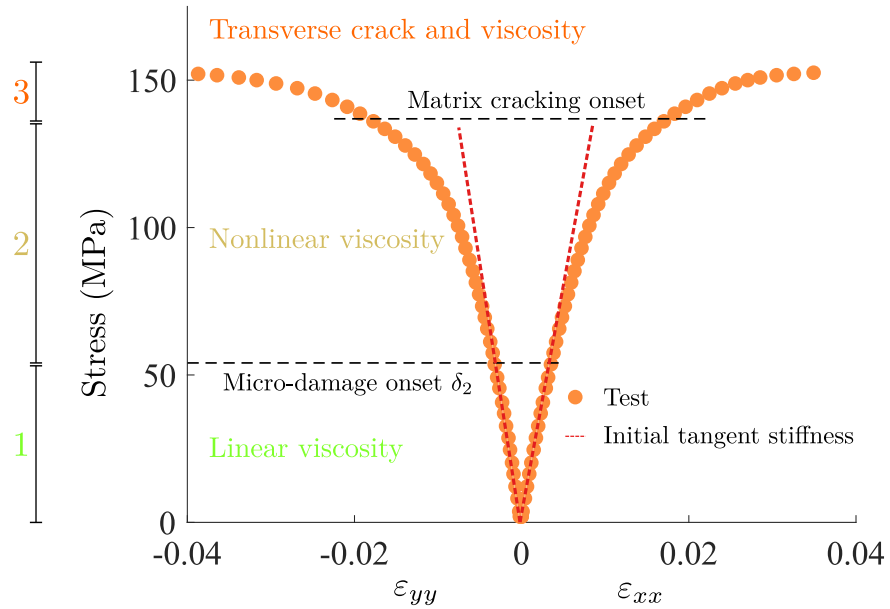

Figure 4.4: Stress-strain response of a $[45°/-45°]_{2s}$ T700/M21 sample loaded in tension [Germain, 2020]

performed at the ONERA [Laurin et al., 2013], a viscous spectral model has been developed in [Germain, 2020] to model accurately the rate effect and the viscous behavior when a ply is loaded in the off-axis direction. Finally, transverse cracks appear and induce a highly nonlinear behavior.

Linear viscoelastic model The linear viscous behavior is modeled using a viscous spectral model. The viscous strain can be decomposed into 50 elementary viscous mechanisms. Each elementary viscous mechanism is defined by a weight μ_i and a relaxation time τ_i. A Gaussian curve provides the weight distribution of each viscous mechanism. Once the temporal spectrum is calculated, the viscous strain of each elementary mechanism ($\boldsymbol{\xi}_i$) is obtained by solving a differential equation presented in EQUATION (4.4). The viscous effects affect the components defined in the effective viscous compliance tensor $\mathbb{S}^0_{vi}$. This tensor is presented in EQUATION (4.5) where the material parameters β_{ij} regulate the viscous contribution toward the elastic stiffness. The choice of a diagonal viscous compliance tensor is proposed as it guarantees the positive definiteness of the tensor. The viscous effects are expressed by the non-null components of $\mathbb{S}^0_{vi}$. The rate viscous strain of each mechanism $\dot{\boldsymbol{\xi}}$ is then calculated. Finally, the viscous strain rate $\dot{\boldsymbol{\varepsilon}}_{ve}$ is obtained by integrating the sum of $\dot{\boldsymbol{\xi}}$ (EQUATION (4.6)).

$$\dot{\boldsymbol{\xi}}_i = \frac{1}{\tau_i}(\mu_i \mathbb{S}^{\text{eff}}_{vi} : \boldsymbol{\sigma} - \boldsymbol{\xi}_i) \tag{4.4}$$

$$\mathbb{S}^{\text{eff}}_{vi} = \mathbb{S}^0_{vi} = \begin{pmatrix} 0 & 0 & \cdots & 0 \\ & \beta_{22}S^0_{22} & & \\ & & \beta_{33}S^0_{33} & \ddots & \vdots \\ & \text{SYM.} & & \beta_{44}S^0_{44} & \\ & & & & \beta_{55}S^0_{55} & 0 \\ & & & & & \beta_{66}S^0_{66} \end{pmatrix} \tag{4.5}$$

$$\dot{\boldsymbol{\varepsilon}}_{ve} = \sum_{i=1}^{50} \dot{\boldsymbol{\xi}}_i \tag{4.6}$$

Nonlinear viscous behavior The viscoelastic model introduced above describes the shear response for low shear. However, when shearing increases, a nonlinear behavior is observed as presented in FIGURE 4.4. In the literature, this behavior is linked to the presence of micro-damage at the fibre-matrix scale, some authors have introduced plasticity to model the nonlinear shear response [Ladevèze et al., 2017]. The coalescence of fibre-matrix debonding and micro-cracks in the matrix could explain this phenomenon. In [Laurin et al., 2013, Germain, 2020], a continuum damage mechanics law describes these diffuse damages. The thermodynamic force Y_m is calculated using the positive stresses ($\sigma^+_{22}, \sigma^+_{12}$ and σ^+_{23}), the reason is explained in the following as the same framework is used for matrix cracking modeling. The nonlinear response does not appear initially, therefore a micro-damage threshold is defined. The micro damage variable δ_2 is calculated using a damage evolution law not presented here. Once calculated, δ_2 affects the components of the effect tensor $\mathbb{H}_{vi}$. These components are defined in EQUATION (4.7), the micro-damages are expressed in the transverse direction $H_{vi,22}$ and in shear directions $H_{vi,44}$ and $H_{vi,66}$. The parameters γ_{ij} allows calibrating the effects of micro-damages on the viscoelasticity. It can be noticed that the micro-damages are not expressed in the out-of-plane shear direction (23) $H_{vi,44} = 0$. Indeed, the identification has been performed only for in-plane loadings. The model has not been extended for out-

of-plane loading. Finally, the viscous effective compliance tensor $\mathbb{S}_{vi}^{\text{eff}}$ is obtained by summing the initial viscous compliance tensor $\mathbb{S}_{vi}^{0}$ with the viscous micro-damages tensor $\delta_2\mathbb{H}_{vi}$ (EQUATION (4.8)). Once calculated, the total viscous strain $\boldsymbol{\varepsilon}_{ve}$ is computed using EQUATIONS (4.4) and (4.6). For more details about the nonlinear viscoelastic model, the reader is exhorted to refer to [Germain, 2020].

$$\mathbb{H}_{vi} = \begin{pmatrix} 0 & 0 & \cdots & 0 \\ & \gamma_{22}S^0_{vi,22} & & \\ & & 0 \quad \ddots & \vdots \\ & \text{SYM.} & \gamma_{44}S^0_{vi,44} & \\ & & & 0 \quad 0 \\ & & & \gamma_{66}S^0_{vi,66} \end{pmatrix} \tag{4.7}$$

$$\mathbb{S}_{vi}^{\text{eff}} = \mathbb{S}_{vi}^{0} + \delta_2\mathbb{H}_{vi} \tag{4.8}$$

The ingredients for modeling accurately the ply elastic behavior prior to transverse cracking have been presented. The local stress-strain relation can be defined as shown in EQUATION (4.9) where $\mathbb{C}^{\text{eff}}$ is the effective stiffness tensor and $\boldsymbol{\varepsilon}$ is the total strain

$$\boldsymbol{\sigma} = \mathbb{C}^{\text{eff}} : (\boldsymbol{\varepsilon} - \boldsymbol{\varepsilon}_{ve} - \boldsymbol{\varepsilon}_{nl}) \tag{4.9}$$

Matrix cracking modeling The damage mechanism related to matrix cracking is now presented. Based on the framework performed in [Laurin et al., 2013] during the WWFE III (Worldwide Failure Exercise), a damage model with an acceptable level of complexity has been developed in [Germain, 2020]. A continuum damage law is considered with two damage variables. The two damage variables are based on the damage observation. Indeed, the two variables are the matrix cracking density (the number of cracks on a given length) and the micro-delamination occurring near the crack tip of the matrix crack. FIGURE 4.5 highlights the two observable variables. These variables have been normalized as shown in EQUATION (4.10), the matrix crack density has been normalized using the ply thickness h. The micro-delamination has been normalized using the distance L between two matrix cracks.

$$\begin{cases} \overline{\rho} = \rho h = \dfrac{N_{cracks}}{L} \\ \overline{\mu} = \frac{\mu}{L} \end{cases} \tag{4.10}$$

Damage threshold The matrix cracking threshold is difficult to define in general as it is influenced by the ply thickness, the neighborhood orientation plies, the state of the matrix (presence of defects, micro-damages). Taking into account all of these parameters will lead to a complex failure criterion [Laurin et al., 2013]. In [Germain, 2020], it has been decided to calculate the strengths as a function of the ply thickness. In the following, we will call Y_{is} and S_{is} respectively the *in situ* transverse and in-plane shear strengths. As these two in-plane strengths depend on the ply-thickness, the strengths are calculated using a mixed criterion considering the maximum value between an energetic and a stress criterion. Indeed, for thick

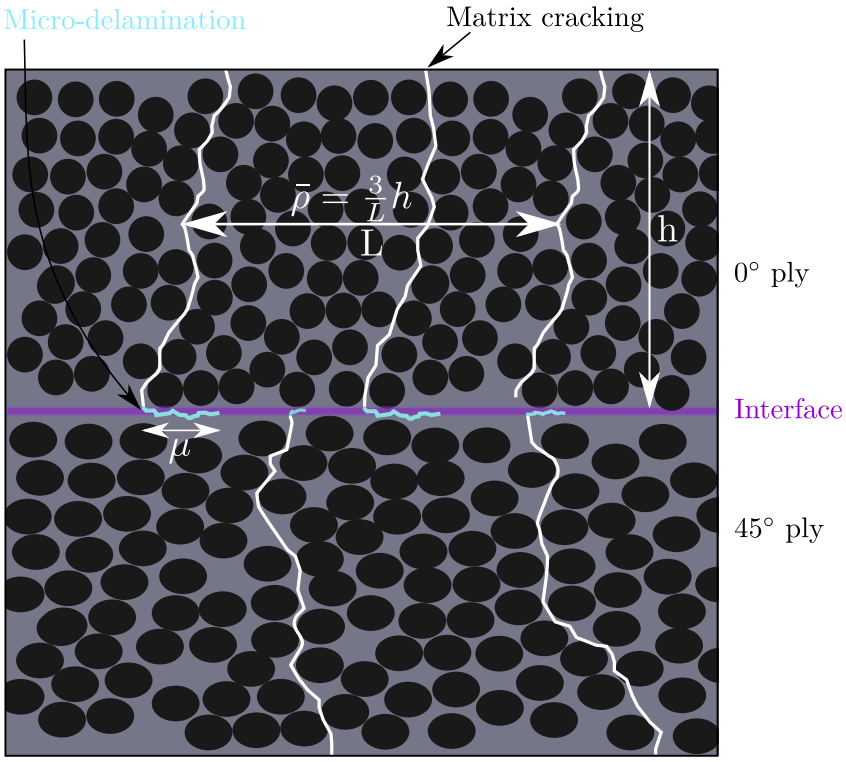

Figure 4.5: Illustration of the two damage variables related to matrix cracking and micro-delamination

plies energetic criterion is first fulfilled and then the stress criterion which governs the ply failure. For thin plies, the stress criterion is first fulfilled and then the energetic criterion is validated. Concerning the out-of-plane shear strength S_{23}, the strength is based on a stress criterion. Only one thermodynamic threshold Y_0 is considered. Y_0 is then expressed using only the *in situ* transverse strength Y_{is} as shown in EQUATION 4.11.

$$Y_0 = \frac{1}{2}(Y_{is}^2 S_{22}^0) \tag{4.11}$$

Thermodynamic force The Thermodynamic force (TF) is defined in EQUATION (4.12). Three different stresses are considered for the calculation of TF (transverse in-plane loading σ_{22}^+, in-plane shear loading τ_{12}^+ and out-of-plane shear loading τ_{23}^+). As detailed in EQUATION 4.11, only one threshold (for transverse loading) is defined. Nevertheless, as the resistance is not equal for each loading direction, coefficients (a_{24}, a_{26}) have been introduced in the TF in order to make sure that the damage threshold for in-plane shear or out-of-plane shear is initiated once the relevant strength is reached. As a matter of fact, the a_{24} coefficient for instance, is calculated using EQUATION (4.12) by assuming only out-of-plane loading $(\sigma_{22}, \tau_{12} = 0)$ and $(Y = Y_0 \Rightarrow \tau_{23} = S_{23})$.

$$Y = \frac{1}{2}(\sigma_{22}^{+\,2} S_{22}^{\text{eff}} + a_{26}\tau_{12}^{+\,2} S_{66}^{\text{eff}} + a_{24}\tau_{23}^{+\,2} S_{44}^{\text{eff}}) \tag{4.12}$$

It can be noticed that the positive part of the stresses is taken into account in the calculation of the TF. Indeed, when combined loadings are applied, such as transverse compressive stress with in-plane shear, a delay in damage onset is observed

thanks to a material reinforcement. This reinforcement is taken into account using the positive stresses (based on the works proposed in [Ju, 1989]). As presented in EQUATION (4.13), the effective stress tensor is first defined where only the components of the stress tensor responsible for matrix damage are non null. Then, the eigenvalues of the stress tensor are computed. Once, obtained the regular and positive spectral projection tensors $(\mathbf{Q}, \mathbf{Q}^+)$ in EQUATION (4.14), (4.15) are expressed using the principal directions p_i of the effective stress tensor. It can be noticed that Q^+ removes the principal direction corresponding to the negative eigenvalues thanks to the Kronecker operator δ (EQUATION (4.16)).

$$\boldsymbol{\sigma} = \begin{pmatrix} 0 & \sigma_{12} & 0 \\ \sigma_{12} & \sigma_{22} & \sigma_{23} \\ 0 & \sigma_{23} & 0 \end{pmatrix}_{(1,2,3)} \xrightarrow{\text{Eigenvalues}} \begin{pmatrix} \sigma_I & 0 & 0 \\ 0 & \sigma_{II} & 0 \\ 0 & 0 & \sigma_{III} \end{pmatrix}_{(I,II,III)} \tag{4.13}$$

$$\mathbf{Q} = \sum_{i=I}^{III} p_i \otimes p_i \tag{4.14}$$

$$\mathbf{Q}^+ = \sum_{i=I}^{III} \delta(\sigma_i > 0) p_i \otimes p_i \tag{4.15}$$

$$\delta = \begin{cases} 0 \text{ if } \sigma_i < 0 \\ 1 \text{ if } \sigma_i \geq 0 \end{cases} \tag{4.16}$$

Introducing the fourth-order positive projection tensor $\mathbb{P}^+$ in EQUATION (4.17), the positive stress tensor $\boldsymbol{\sigma}^+$ is then obtained using the double contracted product in EQUATION (4.18).

$$P^+_{ijkl} = Q^+_{ia} Q^+_{jb} Q_{ka} Q_{lb} \tag{4.17}$$

$$\boldsymbol{\sigma}^+ = \mathbb{P}^+ : \boldsymbol{\sigma} \tag{4.18}$$

Finally, the failure criterion envelope is shown in the positive stresses space as reported in FIGURE 4.7.

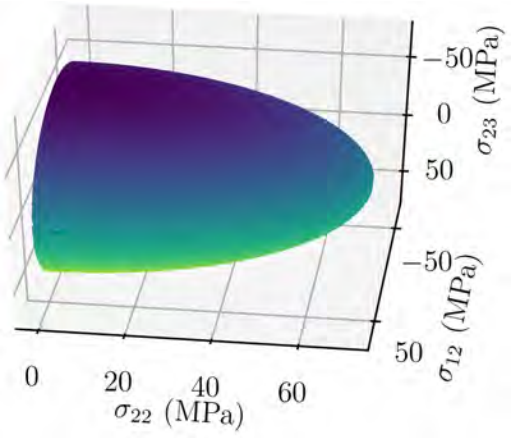

Figure 4.6: 3D representation of the matrix cracking failure envelope

Damage evolution law The damage evolution law quantifies the evolution of the damage variables during the loading. EQUATION (4.19) presents the two damage variables evolution. First of all, it can be shown a strong dependency between the two damage variables. Indeed, experimentally, it has been observed that the micro-delamination tends to slow down the evolution of the matrix crack density. Thus, the higher $\overline{\rho}$, the higher $\overline{\mu}$ and the faster the saturation of $\overline{\rho}$. The second point is the presence of the ply thickness h in the formulation. In fact, experimentally, it is commonly observed in the literature that for thicker plies, matrix cracking occurs earlier ([Parvizi and Bailey, 1978]). Moreover, the thicker the ply, the faster the evolution of the matrix crack density. The kinetics of the matrix cracking density are controlled by the material parameters (α_I, p). The parameter p allows intensifying the TF once the threshold is reached.

$$\begin{cases} \overline{\rho} = (1-\overline{\mu}) h \alpha_I \langle Y - Y_0 \rangle_+^p \\ \overline{\mu} = \langle a_h \overline{\rho}^2 + b_h h \overline{\rho} \rangle_+ \end{cases} \tag{4.19}$$

with the Macaulay bracket $\langle \cdot \rangle_+$.

Damage effects Once the two damage variables are calculated, their effects on the UD ply have to be introduced. Generally, in continuum damage mechanics, the stiffness components are reduced as a function of the damage variable. This damage variable evolves from 0 to 1. However, in our case the two damage variables are not bounded to 1 due to their own definition. Thereby, in light of the works performed in [Ladevèze et al., 2017], a FEM has been developed to identify numerically the effect of damages as reported in FIGURE 4.7. This FEM considers a periodic cell in a cross-ply laminate [0/90/0] with a discrete crack in the central 90° ply. Six different load cases are applied to the model for a designated couple $(\bar{\rho}, \bar{\mu})$. Each load case allows determining one component of the compliance tensor by homogenisation. The evolution of the compliance components as a function of the couple $(\bar{\rho}, \bar{\mu})$ is then established. A tensor effect $\mathbb{H}_{\overline{\rho},\overline{\mu},Sy}$ has been defined to fit the evolution of the discrete damage effects obtained using FEA on the compliance components (EQUATION (4.20)). As shown in EQUATION (4.21), $\mathbb{H}_{\overline{\rho},\overline{\mu},Sy}$ is the sum of three tensors $(\mathbb{H}_{a,Sy}, \mathbb{H}_{b,Sy}, \mathbb{H}_{c,Sy})$ linked to the normalized crack density, the local delamination ratio and a combination of these two damages. This expression of $\mathbb{H}_{\overline{\rho},\overline{\mu},Sy}$ allows fitting the numerical evolution of the damage effects on the compliance tensor, as reported in FIGURE 4.7.

$$\mathbb{S}_{Sy}^{\text{eff}} = \mathbb{S}^0 + \mathbb{H}_{\overline{\rho},\overline{\mu},Sy} \tag{4.20}$$

$$\text{with } \mathbb{H}_{\overline{\rho},\overline{\mu},Sy} = \overline{\rho}\mathbb{H}_{a,Sy} + \frac{\overline{\mu}}{1-\overline{\mu}}\mathbb{H}_{b,Sy} + \frac{\overline{\rho}^2}{1-\overline{\mu}}\mathbb{H}_{c,Sy} \tag{4.21}$$

Crack closure handling When the ply is subjected to compressive stresses, the crack is closed and the initial stiffness normal to the crack surface is recovered. To reproduce numerically this behavior, care must be taken as discontinuity in the stress-strain response could be introduced during the traction/compression shift. In [Germain, 2020], it has been chosen to define an activation function based on the sign of the stress σ_{22}. As detailed in EQUATION (4.22), the effect of damages on only the transverse component (22) of the compliance tensor is vanished in case of

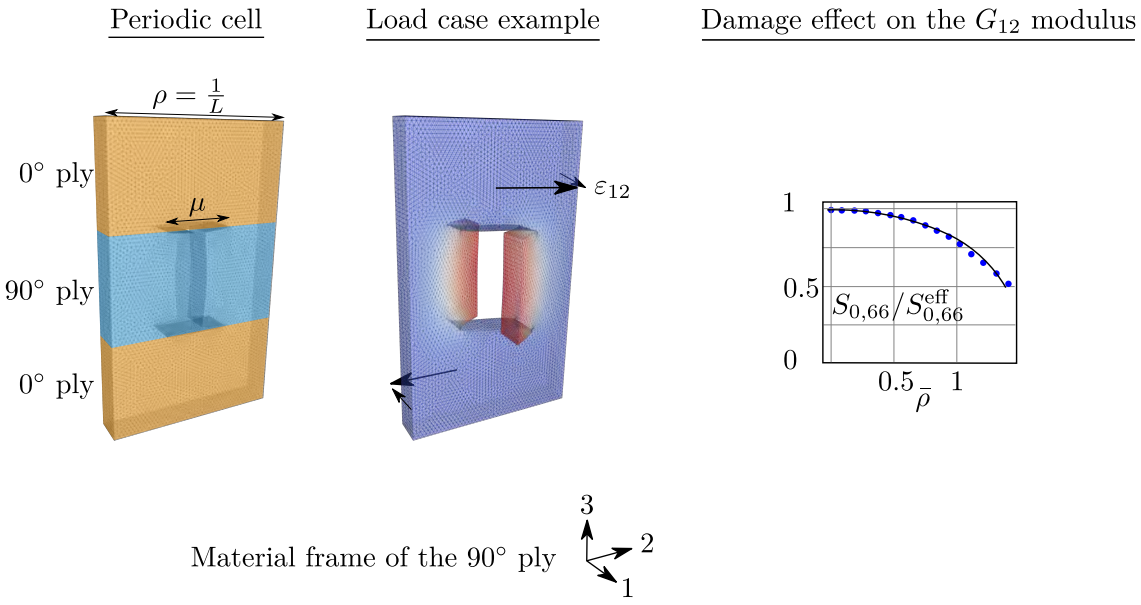

Figure 4.7: Computational strategy to determine the effect tensor [Germain, 2020]

transverse compressive loading ($\sigma_{22} < 0$). Indeed, the initial stiffness component in direction 2 is recovered ($\sigma_{22} < 0$) as $\eta_2 = 0$. The shear components are not affected by the crack closure, meaning that the assumption of null friction is performed at the crack lips.

$$H_{i,22} = \eta_2 h_{i,22} S^0_{22} \text{ with } \eta_2 = \begin{cases} 1 \text{ if } \sigma_{22} > 0 \\ 0 \text{ otherwise} \end{cases} \quad \text{and } i = a, b, c \tag{4.22}$$

Delamination modeling The delamination which is a key damage mechanism in impact is modeled using CZM. The concept has already been developed in the chapter 1. However, the constitutive behavior is remembered for the reader. The damage law is formulated as a stress-displacement jumps ($\sigma - \Delta u$) and is presented in EQUATION (4.23).

$$\boldsymbol{\sigma} = (1-d)\mathbb{K}^0 : \Delta\mathbf{u}$$

$$\begin{pmatrix} \sigma_{13} \\ \sigma_{23} \\ \sigma_{33} \end{pmatrix} = \begin{pmatrix} (1-d)K^0 & 0 & 0 \\ 0 & (1-d)K^0 & 0 \\ 0 & 0 & (1-d)K^0 \frac{\langle \Delta u_n \rangle_+}{\Delta u_n} + \alpha K^0 \frac{\langle \Delta u_n \rangle_-}{\Delta u_n} \end{pmatrix} \begin{pmatrix} \Delta u_{sh_1} \\ \Delta u_{sh_2} \\ \Delta u_n \end{pmatrix} \tag{4.23}$$

Where $\mathbb{K}^0$ is the numerical stiffness, d is the damage variable and α is the penalty parameter for out-of-plane compression. The stiffness is reduced linearly according to the evolution of the damage variable. For the normal component (33), the stiffness tensor is composed of two terms using the Macaulay bracket for the out-of-plane displacement. The damage is taken under consideration for only positive normal displacement jump $\Delta u_n > 0$. Thus, in case of compressive out-of-plane loading, the normal component of the stiffness is conserved at its initial value to avoid interpen-

etration. The damage law shape is presented in FIGURE 4.8 for single-mode and mixed-mode loading.

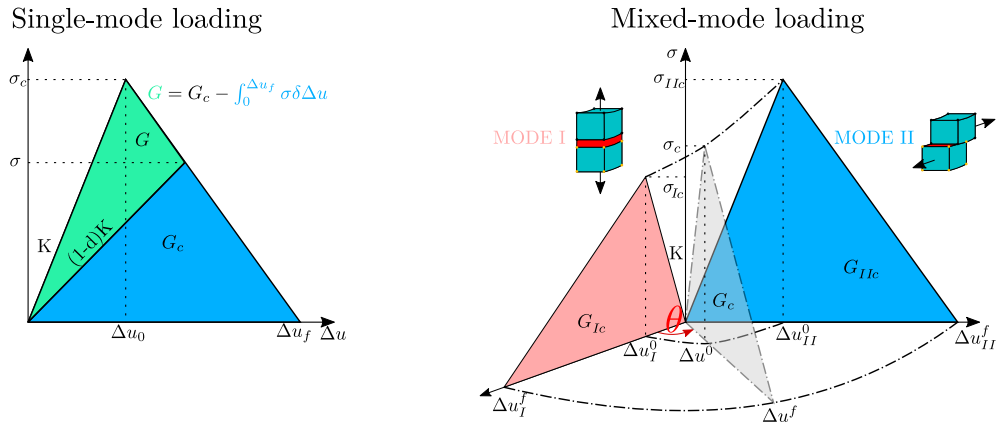

Figure 4.8: Traction-separation presented for single-mode and mixed-mode loadings

In the presence of mixed-mode loading, two criteria are used to calculate the mixed-mode stress threshold σ_c and the mixed-mode energy release rate G_c. A stress criterion and a mixed-mode propagation criterion are defined in EQUATION (4.24) and (4.25).

A classical Hashin stress criterion [Hashin, 1980] is considered. The stress σ_{33} is placed in a Macaulay bracket as it is supposed that no failure occurs for pure compressive out-of-plane loading. The two strengths (S_{33}^R, S_{shear}^R) are identified with four point bending test on L-angle specimen and interlaminar shear strength test on a plate specimen.

Concerning the propagation criterion, the well known Benzeggagh-Kenane criterion [Kenane and Benzeggagh, 1997] determines the mixed-mode fracture toughness G_c. This criterion needs to identify three material parameters. These material parameters (G_{Ic}, G_{IIc}, η) are obtained from experimental tests varying the mode mixing. G_c is calculated taking into account the weight of the dissipated energy in mode II G_{II} on the total dissipated energy $G_{\mathrm{tot}} = G_{\mathrm{I}} + G_{\mathrm{II}}$. More details on the onset and propagation criteria can be found in [Germain, 2020, Camanho and Dávila, 2002].

$$\left(\frac{\langle \sigma_{33} \rangle_+}{S_{33}^R}\right)^2 + \left(\frac{\sigma_{13}}{S_{shear}^R}\right)^2 + \left(\frac{\sigma_{23}}{S_{shear}^R}\right)^2 = 1 \tag{4.24}$$

$$G_c = G_{\mathrm{Ic}} + (G_{\mathrm{Ic}} - G_{\mathrm{IIc}}) \left(\frac{G_{II}}{(G_{\mathrm{I}} + G_{\mathrm{II}})}\right)^{\eta} \tag{4.25}$$

Once the couple (σ_c, G_c) is defined, the displacement jumps at the onset of delamination and the failure can be computed using EQUATION (4.26). The damage variable d is then calculated using the mixed-mode displacement jump Δu in EQUATION (4.27). Finally, the dissipated energy surface G is calculated according to EQUATION (4.28).

$$\Delta u_0 = \frac{\sigma_c}{K} \qquad \Delta u_f = \frac{2G_c}{\sigma_c} \tag{4.26}$$

$$\Delta u = \sqrt{\Delta u_{sh_1}^2 + \Delta u_{sh_2}^2 + \Delta u_n{}^2} \qquad d = \frac{\Delta u_f(\Delta u - \Delta u_0)}{\Delta u(\Delta u_f - \Delta u_0)} \tag{4.27}$$

$$G = G_c - \int_0^{\Delta u_f} \sigma \delta \Delta u \tag{4.28}$$

4.1.2 Discrete Ply Model

4.1.2.1 Discretization of the impact test using FEM

DPM is a composite laminate FEM. It was initially built to perform impact simulations [Bouvet et al., 2012, Rivallant et al., 2013b, Hongkarnjanakul et al., 2013, Abdulhamid et al., 2016]. The FEM is built automatically using a Fortran routine in ABAQUS. As presented in FIGURE 4.9 a mesh-oriented strategy is considered with four possible mesh orientations (0°, 90°, ±45°). This mesh allows inserting cohesive elements at the edge side of volume elements with complete integration (C3D8). No tight constraints are used as the nodes overlap in the thickness direction. Each ply is meshed with one element in the thickness direction. Cohesive elements are placed between plies in red to simulate delamination and at the edge side of each volume element to simulate matrix cracking. It can be underlined that the mesh size (0.6 mm) defines the maximal matrix crack density per ply ($\rho = N_{\text{cracks}}/L$) to be equal to 3.3 mm^{-1}.

The impact model considers the composite laminate, the impact window, and the striker. General contact mechanics with friction is used between the striker-composite plates and the composite plates-impact window. The striker and the impact window are modeled using rigid body assumption (the stiffness is considered infinitely higher than the composite laminate stiffness). Abaqus explicit solver is used to perform the simulation with a time step of 1.25 exp(−8) s, satisfying the CFL condition defined in chapter 1 for a stable simulation. As the simulation requires millions of increments, possible round-off errors have to be alleviated using a double-precision solver. In order to improve the modeling of the dynamic impact event, a bulk viscosity is added. This bulk viscosity introduces damping associated with volumetric strain. Two forms of bulk viscosity are considered (a linear and a quadratic) with the default parameters (linear : $b_1 = 0.06$, quadratic: $b_2 = 1.2$). The linear bulk viscosity is intended to damp spurious effects occurring at a higher frequency. The quadratic bulk viscosity is activated only for compressive volumetric strain. Indeed, pressure prevents the element from collapsing under high-velocity gradients.

4.1.2.2 Overview of the damage laws in DPM

The damage laws describing each damage mechanism occurring in impact will be described in the following.

Matrix cracking Contrary to ONERA framework which uses a continuum damage modeling, the matrix cracking is modeled using discrete damage in the DPM. Indeed, it takes advantage of the oriented mesh to insert cohesive elements at the

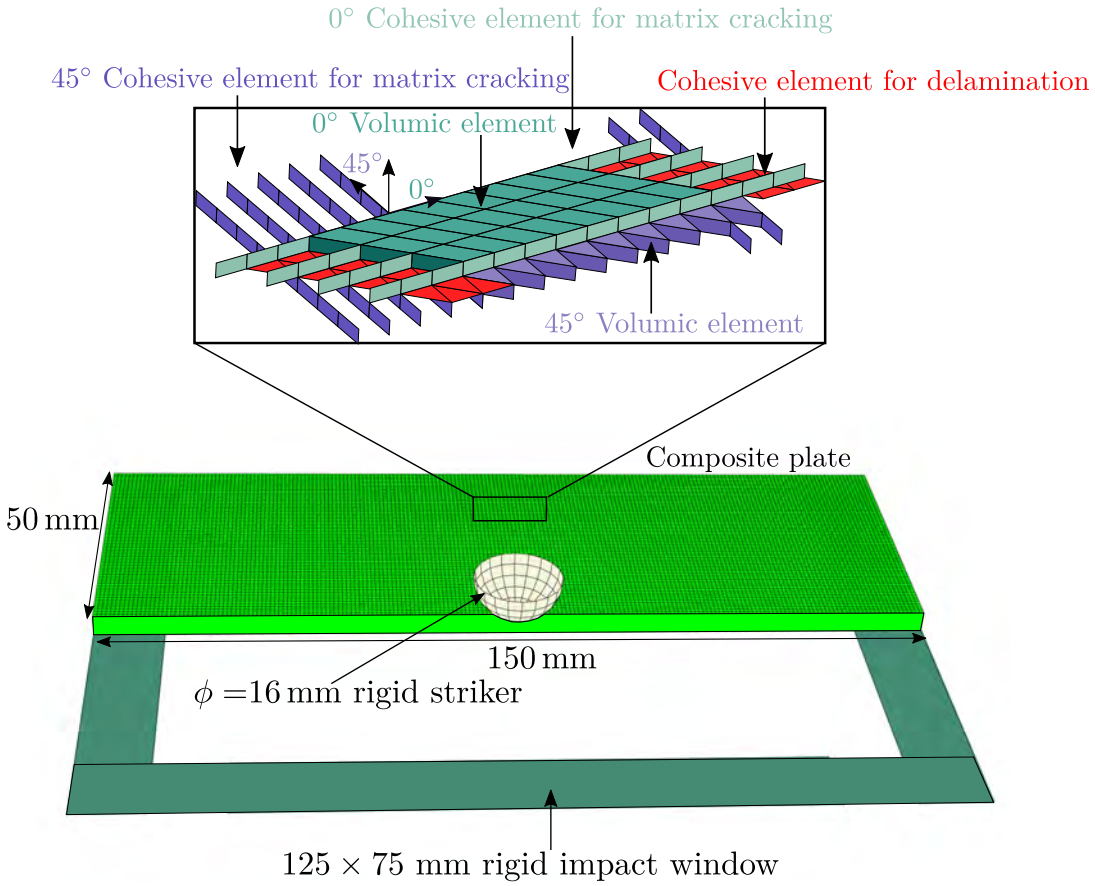

Figure 4.9: FEM highlighting the mesh strategy and impact configuration in DPM

side of the elements stripes. The failure of the cohesive interface is managed in two different manners.

The first one is a Hashin's failure criterion [Hashin, 1980] evaluated at the volume Gauss points neighboring the cohesive interface.

$$\frac{\langle \sigma_{22}^2 \rangle_+}{{S_{22}^R}^2} + \frac{\tau_{12}^2 + \tau_{23}^2}{{S_{23}^R}^2} = 1 \tag{4.29}$$

Once the failure is obtained, the permanent indentation is captured using a residual strain ε_{res}. The residual shear stress τ_{23}^{res} is calculated according to Equation (4.30). τ_{23}^{res} is then retrieved from the shear stress using Equation (4.32) for shear loading.

$$\tau_{23}^{\text{res}} = K_{23}\gamma_{23}^{\text{res}} \tag{4.30}$$

$$\text{with } \gamma_{23}^{\text{res}} = \begin{cases} \text{coef} \cdot \max(\gamma_{23}) \text{ if } \gamma_{23} > 0 \\ \text{coef} \cdot \min(\gamma_{23}) \text{ if } \gamma_{23} < 0 \end{cases} \tag{4.31}$$

$$\tau_{23} = K_{23}\gamma_{23} - \tau_{23}^{\text{res}} \tag{4.32}$$

The residual transverse stress σ_{22}^{res} is calculated according to Equation (4.33). For transverse loading. σ_{22}^{res} is then retrieved from the shear stress using Equa-

TION (4.35).

$$\sigma_{22}^{\text{res}} = K_{22}\varepsilon_{22}^{\text{res}} \tag{4.33}$$

$$\text{with } \varepsilon_{22}^{\text{res}} = \text{coef} \cdot \max(\varepsilon_{22}) \text{ if } \varepsilon_{22} > 0 \tag{4.34}$$

$$\tau_{22} = K_{22}\varepsilon_{22} - \tau_{22}^{\text{res}} \tag{4.35}$$

The second one is a classical mixed-mode traction-separation law. This law is controlled by two criteria, one for the damage initiation and one for the damage propagation. Once the displacement jump in mixed-mode d_{eq} reached its onset value in mode I or II, the failure is initiated. A linear propagation criterion presented in EQUATION (4.36) is used. A linear coupling is established between the mode II, III and the mode I. The contribution of each mode is calculated by adding the ratio of the dissipated energy by modes I, II and III (with the assumption of $G_{\text{IIIc}} = G_{\text{IIc}}$).

$$\frac{G_{\text{I}}}{G_{\text{Ic}}} + \frac{G_{\text{II}}}{G_{\text{IIc}}} + \frac{G_{\text{III}}}{G_{\text{IIc}}} = 1 \tag{4.36}$$

Delamination The cohesive zone model is used with a traction-separation law for the delamination modeling. As presented for matrix cracking, the same framework has been adopted for the delamination with an onset criterion for damage initiation and a linear energy propagation criterion.

Fibre breaks A continuum damage model is considered. Two different damage laws are used for the traction and compression behaviors. Indeed, this choice is explained by the two distinctive failure mechanisms in tension and in compression. The damage law is presented in FIGURE 1.43.

Fibre breaks in compression The damage initiation is governed by a maximum strain criterion. The material parameter ε_c^R is the compressive failure strain. Once the strain is reached, the softening is governed by a damage variable d. This damage variable affects the stiffness components associated with longitudinal and shear behaviors. A permanent strain $\varepsilon_{\text{res}} = \varepsilon_{11}d$ is introduced to model the presence of debris, which block the material from recovering its initial position. The choice of ε_{res} has been used to ensure the continuity once the crushing is initiated (blue point in FIGURE 1.43), once $d = 0.95$, a stress plateau at σ^{crush} is reached.

Fibre breaks in tension The fibre breaks in tension use a traction-separation law, where a maximum strain criterion controls the initiation. The material parameter ε_t^R is the tensile failure strain. The damage variable d controls the softening by degrading the stiffness components associated with longitudinal and shear behavior. A tiny residual stiffness alleviates zeros values in the stiffness tensor avoiding thus numerical difficulties.

Ensuring correct energy dissipation As a continuum damage framework is considered for the fibre breaks modeling, spurious mesh dependency is introduced during the softening. This phenomenon is part of a material instability already discussed in chapter 1. The crack band method has been implemented in previous work to ensure accurate energy dissipation by considering a spatial internal length

L_e. Equation (4.37) links the internal energy and the energy release rate in mode I $G_{\mathrm{Ic}}^{T,C}$ with (T,C) for tension and compression as the energy release rate is not the same, the spatial length L_c is equal to V/S.

$$\int_V \left(\int_0^{\varepsilon_{11}} \sigma_{11} \, \mathrm{d}\varepsilon_{11} \right) \mathrm{d}V = S G_{\mathrm{Ic}}^{T,C} \tag{4.37}$$

$$\frac{G_{\mathrm{I}}^{T}}{G_{\mathrm{Ic}}^{T}} + \frac{G_{\mathrm{I}}^{C}}{G_{\mathrm{Ic}}^{C}} = 1 \tag{4.38}$$

The energy is calculated on the 8 Gauss points of the element, the damage is therefore the same on the 8 Gauss points once one has failed. A linear energy coupling between the fibre breaks in tension and compression is used to ensure the correct energy dissipation (Equation (4.38)).

Damage interactions In DPM a phenomenological coupling is introduced between the fibre breaks and the two other mechanisms (delamination and matrix cracking). Indeed, as introduced in chapter 1, the CDM associated with CZM suffers from a lack of information exchanges. Thus, when fibre break occurs at a Gauss point, it triggers the matrix failure of the same Gauss point and the adjacent cohesive interface element is broken. No artificial coupling is introduced between matrix crack and delamination as the interaction is expressed naturally due to the discrete damage framework for matrix cracking.

4.1.3 Summary of the two damage models

A presentation of the two different damage models has been proposed. Table 4.1 summarizes the different ingredients of the two damage models. OPFM models the ply behavior by introducing two phenomena observed experimentally (the nonlinear elasticity in fibre direction and the viscous behavior of the matrix). Concerning the damage mechanisms, it has been observed that all damage types are present during the experimental campaign. Thus, it is essential to model the entire types of damage as a strong interaction between each damage mechanism is observed in impact damages. The available damage model developed at ONERA at the beginning of this work does not model the fibre break which is a lack of accurate modeling of impact damages for the studied material. The main strengths of DPM are that damage interactions are reproduced thanks to (i) a natural coupling between matrix cracking and delamination and, (ii) an artificial coupling between fibre break and matrix cracking/delamination. In order to evaluate the predictive capability of OPFM, two main works have been carried out to, first, model the fibre break and then, introduce damage couplings. Therefore, the next section is dedicated to the developments performed in OPFM.

Parameters needed for the two damage models

The parameters required for the two models are presented in Tables 4.2–4.3. Two kinds of parameters are presented. Numerical parameters are identified in the simulation, they have no physical meaning. Material parameters are identified using experimental tests. OPFM requires 37 parameters for complete modeling of the ply behavior and the modeling of the matrix cracking and the delamination. DPM requires 19 material parameters to describe the ply behavior and the damages (matrix

Ply behavior	**OPFM**	**DPM**
Nonlinear longitudinal elasticity	✓	✗
Viscous behavior	✓	✗
Damage mechanisms	**OPFM**	**DPM**
Matrix cracking	CDM	CZM
Delamination	CZM	CZM
Fibre break	✗	CDM
Damage coupling	**OPFM**	**DPM**
Fibre break → Matrix cracking	✗	✓
Fibre break → Delamination	✗	✓
Matrix cracking → Delamination	✗	✓

Table 4.1: The key points of the different models at the beginning of this work

cracking, delamination and fibre breaks), which highlight the main strength of DPM with a few parameters required. DPM takes advantage of using an adapted mesh for UD ply (oriented mesh).

The higher the number of material parameters, the more complex its transfer toward industrials. The industrial need requires a few material parameters with fast identification. At this point, the two damage models are good candidates to be transferred into industries.

Elastic parameters	Numerical	Material
Medium Young's modulus in fibre direction, E_{11}	✗	✓
Transverse Young's modulus in fibre direction, E_{22}	✗	✓
In-plane shear modulus, G_{12}	✗	✓
Out-of-plane shear modulus, G_{23}	✗	✓
Poisson's ratio fibre/matrix, ν_{12}	✗	✓
Poisson's ratio matrix/matrix, ν_{23}	✗	✓
Density ρ	✗	✓
Non-linear elastic parameters	Numerical	Material
Asymptotical compressive modulus in fibre direction, E_{1C}	✗	✓
Asymptotical tensile modulus in fibre direction, E_{1T}	✗	✓

Strain defining the stiffening onset, ε_{10T}	✗	✓
Strain defining the softening onset, ε_{10C}	✗	✓
Viscous spectrum parameters	Numerical	Material
Gaussian viscous parameter, n_0 n_c	✗	✓
Number of viscous mechanisms, n_p	✗	✓
Bounds of the viscous mechanism values, $[n_1, n_2]$	✗	✓
Linear viscoelastic model parameters	Numerical	Material
Viscous parameters in S_{vi}^{eff}, β_{22} β_{33} β_{55} β_{66}	✓	✗
Nonlinear viscoelastic model parameters	Numerical	Material
Viscous parameters in S_{vi}^{eff}, γ_{22} γ_{44} γ_{66}	✓	✗
Micro-damage threshold, Y_{0m}	✗	✓
Kinetics parameters of the micro-damage law, Y_{cm} p_m	✓	✗
Matrix cracking damage parameters	Numerical	Material
Viscous parameter regularization, τ_Y	✓	✗
Damage threshold, Y_0	✗	✓
Kinetics parameters of $\bar{\rho}$ law, α_I p	✗	✓
Kinetics parameters of $\bar{\mu}$ law, a_h b_h	✗	✓
Delamination parameters		
Tensile failure stress in transverse direction, $S^R{}_{33}$	✗	✓
Out-of-plane shear failure stress, S^R_{shear}	✗	✓
Interface fracture toughness in mode I, G_{Ic}	✗	✓
Interface fracture toughness in mode II, G_{IIc}	✗	✓
Mixed-mode parameter, η	✗	✓

Table 4.2: Parameters required for OPFM

4.2 Improvements of OPFM

OPFM has been enriched to predict all the damage mechanisms and interactions during a low-velocity impact simulation. The first scope is dedicated to fibre break modeling with a gradient damage approach. Then, the requirement of damage cou-

Elastic parameters	Numerical	Material
Tensile Young's modulus in fibre direction, E_{11t}	✗	✓
Compressive Young's modulus in fibre direction, E_{11c}	✗	✓
Transverse Young's modulus in fibre direction, E_{22}	✗	✓
In-plane shear modulus, G_{12}	✗	✓
Out-of-plane shear modulus, G_{23}	✗	✓
Poisson's ratio, ν_{12}	✗	✓
Density ρ	✗	✓
Fibre damage parameters	Numerical	Material
Tensile failure strain in fibre direction, ε^R_{11t}	✗	✓
Compressive failure strain in fibre direction, ε^R_{11c}	✗	✓
Tensile fracture toughness in fibre direction, G^T_{Ic}	✗	✓
Compressive fracture toughness in fibre direction, G^C_{Ic}	✗	✓
Crushing stress in compression, σ^{crush}	✗	✓
Matrix cracking damage parameters	Numerical	Material
Tensile failure stress in transverse direction, S^R_{22}	✗	✓
In-plane and out-of-plane shear failure stresses, S^R_{23}	✗	✓
Coefficient for permanent strain, coef	✓	✗
Delamination parameters	Numerical	Material
Tensile failure stress in transverse direction, $S^R{}_{33}$	✗	✓
Out-of-plane shear failure stress, S^R_{shear}	✗	✓
Interface fracture toughness in mode I, G_{Ic}	✗	✓
Interface fracture toughness in mode II, G_{IIc}	✗	✓

Table 4.3: Parameters required for DPM

pling to predict impact damages accurately is presented. Finally, an enhancement of the CZM for combined shear and out-of-plane compressive loading is also introduced.

4.2.1 Fibre breaks modeling

The development of a damage law for the fibre failure will be presented in the following. A thought process toward the chosen accurate fibre breaks modeling has been performed with two potential candidates.

The first one ensured the CDM framework. However, as presented in Chapter 2, a regularization method has to be used to avoid spurious mesh dependency in the results and to dissipate the correct energy. Several solutions have been presented with their advantages and disadvantages in Chapter 1. In our opinion, the better compromise is the gradient damage family, as it does not introduce any strain-rate dependency (contrary to viscous damage method). Besides, this family is known for its regularized properties. Non-local damage gradient has been chosen as it ensures freedom in the establishment of the local constitutive behavior. Nevertheless, it has revealed some classical pathologies associated to non-local damage such as damage overspreading, delayed damage evolution, significant residual stiffness (section 4.2.1.1).

Thus, it has been decided to investigate another gradient damage model, the phase-field variational approach (section 4.2.1.2). The phase-field is different from a CDM, the framework is based on the variational approach of the brittle failure. Therefore, the phase-field is not a damage model which links the stress-strain using a local damage law. The phase-field approach involves a strong link between the damage onset, the energy release rate, and the internal length. In other words, the choice of two parameters determines the third. This can be harmful when the internal length obtained from the two other parameters is not appropriate.

The gradient damage framework requires another approach to the problem resolution as it introduces an additional field that enter in the functional algorithm to minimize. Two minimization schemes are possible and will be discussed at the end (section 4.2.1.4).

4.2.1.1 Non-local damage approach

The non-local damage approach will be presented here. Firstly, the local constitutive behavior is detailed with the two different damage laws for the fibre breaks in compression and in tension.

Local equations of the CDM

Fibre breaks in compression A maximum strain criterion is considered for the damage onset. Once the strain at failure ε_{11c}^R is reached, the softening behavior is initiated due to damage evolution.

The damage evolution law developed for concrete in [Pijaudier-Cabot and Mazars, 2001] has been considered. A stress plateau models the contact with the debris during compressive strain. Equation (4.39) presents the evolution law of the local damage variable D_c^l.

$$D_c^l = 1 - \overbrace{\frac{\varepsilon_{11c}^R(1-A_c)}{\varepsilon_{11}}}^{\text{Block 1}} - \overbrace{A_c \exp\left(-B_c\langle\varepsilon_{11} - \varepsilon_{11c}^R\rangle_-\right)}^{\text{Block 2}} \tag{4.39}$$

Where (A_c, B_c) are material parameters, ε_{11} is the longitudinal strain. As it can be observed, two main blocks (1 and 2) are contributing to the evolution of the damage law. Figure 4.10 highlights the effect of blocks 1 and 2 in the local stress-strain response. Block 1 controls the stress value at which the plateau is initiated. The higher 1, the lower the plateau's stress initiation. Block 2 controls the softening

response once the failure is initiated. A low value of 2 will bring a sudden failure. It can be seen that once the plateau is initiated, the damage law continues to dissipate energy. The value of A has been fixed in order to get the exact value of the crushing stress used σ^{crush} in DPM.

The damage variable is plotted in cyan, as expected before the failure onset the local damage variable is null. Then it starts growing faster, once the stress plateau is reached, the damage variable grows slowly. During the elastic unloading, the irreversible property of the damage law is highlighted with a non-decrease of the local damage variable.

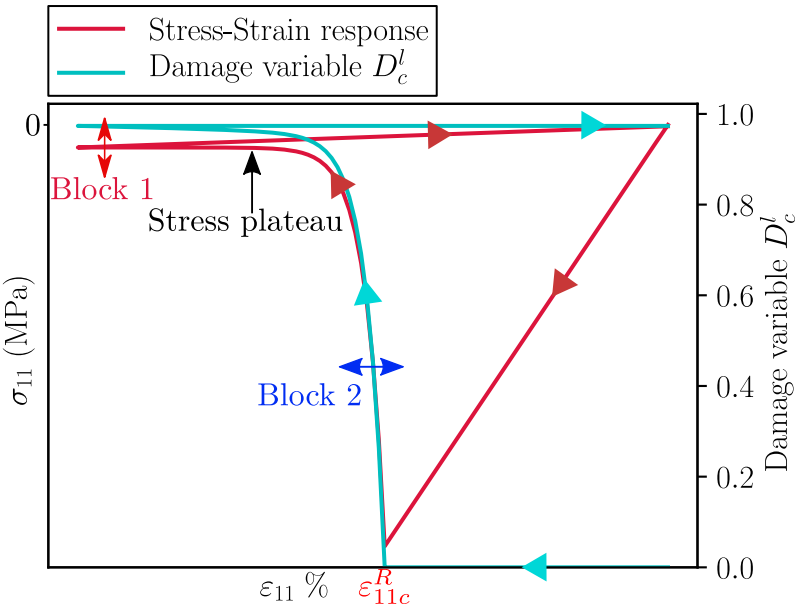

Figure 4.10: Local stress-strain response for the implemented Mazars law for fibre breaks in compression

Fibre breaks in tension As exposed to fibre breaks in compression, a maximum strain criterion is considered. Once the longitudinal strain has reached the strain at failure ε_{11t}^R, the softening is initiated.

The brittle failure in tension involves a separation of the fibres without the presence of debris between the broken fibres. Thus, the damage evolution law is different from the Mazars framework. The damage evolution law is presented in Equation (4.40) (similar to the block B in Mazars law).

$$D_t^l = 0.999 - \exp\left(-B_t \cdot \langle \varepsilon_{11} - \varepsilon_{t,11}^R \rangle_+\right) \tag{4.40}$$

Where B_t is a material parameter that controls the softening response. The Macaulay bracket is used in order to avoid damage when the longitudinal strain ε_{11} has not reached the damage threshold ε_{11t}^R. The stress-strain response is illustrated in Figure 4.11. The softening is performed after the failure onset until the stress σ_{11} reaches a quasi-null value.

The foundation of the local constitutive behavior has been presented without the damage effects on the compliance tensor. Indeed, it is not the local damage variables D_c^l resp. D_t^l that affect the compliance components. It has been chosen to perform

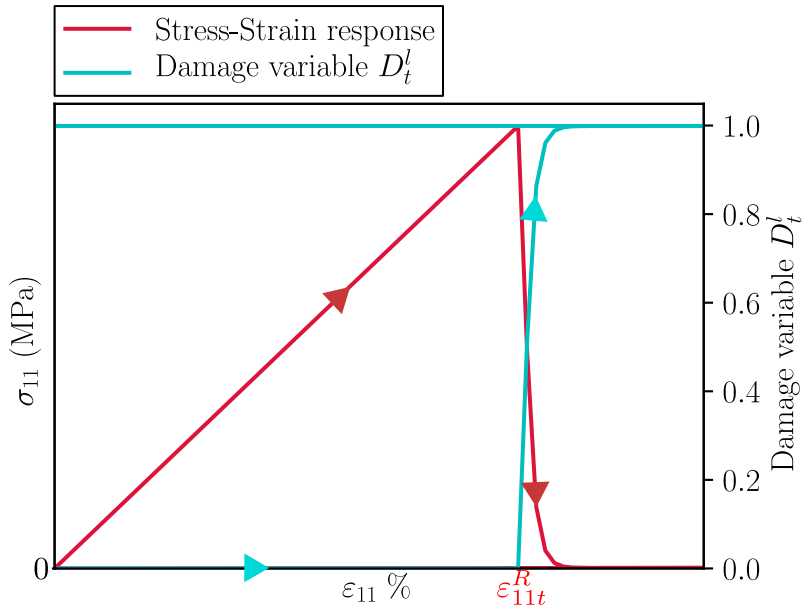

Figure 4.11: Local stress-strain response for the failure law in tension

the regularization on the local damage variables. Then, the regularized damage variables are called non-local damage variables in the following D_c^{nl} resp. D_t^{nl} affect the compliance components. The non-local approach will be detailed hereafter.

Non-local constitutive behavior The non-local formulation developed in [Peerlings et al., 1996] has been used in this work. Before presenting the diffusion equation, choosing which variable to regularize is necessary. A first attempt has been performed to regularize the driving force $Y^l = \langle \|\varepsilon_{11}\| - \|\varepsilon_{11}^R\| \rangle_+$. However, it has been observed that the damage threshold is delayed. Once the strain threshold has been reached for the local quantity ($Y^l > 0$), the threshold has not necessarely been reached for the non-local quantity ($Y^{nl} = 0$). Indeed, the sharpness of the local quantity Y^l is smoothed over the neighborhood thanks to the diffusion equation, resulting in a reduced value for Y^{nl}. The regularization is therefore carried on the local damage variables (D_c^l, D_t^l). Two fields are defined to distinguish the fibre breaks in tension from the fibre breaks in compression. Equation (4.41) presents the non-local diffusion equation.

$$\begin{cases} D_c^{nl} - \ell^2 \Delta D_c^{nl} = D_c^l \\ D_t^{nl} - \ell^2 \Delta D_t^{nl} = D_t^l \\ \boldsymbol{\nabla} D_c^{nl} \cdot \boldsymbol{n} = 0 \text{ on } \partial\Omega \\ \boldsymbol{\nabla} D_t^{nl} \cdot \boldsymbol{n} = 0 \text{ on } \partial\Omega \end{cases} \tag{4.41}$$

where D_c^{nl} resp. D_t^{nl} is the regularized damage variable, D_c^l resp. D_t^l is the localized damage variable, and ℓ is the internal length (the same internal length is used in traction and compression). It can be shown that the internal length ℓ controls the spatial operator of the damage. The higher the internal length, the more the localized damage is spread over the neighborhood. It can be noticed that a scalar value has been considered for the internal length meaning that an isotropic damage spreading is considered. In [Médeau, 2019], the question of introducing an

anisotropic tensor to define different internal lengths according to the direction has been studied which has not been considered for the sake of simplicity. The non-local equations define two boundary conditions (null flux at the free edge), in order to solve the partial differential equation's problem (EQUATION (4.41)).

Damage effects Once the regularized damage variables are calculated, the damage effects on the stress-strain behavior are performed. It has been decided to adopt the same formalism presented in [Germain, 2020], where the damage effects were taken by adding additional compliance using tensor effects. As the regularized damage variables evolve from $[0, 1]$, the classical form used to handle the damage effect on the stiffness components $(1 - d)$ cannot be used directly. Thus, a change of variable is performed on the two regularized damage variables defined in EQUATION (4.42). From EQUATION (4.42), when $D^{nl} = 0$, $d^{nl} = 0$, there is no damage effect. Where $D^{nl} = 1$, d^{nl} tends to an infinite value.

$$\begin{cases} d_c^{nl} = \frac{D_c^{nl}}{1-D_c^{nl}} \\ d_t^{nl} = \frac{D_t^{nl}}{1-D_t^{nl}} \end{cases} \tag{4.42}$$

Then, as shown in EQUATION (4.43), the effective compliance tensor is calculated by taking into account each damage mechanism. The contribution of each damage mechanism is added to the initial compliance tensor $\mathbb{S}^0$:

$$\mathbb{S}^{\text{eff}} = \mathbb{S}^0 + \mathbb{S}^{\text{eff}}(\overline{\rho}, \overline{\mu}) + d_c^{nl}\mathbb{H}_f + d_f^{nl}\mathbb{H}_f \tag{4.43}$$

$$\text{with } \mathbb{H}_f = \begin{pmatrix} h_{11}^{ff} S_{11}^0 & 0 & \cdots & & 0 \\ & 0 & & & \vdots \\ \text{SYM.} & & h_{44}^{ff} S_{44}^0 & \ddots & \\ & & & 0 & 0 \\ & & & & h_{66}^{ff} S_{66}^0 \end{pmatrix} \tag{4.44}$$

For the fibre break modeling, it has been decided to add the contribution of the fibre breaks in tension and compression using the same damage effect tensor $\mathbb{H}_f$ (EQUATION (4.44)). The non-null diagonal components of $\mathbb{H}_f$ will affect the longitudinal stiffness and the three shear modulus. As $E_{11} >> G_{ij}$, material parameters h_{ii} are introduced to avoid a high decrease of the shear moduli. It can be noticed that the components related to Poisson coefficient (H_{12}, H_{13}) are assumed to not affected by the fibre failure. Indeed, to guarantee the positive-definiteness of the compliance tensor, it has been decided to not affect the off-diagonal components. One issue raised from EQUATION (4.43) is how it should be handled if the regularized damage variables $(D_c^{nl}, D_t^{nl}) > 1$ are activated at the same time ? For example, if the fibre breaks in compression have previously occurred, and then fibre breaks in tension occur, the two damage effects will be activated with the current formulation. A solution was to introduce an indice function ξ depending on $\text{sign}(\varepsilon_{11})$ as shown in EQUATION (4.45). ξ will activate/deactivate the damage effects as a function of the local strain state (traction or compression).

$$\mathbb{S}^{\text{eff}} = \mathbb{S}^0 + \mathbb{S}^{\text{eff}}(\overline{\rho}, \overline{\mu}) + (1-\xi)d_c^{nl}\mathbb{H}_c + \xi d_t^{nl}\mathbb{H}_t \quad \text{with } \xi = \begin{cases} 1 \text{ if } \varepsilon_{11} > 0 \\ 0 \text{ if } \varepsilon_{11} < 0 \end{cases} \tag{4.45}$$

Nevertheless, this method has generated a discontinuity during traction $\rightleftharpoons$ compression shift. These discontinuities were responsible for convergence issues of the Newton-Raphson solver. Another possibility is to create only one fibre failure damage variable d_m^{nl}, which is calculated using the max of the two damage variables (EQUATION (4.46)). Finally, the effective compliance tensor will be calculated considering only the effect due to d_m^{nl} (EQUATION (4.47)).

$$d_m^{nl} = \max(d_c^{nl}, d_t^{nl}) \tag{4.46}$$

$$\mathbb{S}^{\text{eff}} = \mathbb{S}^0 + \mathbb{S}^{\text{eff}}(\overline{\rho}, \overline{\mu}) + d_m^{nl}\mathbb{H} \tag{4.47}$$

So far, this method has not been implemented as it will not correct the non-local pathology exposed hereafter. Thus, it has been decided to conserve the two damage effects activated if $(D_c^{nl},\ D_t^{nl}) > 1$.

Simulation of fibre breaks using FEA and actual limitation of non-local damage The FEA has been performed on the Q16 laminate for each energy level. As the 35 J impact test generates the maximum of fibre damage in tension and compression, the results of this simulation will be presented and discussed hereafter.

Fibre breaks damage patterns The damage patterns are presented in FIGURE 4.12. It can be highlighted that the model accurately captures the fibre breaks orientation in compression D_c^{nl} and in tension D_t^{nl}. Indeed, fibre breaks occur in all plies. Fibre breaks in compression are present for the top four plies. Concerning the fibre breaks in tension, it occurs first for the lowest plies. The loss of stiffness due to fibre breaks in tension emphasizes the local curvature with a midline shifting toward the top. Thus, the top plies are loaded in traction at the center which triggers the failure of fibres.

In FIGURE 4.13, two quantities have been plotted over the red line (segment AB). Three points can be relieved from the plot.

- The regularizing properties are straightforwardly observed as a smooth damage gradient profile is observed with a Gaussian shape;
- The overspreading pathology observed with non-local is highlighted here with a high damage width for the crack. In this study, it has been decided to choose the lowest allowable internal length in order to minimize the diffusion in the width considering the actual mesh size;
- Due to overspreading, the non-local damage variables cannot reach their maximum values. To illustrate this effect, the residual stiffness $1/S_{11}^{\text{eff}} = E_{11}^{\text{eff}}$ has been plotted in cyan. Although the stiffness is highly reduced, a residual value is observed, which allows the Gauss point to still sustain a part of the load and to prevent it from the total failure.

Macroscopic response To complete the analysis, the macroscopic behavior is presented in FIGURE 4.14 by comparing the experimental and the numerical responses. The load-displacement responses on the left show that the same path is followed for the two curves. However, at 5 mm, the numerical model does not reproduce the response observed experimentally.

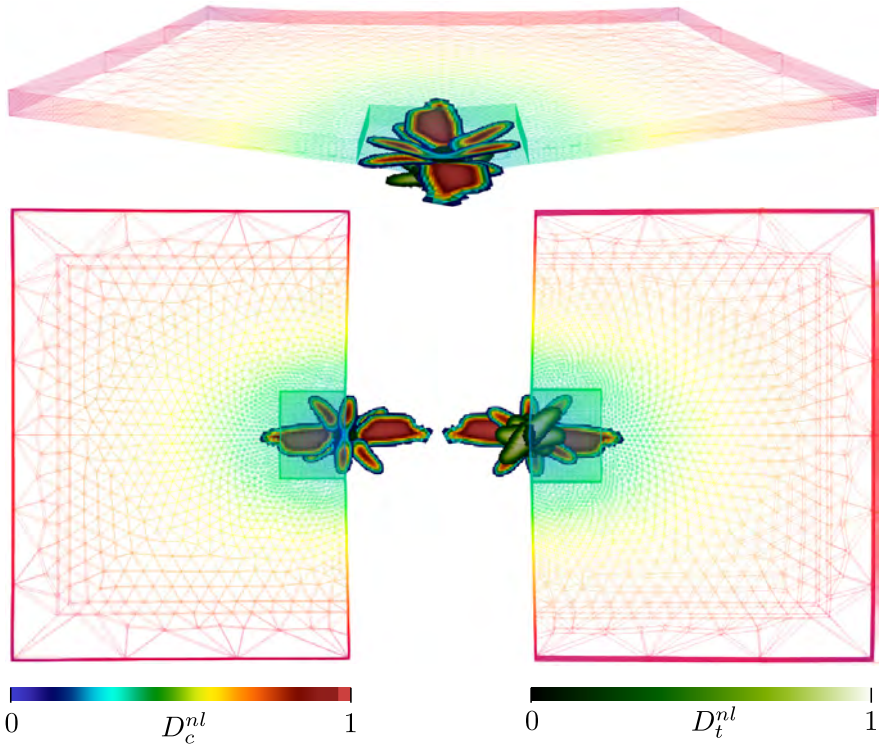

Figure 4.12: Simulation of a 35 J impact on the quasi-isotropic laminate Q16 highlighting the fibre breaks in compression and in tension using non-local damage

At 5 mm, the load drops observed on the experimental responses are induced by fibre breaks in tension (chapter 3). The current model captures the fibre breaks in tension, however, it does not reproduce the load drop observed in the experimental response. Indeed, due to the artificial residual stiffness, the load is still carried by the damaged Gauss point. The transition between damage and failure is not respected. The residual stiffness allows the Gauss point to bear the load. It explains the overestimation of the contact load. Another point to relieve is the energy dissipation, the experimental response dissipates 2.5× more energy than the simulated one.

To summarize, the non-local damage smooths the macroscopic response preventing "rough" behavior as load drops and oscillations.

If we look at the load-time response, it can be highlighted that the contact time duration predicted by the model is relatively lower than the experimental contact time. 2 main reasons can be brought. The first one is numerical, the contact time T depends on the stiffness of the sample as presented in Equation (4.48).

$$T = f\left(\sqrt{\frac{m}{k}}\right) \tag{4.48}$$

where m is the laminate sample mass in kg and k the stiffness of the laminate sample in N/m. In consequence, despite the damage effects on the laminate stiffness, the damage model for the fibre breaks overestimates the stiffness, leading to incorrect contact times. The second reason is due to the clearance introduced into the experimental setup which is not modeled in the actual impact FEM.

Based on the lack of non-local damage to model faithfully the fibre breaks (overspreading of the damaged surface), it has been decided to turn to another gradient

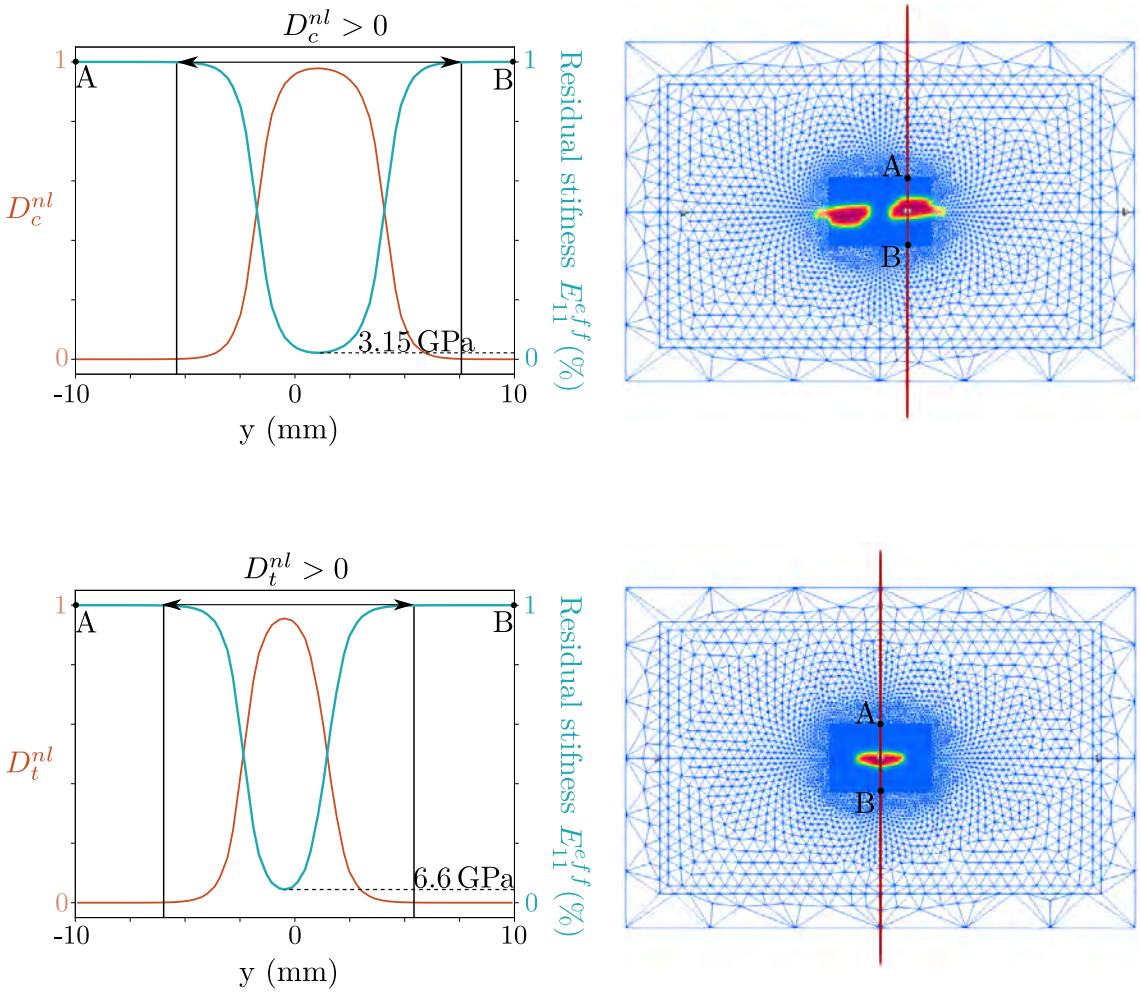

Figure 4.13: Non-local damage variables plotted over the segment [AB], and highlighting the residual stiffness E_{11}^{ff}

damage model, the phase-field.

4.2.1.2 Phase-field variational approach

As presented in the chapter 1, the phase-field approach belongs to the gradient damage family. A damage variable ϕ approximates the sharp crack topology encountered for a real crack. A spatial internal length ℓ controls the diffuse damage band of ϕ. The growing attractiveness of this method is linked to the notion of $\Gamma-$convergence which guarantees, for brittle materials, a convergence towards a discrete crack and towards Griffith's theory when the internal length tends towards 0. Thus, it has been decided to use this formulation.

Classical phase-field formulation The initial phase-field approach was developed for isotropic material [Bourdin et al., 2008]. Equation (4.49) details the weak form of the phase-field model:

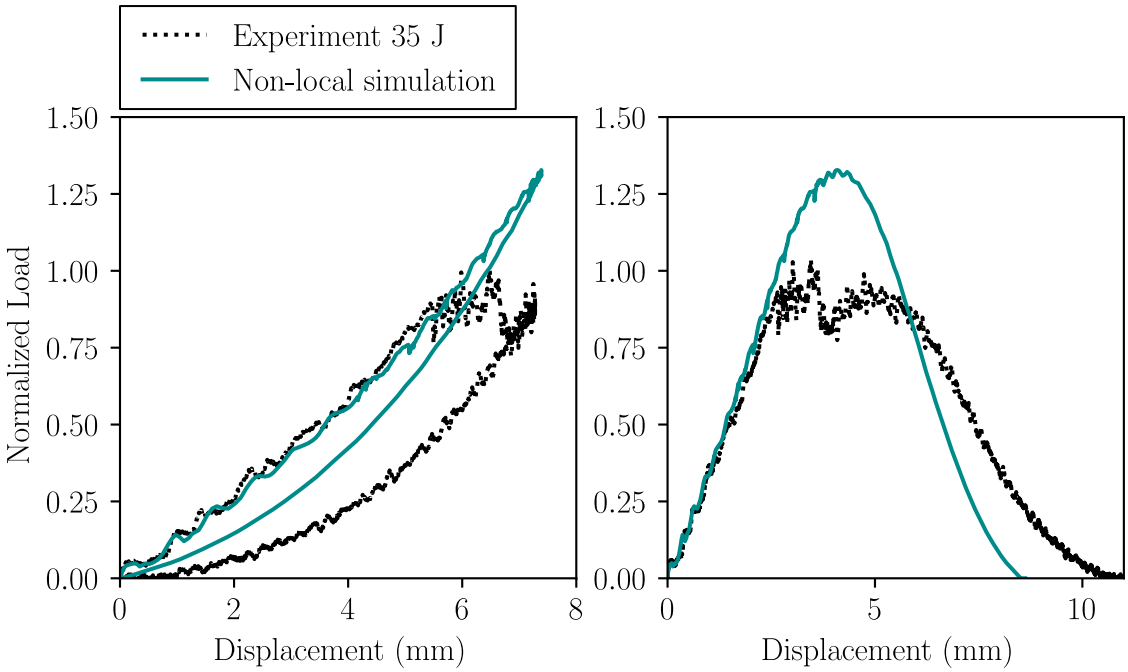

Figure 4.14: Comparison of the physical responses at a 35 J impact performed on a Q16 laminate

$$\mathfrak{E}(u,\phi) = \overbrace{\int_\Omega g(\phi)\psi_0(\varepsilon(u))\,\mathrm{d}V}^{\mathfrak{E}_{\text{bulk}}} + \overbrace{\int_\Omega G_c\gamma(\phi,\nabla\phi)\,\mathrm{d}V}^{\mathfrak{E}_{\text{frac}}} \tag{4.49}$$

$$\text{where } \mathfrak{E}_{bulk}(\varepsilon,\phi) = g(\phi)\Psi_{\text{elas}} = g(\phi)\frac{1}{2}(\sigma:\varepsilon) \tag{4.50}$$

$$\text{and } \mathfrak{E}_{frac}(\phi,\nabla\phi) = \begin{cases} G_c\frac{1}{2l}(\phi^2 + \ell^2\nabla\phi\nabla\phi) & \text{for AT2} \\ G_c\frac{3}{8l}(\phi + \ell^2\nabla\phi\nabla\phi) & \text{for AT1} \end{cases} \tag{4.51}$$

where $\mathfrak{E}_{bulk}(\varepsilon,\phi)$ is the degraded elastic energy density (Equation (4.50)). The elastic energy density Ψ_{elas} is multiplied by a degradation function $g(\phi)$. $\mathfrak{E}_{frac}(\phi,\nabla\phi)$ is the energy contribution due to the fracture (Equation (4.51)). For this classical formulation, two impediments can be highlighted.

Anisotropic formulation and damage effects The first impediment is how to handle anisotropy. Indeed, the classical formulation adopted in [Bourdin et al., 2008] takes the contribution of all directions to calculate the elastic energy density ($0.5 \cdot \sigma_{ij}\varepsilon_{ij}$). However, in our case, the fibre breaks occur in the longitudinal direction. Therefore, only the elastic energy density in direction 1 should be taken into account. Considering the work performed by [Bleyer and Alessi, 2018], the authors have introduced a damage-dependent elasticity tensor $\mathbb{C}$. As presented in Equation (4.52), $\mathbb{C}$ is calculated using the classical stiffness tensor $\mathbb{C}^0$ and a damage tensor $\mathbb{D}$ (Equation (4.53)). The damage tensor has a null value for all components, excluding the components where the effect of damage should be acting (longitudinal direction D_{11}, shear components D_{44} and D_{66}). From Equation (4.54),

the degraded elastic energy density $W_{bulk}(\varepsilon, \phi)$ is calculated.

$$\mathbb{C}(\phi) = \mathbb{D}(\phi) : \mathbb{C}^0 : \mathbb{D}(\phi) \tag{4.52}$$

$$\mathbb{D}(\phi) = \begin{pmatrix} (1-\phi) & 0 & \dots & \dots & \dots & 0 \\ 0 & \vdots & \vdots & \vdots & \vdots & \vdots \\ \vdots & \vdots & \vdots & \vdots & \vdots & \vdots \\ \vdots & \vdots & \vdots & \vdots & 0 & \vdots \\ \vdots & \vdots & \vdots & \vdots & (1-\phi) & 0 \\ 0 & \dots & \dots & \dots & 0 & (1-\phi) \end{pmatrix} \tag{4.53}$$

$$\mathbb{C}(\phi) = \begin{pmatrix} (1-\phi)^2 C_{11}^0 & 0 & \dots & \dots & \dots & 0 \\ 0 & \vdots & \vdots & \vdots & \vdots & \vdots \\ \vdots & \vdots & \vdots & \vdots & \vdots & \vdots \\ \vdots & \vdots & \vdots & \vdots & 0 & \vdots \\ \vdots & \vdots & \vdots & \vdots & (1-\phi)^2 C_{55}^0 & 0 \\ 0 & \dots & \dots & \dots & 0 & (1-\phi)^2 C_{66}^0 \end{pmatrix} \tag{4.54}$$

$$\mathfrak{E}_{bulk}(\varepsilon, \phi) = g(\phi)\frac{1}{2}\varepsilon^t \mathbb{C}(\phi)\varepsilon = (1-\phi)^2 \frac{1}{2}(\sigma_{11}\varepsilon_{11} + 2\sigma_{12}\varepsilon_{12} + 2\sigma_{13}\varepsilon_{13}) \tag{4.55}$$

The drawback of such formulation is the introduction of the energy density due to the shear contribution to calculate the bulk energy density. It implies that fibre breaks could occur if the ply is sufficiently loaded in shear, which is not relevant. Thus, it has been decided to remove the shear contributions for the calculation of the bulk energy density $\mathfrak{E}_{bulk}(\varepsilon, \phi)$ (as reported in Equation (4.56)). Nevertheless, the damage effects remains activated on shear components as once fibre breaks occur, shear loads are no more sustained.

$$\mathfrak{E}_{bulk}(\varepsilon, \phi) = \frac{(1-\phi)^2}{2}(\sigma_{11}\varepsilon_{11} + 2\sigma_{12}\varepsilon_{12} + 2\sigma_{13}\varepsilon_{13}) \tag{4.56}$$

Introduction of a damage threshold

AT1 threshold The second impediment is due to the damage threshold control. Contrary to AT2 formulation, AT1 formulation introduces a hidden damage threshold. The link between ℓ, G_c and σ_c is often studied through an homogeneous analysis of the phase-field model as it provides an analytic solution. Indeed, for a homogeneous solution of a 1D problem (ϕ is uniform), the gradient of the damage

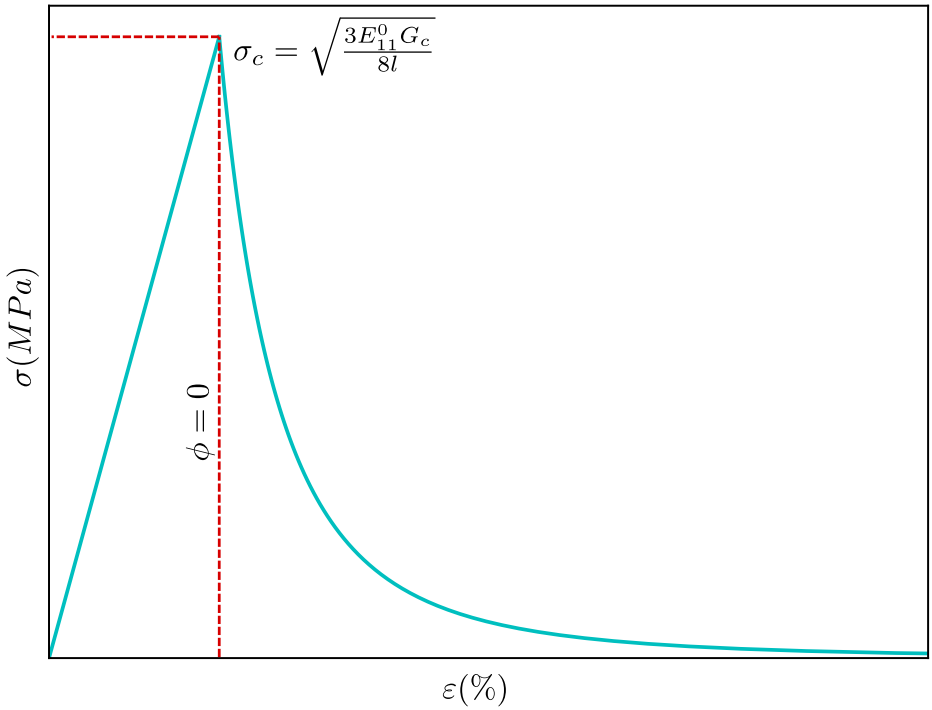

Figure 4.15: Local stress-strain response using AT1 formulation for the fibre breaks in tension

variable $\nabla\phi$ used in $W_{frac}(\phi, \nabla\phi)$ is null. Thus, it is possible to link the maximum stress σ_c with the energy release rate G_c and the internal length ℓ. In FIGURE 4.15, the stress-strain response is presented for a 1D homogeneous solution. It highlights an elastic stage where no softening occurs until σ_c is reached. In 3D, the link is written as $\boldsymbol{\varepsilon} : C^0 : \boldsymbol{\varepsilon} = \dfrac{3G_c}{8\ell}$.

Energetic threshold Based on the work performed in [Miehe et al., 2015, Quintanas-Corominas et al., 2019], the authors have introduced an explicit stress threshold for each damage mechanism. In [Miehe et al., 2015], the authors have considered a new fracture energy density $\mathfrak{E}_{frac}(\phi, \nabla\phi)$ presented in EQUATION (4.57).

$$\mathfrak{E}_{frac}(\phi, \nabla\phi) = 2\Psi^0 \left[\phi + \frac{\ell^2}{2}\nabla\phi\nabla\phi\right] \tag{4.57}$$

Where Ψ^0 is the fracture onset energy density (J/mm^3), this formulation does not use the fracture toughness G_c (J/mm^2). In EQUATION (4.58), the total energy density $\mathfrak{E}_{\text{tot}}(\varepsilon, (\phi, \nabla\phi))$ has been written considering the new fracture energy density. However, by introducing the term $(1-\phi)^2\Psi^0$ and reshaping EQUATION (4.59). The threshold is explicitly shown in EQUATION (4.60). A Macaulay bracket has been

introduced in order to avoid negative value when $\Psi_{\text{elas}} < \Psi^0$.

$$\mathfrak{E}_{\text{tot}}(\varepsilon,(\phi,\nabla\phi)) = (1-\phi)^2\Psi_{\text{elas}} + 2\Psi^0\left[\phi + \frac{\ell^2}{2}\nabla\phi\nabla\phi\right] \tag{4.58}$$

$$\mathfrak{E}_{\text{tot}}(\varepsilon,(\phi,\nabla\phi)) = (1-\phi)^2\Psi_{\text{elas}} + (1-\phi)^2\Psi^0 - (1-\phi)^2\Psi^0 + 2\Psi^0\left[\phi + \frac{\ell^2}{2}\nabla\phi\nabla\phi\right] \tag{4.59}$$

$$\mathfrak{E}_{\text{tot}}(\varepsilon,(\phi,\nabla\phi)) = (1-\phi)^2\overbrace{\langle\Psi_{\text{elas}} - \Psi^0\rangle_+}^{\text{Threshold}} + \Psi^0 + \Psi^0(\phi^2 + \ell^2\nabla\phi\nabla\phi) \tag{4.60}$$

Comparison between AT1 and MIEHE formulation A correspondence can be made between Ψ^0 and G_c by comparing the two facture energy densities for AT1 and MIEHE.

$$\begin{cases} \mathfrak{E}_{frac}(\phi,\nabla\phi) = G_c\dfrac{3}{8\ell_{\text{AT1}}}(\phi + \ell^2\nabla\phi\nabla\phi) & \text{for AT1} \\ \mathfrak{E}_{frac}(\phi,\nabla\phi) = 2\Psi^0\left(\phi + \dfrac{\ell_M^2}{2}\nabla\phi\nabla\phi\right) & \text{for MIEHE} \end{cases} \tag{4.61}$$

$$\text{if } \ell_{\text{AT1}} = \frac{\ell_M}{\sqrt{2}} \Rightarrow \Psi_0 = G_c\frac{3}{16\ell} \tag{4.62}$$

Contrary to AT1, MIEHE formulation introduces explicitly the threshold as highlighted in red in Equation (4.60), when $\Psi_{\text{elas}} < \Psi^0$, $\phi = 0$.

Phase-field formulation considering anisotropy and damage threshold The phase-field formulation implemented in OPFM for the fibre breaks modeling combines the MIEHE and the anisotropic formulations. The total energy is expressed in Equation (4.64)

$$\mathfrak{E}_{\text{tot}}(\varepsilon,(\phi,\nabla\phi)) = \mathfrak{E}_{bulk}(\varepsilon,\phi) + \mathfrak{E}_{frac}(\phi,\nabla\phi) \tag{4.63}$$

$$\begin{aligned} \mathfrak{E}_{\text{tot}}(\varepsilon,(\phi,\nabla\phi)) = {} & \frac{1}{2}\langle\boldsymbol{\varepsilon}^t : \mathbb{C}(\phi,\nabla\phi) : \boldsymbol{\varepsilon} - \boldsymbol{\varepsilon}_0^t : \mathbb{C}(\phi,\nabla\phi) : \boldsymbol{\varepsilon}_0\rangle_+ \\ & + \Psi^0 + \Psi^0(\phi^2 + \ell^2\nabla\phi\nabla\phi) \end{aligned} \tag{4.64}$$

$$\boldsymbol{\varepsilon}_0^t = \begin{pmatrix} \varepsilon_{11}^R & 0 & 0 & 0 & 0 & 0 \end{pmatrix}$$

Six more parameters are required to identify the phase-field model. These parameters are presented in Table 4.4. All of these parameters have not been identified experimentally since CC/CT samples were not available. The values have been obtained using several simulations which provide the results close to the impact results.

4.2.1.3 Comparison of the phase-field and the non-local approaches

The two damage gradient formulations have been compared on a numerical test case. A FEA of a classical three-point flexural test has been performed. A laminate of four plies $[0/90_2/0]$ is meshed using C3D8 elements. The element size is $0.25 \times 0.5 \times 0.25$ mm for the respective directions (1,2,3). The same internal length is considered for the two models with a value equal to the element size in the direction

Fibre damage parameters	Numerical	Material
Tensile failure strain in fibre direction, ε^R_{11t}	✗	✓
Compressive failure strain in fibre direction, ε^R_{11c}	✗	✓
Energy density threshold in compression, Ψ^0_c	✗	✓
Energy density threshold in tension, Ψ^0_t	✗	✓
Internal length in compression, ℓ_c	✗	✓
Internal length in tension, ℓ_t	✗	✓

Table 4.4: Parameters required for the phase-field in OPFM

1 ($\ell = 0.25\,\text{mm}$). FIGURE 4.16 presents the FEA configuration. The composite plate is clamped over two lines where the right segment allows for displacement along direction 1. A 3 mm imposed displacement is applied on a line located at the center of the plate on the upper face. The two damage variables and the residual longitudinal stiffness have been plotted on the segment [AB] for $u_2 = 3\,\text{mm}$. This segment is placed on the rear face where fibre breaks in tension have occurred. The phase-field method's curves are plotted in solid lines, whereas the non-local model's results are plotted in dotted lines. At first glance, although the damage shapes are similar, the phase-field method has a more localized damage shape. This fact is also observed when the variables are plotted over [AB], the trend followed by the two curves are similar. However, it can be noticed that the phase-field variable reached its maximum value ensuring a quasi-null value of the residual stiffness E^{eff}_{11}. This is not the case for the non-local damage where a residual stiffness is maintained (5 GPa).

The global responses of the plate have been plotted in FIGURE 4.17. The load-displacement curves are compared for the two models. The responses describe an elastic stage with no fibre damage. It can be noticed that the failure starts earlier for the non-local damage with a lower softening. The phase-field exhibits a brittle failure with a high load drop, whereas for the non-local approach the softening is smoothed. This phenomenon is explained by the residual stiffness allowed by the non-local model, the damaged Gauss points are still sustaining load. In consequence, the slope obtained using non-local damage is stiffer than that obtained with phase-field modeling. Using an improved non-local method with an evolving internal length for instance [Geers et al., 1998] or another non-local formulation [Desmorat et al., 2015] would avoid the actual limitation.

4.2.1.4 Finite element implementation and algorithmic resolutions of the phase-field model

Local equations Before introducing the finite element discretization and the algorithm 's resolution, the mechanical and damage gradient equations in their strong forms are reminded in EQUATION (4.65). The equations satisfy the boundary con-

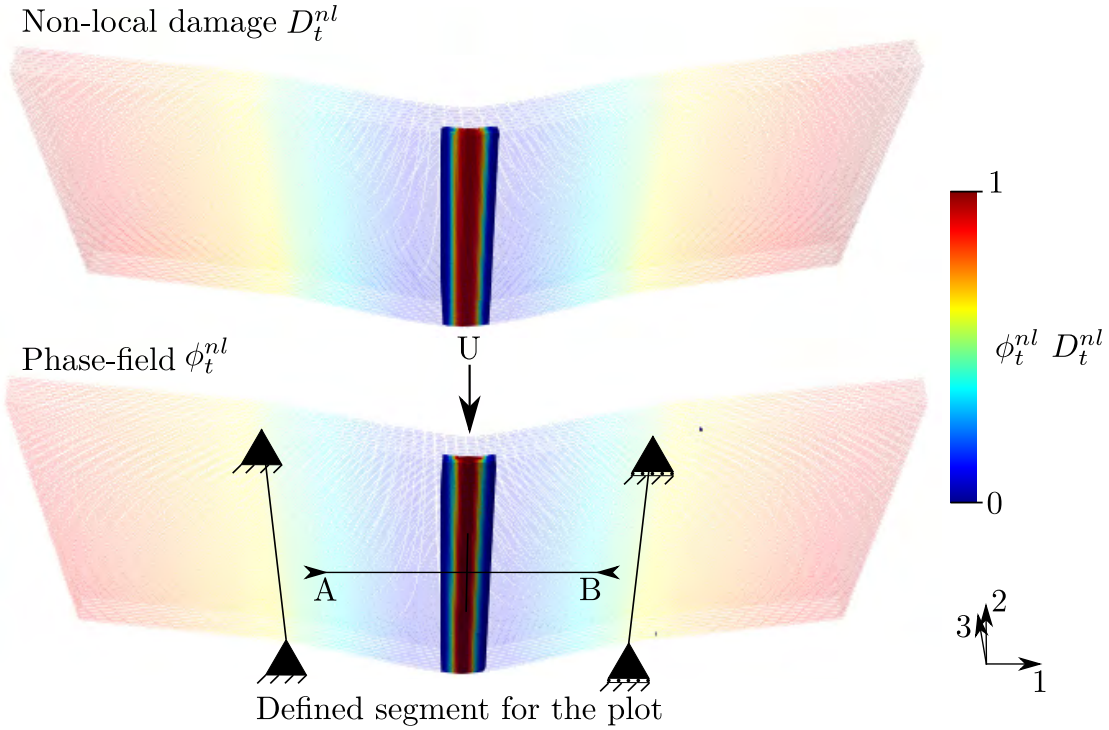

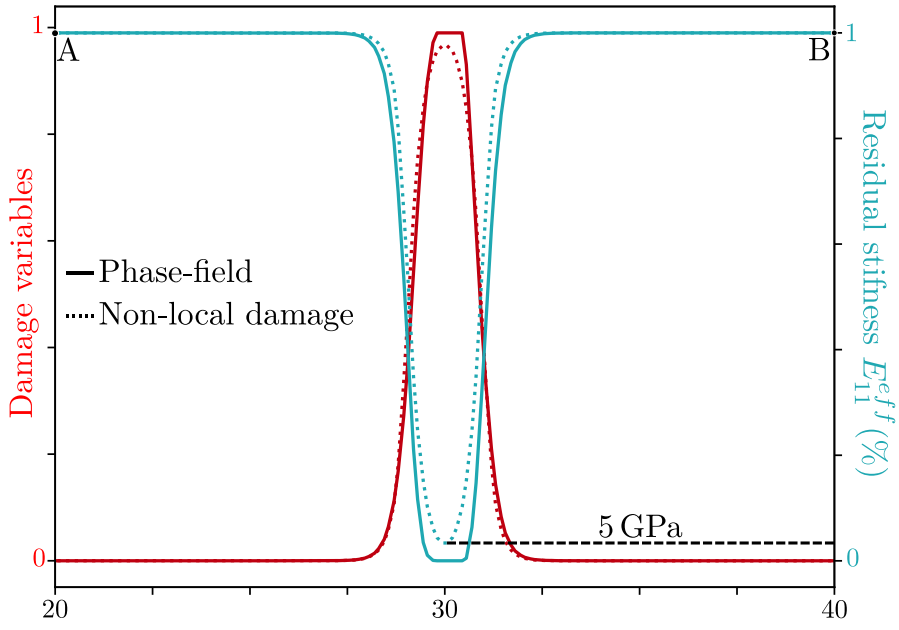

Figure 4.16: Comparison of the failure in tension using non-local damage and phase-field

ditions as reported in EQUATION (4.66).

$$\begin{cases} \mathbf{div}(\boldsymbol{\sigma}) + \mathbf{f} = \rho\boldsymbol{\gamma} \ \text{ on } \ \Omega \\ -\dfrac{\partial \Psi_{\text{tot}}}{\partial \phi} = 2\Psi_0(\phi - \ell^2\nabla^2\phi) \ \text{ on } \ \Omega \end{cases} \tag{4.65}$$

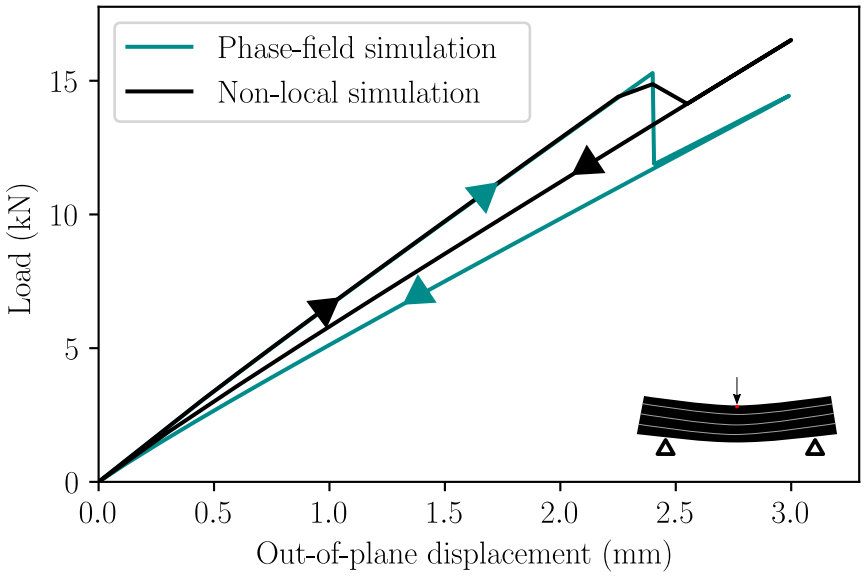

Figure 4.17: Load-displacement responses of the laminate under three-point flexural loading for the two fibre breaks damage models

$$\begin{cases} \boldsymbol{\sigma}\mathbf{n} = \mathbf{t} \ \text{ on } \partial\Omega_{\mathrm{t}} \\ u = u_d \ \text{ on } \partial\Omega_{\mathrm{d}} \\ \boldsymbol{\nabla}\phi \cdot \mathbf{n} = 0 \ \text{ on } \partial\Omega \end{cases} \tag{4.66}$$

Variational formulations The variational formulations are presented in Equation (4.67) for the mechanical and the phase-field problems. The Equation (4.67) is valid for all fields (u, ϕ) satisfying Equation (4.66).

$$\begin{cases} \int_\Omega \boldsymbol{\sigma} : \nabla^s \delta u \ \mathrm{dV} + \int_\Omega \rho \ddot{\boldsymbol{u}} \cdot \delta u \ \mathrm{dV} = \int_\Omega \boldsymbol{f} \delta u \ \mathrm{dV} + \int_{\partial\Omega} \boldsymbol{T} \delta u \ \mathrm{dS} \\ \int_\Omega \frac{\partial \Psi_{\mathrm{tot}}}{\partial \phi} + 2\Psi_0(\phi - \ell^2 \nabla^2 \phi)\delta\phi \ \mathrm{dV} = -2\Psi_0 \int_{\partial\Omega} \nabla\phi \cdot \boldsymbol{n} \delta\phi \ \mathrm{dS} \end{cases} \tag{4.67}$$

Finite element discretization From the variational formulations, the finite element discretization is derived for the displacement and the phase-field damage variables in Equations (4.68) to (4.71). u and ϕ are interpolated using the same order ($\mathcal{C}^1$).

$$u(x) = \sum_I N_I(x) u_I \tag{4.68}$$

$$\frac{\partial u(x)}{\partial x} = \sum_I \frac{\partial N_I(x)}{\partial x} u_I = B_I(x) u_I \tag{4.69}$$

$$\phi(x) = \sum_I N_I(x) \phi_I \tag{4.70}$$

$$\frac{\partial \phi(x)}{\partial x} = \sum_I \frac{\partial N_I(x)}{\partial x} \phi_I = B_I(x) \phi_I \tag{4.71}$$

Expression of the residuals and tangent matrix The expression of the residual and the tangent matrix are performed using the discretization of the variational

principle weak form. The classical displacement residual is presented in EQUATION (4.72) and the phase-field residual is presented in EQUATION (4.73)

$$r^u = \overbrace{\int_\Omega \boldsymbol{f}\boldsymbol{N}\ \mathrm{dV} + \int_{\partial\Omega} \boldsymbol{T}\boldsymbol{N}\ \mathrm{dS}}^{f^{\mathrm{ext}}} - \overbrace{\int_\Omega \left(\boldsymbol{B}^{\boldsymbol{T}}\boldsymbol{\sigma} + \boldsymbol{N}^{\boldsymbol{T}}\rho\boldsymbol{N}\ddot{u}_I\right)\mathrm{dV}}^{f^{\mathrm{int}}} \tag{4.72}$$

$$r^\phi = \int_\Omega \frac{\boldsymbol{\partial}\boldsymbol{\Psi}_{\mathrm{tot}}}{\boldsymbol{\partial}\boldsymbol{\phi}}\boldsymbol{N_I} + 2\Psi_0(\boldsymbol{N_I}\boldsymbol{N_J} + \ell^2\boldsymbol{B_I}\boldsymbol{B_J})\boldsymbol{\phi_i}\,\mathrm{dV} \tag{4.73}$$

There are two ways to proceed with the resolution of the two problems.

The first one is based on a monolithic resolution of the two problems ([Germain, 2006]). A simultaneous resolution of the two fields (u, ϕ) is performed using a Newton-Raphson solver. It requires defining the tangent matrix with the calculation of the coupling operators $(K^{u\phi},\ K^{\phi u})$. In [Médeau, 2019], the authors have highlighted numerical convergence issues with the Newton-Raphson algorithm.

Thus, the authors have decided to choose another approach, the alternate resolution. The two problems are uncoupled and resolved alternately. It implies that the coupled operators $(K^{u\phi},\ K^{\phi u})$ of the tangent matrix are neglected (EQUATION (4.74)). The mechanical residual is calculated first using EQUATION (4.75) with fixed values of ϕ_I. Then, the residual of the phase-field problem is computed using EQUATION (4.76) with fixed values of u_I.

$$\begin{Bmatrix} r^u \\ r^\phi \end{Bmatrix} = \begin{bmatrix} K^{uu} & \cancel{K^{u\phi}} \\ \cancel{K^{\phi u}} & K^{\phi\phi} \end{bmatrix} \begin{Bmatrix} \delta u_I \\ \delta\phi_I \end{Bmatrix} \text{ with } K^{\phi u} = K^{u\phi} = 0 \tag{4.74}$$

$$K^{uu} = \int_\Omega B_I^T \frac{\partial\sigma}{\partial\varepsilon} B_J\ \mathrm{dV} \text{ considering constant } \boldsymbol{\phi}_{\mathrm{I}} \tag{4.75}$$

$$K^{\phi\phi} = \int_\Omega \frac{\partial^2\Psi_{\mathrm{tot}}}{\partial\phi^2} N_I N_J + 2\Psi_0(N_I N_J + \ell^2 B_I B_J)\,\mathrm{d}V \text{ considering constant } \boldsymbol{u_I} \tag{4.76}$$

Alternate algorithm architecture As the two problems are solved in a decoupled way, the convergence is more robust. However, it is intrusive to build such architecture. In our case, a coupling performed by Python module in Z-set has been developed to transfer the different fields $(\Psi_{\mathrm{tot}}; [\phi_c,\ \phi_t])$ for each alternate iteration. Indeed, as illustrated in FIGURE 4.18, when the increment $t \to t + \Delta t$ has started, the phase-field damage variables $(\phi_c,\ \phi_t)$ are sent to the mechanical problem. Once received, the mechanical problem is solved at time $t + \Delta t$. When equilibrium is obtained for the mechanical problem (the equilibrium resolution is a highly nonlinear problem), the elastic potential is sent to the phase-field problem to update the new couples $(\phi_c,\ \phi_t)$. Once the fields $(\phi_c,\ \phi_t)$ are calculated, a stagnation criterion is verified according to EQUATION (4.77). This stagnation criterion compares for each Gauss point the damage variable variations between two iterations. If the variation of a Gauss point has exceeded ϵ, the increment is considered as not converged and an additional iteration is performed until the stagnation criterion is fulfilled.

$$\begin{cases} \|{\phi_c}^i - {\phi_c}^{i-1}\|_\infty \leq \epsilon \\ \|{\phi_t}^i - {\phi_t}^{i-1}\|_\infty \leq \epsilon \end{cases} \tag{4.77}$$

A maximum number of iterations is defined by the user, if exceeded, a cutback of the time increment Δt is performed.

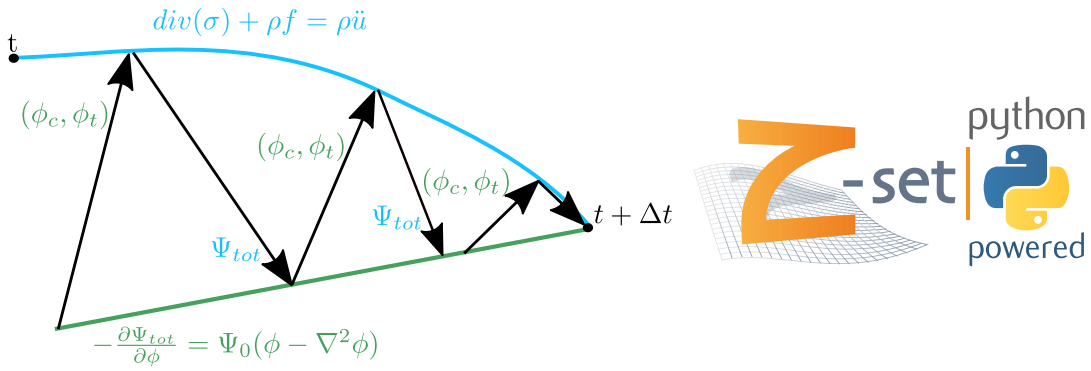

Figure 4.18: Illustration of the exchange fields between the mechanical and the phase-field problems

4.2.2 Cohesive law reinforcement for combined shear and compressive out-of-plane loading

4.2.2.1 Literature review

As observed in the CT-scans (FIGURE 4.19), there is no damage below the impact zone. Experimental evidence have been brought in the literature on the interlaminar shear strength reinforcement in the presence of compressive out-of-plane stress σ_{33} [Cui et al., 1994, Catalanotti et al., 2017].

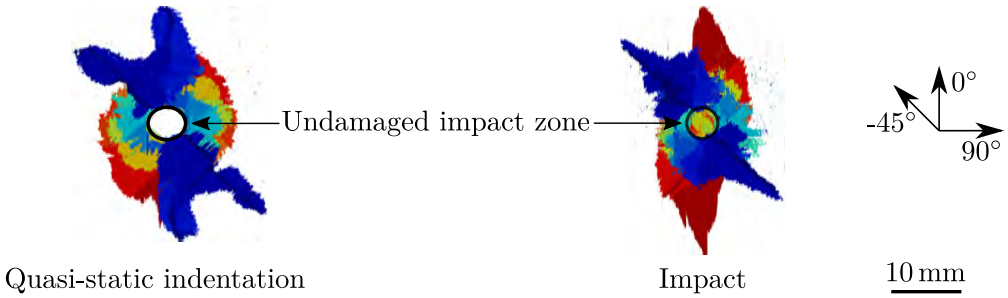

Figure 4.19: Projected damaged area obtained from the X-ray segmentation for a QSI and 20 J impact tests

Numerically, this behavior has been reproduced in cohesive zone modeling. Indeed, in [Li et al., 2008], three different shapes of traction-separation laws have been presented. These laws show a dependence of the interfacial parameters (onset and fracture toughness) as a function of $\langle\sigma_{33}\rangle_-$ using a material parameter η_f. EQUATION (4.78) presents one of the three models.

$$\begin{cases} \sigma_c^{\text{enh}} = \sigma_c \left(1 - \eta_f \dfrac{\langle\sigma_{33}\rangle_-}{\sigma_c}\right) \\ G_{\text{IIc}}^{\text{enh}} = G_{\text{IIc}} \left(1 - \eta_f \dfrac{\langle\sigma_{33}\rangle_-}{\sigma_c}\right)^2 \end{cases} \tag{4.78}$$

Where the couples $(\sigma_c^{\text{enh}}, G_{\text{IIc}}^{\text{enh}})$ are the new reinforced interfacial parameters for delamination in mode II, η_f being an adimensional friction coefficient, introducing a

dependence on the compressive out-of-plane stress σ_{33}. This formulation is interesting as it performs an homothety of the initial traction-separation law. Therefore, the slope is unchanged once the softening is initiated, avoiding numerical issues. In [Catalanotti et al., 2017], a similar formulation presented in [Li et al., 2008] has been used. A dependence on $\langle\sigma_{33}\rangle_-$ using a material parameter was introduced to calculate the enhanced interface toughness in mode II ($G_{\text{IIc}}^{\text{enh}}$). The frameworks presented above show ease in implementing the reinforcement of the cohesive law parameters in mode II. Thus, it has been decided to implement this framework in the cohesive law.

4.2.2.2 Introduction of the reinforcement

A similar formulation presented in ([Li et al., 2008]) has been adopted in the current cohesive zone model. The enhancement of the interfacial properties in mode II is presented in FIGURE 4.20. Before the reinforcement, the traction-separation law is shown in blue. The higher the material parameter μ, the higher the couple (σ_c^{enh}, G_{IIc}^{enh}). On the contrary to the formulation introduced in EQUATION (4.78), σ_{33} is not divided by σ_c. The difficulty of identifying μ experimentally leads to perform numerous simulations with different values of μ. The criterion to select the correct value of μ was based on capturing the correct undamaged zone below the impact.

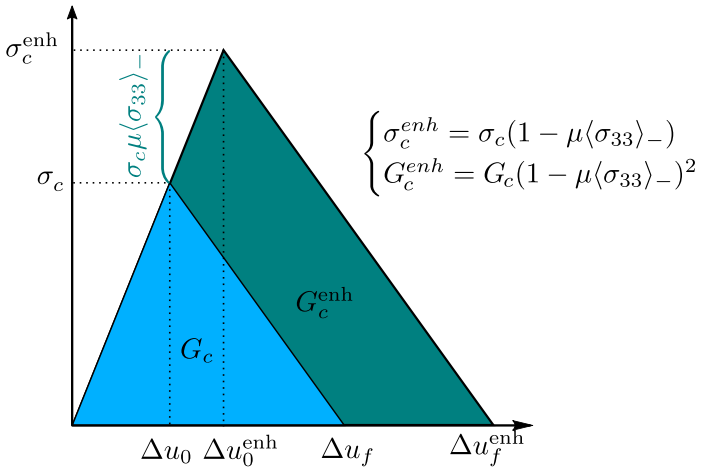

Figure 4.20: Illustration of the effect of the reinforcement equations on the cohesive interfacial properties in mode II

FIGURE 4.21 compares the evolution of the shear onset stress criterion with and without the reinforcement. It can be observed that both criteria are the same for positive values of σ_{33}. However, once $\sigma_{33} < 0$, σ_{shear} starts to increase as expected.

4.2.3 Introduction of the damage coupling

As highlighted in Chapters 2 and 3, a strong interaction between all damage mechanisms is observed for this material. The current OPFM does not provide any interaction between the different damages. Indeed, it was first assumed that the loading transfer induced by fibre breaks or matrix cracking would trigger the delamination.

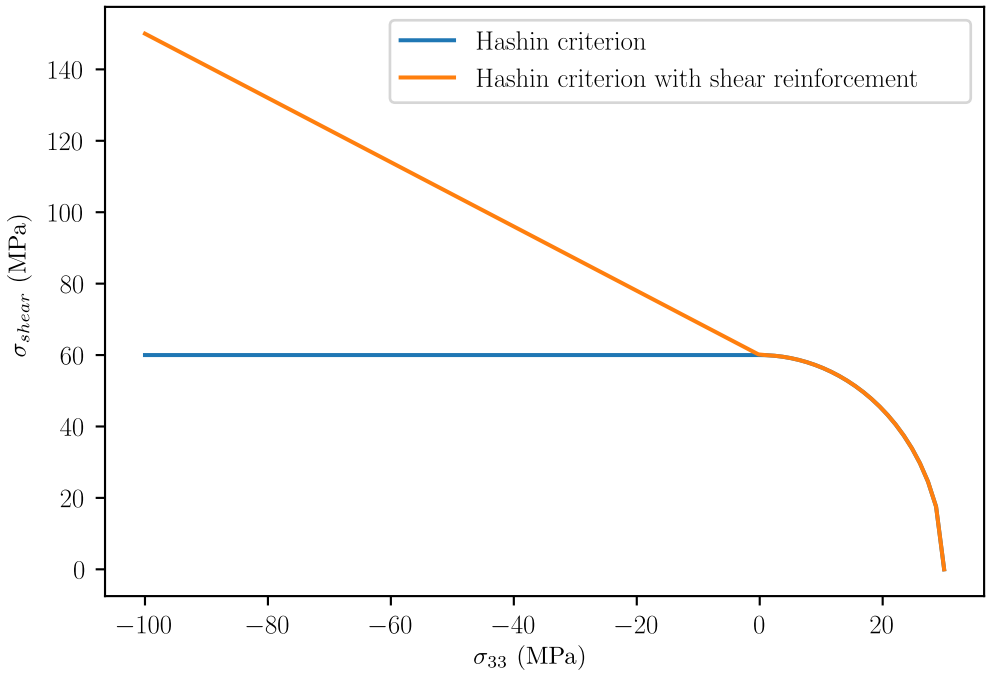

Figure 4.21: Hashin criterion plotted with and without the shear/compression reinforcement

4.2.3.1 Influence of the matrix cracking modeling on the damage interaction

The two damage models (DPM and OPFM) have been first compared on a 20 J impact on quasi-isotropic laminate. In this study, only the matrix cracking and the delamination have been modeled. The viscoelastic and nonlinear elasticity have been deactivated to minimize the differences between the two models. The main difference is based on the matrix cracking modeling as DPM uses discrete damage modeling instead of CDM for OPFM. The matrix damage and the delamination have been compared for the two models. The two damage patterns are compared at 4 ms where almost all the kinetic energy has been converted onto the internal plate's energy. Figure 4.22 presents the experimental response at 20 J and the responses obtained by DPM and OPFM. First-of-all, it can be shown that the two numerical responses are overlapped with the same maximum load and contact time. Besides, it shows that the delamination and the matrix cracking are not responsible for load drops or oscillations. As the fibre break is not modeled, the normalized load is overestimated. The predicted contact time is shorter than the experimental contact times. Two reasons explain the difference. The first one is the experimental setup's mechanical clearances, which are not considered in the simulation as modified boundary conditions. The second reason is the dependence of the contact time on the laminate stiffness. As fibre breaks in tension occur at this impact energy. It induces a drop in the laminate stiffness.

In Figure 4.23, the matrix cracking and delamination patterns have been compared for the two damage models at 4 ms. It can be shown that the delamination show very similar patterns between the two models. Indeed, the same interface

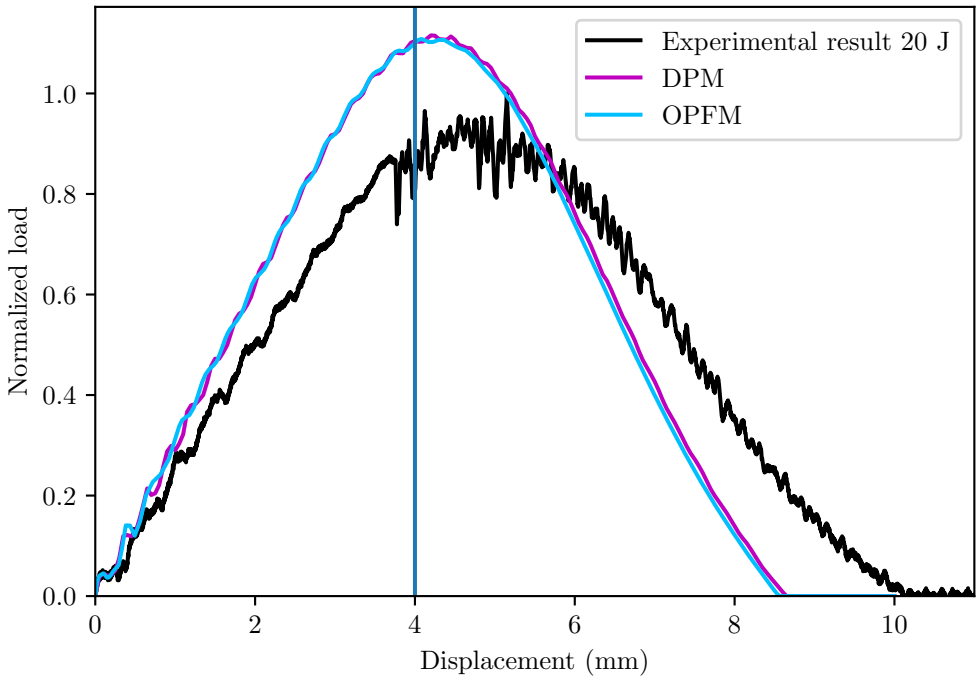

Figure 4.22: Numerical and experimental load-time responses for the Q16 laminate impacted at 20 J. Both models consider only matrix cracking and delamination

parameters have been used with similar stress and energy criteria. Nevertheless, it should be highlighted that the last interface (red) is damaged in DPM model, whereas there is no damage in OPFM model. Indeed, as matrix splitting cracks occur on the rear face, it triggers the delamination of the lowest interface due to the discrete representation of matrix cracking. This point must be introduced in OPFM to improve the accuracy of the model. The delamination of the lowest interface is not captured with a continuum damage framework used in OPFM. The two models capture important matrix cracking for the lower interfaces. It is due to critical transverse positive stresses due to bending. The DPM captures more matrix damages near the impacted surface. In any case, similar results are obtained between the two damage models despite the two different modeling strategies for matrix cracking.

4.2.3.2 Interactions between all the mechanisms, influence of the fibre breaks on the total damage scenario

Figure 4.24 compares the two responses with the experimental response by introducing the fiber breaks in the two models. It can be highlighted that DPM captures accurately the load drop. OPFM captures the fibre breaks later with a higher load drop. The fibre breaks modeling allows accurate prediction of the maximum load. The two responses follow the same unloading stage. Although the fibre breaks modeling increased the predicted contact time, the contact time is still underestimated due to the mechanical clearances in the experimental setup.

The delamination and matrix cracking patterns have been compared at two different times (2 ms and 4 ms) to evaluate the differences between the two damage models (Figure 4.25).

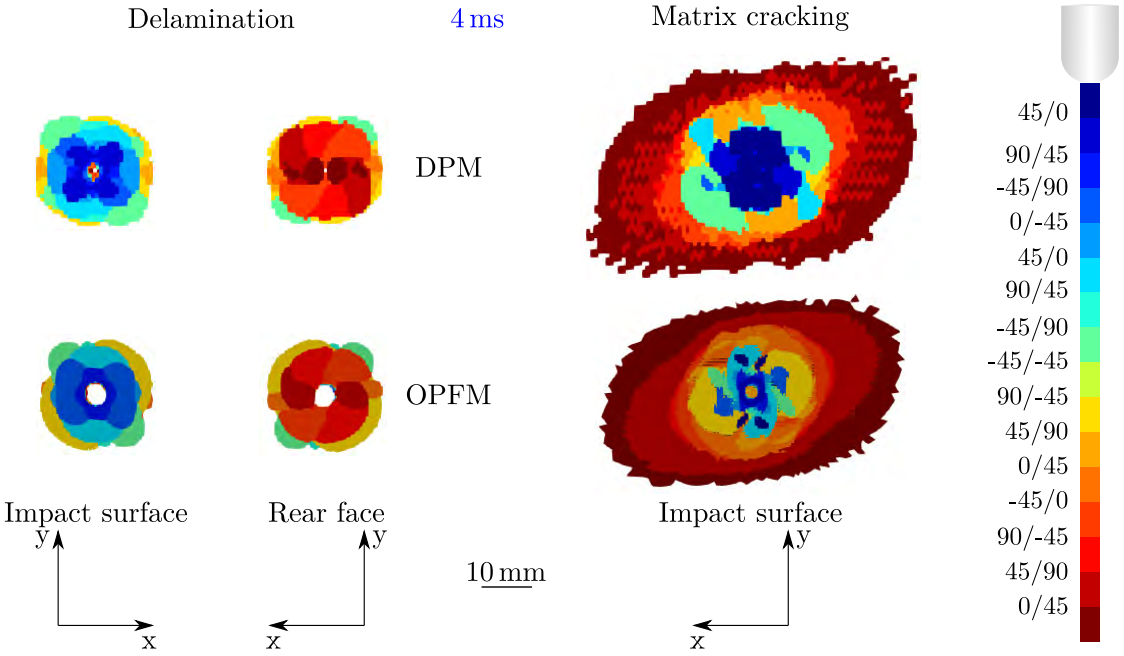

Figure 4.23: Delamination and matrix cracking patterns captured at 4 ms for the Q16 laminate impacted at 20 J. Both models consider only matrix cracking and delamination modeling

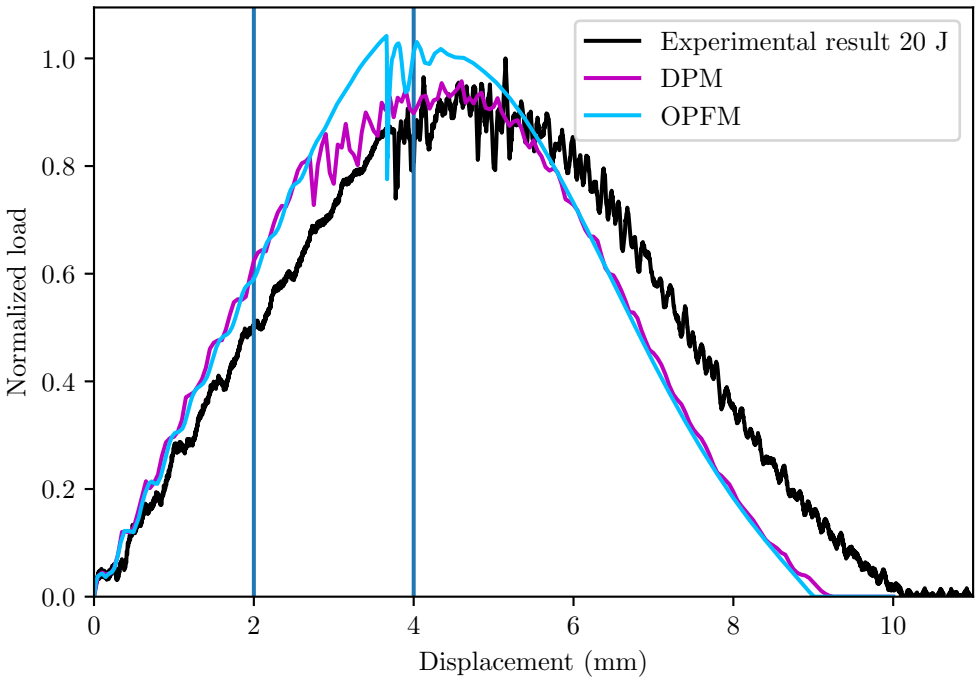

Figure 4.24: Numerical and experimental load-time responses for the 20 J impact test and considering all damage mechanisms

- **2 ms**. The delamination is similar on the rear face for both models. However, there is a difference for the impacted surface. The empirical coupling introduced in DPM between the fibre breaks and delamination is responsible for this difference. Indeed, the fibre breaks have occurred near the impacted surface and the delamination is therefore triggered due to the coupling. Concerning the matrix cracking pattern, the same conclusion presented just before can be dressed;

- **4 ms**. The similarities observed at 2 ms are no more observed for the delamination. The fibre breaks in compression have occurred on the impacted surface for both models. Interestingly, with OPFM, the load transfer is insufficient to capture the delamination where fibre breaks have occurred. Using DPM, the delamination follows the fibre breaks in the compression path due to the empirical coupling.

  On the rear face, the delamination of the lowest interface is captured by DPM, whereas it is still not captured by OPFM. Experimentally, the delamination of the lowest interface is explained by the fibre breaks in tension in the upper ply, pushing the matrix splitting on the lower ply to open. The splittings trigger the delamination of the lowest interface. The splitting is naturally captured by discrete damage modeling. In OPFM, the continuum damage framework does not reproduce the splitting aperture, which prevents delamination from initiating and propagating within the lowest interface. Concerning the matrix cracking, DPM shows more damage near the impacted surface. However, experimentally, the matrix cracking is mainly observed for the interfaces located at mid-thickness or those close to the rear.

To summarize, by comparing the two models, it highlights the requirement of damage couplings to perform sound simulations of impact on laminated composites. These interactions between the damages is intensified when fibre breaks occur. Therefore, a damage interaction has been introduced for the fibre break → delamination and the matrix cracking → delamination in OPFM.

4.2.3.3 Development and introduction of an intraply → interply damage coupling

The degradation of the cohesive law as a function of the state of the volume Gauss point (damaged or undamaged) will be presented first. Then, the connectivity between the volume-interface Gauss points and the information exchanges will be discussed.

Geometric establishment of the coupling FIGURE 4.26 presents the geometric information exchange between the Gauss points in the solid elements and the interfaces Gauss points. Each interface element has four Gauss points. Each interface Gauss point has two adjacent volume Gauss points. The interface Gauss point receives the damage state of the two adjacent volume Gauss points (top and bottom) as presented in EQUATION (4.80). The transferred fields are the two fibre damage variables (ϕ_c, ϕ_t) and a bounded variable for the matrix damage D_{mat} defined hereafter. Then, the maximum damage values is taken between the top and the bottom volume Gauss points.

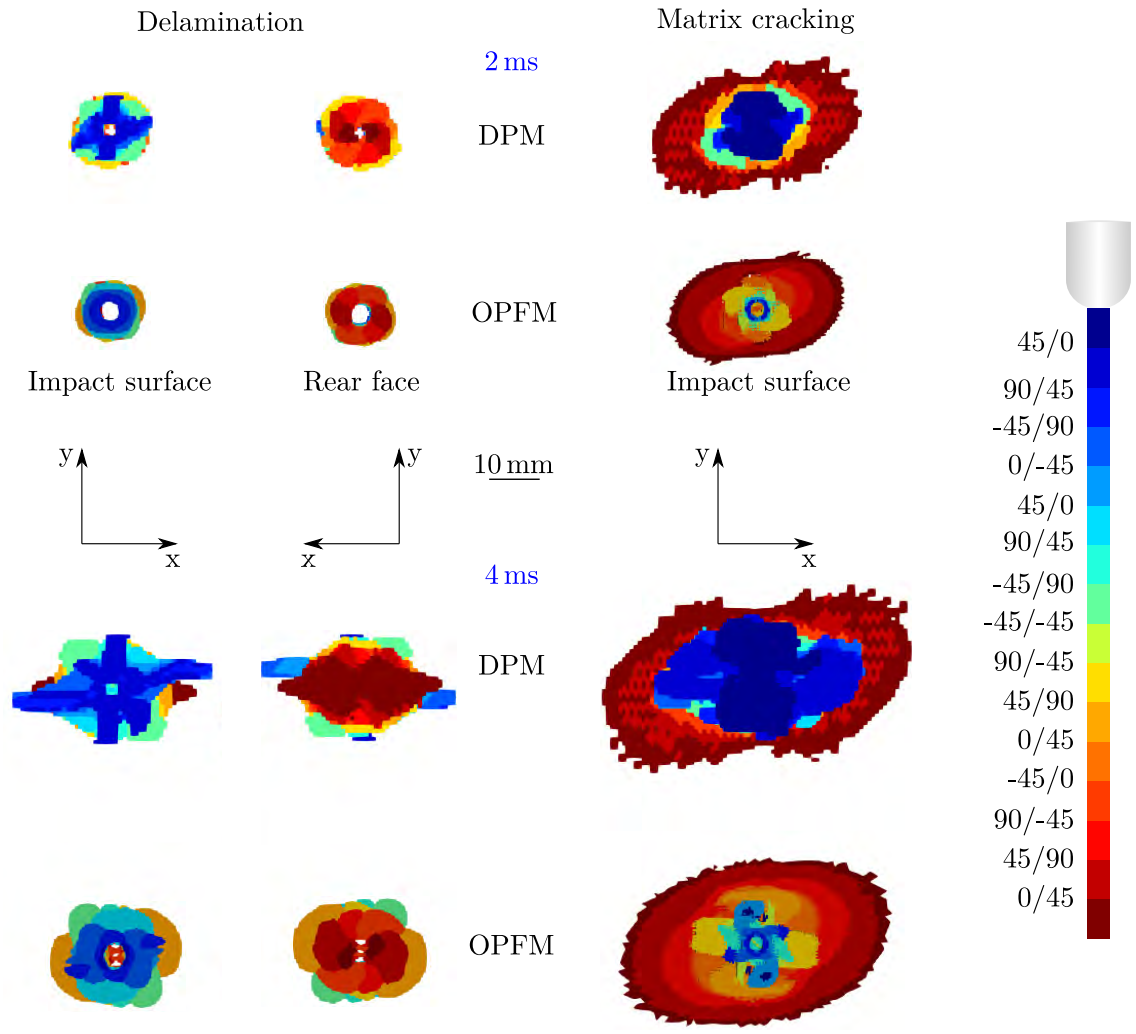

Figure 4.25: Matrix cracking and delamination captured at 2 ms and 4 ms for DPM and OPFM in the presence of all damage mechanisms

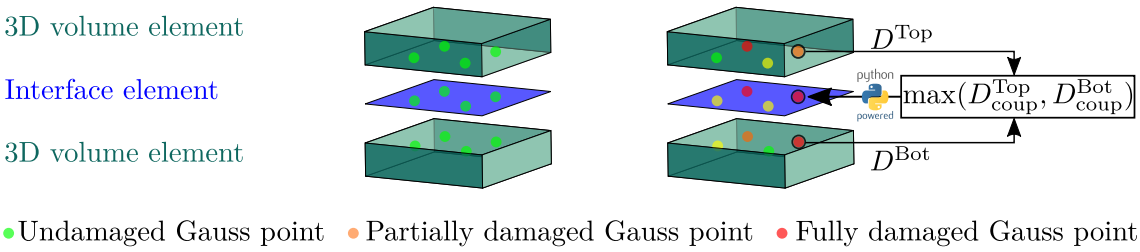

Figure 4.26: Geometric scheme of the damage coupling approach in OPFM

Effect of the intraply damage on the cohesive interfacial property Once the damaged states of the volume Gauss point are transferred to the adjacent interface Gauss point. The mixed-mode stress onset and interface toughness are reduced according to Equation (4.79).

$$\begin{cases} \sigma_c &= \langle 1 - D_{\mathrm{coup}} \rangle_+ \cdot \sigma_c + \xi_1 \\ G_c &= \langle 1 - D_{\mathrm{coup}} \rangle_+^2 \cdot G_c + \xi_2 \end{cases} \tag{4.79}$$

with $D_{\text{coup}} = \max(D_{\text{coup}}^{\text{Top}}, D_{\text{coup}}^{\text{Bot}})$. ξ_1 and ξ_2 are numerical parameters to avoid a null value for σ_c and G_c. The values of ξ_1 and ξ_2 are very low. D_{coup} can be written as

$$D_{\text{coup}} = \max\left(\overbrace{\underbrace{\max(\phi_c^{\text{Top}}, \phi_t^{\text{Top}})}_{\text{Fibre damage}} + \underbrace{D_{\text{mat}}^{\text{Top}}}_{\text{Matrix damage}}}^{\text{Top volume's Gauss point}}; \overbrace{\max(\phi_c^{\text{Bot}}, \phi_t^{\text{Bot}}) + D_{\text{mat}}^{\text{Bot}}}^{\text{Bottom volume's Gauss point}}\right) \tag{4.80}$$

where $D_{\text{mat}} = (1 - [E_{22}^{\text{eff}}/E_{22}^{0}])$ with E_{22}^{eff} the effective modulus value in transverse direction.

Algorithm connectivity and information exchanges Algorithmic developments are needed to exchange information between the interfaces and volumes Gauss points. The first task is to establish the table connectivity at the beginning of the simulation. The connectivity between each interface Gauss point and their relative volume Gauss points is built using a built-in function in Z-set that is interfaced with Python. The volume and the interface element sets are used to identify the neighboring Gauss points of each interface Gauss point. Once the connectivity is performed, each interface Gauss point is linked to its two adjacent volume's Gauss points.

The transferred fields (matrix cracking and fibre damages) of the volume Gauss points are then transferred in the cohesive damage law routine of the respective interface Gauss point. Two different cases can be observed for the coupling:

- The first one is with the absence of fibre breaks occurrence ($\phi_c = 0$ or $\phi_t = 0$). In this case, the drawback is a time increment delay between two consecutive increments for the coupling. Indeed, the transferred fields at time t are those of the increment $t - \Delta t$ as the alternate solver converges in one iteration (shown in blue in FIGURE 4.27). Thus, the couples (σ_c, G_c) are reduced using the coupling fields obtained from the previous converged increment $D^{\text{t}-\Delta\text{t}}$;

- However, when the fibre damages occur ($\phi_c > 0$ or $\phi_t > 0$), as shown in red in FIGURE 4.27, the alternate solver iterates until the stagnation criterion is fulfilled. Consequently, during the iterations, the transferred fields are updated, highlighting the explicit character of the artificial damage interaction.

Influence of the coupling on the projected delaminated area The damage interactions have been introduced progressively to demonstrate the interest of coupling. FIGURE 4.28 shows the effect of the different couplings on the delamination. Firstly, the matrix cracking → delamination coupling changes the delamination shape for the lower interfaces, the coupling captures the delamination of the lowest interface. Few matrix cracking is responsible for the negligible influence of the delamination near the impacted surface.

When the fibre breaks → delamination coupling is introduced, a strong influence on the delamination near the impacted surface is observed. Indeed, the fibre breaks in compression trigger the delamination. The delamination follows the fibre breaks path as observed with DPM and experimentally.

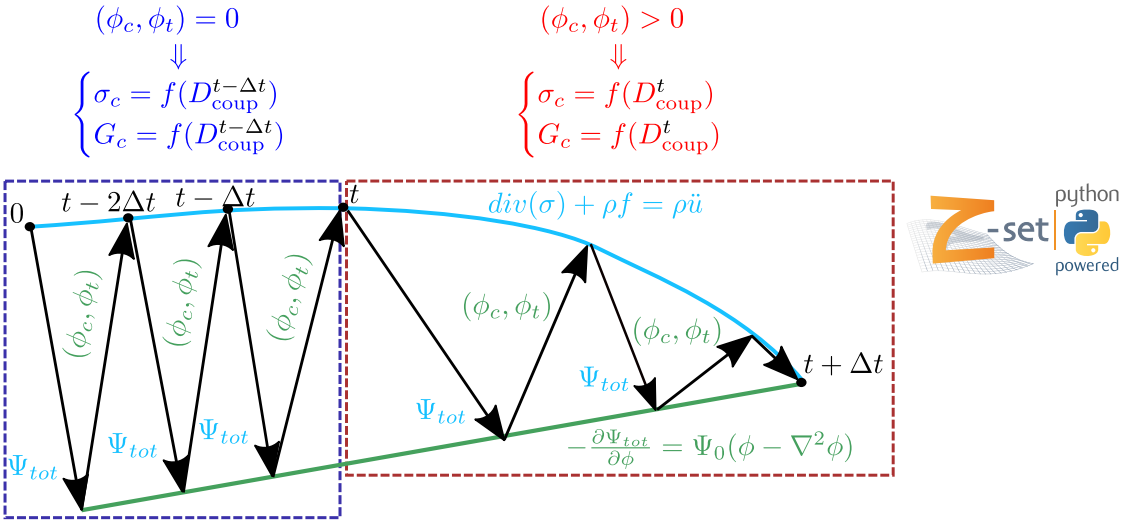

Figure 4.27: Alternate scheme with no fibre breaks (from 0 to t in blue) and with fibre breaks (from t to t + Δt in red). The scheme highlights the explicit character of the damage coupling (D^t_{coup}) when fibre breaks occur

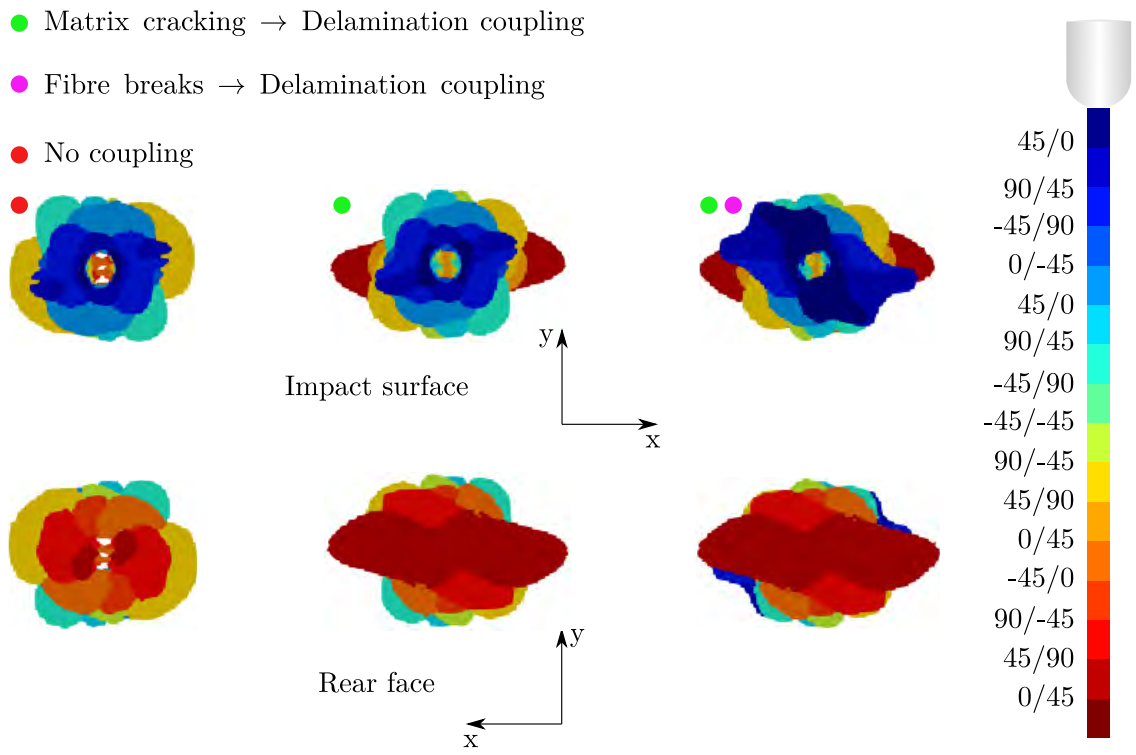

Figure 4.28: Influence of the damage coupling on the projected delaminated area for the Q16 laminate impacted at 20 J

4.2.3.4 Summary of the damage coupling modelings

The comparison between the DPM and the OPFM has emphasized how critical is the damage interactions with the delamination patterns. Moreover, it shows that continuum damage modeling for intraply damage and cohesive zone modeling for

interply damage are suffering from a lack of information exchange. The load transfer is insufficient to trigger the delamination when intraply damage occurs. A solution using an artificial coupling has been developed in Zset. The progressive introduction of the damage coupling has highlighted that the delamination of the lower interfaces is influenced by the matrix cracking. Besides, the fibre breaks → delamination coupling has enabled to capture the delamination near the impacted surface.

4.2.4 Toward the simulation of low-velocity impact

Based on the drawbacks observed for the previous using of OPFM, this section has introduced all the developments to predict accurately the impact damage. Three main improvements have been presented:

- Fibre breaks modeling using the phase-field variational formulation with two different fibre damage variables;
- An enhancement of CZM with a strength reinforcement in the presence of compressive out-of-plane loading;
- An interaction of damages by introducing an intraply → interply damage coupling.

All of these three developments have been justified considering experimental evidence (chapter 2 and 3). The comparisons with DPM emphasize the strong need for damage coupling in impact damage.

The following section will be dedicated to the simulation of low-velocity impact using the two damage models. The predictive capabilities of the two models will be presented and discussed.

4.3 Prediction of damages induced by low-velocity impacts

The results obtained from the simulation for both damage models will be compared to the experimental data. The first comparisons are performed on the global responses (load-time and load-displacement responses). Then, the projected damaged areas for the delamination are presented. Finally, all the damage mechanisms are compared for each ply and interface.

4.3.1 Study of the global responses

The load-displacement and the load-time responses for the Q16 and C20 laminates are plotted in Figures 4.29-4.30. The responses are normalized according to the peak load observed for each impact energy level.

The numerical responses obtained from both models are very similar for the lower impact energies (6.5 J and 11 J), the numerical responses obtained from both models are very similar. The predicted load peaks is more overestimated for the C20 laminate than for the Q16 laminate. The predicted contact times are lower than in the experiments for both models. As explained previously, the contact time depends on the experimental setup stiffness. The actual experimental setup has

mechanical clearances due to numerous stacked tools that are not considered in the numerical modeling. The impact window is pinned (u_1, u_2, u_3) = 0, which is not strictly representative of the actual boundary conditions, as observed with the Keyence sensors.

At 20 J, fibre breaks in tension have occurred for the Q16 laminate only. Both models capture the load drop and the oscillations observed experimentally for the Q16 laminate. The load drop arises earlier for the DPM than OPFM. In any case, the maximum load is well captured for both models. For the C20 laminate, the two predicted responses are overlapped until 4.54 mm where DPM exhibits a load drop. At 20 J, fibre breaks in tension have not been observed. However, DPM predicts the failure of fibres in tension responsible for the load drop.

At 35 J, all the damage mechanisms are present. The load drop is more pronounced in OPFM than in DPM. Good predictions are observed for both models for the Q16 laminate. For the C20 laminate, OPFM exhibits a load drop not observed experimentally.

Figure 4.31 compares the maximum load peak and the normalized dissipated energy for each impact test.

For the Q16 laminate, the normalized load peaks of both models evolve between 90% and 110% (the two horizontal blue lines) of the experimental normalized load peak. For the C20 laminate, the normalized load peaks of both models evolve between 100% and 115% of the experimental normalized load peaks.

The normalized dissipated energies have been plotted for each impact energy level. It can be observed that no trend could be established for the predicted values. For higher energies, the predictions are better for the Q16 laminate for both models. However, care must be taken as the experimental normalized dissipated energies are calculated considering the machine displacement. The experimental displacement contains spurious displacements associated with the experimental setup. Consequently, the dissipated energies have a contribution induced by the machine clearance.

4.3.2 Comparison of the projected damaged area for the delamination

The projected damaged areas associated to the delamination have been compared with CT-scan images. An in-depth coded color has been used for this comparison. It should be noticed that the undeformed coordinates from the simulations have been used for the comparison. The higher the impact energy, the higher the sample is warped, which could induce the wrong color for the CT-scan images. In any case, the main objective of this comparison is to visualize the global shape of the projected damaged area. The following subsection will compare for each ply/interface the different damage mechanisms.

For the Q16 laminate (Figure 4.32), the comparisons highlight each model's predictive capabilities in capturing the different damages. The damage extends obtained from the two models are similar to the CT-scan images. Both models capture the latest interface (red). It should be noticed that DPM captures an elegant shape of the latest damaged interface thanks to the discrete damage modeling. Despite the artificial coupling, the delamination extends for the lowest interfaces obtained from OPFM is not extended as for DPM. The main reason that can be suggested is

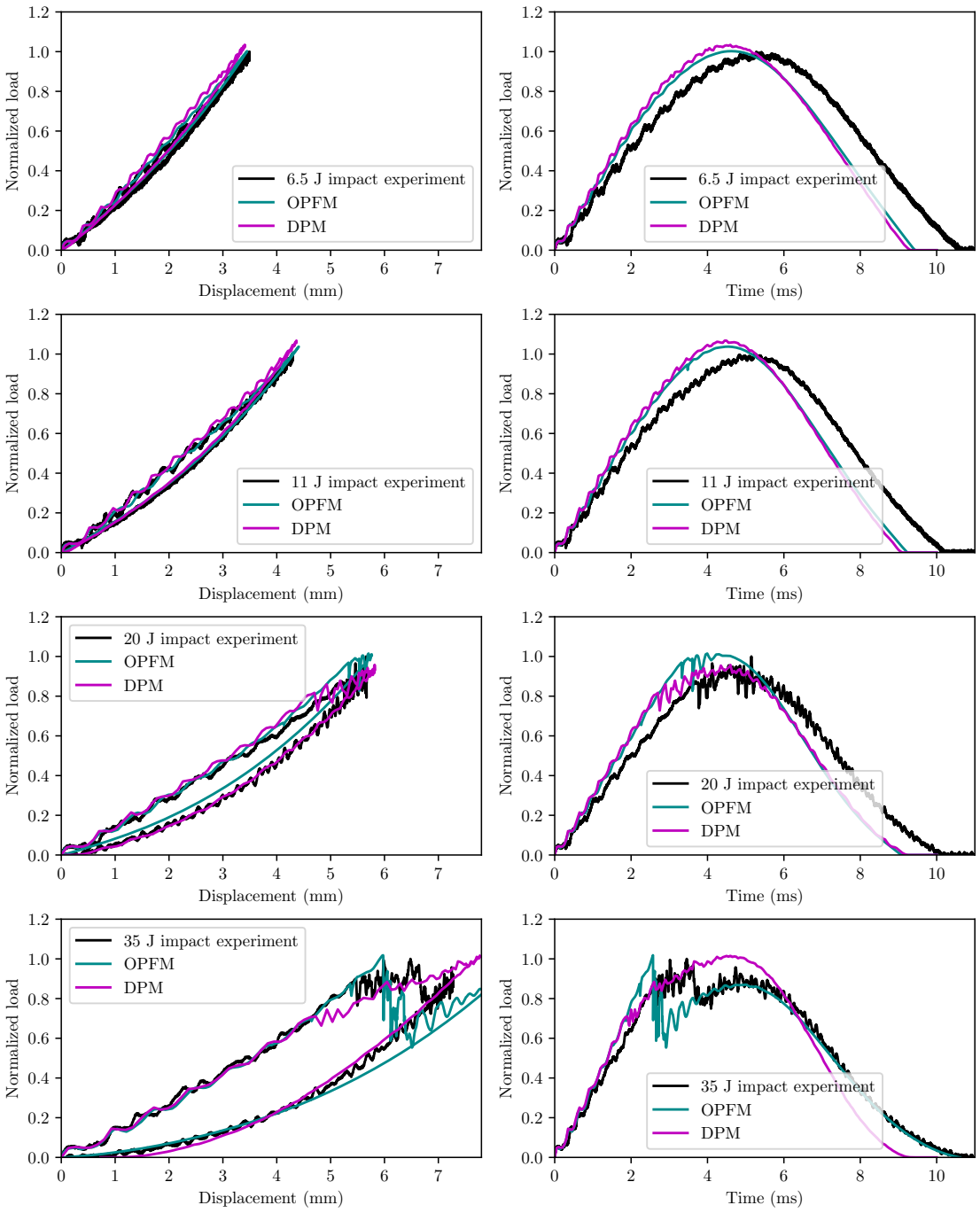

Figure 4.29: Comparison of the global responses for the Q16 laminate

the damage-failure transition which is not respected due to the existing framework. Indeed, the matrix crack density is slowed down by the micro-delamination. Thus, a residual stiffness value is still available, allowing load carrying. For the damages occurring near the impacted surface (blue) both models capture the fibre breaks in compression of the most top plies. These fibre breaks induce a high amount of delamination as observed experimentally. The success of the fibre breaks $\rightarrow$ delamination coupling used for both models allows capturing the accurate orientation of the delamination for the most top interfaces.

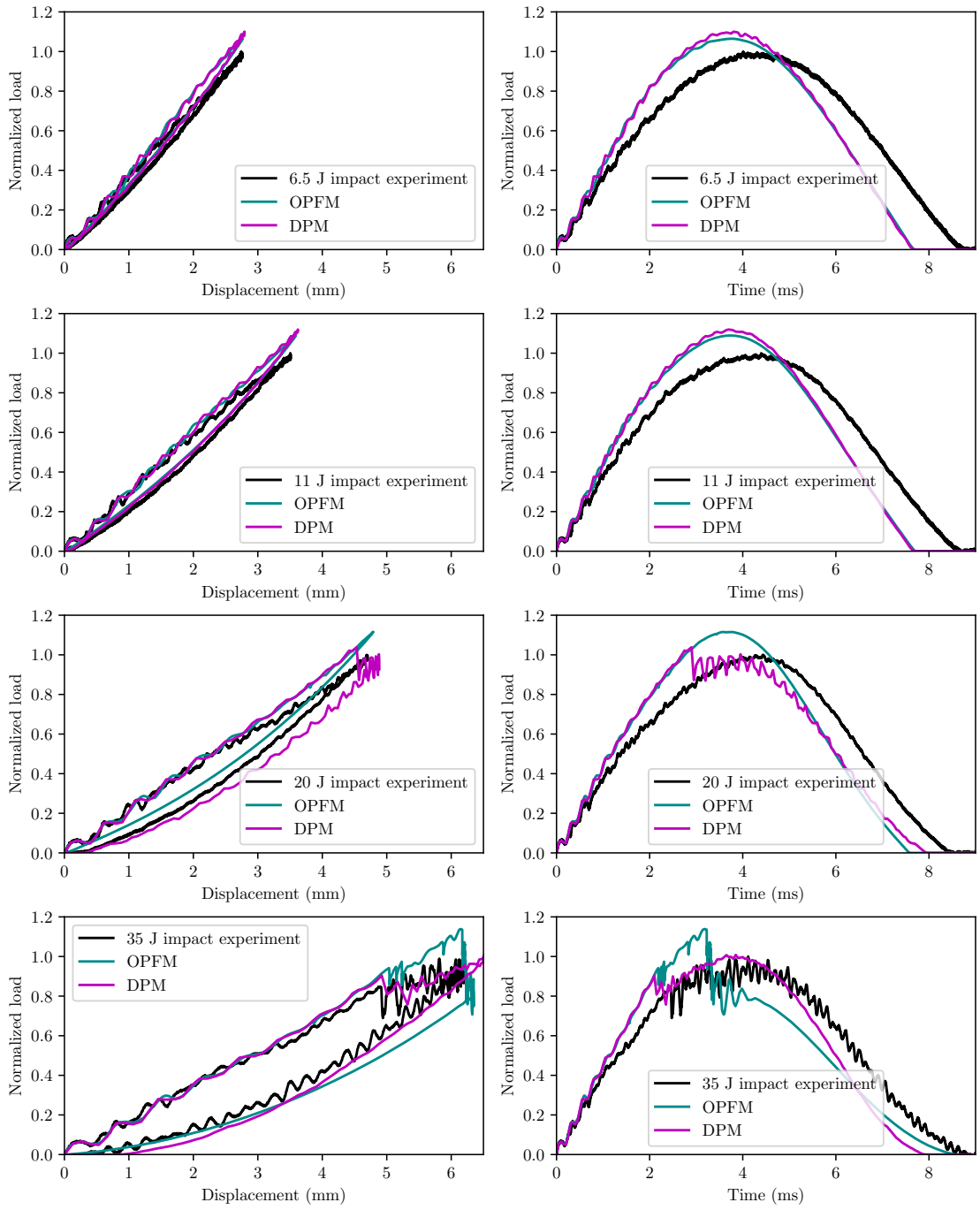

Figure 4.30: Comparison of the global responses for the C20 laminate

For the C20 laminate (FIGURE 4.33), similar damage extends are observed between the predicted and the CT-scan images. The fibre breaks in compression are still captured for both models, however, it can be observed that for OPFM, the fibre breaks in compression is not predicted at 6.5 J. At 35 J, the fibre breaks in compression induce a high amount of delamination, especially at 45°, the two models capture these damages but are still less pronounced than the experiment. For the lower interfaces, DPM accurately captures the delamination shape, whereas OPFM overpredicts the delamination. The overprediction of OPFM has been observed since

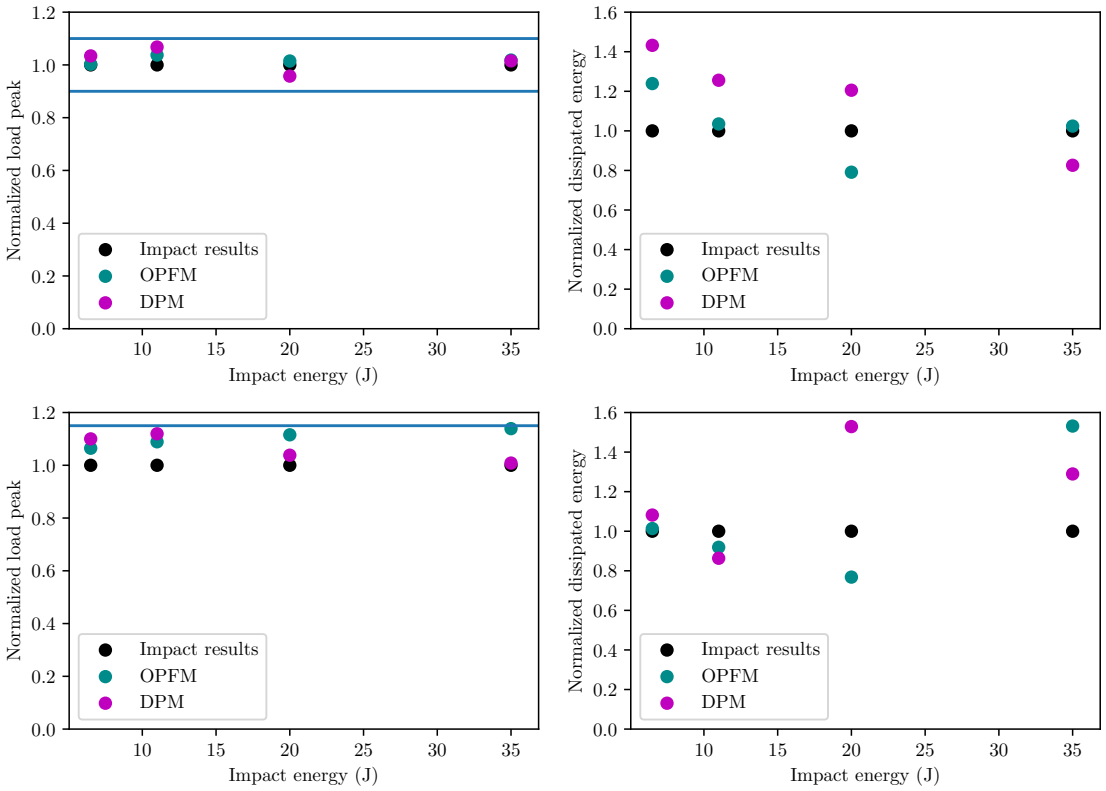

Figure 4.31: Load peak and dissipated energies predicted by the models and normalized by each impact energy level for the Q16 laminate (top plots) and the C20 laminate (bottom plots)

6.5 J.

A first insight on the predictive capabilities of the two models has been presented. However, it is not sufficient to accurately evaluate the two damage model's sturdiness. Hence, a local comparison of each damage mechanism is performed in the following.

4.3.3 Deeper comparisons (ply by ply and interface by interface) for the evaluation of the predictive capabilities of the two damage models

Each damage mechanism is compared with the CT-scan slices. Interface damage obtained by CT-scans in green are compared with the delamination predicted by the two models. Intraply damages (fibre breaks and matrix cracking) obtained by CT-scans in red are compared with the intraply damages predicted by the models. For the Q16 laminate impacted at 20 J, the sample is highly warped, and therefore all the damage mechanisms are observed for the slices located near the rear face.

4.3.3.1 Fibre breaks

The fibre break patterns are presented first for the Q16 and C20 laminates impacted at 20 J. For the Q16 laminates, the fibre breaks in compression are shown in Fig-

URE 4.34. The OPFM predicts the failure of the top three plies in compression. The fibre breaks orientation is well captured for the second and third plies. However, for the first 0° ply the failure is perpendicular to the ply orientation, which is not the case experimentally (-45° orientation). A possible reason is the high in-plane shear stress (σ_{12}) induced by the contact with the impactor, which could influence the fibre break onset. The same problem is observed for DPM. Using the phase-field or the crack band models could not bring a solution to capture the good fibre break orientation. A possible way is to introduce a dependence of the strain threshold on the shear stress $\varepsilon_{11}^{R} = f(\sigma_{12})$. OPFM does not predict the fibre breaks for the fourth -45 ply. Concerning DPM, the fibre breaks of the top four plies are captured. A complex crack path is observed for the second 45° ply with failure oriented at -45° and 0°.

The fibre breaks in tension are observed in FIGURE 4.35. Experimentally, it occurs in the lowest six plies starting from the 45° ply (45°, 90°,-45°, 0°, 45°, 90°). OPFM predicts the first failure in the 90°, which is followed instantaneously by the 45° ply. DPM captures the fibre breaks in all the designated plies. However, the failures occur also in FIGURE 4.34 for the lowest 45° and 90° plies. Another point to notice in DPM is the apertures created due to matrix cracking which are straightforwardly observed for the lowest 0° ply.

For the C20 laminate, the fibre breaks in compression are presented in FIGURE 4.36. At this energy level, only fibre breaks in compression have occurred for the top six plies. OPFM predicts the fibre breaks in compression of the top two plies. The same problem previously shown with the wrong crack orientation of the first ply is observed. For DPM, the fibre breaks are predicted for the top six plies. The fibre break orientation is captured accurately for the second -45° ply. In FIGURE 4.37, DPM also predicts the fibre breaks in tension for all plies except for the 0° plies. Again the apertures due to matrix cracking is easily observed.

In-plane tensile and compressive tests on 0° laminates have been performed to identify the strain threshold in [Germain, 2020]. The results show underestimated values of the strain thresholds when introduced in the different damage models. Thus, different simulations have been performed to identify the better values for each model. However, the energetic fibre breaks threshold used in OPFM for the fibre breaks in compression and in tension is too high. For DPM, the fibre breaks strain threshold in tension is low as it predicts the fibre breaks for the C20 laminate whereas it is not observed experimentally. Concerning the energy release rate ($G_{Ic}^{T,C}$), compact tension and compact compression tests for fibre breaks must be performed to identify the correct energy release rate in compression and tension. The phase-field formulation shows a better potential than the crack-band framework to capture accurately the crack shape.

4.3.3.2 Delamination

The delamination patterns are now compared with the X-ray slices for each interface.

Firstly, for the Q16 laminate, almost all the damaged interfaces predicted by both models agree with the experimental results (FIGURES 4.38 - 4.39). The delamination orientation and shape are powerfully captured from both models. For the delamination near the impacted side, OPFM captures the delamination orientation and shape thanks to the fibre breaks ⇒ delamination coupling. For the DPM, the delamination of the first interface does not show two lobes oriented at -45° as

observed in OPFM. DPM captures another delamination's orientation for the top three interfaces. This 0° orientation is linked to the fibre breaks in compression of the third 90° ply.

The delamination patterns are presented in FIGURES 4.40–4.41 for the C20 laminate. The two models capture the 45° delamination's orientation for the first two interfaces. The wrong orientations are reproduced for the delamination patterns due to the fibre breaks in compression ⇒ delamination coupling. Thus, for the top 45°/0°, 0°/45° 90/0° interfaces, the damaged interfaces predicted by DPM are not correctly captured.

OPFM captures the delamination for the lowest $0°/-45°$ interface, whereas no damage is obtained. This is due to the matrix cracking ⇒ delamination coupling, which triggers the delamination on the lowest interface. Concerning DPM, the interface $0°/-45°$ is damaged due to the fibre breaks in tension of the -45°.

The good prediction of the delamination of almost all interfaces demonstrates that CZM is a suitable framework for modeling interply damage in this material. The delamination orientation is highly influenced by the fibre break patterns. Thus, accurate fibre breaks prediction is needed to capture relevant delamination patterns.

4.3.3.3 Matrix cracking

The matrix cracking is finally compared for both models with the CT scan slices. The comparison is more challenging as the matrix cracking require small voxel size to be captured.

FIGURES 4.42–4.43 introduces the matrix cracking patterns obtained from both models for the Q16 laminate. OPFM accurately captures the matrix cracking orientation. Moreover, the closer the ply to the impact surface, the lower the matrix cracking extends. The strength reinforcement explains it in the presence of negative transverse stresses σ_{22}. The matrix cracking are more extended for the DPM. The broken elements in red are concentrated around the impact center.

FIGURES 4.44–4.45 introduces the matrix cracking patterns obtained from both models for the C20 laminate. As explained for the Q16 laminate, the same comments can be established for both models.

As IR thermography captures the thermal signatures related to the matrix cracking. The predicted matrix damages have been compared to the IR images in FIGURE 4.46. It can be highlighted that the damage orientations of both models are in agreement with the IR images.

4.4 Conclusion

This chapter has presented the two damage models, DPM and OPFM. Based on the experimental analysis, OPFM has been enriched with a fibre break modeling with two damage variables (one for the compression and one for the tension). Different regularization methods have been considered. The phase-field has shown interesting capabilities in predicting fibre breaks. The comparisons between the two models have shown the lack in interacting intraply and interply damages for OPFM. An artificial coupling has been developed in OPFM and has shown the different effects and benefits. Once enriched, the predictive capabilities of the two models have been investigated by comparing the impact responses. The projected damaged areas have

then been compared to visualize the damage extends. Finally, a deep comparison of each ply and interface damages have been carried out. The two damage models have shown interesting predictive capabilities.

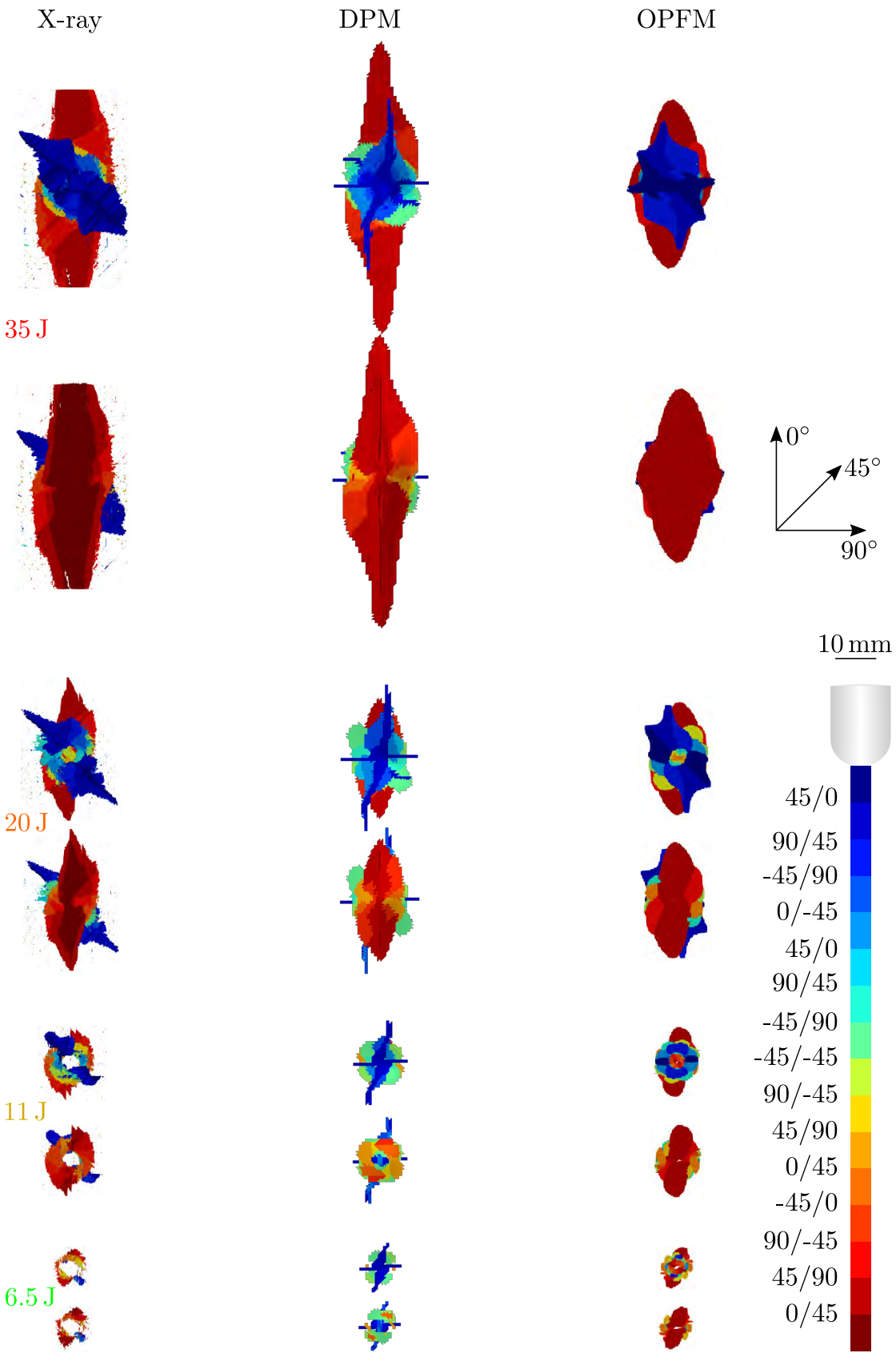

Figure 4.32: Experimental and numerical projected damaged area for the Q16 laminates (impacted and rear faces)

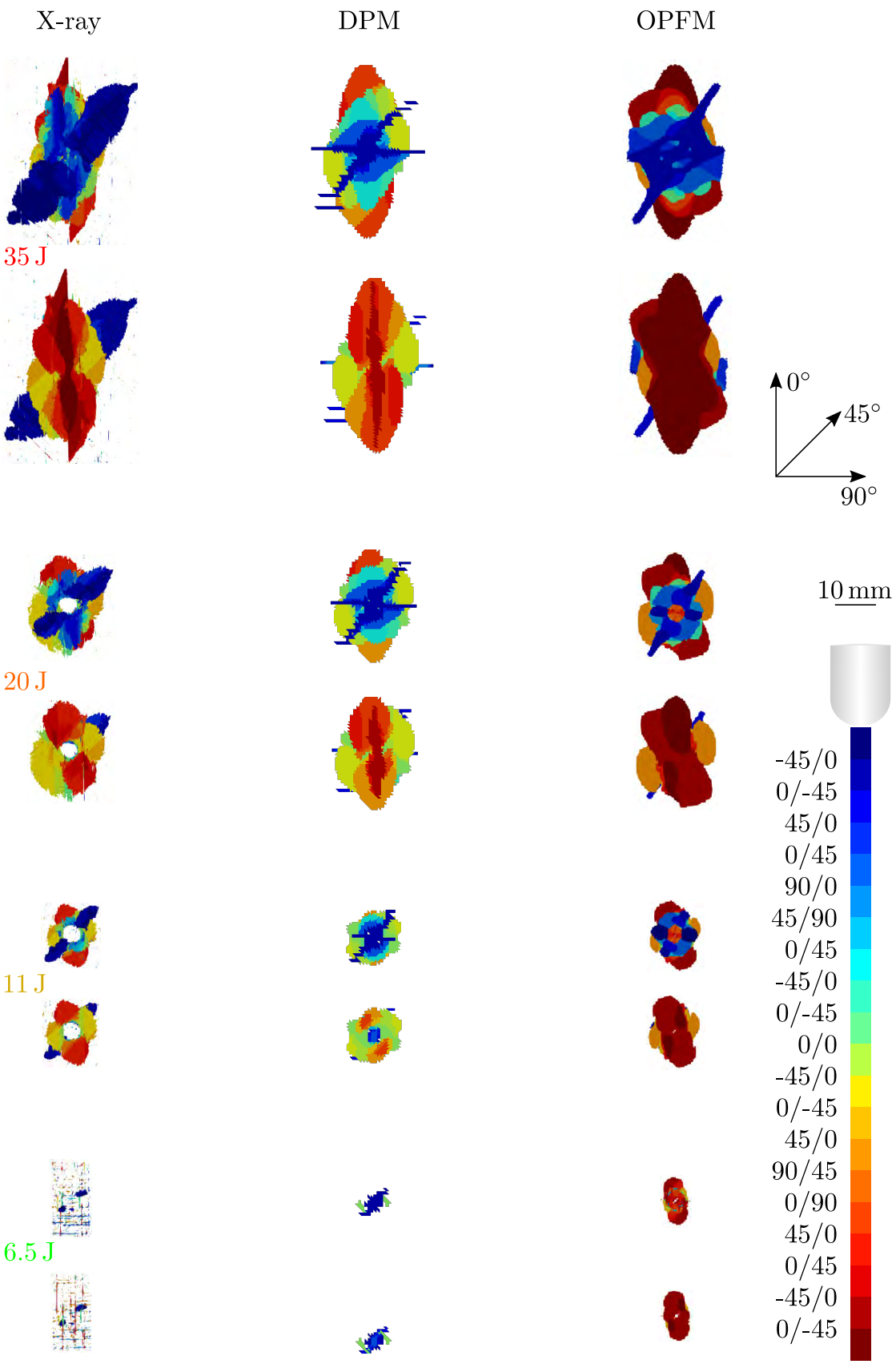

Figure 4.33: Experimental and numerical projected damaged area for the C20 laminates (impacted and rear faces)

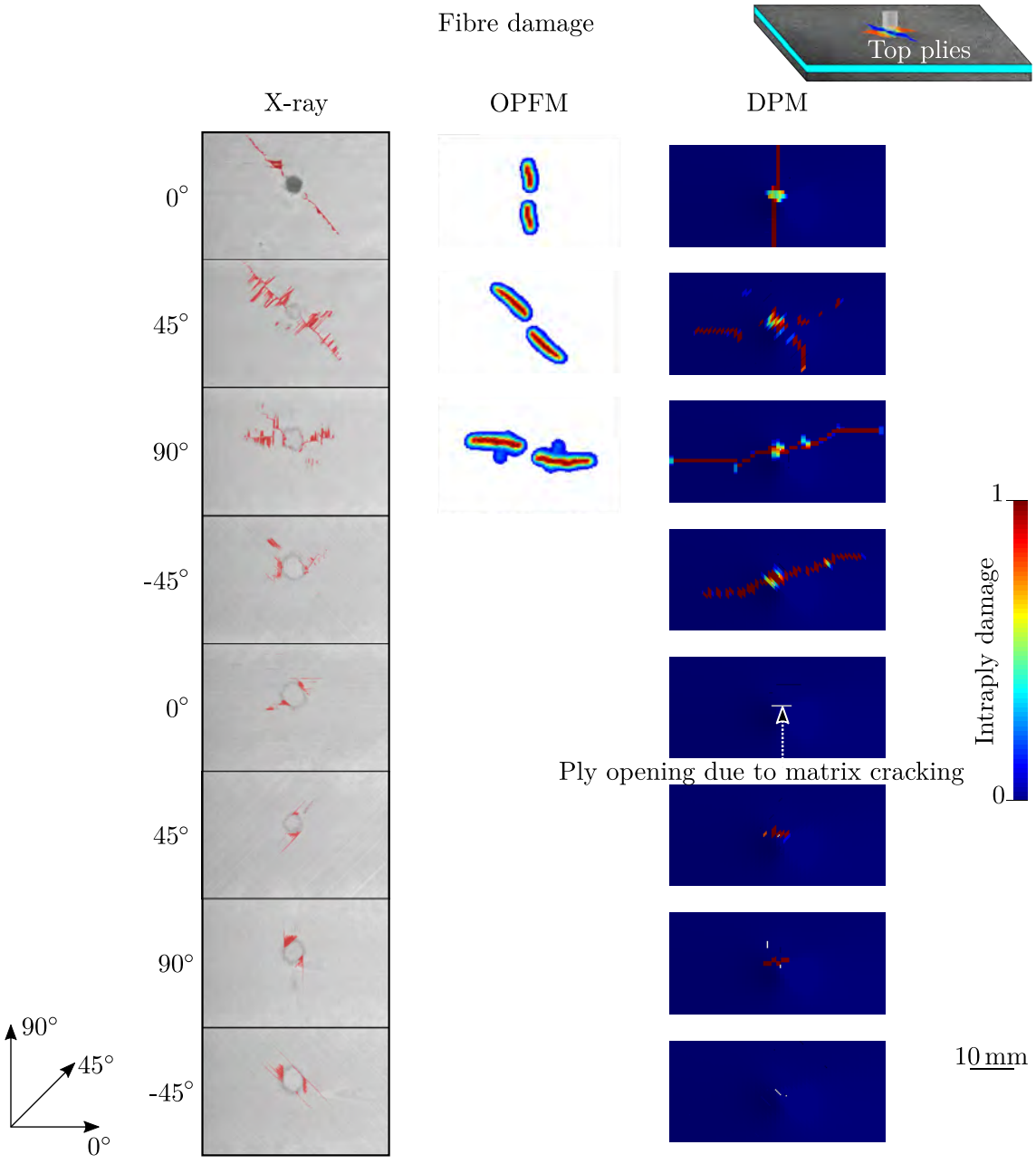

Figure 4.34: Comparison of the intraply damages (X-ray slices) with the fibre break damages for the 8 highest plies of the Q16 laminate impacted at 20 J

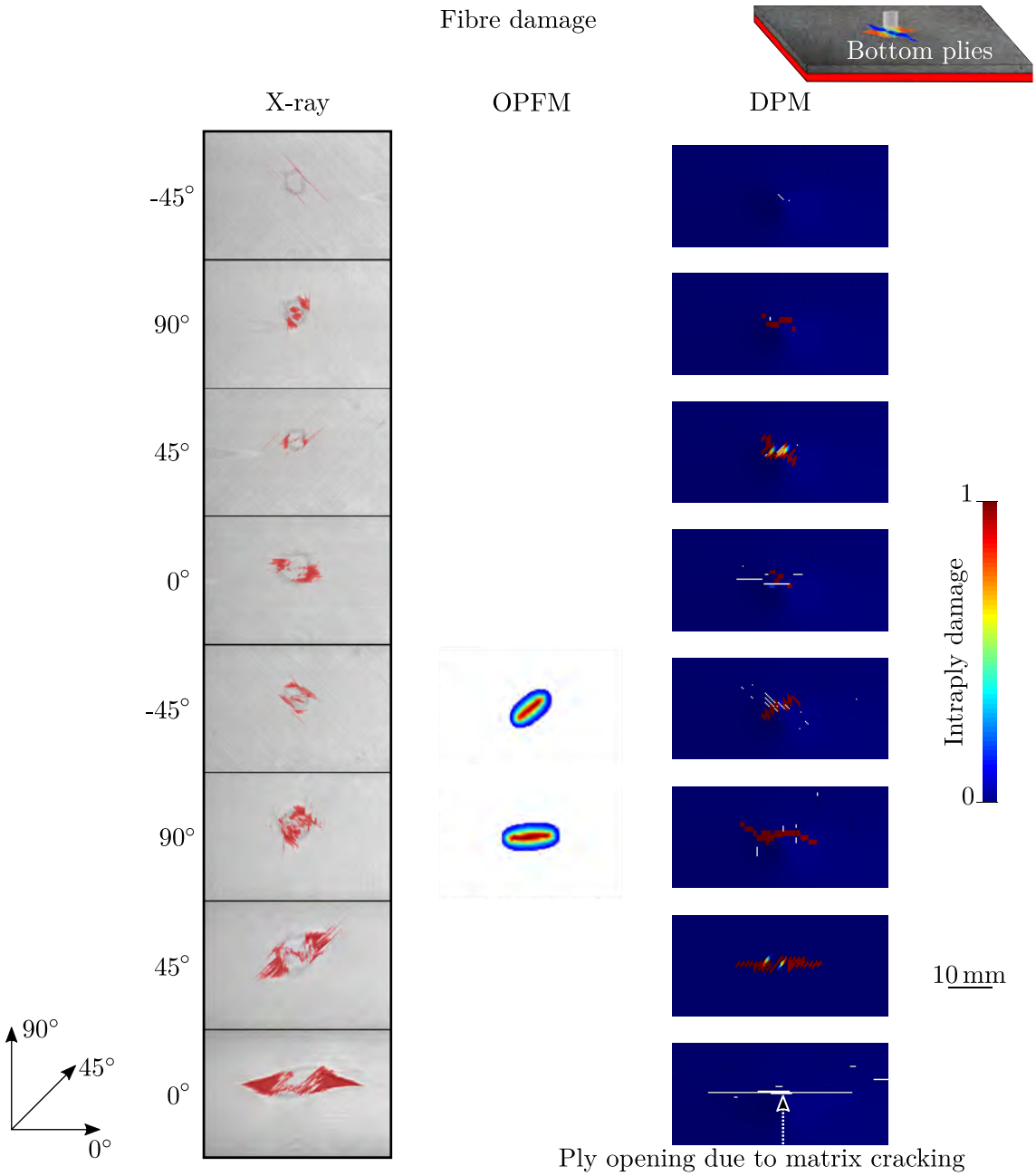

Figure 4.35: Comparison of the intraply damages (X-ray slices) with the fibre break damages for the 8 lowest plies of the Q16 laminate impacted at 20 J

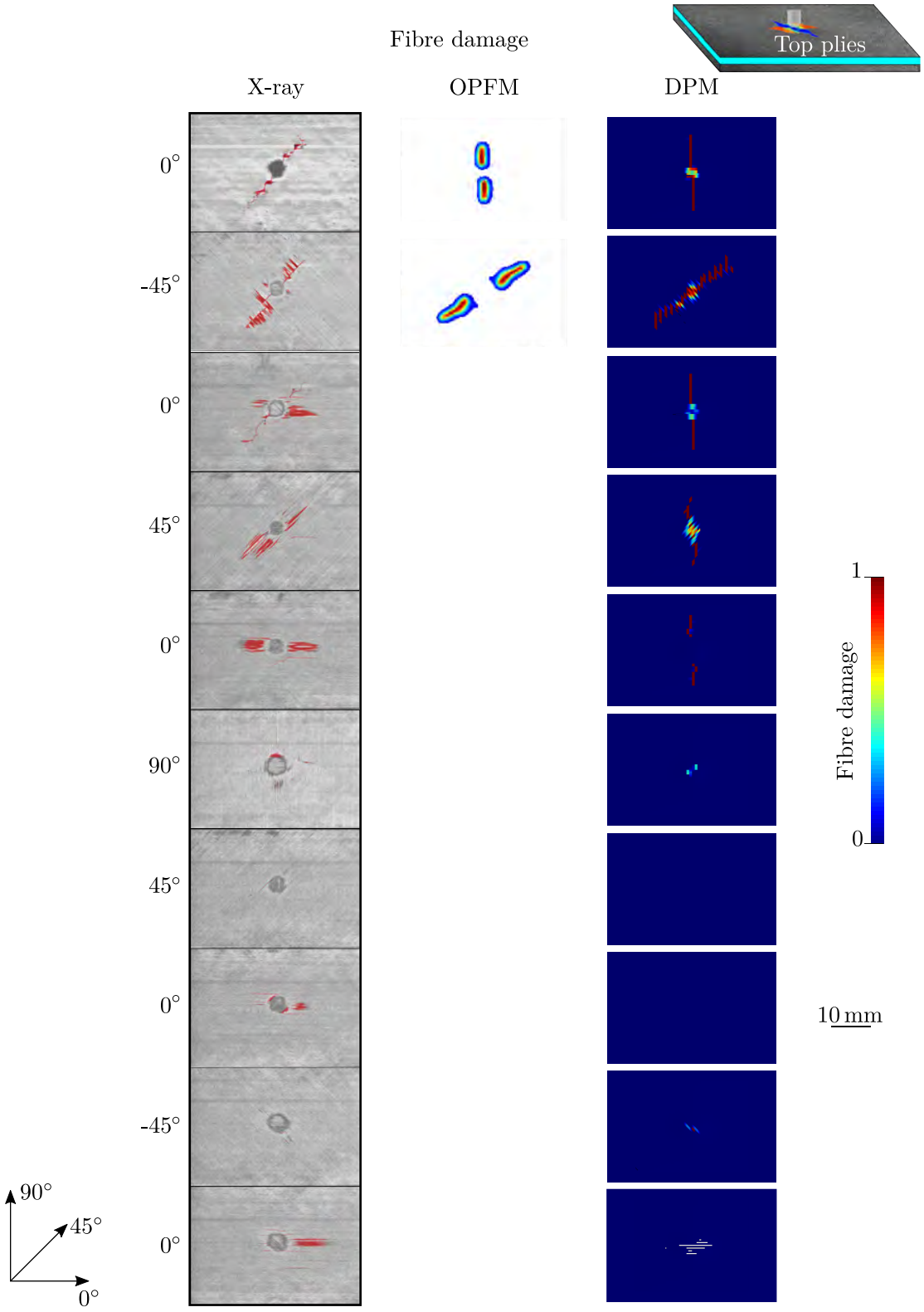

Figure 4.36: Comparison of the intraply damages (X-ray slices) with the fibre break damages for the 10 highest plies of the C20 laminate impacted at 20 J

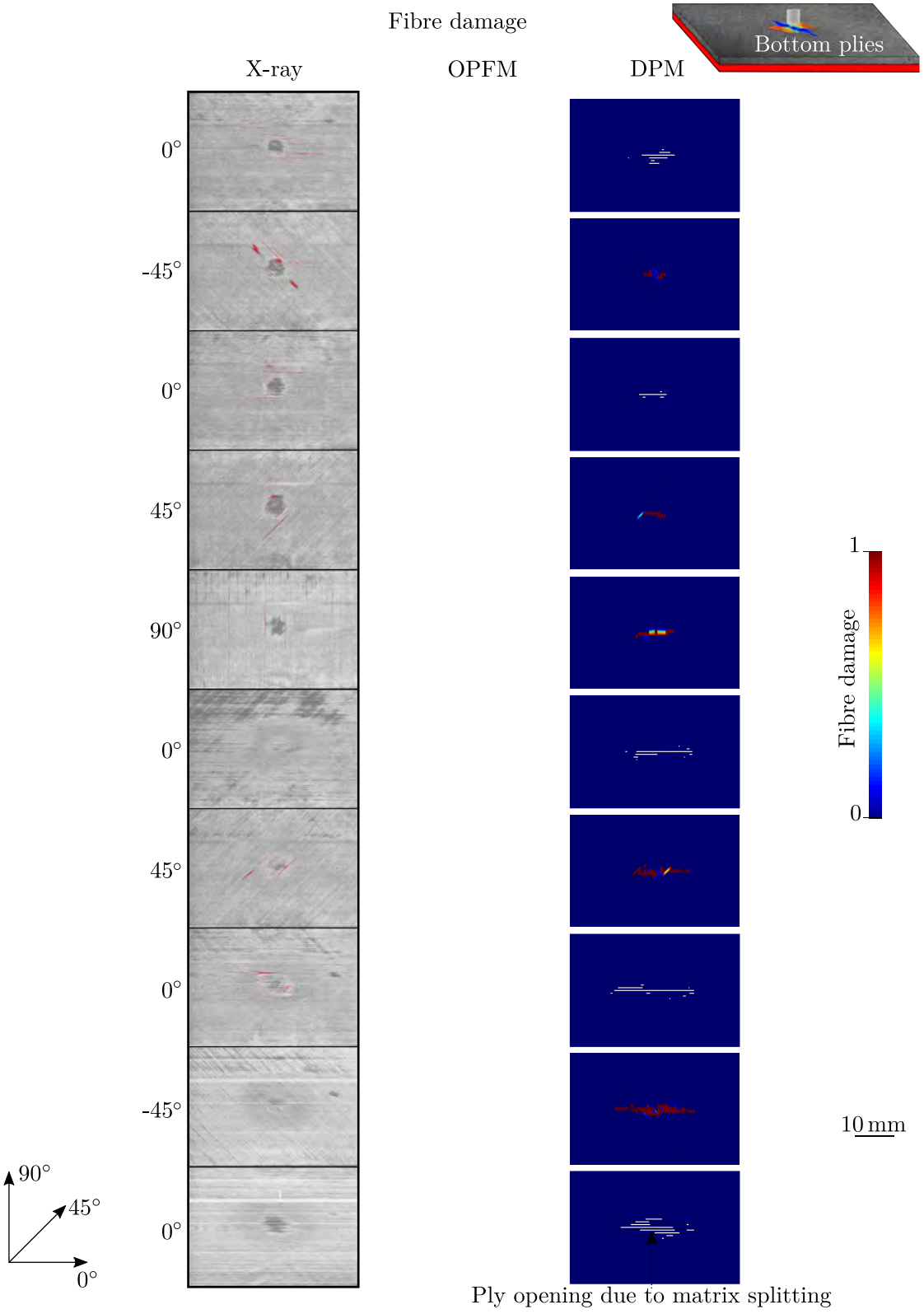

Figure 4.37: Comparison of the intraply damages (X-ray slices) with the fibre break damages for the 10 lowest plies of the C20 laminate impacted at 20 J

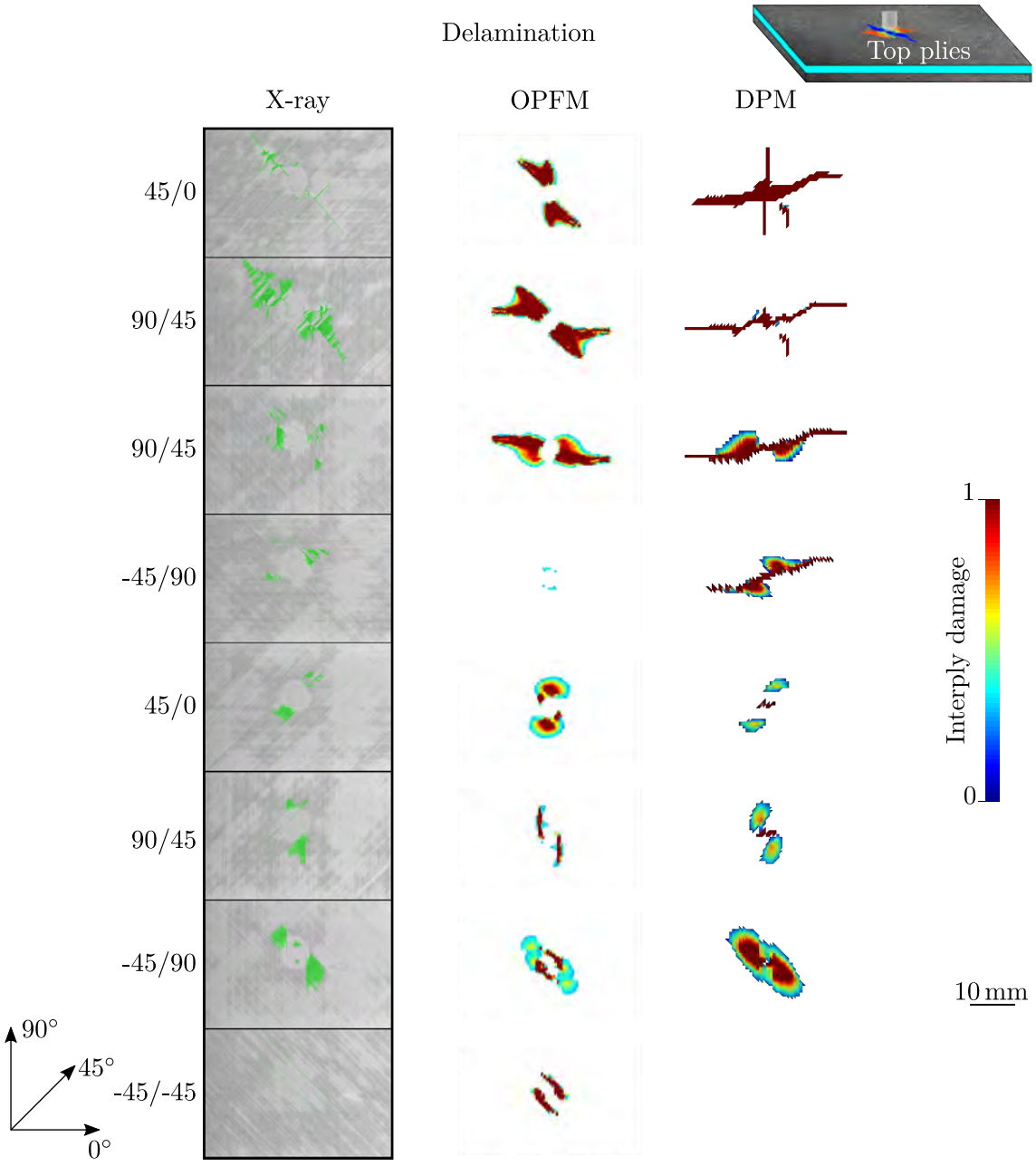

Figure 4.38: Comparison of the interply damages (X-ray slices) with the delamination damages for the 8 highest interfaces of the Q16 laminate impacted at 20 J

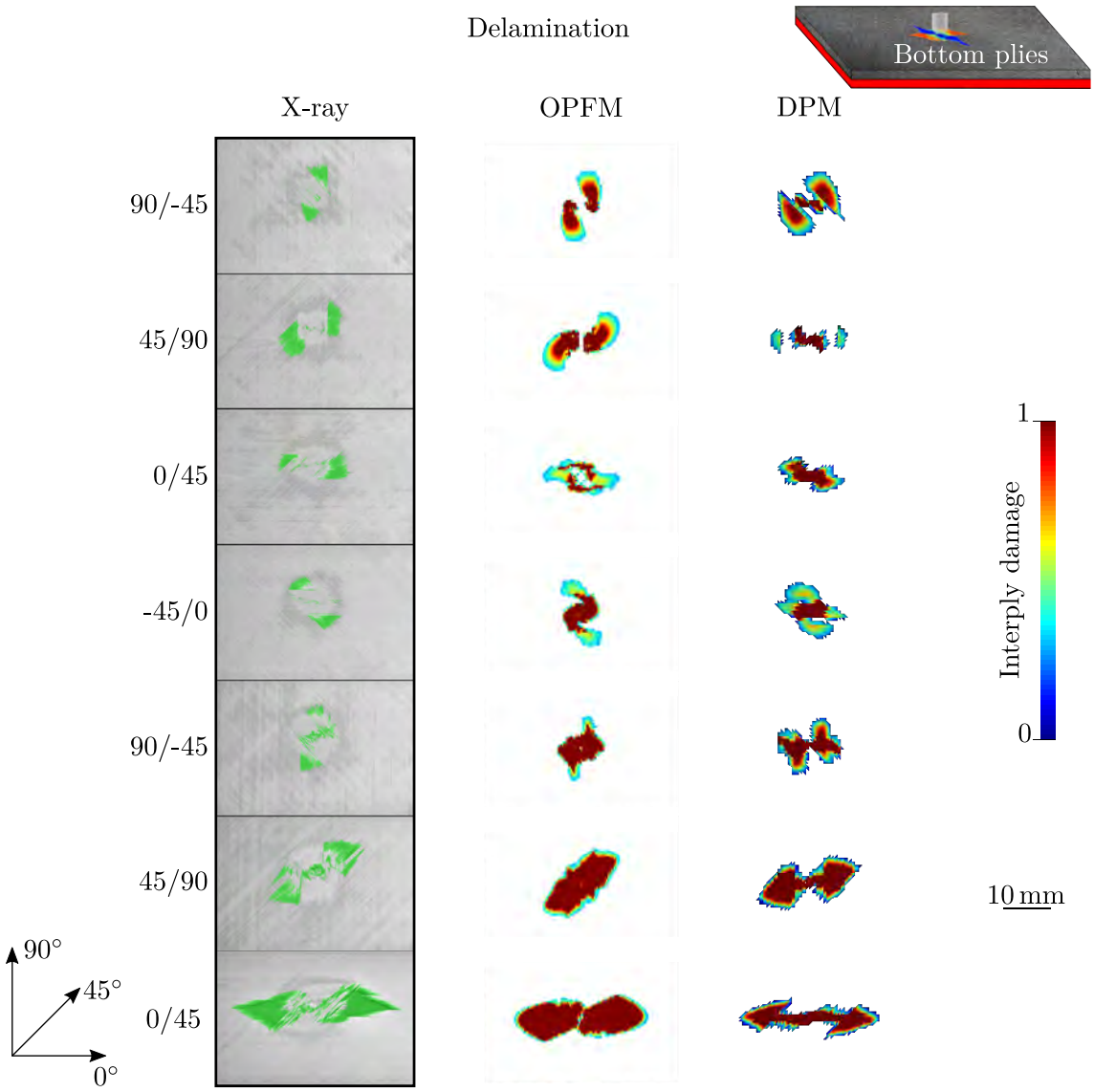

Figure 4.39: Comparison of the interply damages (X-ray slices) with the delamination damages for the 7 lowest interfaces of the Q16 laminate impacted at 20 J

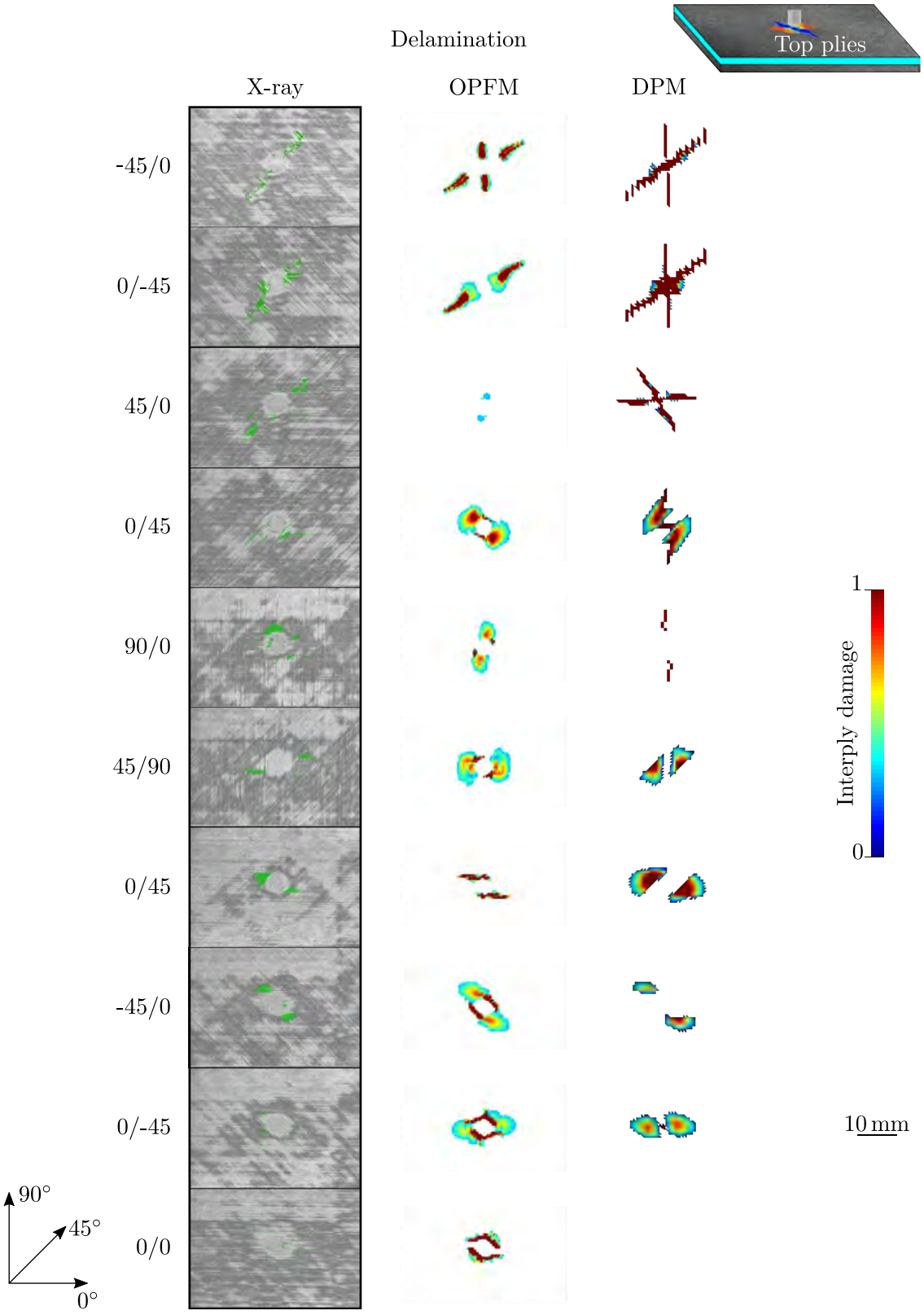

Figure 4.40: Comparison of the interply damages (X-ray slices) with the delamination damages for the 10 highest interfaces of the C20 laminate impacted at 20 J

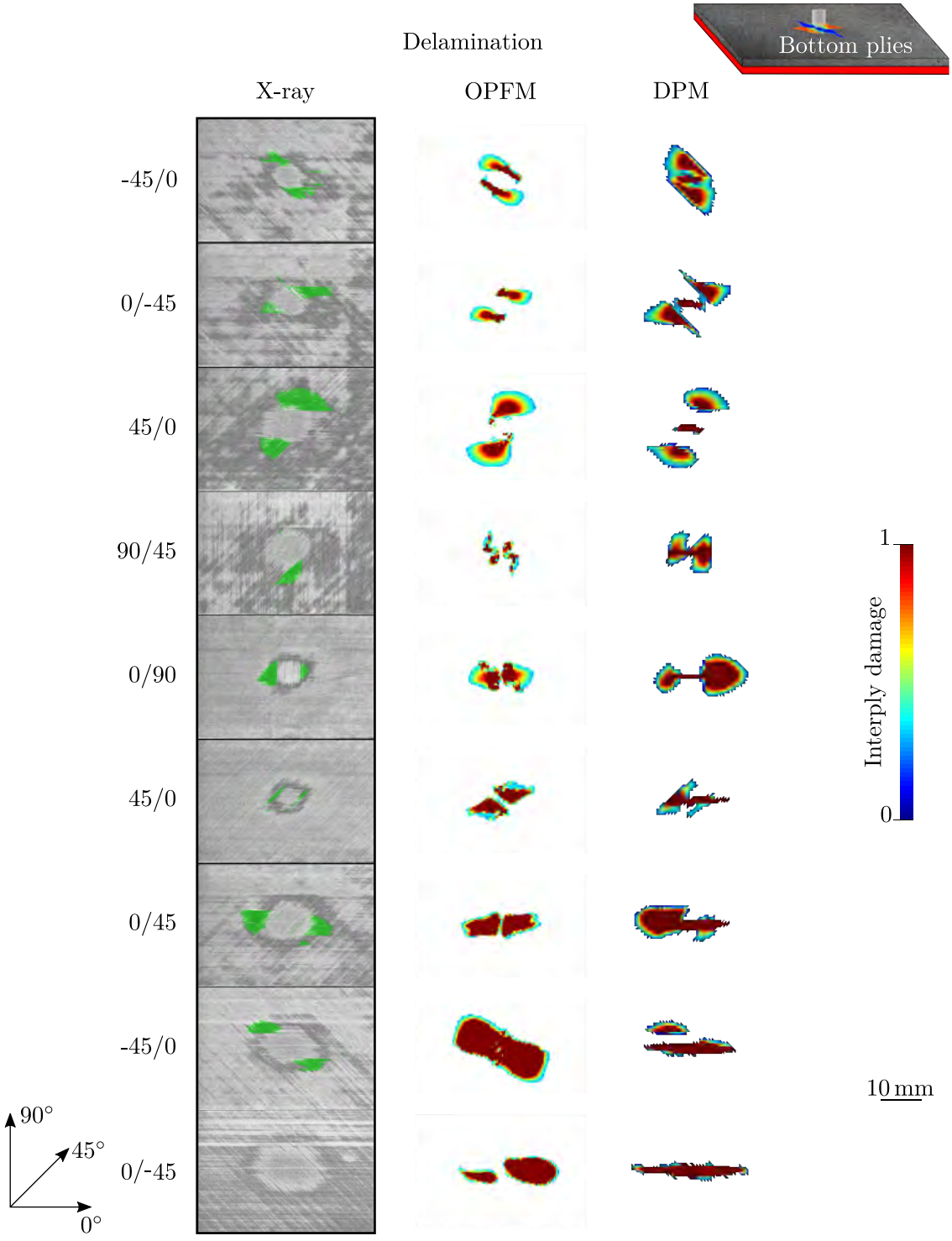

Figure 4.41: Comparison of the interply damages (X-ray slices) with the delamination damages for the 9 lowest interfaces of the C20 laminate impacted at 20 J

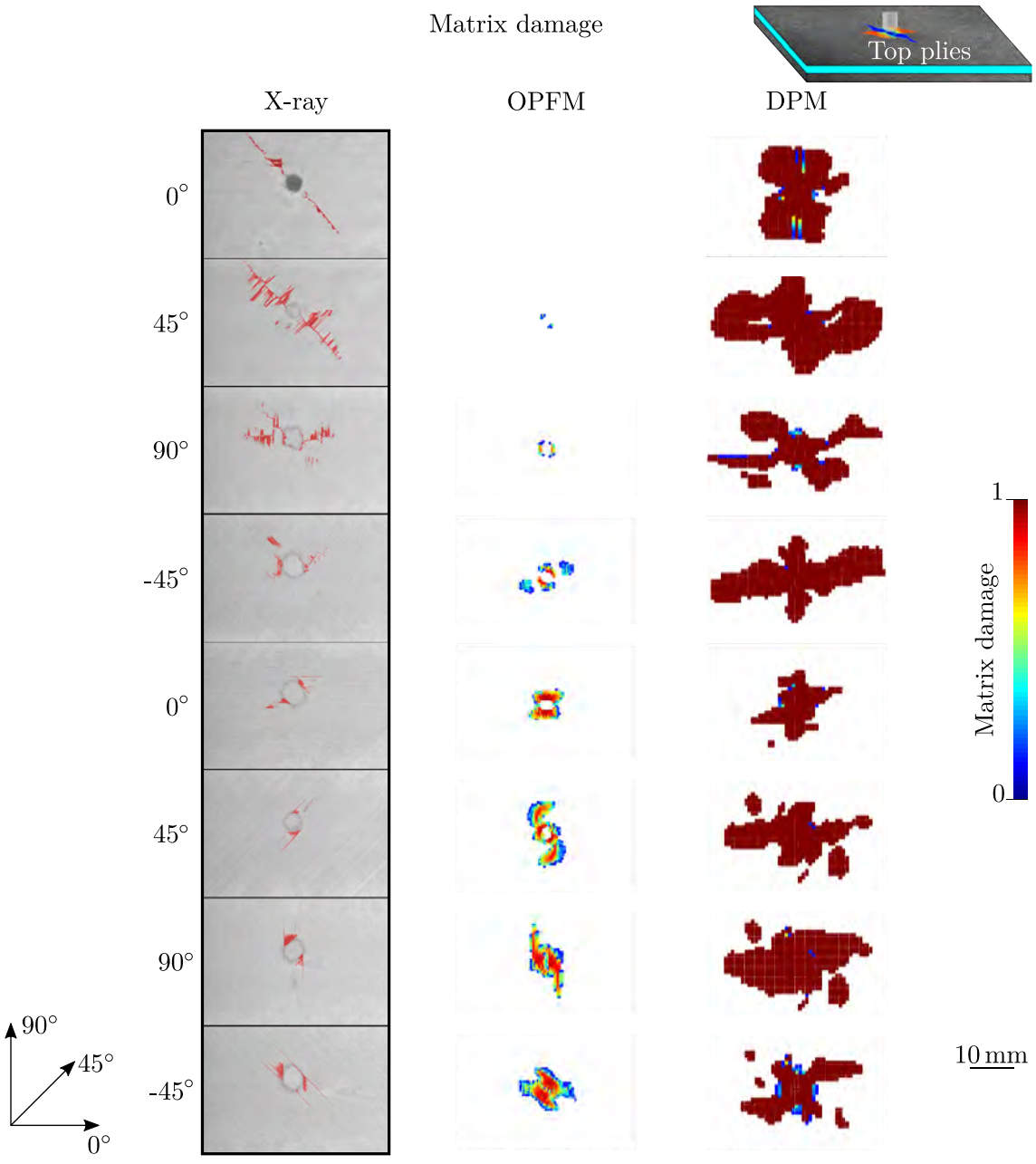

Figure 4.42: Comparison of the intraply damages (X-ray slices) with the matrix cracking damages for the 8 highest plies of the Q16 laminate impacted at 20 J

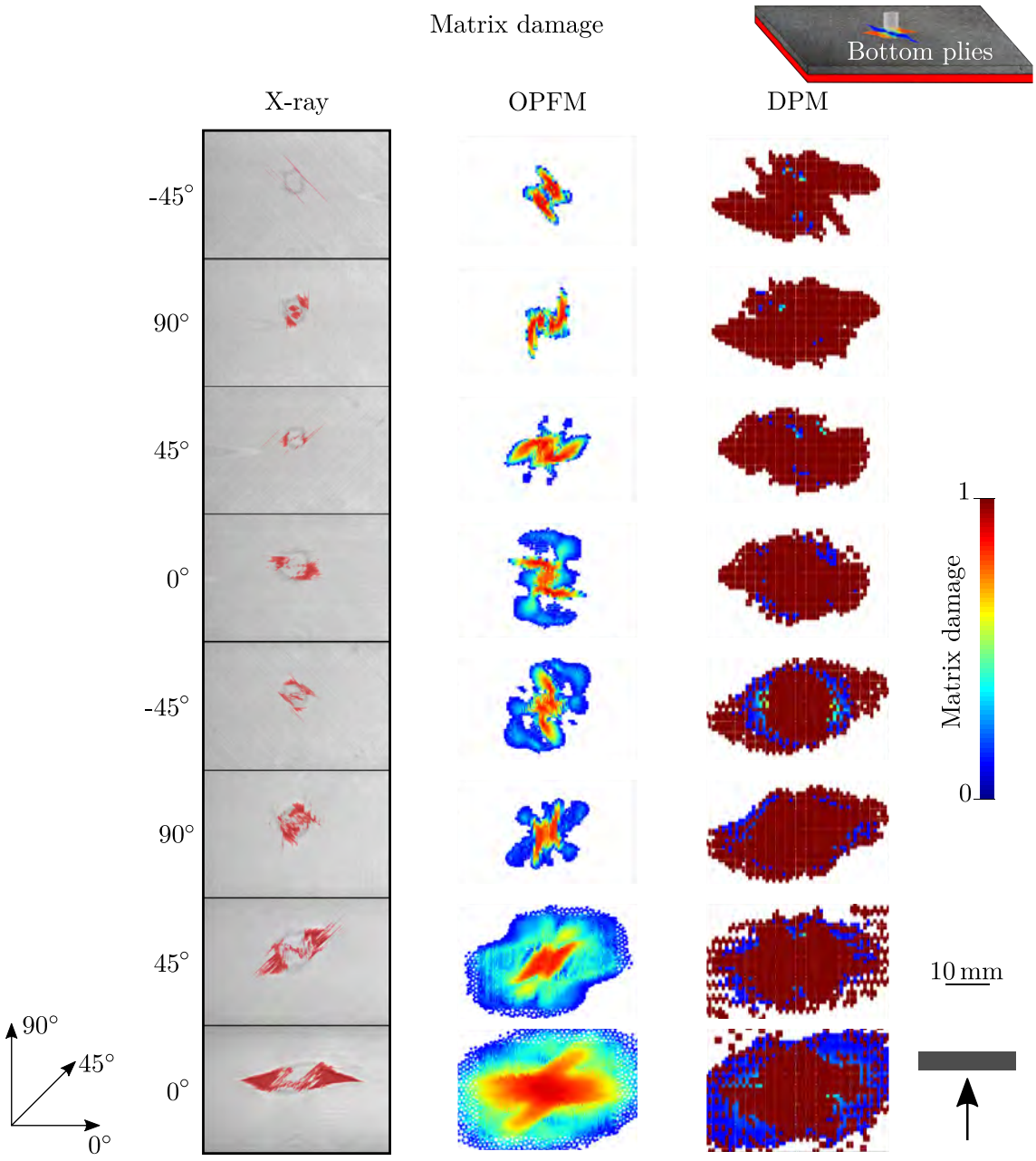

Figure 4.43: Comparison of the intraply damages (X-ray slices) with the matrix cracking damages for the 8 lowest plies of the Q16 laminate impacted at 20 J

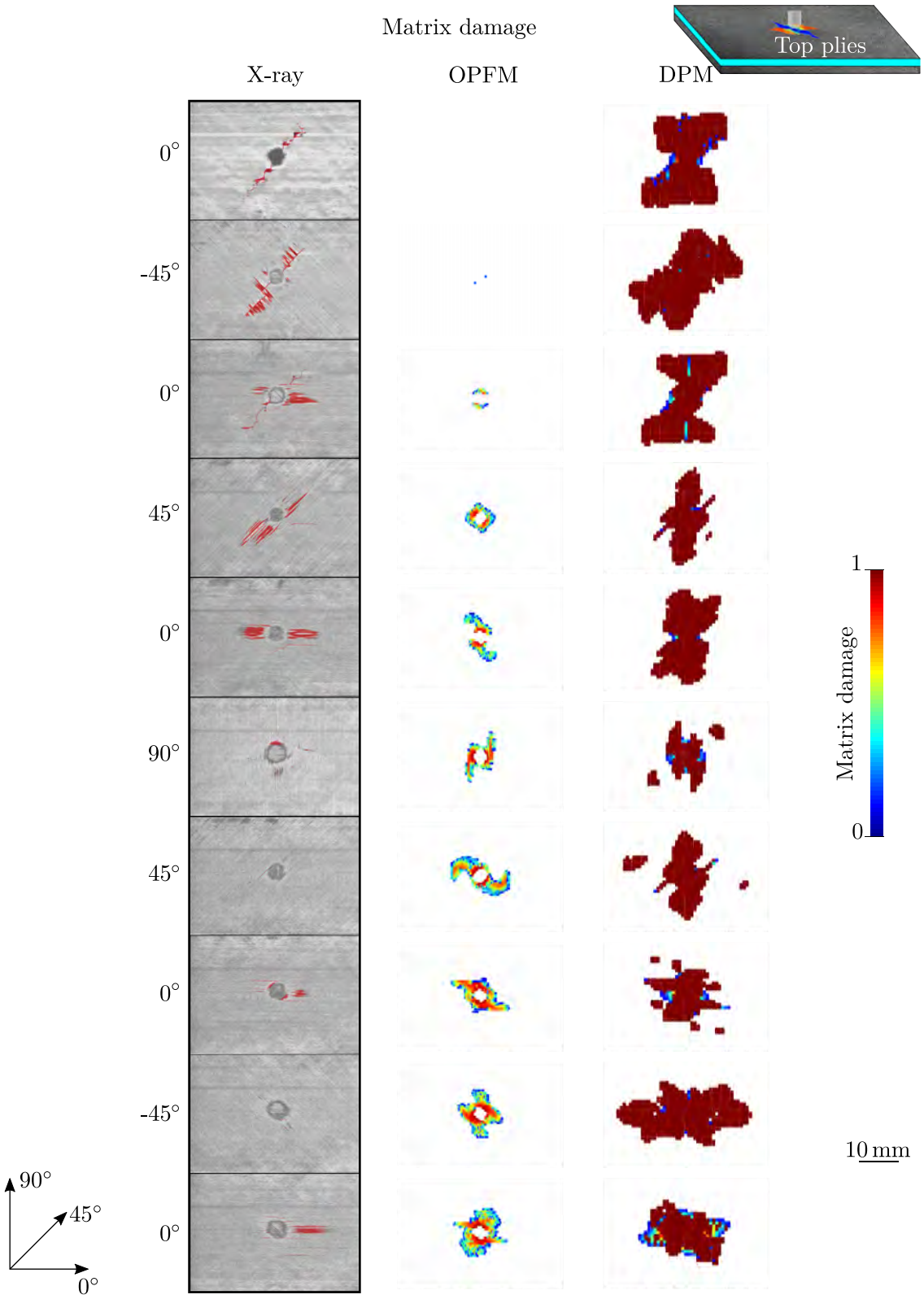

Figure 4.44: Comparison of the intraply damages (X-ray slices) with the matrix cracking damages for the 10 highest plies of the C20 laminate impacted at 20 J

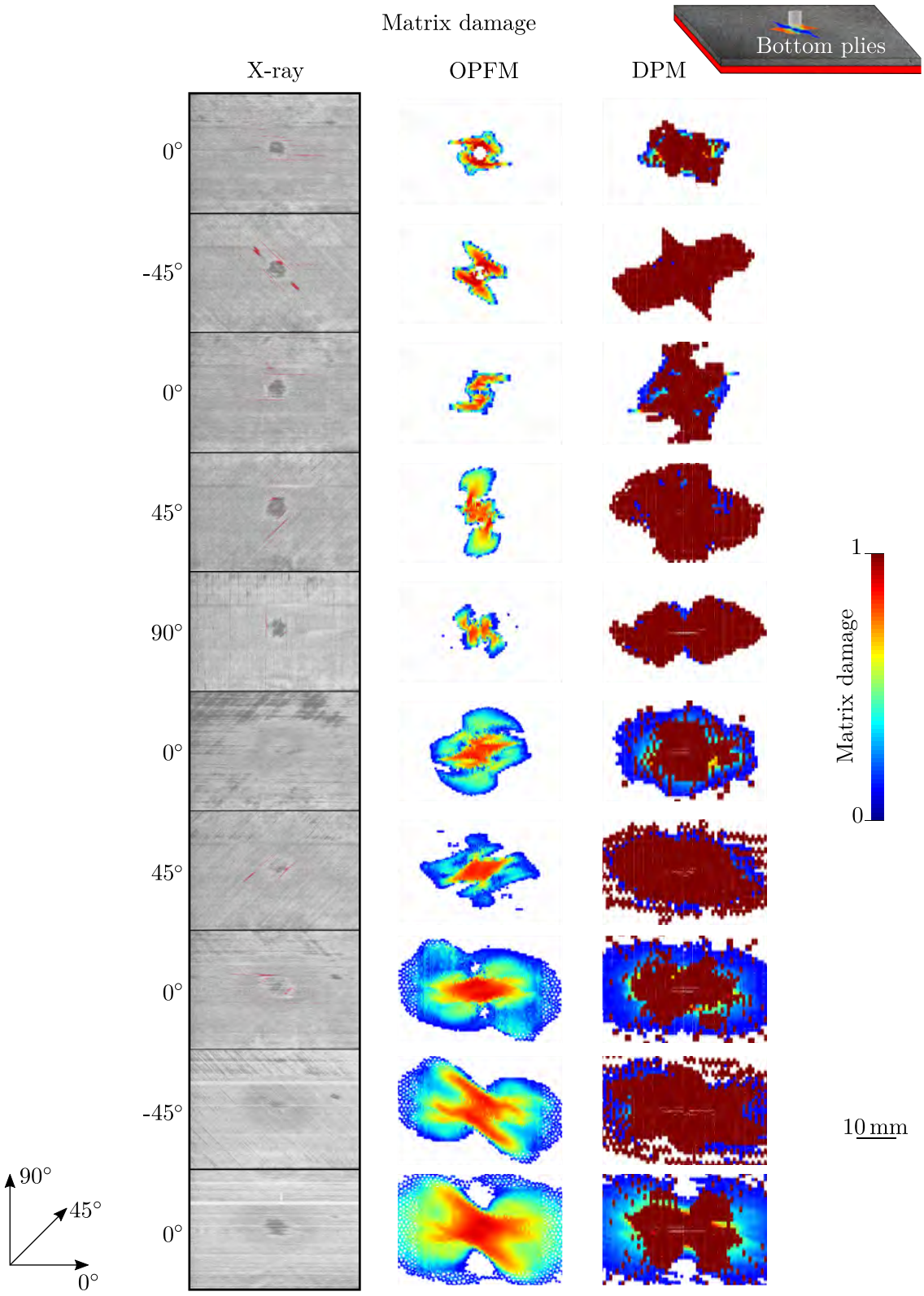

Figure 4.45: Comparison of the intraply damages (X-ray slices) with the matrix cracking damages for the 10 lowest plies of the C20 laminate impacted at 20 J

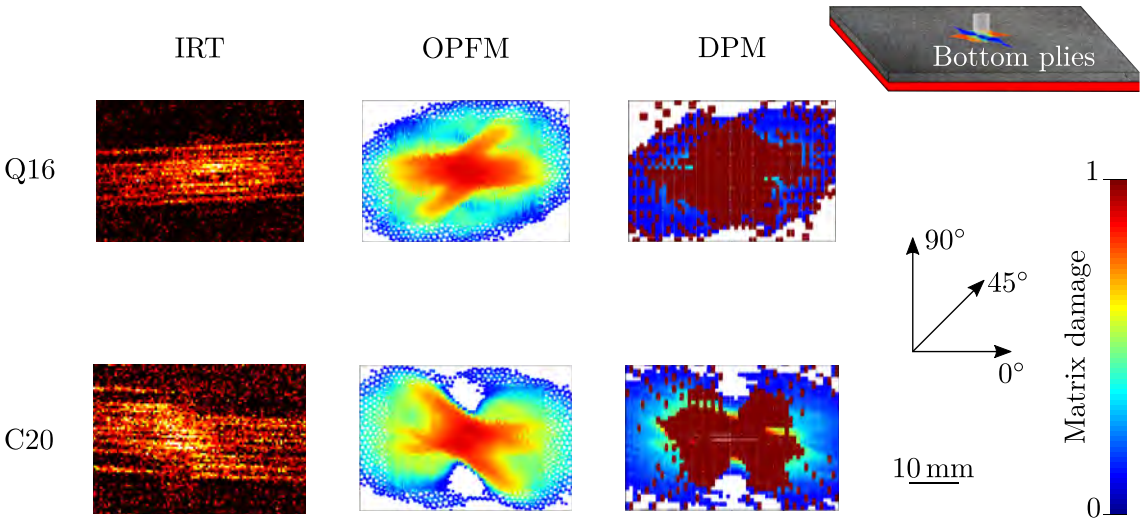

Figure 4.46: Comparison of the predicted matrix damages with the IRT thermal signatures for the Q16 and C20 laminates impacted at 20 J

Conclusion

This work was a part of an industrial research/development project called MARCOS 2 (Advanced modeling of the failure of laminated composites) with a consortium composed of Dassault Aviation, ONERA ICA, and ENPC. Due to the complex failure phenomenon encountered in laminated composite structures, the objective was to introduce the numerical modeling of each damage mechanism induced by a low-energy/low-velocity impact in the sizing of aeronautical composite structures. In this project, Dassault Aviation has defined two technical objectives assigned to ONERA:

- The first one was the understanding of the damage mechanisms induced by a quasi-static indentation or a low-energy/low-velocity impact test using enriched instrumentation;
- The second one was the modeling of the degradation mechanisms in composite laminates induced by QSI or a low-energy/low-velocity impact and the robust numerical implementation into a finite element code;

Thus, the present work balances between the experimental investigation of impact damages and the numerical modeling of a low-energy/low-velocity impact of a recent generation of carbon/epoxy composite laminates. Four chapters have been defined to meet the objectives.

The first chapter introduces the low-energy/low-velocity impact on composite laminates. Four sections have been identified to highlight the actual challenges. The first challenge is related to the damage tolerance of composite structures by industrial and how the substantiation is brought to the certification authorities. The actual industrial methodology and the associated technical issues have been dressed for the damage tolerance of composite structures subjected to a low-energy/low-velocity impact. It has shown that lengthy and costly experimental test campaigns are needed to perform abacus for the sizing of composite structures, and therefore, simulations are needed to design faster composite structures.
The second section presents a state-of-the-art of the actual works performed by academics in low-energy/low-velocity impact. These last decades, research on impact dynamics on composite laminates has enabled an understanding of the physical response during the impact event. The comprehension of the damage mechanisms is performed using *post mortem* analysis with destructive and non-destructive inspection means. Recently, the μ-tomography has opened new doorways in investigating impact damages thanks to the 3D character of the volume inspection. Moreover, thanks to the recent advancements in high-frequency acquisition, impact tests are more and more monitored by high-speed cameras (infrared and visible). Nevertheless, few studies are currently available to perform *in-situ* damage monitoring due

to the required sophisticated instrumentation.
The third section presents the damage modeling and the simulation of a low-energy /low-velocity impact using FEA. Several damage models with different approaches and complexities have been presented. The limitations of each modeling strategy have been discussed, especially for the CDM, where regularization methods are needed.
Finally, the last section briefly introduced the CAI test's experimental and numerical modeling to estimate the residual compression strength after an impact. To conclude, this chapter describes the actual state of the art of impact dynamics on laminated composites. It has shown the actual strengths and lacks in the experimental investigation and numerical modeling of impact damages. The research needs to be continued experimentally on the damage assessment and the establishment of the damage scenario for such complex materials. Numerically, the actual simulations have highlighted the complexity of developing damage models that efficiently simulate the damage mechanisms while mastering the model complexity. Thus, In the light of the current state of the art, the subsequent chapters tackle the current scientific issues.

Chapters 2, 3, and 4 present the scientific work performed during this work. Chapters 2 and 3 were dedicated to the experimental investigations of impact damage mechanisms. Chapter 2 has used the classical methodology for the damage assessment of two industrial laminates (Q16 and C20) made of a carbon/toughened epoxy UD plies. Physical impact responses and *post mortem* analysis have been carried out. Particular attention has been given to the segmentation of impact damages obtained from CT scans. Indeed, a deep learning approach has been used to segment the different damages within the laminate. The segmented damage extent has been obtained, giving precious information for the comparison with the numerical simulation results. The different *post mortem* controls have enabled an understanding of the damage mechanisms occurring in this specific material (with a high amount of fibre breaks in compression and delamination occurring inside the ply).

In chapter 3, the investigation of impact damages has been pushed further using damage monitoring. Four high-speed cameras have enriched the instrumentation of the impact experimental setup (two IR cameras and two visible cameras to perform DIC). The transverse displacement field obtained from DIC has highlighted the matrix splitting occurring on the rear face. The out-of-plane displacement obtained from DIC has shown that spurious out-of-plane displacements are introduced due to the experimental setup clearance. Moreover, it has been highlighted that the cameras must be isolated from the impact machine to avoid a measurement disruption induced by the stress wave propagation during the rebound phase. A special effort on the IR thermography was considered. The main objective was to link the different thermal signatures observed during the test with the different impact damage mechanisms. The thermal images have enabled a good understanding of the damage temporality occurring in such material. The TELOPS camera placed on the rear face has captured the thermal signature related to the different damages occurring near the surface. The other objective of this chapter was to study the strain rate effect for QSI loading. A comparison of the physical responses and the damaged

area obtained from CT scans has been conducted. Due to similar results, it has been concluded that this material could be considered insensitive to the strain rate effect. This chapter has enriched the comprehension of the mechanical degradation occurring in the studied material, especially considering the chronology of the damage events.

Chapter 4 deals with the modeling of the different damage mechanisms encountered in this material and the simulations using FEA. Two different damage models have been considered (OPFM developed at ONERA and DPM developed at ICA). A description of the two damage models has been firstl performed. As the DPM has been developed for decades with a particular focus on low-energy/low-velocity impact simulations, it has permitted to highlight some of the lacks in OPFM. Thus, a fibre break model with a phase-field approach and a damage coupling between the different damage mechanisms has been implemented in OPFM. These models consider two different frameworks. The first difference is related to the temporal discretization scheme, OPFM uses an implicit solver ($\alpha-$method) while DPM uses an explicit solver. The second difference is related to the material modeling approach, DPM uses a mesh-oriented strategy to perform discrete modeling of the matrix cracking, while OPFM uses a mesh with no bias, and a continuum damage law is considered for the matrix cracking modeling. Working with these two models has been an enriching experience allowing me to take a step back. The low-energy/low-velocity impact simulations have been performed for the Q16 and C20 laminates at each impact energy level. The comparisons were performed on the global responses, the projected damage, and at the ply/interface scale. The two models have simulated accurately impact damages.

Thanks to a complementarity between the enriched instrumentation and the *post mortem* analysis, this work has provided a deep understanding of the degradation mechanisms occurring in the recent carbon/epoxy toughened laminated composite material. It has revealed how complex the impact damages are with a strong interaction between each kind of damage. Based on the impact damage assessment and from the comparison with DPM, OPFM has been enhanced to accurately model this specific laminate's mechanical degradation. Additionally, the simulations of impact damages have been carried out with the two damage approaches proposed by DPM and OPFM. To conclude, the initial objectives have been fulfilled experimentally and numerically.

Due to the material architecture of composite laminates and the complexity of impact damages, researches need to be continued by the scientific community in both experimental and numerical modeling to express the strong potential of such material in the sizing of primary aeronautics structures.

Perspectives

Several experimental and numerical investigations were performed, validating the damage assessment and scenario for different stacking sequences and energy levels. Nevertheless, the lack of time for investigating new solutions or the complexity of the problem makes many questions unanswered. Thus, the experimental and numerical perspectives on the outcome of this work are presented below.

Experimental outlooks

Material identification

Different experimental tests have been defined in the MARCOS II experimental campaign to characterize the elastic and damaged behavior of the material under study. Classical out-of-plane tests (three-point flexural test, rotated flexural test, compact tension and compression test...) were not presented in this work as the results are currently being analyzed. The different studies are presented below.

Compressive behavior

As in-plane compression tests are difficult to perform, three-point and rotated flexural tests have been performed to characterize the compressive behavior of such material. These two tests have three objectives:

- Identification of the elastic properties;
- Identification of the strain onset of the fibre breaks in compression;
- Analysis of the damage mechanisms.

FIGURE 4.47 presents the experimental setup for the rotated flexural test, enriched instrumentation have been taken into consideration as performed in [Hamdi et al., 2021]. FIGURE 4.48 presents the first results obtained (the global responses and the fibre breaks in compression captured by the IR camera). The IR thermography highlights that fibre breaks occurred at the center of the sample, where the longitudinal strain is higher. Moreover, as the failure occurs near the center, it confirms that this experimental setup is efficient in avoiding the failure near the jaws. However, the longitudinal strain measured for the black cross is high (2.3× the value measured for the classical in-plane compression test). As presented in [Grandidier, 1991], the compressive failure is caused by local structural instability (i.e. micro-buckling of the fibres). This micro-buckling seems to be dependent on the state of the local curvature. Indeed, the enhancement of the compressive failure strain could be explained by the fibre buckling without breaking, thanks to the

local curvature. Further investigations need to be performed with different length sizes of the sample in order to evaluate the compressive failure strain as a function of the local curvature. Moreover, a *post mortem* investigation using micrographs observation must be performed to visualize the topology of the damages.

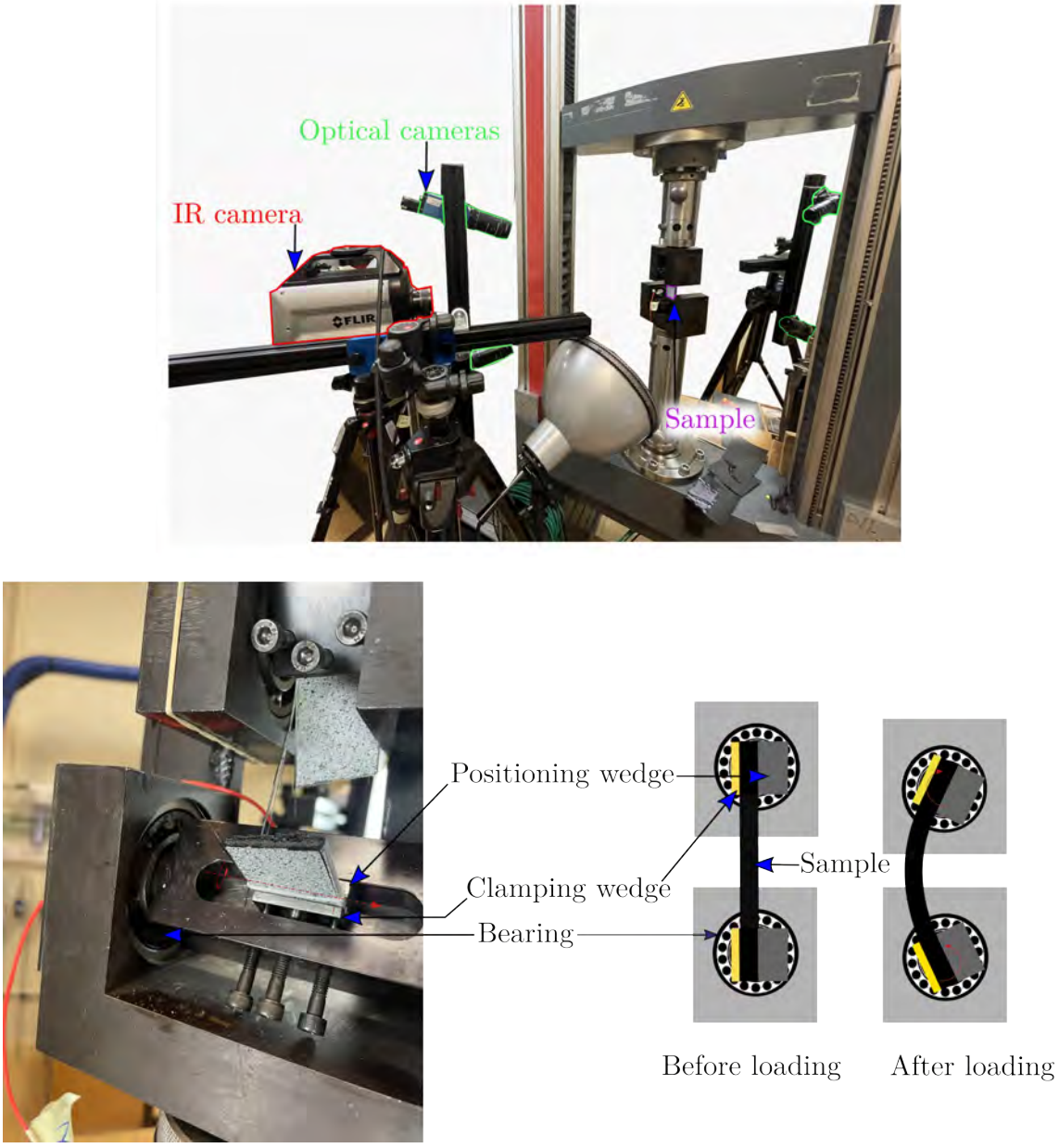

Figure 4.47: Rotated flexural experimental setup using an enriched instrumentation

Identification of the fibre fracture toughness in Mode I

The phase-field model for fibre failure in tension and in compression requires a material parameter which is fracture toughness. Due to the manufacturing and the machining of the samples, the test could not be performed earlier. Therefore, several impact simulations have been performed to fit the best value for (G_{Ic}) according to the load-displacement responses. The mode I fracture toughness (G_{Ic}) needs to be identified using compact tension and compact compression tests (CT, CC

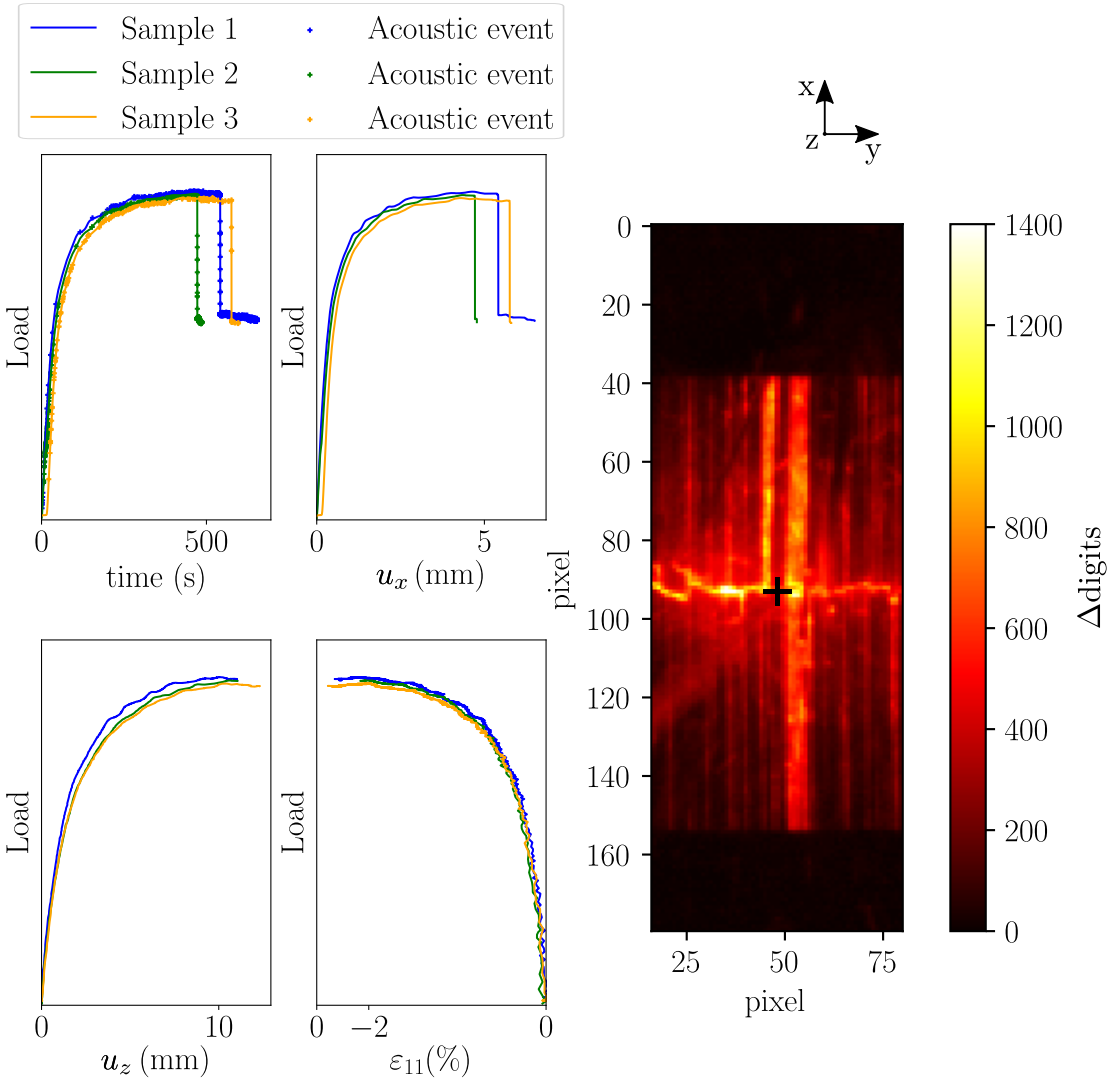

Figure 4.48: Global responses and thermal signature related to the fibre breaks in compression obtained from a rotated compression testing device for the C20 laminate

tests). FIGURE 4.49 presents the different samples for CC CT tests. The two faces are speckled to perform DIC. An IR camera has been used to track the thermal signature related to the fibre breaks. The fracture toughness will be calculated using the R-curves. Once identified, the fracture toughness (G_{Ic}) will be used as a material parameter in the phase-field model, and CC/CT tests will be simulated to calibrate the model. CT tests present irrelevant failure (FIGURE 4.49) and should be performed again soon.

Identification of the interfacial properties and analysis of the mechanical degradation

Interlaminar shear strength (ILSS) tests have been performed on different laminates (Q16, C20, $[0_{16}]$, $[90_{16}]$, and C40, a highly oriented 40 plies) to investigate the failure of the sample caused by the delamination and to identify the damage stresses threshold (σ_{13}^R, σ_{23}^R). As presented in FIGURE 4.50, this test is a three-point flexural test, however, the outer rollers are brought closer to minimize the flexural contribution. The failure is caused by the high out-of-plane shear stresses (σ_{13}, σ_{23}), which trigger

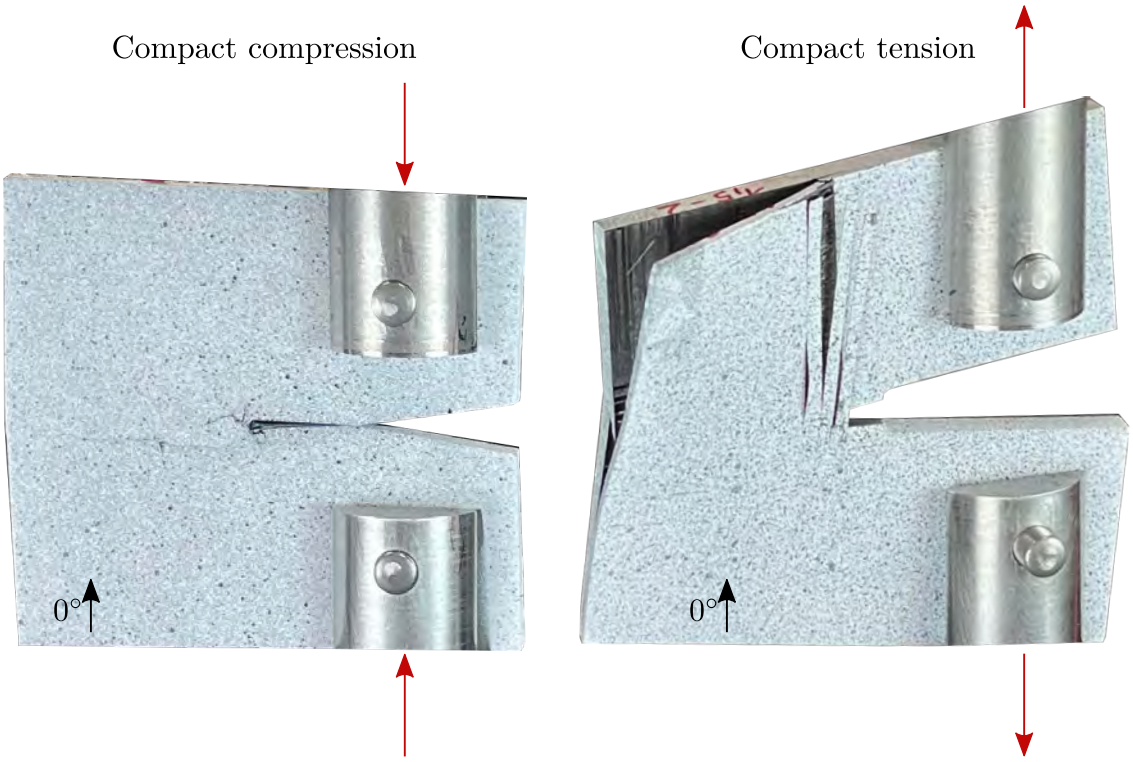

Figure 4.49: CC, CT tests performed at ONERA

the matrix cracking and the delamination. The enriched instrumentation (acoustic

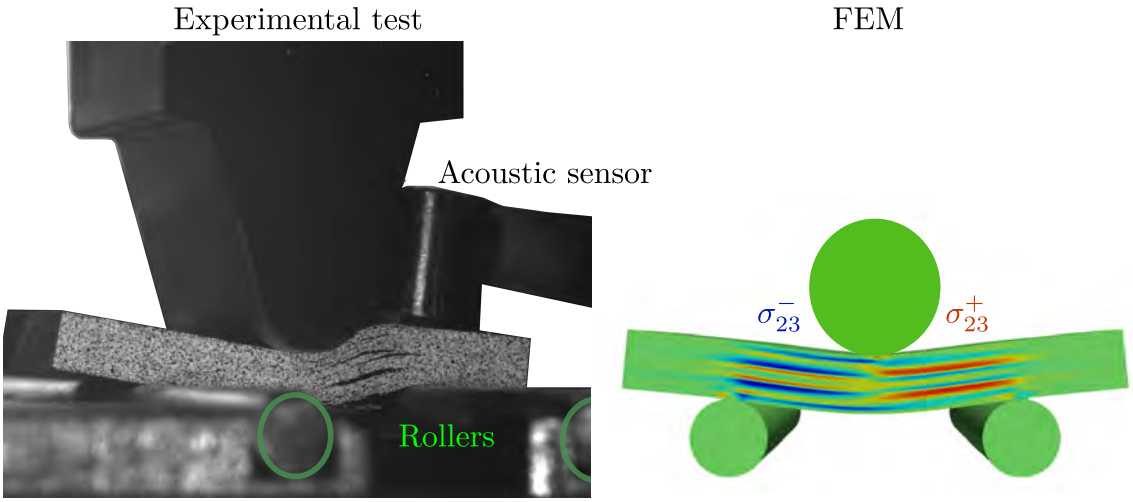

Figure 4.50: ILSS experimental setup performed on a Q16 laminate and compared with FEA

emission, DIC on the speckled face and an optical camera on the rear face) coupled with *post mortem* analysis (micrographs observations) will allow an understanding of the damage mechanisms and the damage coupling between matrix cracking and delamination. Moreover, these tests will allow calibrating the numerical coupling between the matrix cracking and the delamination.

As the interface toughness in mode II (G_{IIc}) is a crucial material parameter in impact simulations. Three-point end notched flexure (ENF) and four-point ENF

tests will be performed on symmetric laminates with an [0/0] interface and unsymmetrical laminates with an [0/45] interface to evaluate the influence of the mismatch angle on the G_{IIc}. The classical standard [Davies et al., 1998] requires an [0/0] interface, however the value of G_{IIc} obtained is not representative of the experimental conditions. Indeed, the delamination propagates between interfaces with different orientations. The value of the identified G_{IIc} will be used as a material parameter in the CZM.

Toward other Impact configurations

In this work, impact tests according to the standard [AST, 2007b] have been performed. However, in the MARCOS II project, other configurations have been defined with different impact window sizes (90×90 mm, 230×140 mm), impactor diameters (ϕ 40 mm), and impact locations. The results will be crossed to analyze the damage severity and the most constraining configurations. Figure 4.51 presents different impact configurations to evaluate the influence of the impact location on the projected damaged area obtained from C-scan. Dassault Aviation has performed those tests and the C-scan. The predictive capabilities of the models should be evaluated on those specific configurations.

Image processing in X-ray

As explained in chapter 2, it is difficult to establish the damage assessment using X-ray CT scans for higher impact energy levels as the sample is highly warped. Indeed, as shown in Figure 4.52, the orthogonal X-ray slice is not lined up with the ply due to the warped sample. Therefore, the X-ray slice contains multiple information from different plies/interfaces, which makes the understanding complex. A possible solution is to use a B-spline slice. The slice will follow the curvature described by the warped sample. Another possibility is based on ply detection as performed in [Ellison, 2020]. However, it is not easy to detect the ply due to the presence of damages. The user needs to perform several corrections and morphological operations. Figure 4.53 presents an example performed on a slice of a Q16 laminate impacted at 20 J. It can be observed that the ply detection works very well far from the damaged zone. Nevertheless, in presence of damages, detection is much more difficult. Coupled with deep learning, the ply detection will be easier as the segmented damaged pixels can be masked from the X-ray image.

Estimation of the residual compression strength

To establish design criteria, industrials perform CAI tests to estimate the residual strength. In the Marcos II project, four samples (two Q16 and two C20 laminates) have been impacted at 20, 35 J. Once impacted, the samples were tested using a CAI device according to the standard [AST, 2007a]. The tests have been instrumented using three optical cameras (two for DIC on the impacted face and one on the rear face), the two faces have been speckled. Moreover, an IR camera captured the thermal signature related to fibre breaks on the impacted face. An acoustic emission sensor has been used to detect the onset of damage. The results provided by the instrumentation will be analyzed in order to investigate the sample behavior until

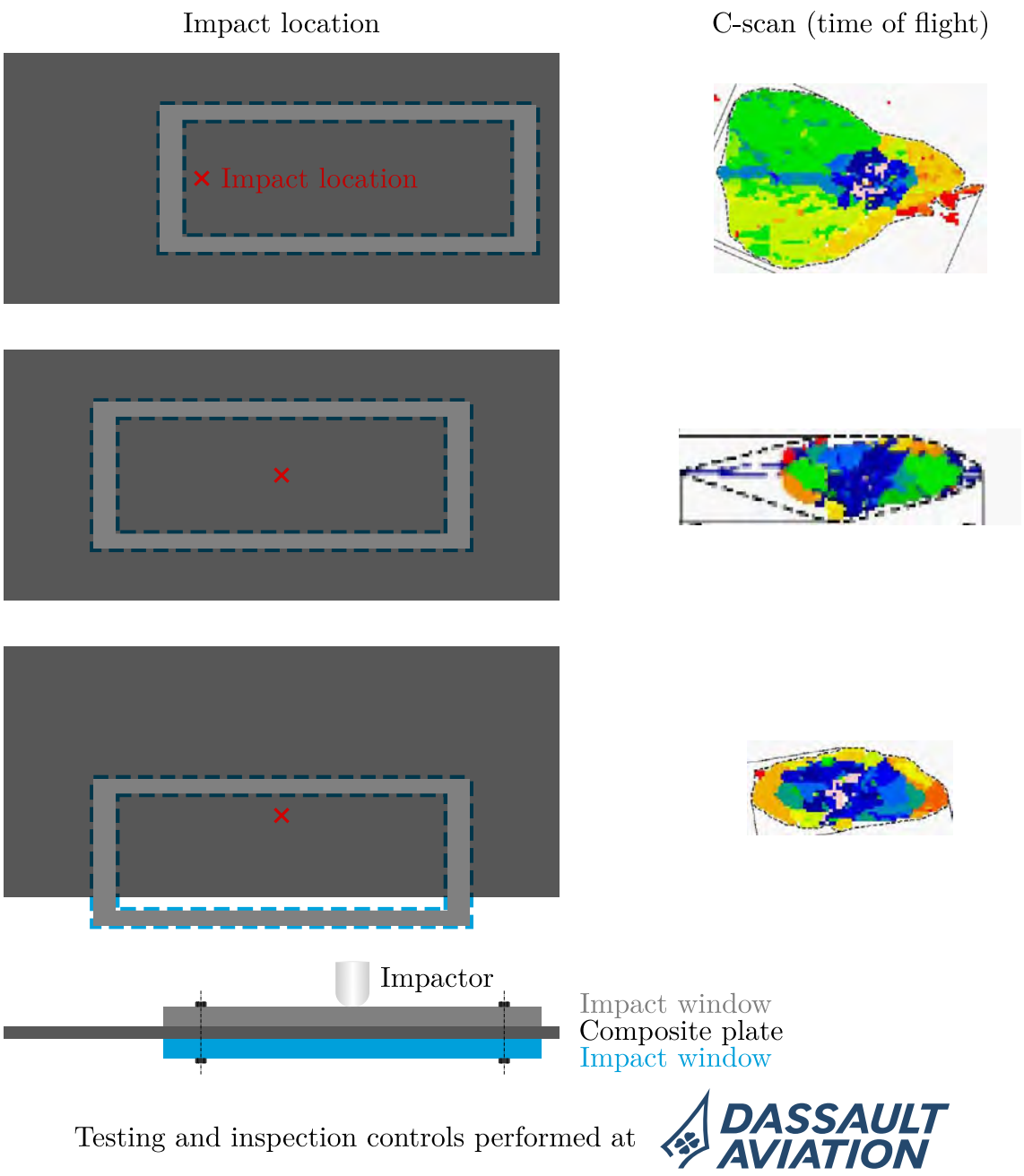

Figure 4.51: Impact tests performed with different impact locations at Dassault Aviation.

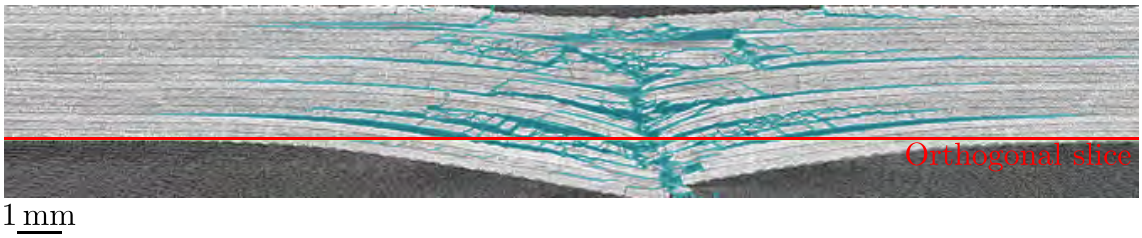

Figure 4.52: X-ray slice highlighting the warped sample through the thickness for the Q16 laminate impacted at 31.15 J

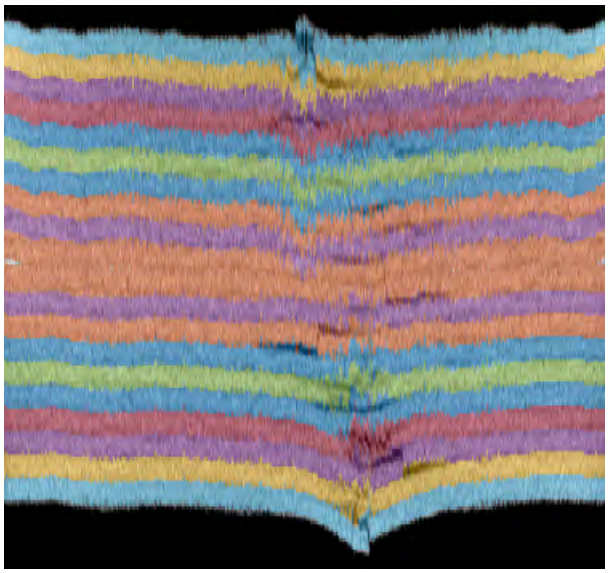

Figure 4.53: Ply detection for the Q16 laminate impacted at 20 J

the failure. FIGURE 4.54 presents the load-displacement response, the macroscopic failure observed on the impacted face, and the thermal signature related to fibre breaks for the C20 laminate impacted at 20 J.

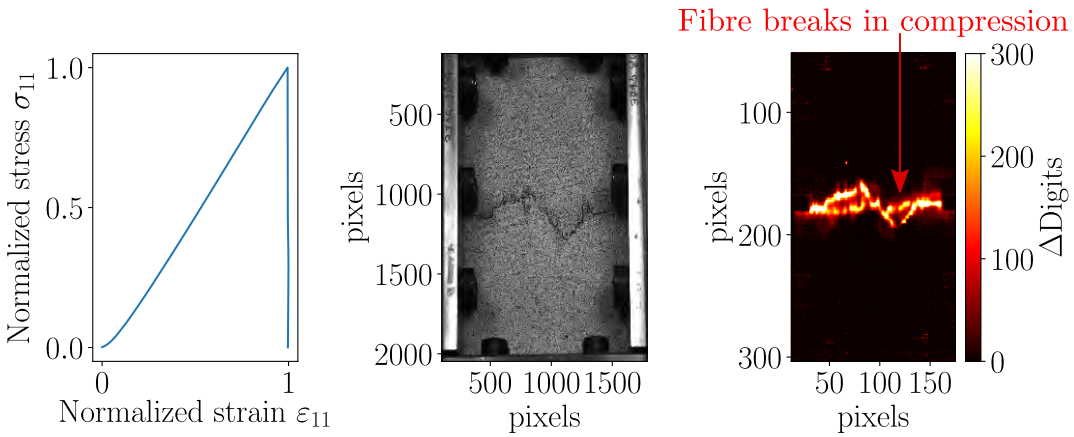

Figure 4.54: Load-time response, DIC and thermal images obtained on CAI test performed on the C20 laminate impacted at 35 J

Numerical outlooks

Material modeling

Advanced phase-field model with insensitive internal length

The initial phase-field models (AT1, AT2) establishes a dependency between the critical stress σ_c, the energy release rate G_c and the internal length ℓ (for instance $\sigma_c = \sqrt{\frac{3E_0G_c}{8\ell}}$ for AT1 in a 1D homogeneous case). By fixing σ_c and G_c, the internal

length ℓ is obtained. For some problems, the obtained internal length is not suitable with the mesh size. To overcome this issue, [Wu and Nguyen, 2018] have proposed other functions for the sharp crack topology α and the energetic degradation function $g(\phi)$ as presented below:

$$\begin{cases} z\alpha(\phi) = \xi + (1-\xi)\phi \\ g(\phi) = \dfrac{(1-\phi)^p}{(1-\phi)^p + a_1\phi P(\phi)} \end{cases} \quad \text{with } P(\phi) = 1 + a_2\phi + a_2a_3\phi^2 + \dots \tag{4.81}$$

Where ϕ is the damage variable, ξ, p, a_1, a_2 and a_3 are parameters. p and ξ are determined to ensure numerical stability. To overcome the dependence on the internal length, the critical stress σ_c is treated as an intrinsic material property, the parameter a_1 is calculated assuming ℓ as a numerical parameter. In this case, the failure stress σ_c and the softening law are independent of the internal length ℓ. The authors have simulated different tests cases by changing the internal length ℓ and the mesh size, they have shown that the failure stress and the dissipated energy remained unchanged. This point should be addressed in the future.

Matrix cracking using gradient damage model

The actual CDM for the matrix cracking modeling in OPFM is regularized using viscous damage law. The damage law becomes strain-rate dependent. As proposed in [Quintanas-Corominas et al., 2019], the phase-field could be also a good candidate for the modeling of matrix cracking. The anisotropy will be handled as for the fibre breaks using the framework of [Bleyer and Alessi, 2018]. However, the phase-field framework does not provide the freedom of defining damage laws depending on the ply thickness or the effect of the neighboring ply orientation. A non-standard framework for phase field approach can thus be proposed.

FEM

Domain decomposition using high-performance computing

The actual impact simulations using Zset are lengthy (3 weeks) for the highest impact energy (35 J). Introducing domain decomposition would save precious computational times. In [Rannou, 2022], simulations using phase-field of the transverse cracking on a ceramic composite using domain decomposition have been performed on significant meshes with a high amount of degrees of freedom. The domain decomposition has not been tried in our present study as the contact mechanics is not handled for now, but is currently considered at ONERA in another thesis.

CAI impact simulations

The simulation of impact damages have been performed for both models (DPM OPFM). The DPM can perform CAI simulations as shown in Figure 4.56. The evolution of the delamination is highlighted during the compressive loading for the C20 laminate impacted at 35 J. Consequently, the samples that have been tested in CAI will be simulated using DPM to evaluate the predictive capabilities in estimating the residual compression strength. Concerning OPFM, the definition of a CAI step will be the next task in the MARCOS II project.

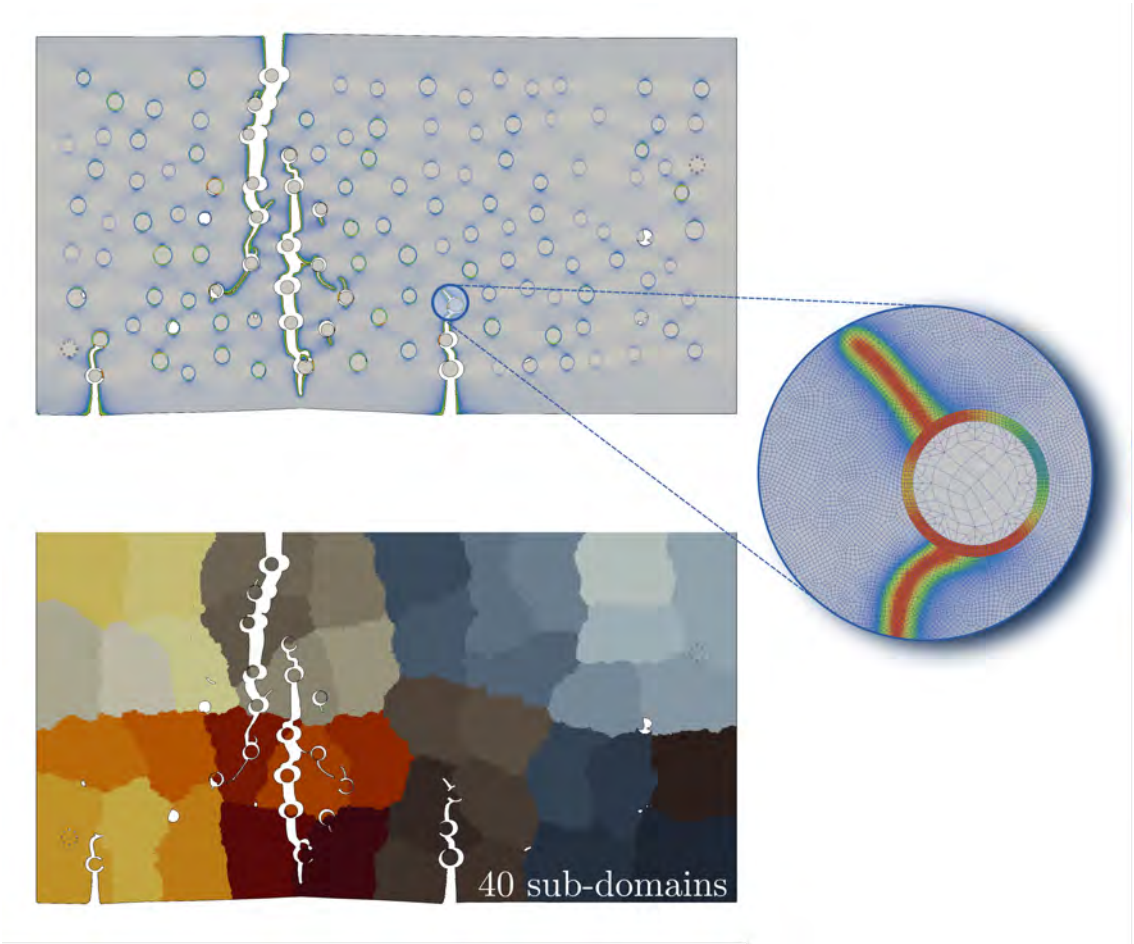

Figure 4.55: Matrix cracking using domain decomposition on a ceramic composite microstructure [Rannou, 2022]

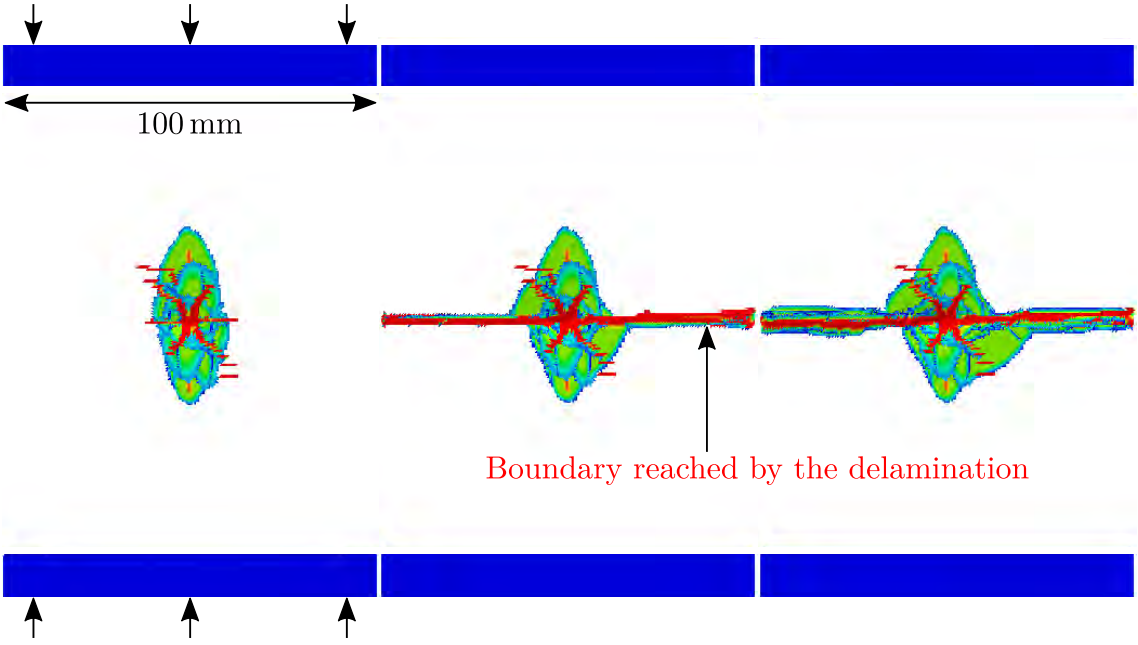

Figure 4.56: CAI simulations performed using DPM on the C20 laminate impacted at 35 J

Toward the simulations of substructures

The simulation of a LE/LV impact on a 150×100 mm sample has shown its difficulty with high computation resource needs. This is actually the critical limitation in virtual testing as the certification requires sweeping from the coupon to structure scale. Thus, the introduction of virtual testing for the simulation of large panels, substructures or even primary structures requires meshing strategies. Studies are actually performed on multiscale meshing ([Borakiewicz, 2021]) or other mesh strategies such as shell-volume element coupling to allow computational time saving.

Bibliography

[AST, 2007a] (2007a). Standard test method for compressive residual strength properties of damaged polymer matrix composite plates.

[AST, 2007b] (2007b). Standard test method for measuring the damage resistance of a fiber-reinforced polymer matrix composite to a drop-weight impact event.

[JPE, 2019] (2019). *Experimental Methods in Materials for Structural Impact Dynamics*.

[Abdulhamid et al., 2016] Abdulhamid, H., Bouvet, C., Michel, L., Aboissiere, J., and Minot, C. (2016). Numerical simulation of impact and compression after impact of asymmetrically tapered laminated cfrp. *International Journal of Impact Engineering*, 95:154–164.

[Abir et al., 2017] Abir, M., Tay, T., Ridha, M., and Lee, H. (2017). Modelling damage growth in composites subjected to impact and compression after impact. *Composite Structures*, 168:13–25.

[Abisset, 2012] Abisset, E. (2012). *Un mésomodèle d'endommagement des composites stratifiés pour le virtual testing : identification et validation*. PhD thesis. Doctorate thesis, Ecole normale supérieure Cachan.

[Abisset et al., 2016] Abisset, E., Daghia, F., Sun, X., Wisnom, M., and Hallett, S. (2016). Interaction of inter- and intralaminar damage in scaled quasi-static indentation tests: Part 1 – experiments. *Composite Structures*, 136:712–726.

[Action and Flores, 2018] Action, J. and Flores, M. (2018). Icme approach to compression strength after impact modeling. In *2018 AIAA/ASCE/AHS/ASC Structures, Structural Dynamics, and Materials Conference*, page 1899.

[Ahrens et al., 2005] Ahrens, J., Geveci, B., and Law, C. (2005). Paraview: An end-user tool for large data visualization. *The visualization handbook*, 717(8).

[Allix, 2013] Allix, O. (2013). The bounded rate concept: A framework to deal with objective failure predictions in dynamic within a local constitutive model. *International Journal of Damage Mechanics*, 22(6):808–828.

[Allix et al., 1994] Allix, O., Ladeveze, P., and Vittecoq, E. (1994). Modelling and identification of the mechanical behaviour of composite laminates in compression. *Composites science and technology*, 51(1):35–42.

[Aoki et al., 2007] Aoki, Y., Suemasu, H., and Ishikawa, T. (2007). Damage propagation in cfrp laminates subjected to low velocity impact and static indentation. *Advanced Composite Materials*, 16(1):45–61.

[Aymerich and Meili, 2000] Aymerich, F. and Meili, S. (2000). Ultrasonic evaluation of matrix damage in impacted composite laminates. *Composites Part B: Engineering*, 31(1):1–6.

[Aymerich and Priolo, 2008] Aymerich, F. and Priolo, P. (2008). Characterization of fracture modes in stitched and unstitched cross-ply laminates subjected to low-velocity impact and compression after impact loading. *International Journal of Impact Engineering*, 35(7):591–608. Eighth International Conference on Engineering Systems Design and Analysis (ESDA 2006).

[Badran et al., 2020] Badran, A., Marshall, D., Legault, Z., Makovetsky, R., Provencher, B., Piché, N., and Marsh, M. (2020). Automated segmentation of computed tomography images of fiber-reinforced composites by deep learning. *Journal of Materials Science*, 55(34):16273–16289.

[Baluch et al., 2019] Baluch, A. H., Falco, O., Jimenez, J. L., Tijs, B. H., and Lopes, C. S. (2019). An efficient numerical approach to the prediction of laminate tolerance to barely visible impact damage. *Composite Structures*, 225:111017.

[Bažant and Oh, 1983] Bažant, Z. P. and Oh, B. H. (1983). Crack band theory for fracture of concrete. *Matériaux et construction*, 16(3):155–177.

[Bazant and Pijaudier-Cabot, 1988] Bazant, Z. P. and Pijaudier-Cabot, G. (1988). Nonlocal continuum damage, localization instability and convergence. *Journal of Applied Mechanics*, 55(2):287–293.

[Benallal et al., 1993] Benallal, A., Billardon, R., and Geymonat, G. (1993). *Bifurcation and Localization in Rate-Independent Materials. Some General Considerations*, pages 1–44. Springer Vienna, Vienna.

[Berthe and Ragonet, 2018] Berthe, J. and Ragonet, M. (2018). Passive infrared thermography measurement of transverse cracking evolution in cross-ply laminates. *Strain*, 54(6):e12293.

[Berthelot, 1999] Berthelot, J.-M. (1999). *Matériaux composites*, volume 4. Editions Tec & Doc Paris, France.

[Bleyer and Alessi, 2018] Bleyer, J. and Alessi, R. (2018). Phase-field modeling of anisotropic brittle fracture including several damage mechanisms. *Computer Methods in Applied Mechanics and Engineering*, 336:213–236.

[Boccardi, 2017] Boccardi (2017). Infrared thermography to locate impact damage in thin and thicker carbon/epoxy panels. *Polymer Engineering & Science*, 57(7):657–664.

[Borakiewicz, 2021] Borakiewicz, E. (2021). *An adaptive multi-model approach for damage propagation simulations in large composite structures*. Doctorate thesis, université Paris-Saclay.

[Bourdin et al., 2008] Bourdin, B., Francfort, G. A., and Marigo, J.-J. (2008). The variational approach to fracture. *Journal of elasticity*, 91(1):5–148.

[Bouteiller, 2022] Bouteiller, P. (2022). *Simulation de la rupture des composites stratiés dans le cadre de modèle de plaques multicouches*. Doctorate thesis.

[Bouvet et al., 2009] Bouvet, C., Castanié, B., Bizeul, M., and Barrau, J.-J. (2009). Low velocity impact modelling in laminate composite panels with discrete interface elements. *International Journal of Solids and Structures*, 46(14-15):2809–2821.

[Bouvet et al., 2012] Bouvet, C., Rivallant, S., and Barrau, J.-J. (2012). Low velocity impact modeling in composite laminates capturing permanent indentation. *Composites Science and Technology*, 72(16):1977–1988.

[Bouvet et al., 2020] Bouvet, C., Serra, J., and Perez, P. G. (2020). Strain rate effect of mode ii interlaminar fracture toughness on the impact response of a thermoplastic peek composite. *Composites Part C: Open Access*, 2:100031.

[Bull et al., 2013] Bull, D., Helfen, L., Sinclair, I., Spearing, S., and Baumbach, T. (2013). A comparison of multi-scale 3d x-ray tomographic inspection techniques for assessing carbon fibre composite impact damage. *Composites Science and Technology*, 75:55–61.

[Bull et al., 2014] Bull, D., Scott, A., Spearing, S., and Sinclair, I. (2014). The influence of toughening-particles in cfrps on low velocity impact damage resistance performance. *Composites Part A: Applied Science and Manufacturing*, 58:47–55.

[Bull et al., 2015] Bull, D., Spearing, S., and Sinclair, I. (2015). Investigation of the response to low velocity impact and quasi-static indentation loading of particle-toughened carbon-fibre composite materials. *Composites Part A: Applied Science and Manufacturing*, 74:38–46.

[Camanho et al., 2013] Camanho, P., Bessa, M., Catalanotti, G., Vogler, M., and Rolfes, R. (2013). Modeling the inelastic deformation and fracture of polymer composites–part ii: Smeared crack model. *Mechanics of Materials*, 59:36–49.

[Camanho and Dávila, 2002] Camanho, P. P. and Dávila, C. G. (2002). Mixed-mode decohesion finite elements for the simulation of delamination in composite materials.

[Catalanotti et al., 2013] Catalanotti, G., Camanho, P., and Marques, A. (2013). Three-dimensional failure criteria for fiber-reinforced laminates. *Composite Structures*, 95:63–79.

[Catalanotti et al., 2017] Catalanotti, G., Furtado, C., Scalici, T., Pitarresi, G., Van Der Meer, F., and Camanho, P. (2017). The effect of through-thickness compressive stress on mode ii interlaminar fracture toughness. *Composite Structures*, 182:153–163.

[Chaboche et al., 2001] Chaboche, J. L., Feyel, F., and Monerie, Y. (2001). Interface debonding models: a viscous regularization with a limited rate dependency. *International journal of solids and structures*, 38(18):3127–3160.

[Chang and Chen, 1987] Chang, F.-K. and Chen, M.-H. (1987). The in situ ply shear strength distributions in graphite/epoxy laminated composites. *Journal of Composite Materials*, 21(8):708–733.

[Ciampa et al., 2018] Ciampa, F., Mahmoodi, P., Pinto, F., and Meo, M. (2018). Recent advances in active infrared thermography for non-destructive testing of aerospace components. *Sensors*, 18(2).

[Cui et al., 1994] Cui, W., Wisnom, M. R., and Jones, M. (1994). Effect of through thickness tensile and compressive stresses on delamination propagation fracture energy. *Journal of Composites, Technology and Research*, 16(4):329–335.

[Davies et al., 1998] Davies, P., Blackman, B. R. K., and Brunner, A. J. (1998). Standard Test Methods for Delamination Resistance of Composite Materials: Current Status. *Applied Composite Materials*, 5(6):345–364.

[DE BORST et al., 2022] DE BORST, R., SLUYS, L. J., MUHLHAUS, H., and PAMIN, J. (2022). Fundamental issues in finite element analyses of localization of deformation. *Engineering Computations*, 10(2):99–121.

[Desmorat et al., 2015] Desmorat, R., Gatuingt, F., and Jirásek, M. (2015). Nonlocal models with damage-dependent interactions motivated by internal time. *Engineering Fracture Mechanics*, 142:255–275.

[Deü, 1997] Deü, J.-F. (1997). *Rupture des composites stratifiés sous chargement dynamique: apport des méso-modèles avec endommagement retardé.* Doctorate thesis, Cachan, Ecole normale supérieure.

[Dragonfly, 2021] Dragonfly (2021). *Dragonfly 2021.1 [Linux software]. Object Research Systems (ORS) Inc, Montreal, Canada, 2021; software available at http://www.theobjects.com/dragonfly.*

[Ebina et al., 2018] Ebina, M., Yoshimura, A., Sakaue, K., and Waas, A. M. (2018). High fidelity simulation of low velocity impact behavior of cfrp laminate. *Composites Part A: Applied Science and Manufacturing*, 113:166–179.

[Elias, 2015] Elias, A. (2015). *Nocivité des défauts induits par impact pour les structures composites tissées 3D à matrice organique.* Doctorate thesis.

[Ellison, 2020] Ellison, A. C. (2020). *Segmentation of X-ray CT and Ultrasonic Scans of Impacted Composite Structures for Damage State Interpretation and Model Generation.* PhD thesis.

[Falcó et al., 2022] Falcó, O., Lopes, C., Sommer, D., Thomson, D., Ávila, R., and Tijs, B. (2022). Experimental analysis and simulation of low-velocity impact damage of composite laminates. 287:115278.

[Feng and Aymerich, 2014] Feng, D. and Aymerich, F. (2014). Finite element modelling of damage induced by low-velocity impact on composite laminates. *Composite Structures*, 108:161–171.

[Flores et al., 2017] Flores, M., Mollenhauer, D., Runatunga, V., Beberniss, T., Rapking, D., and Pankow, M. (2017). High-speed 3d digital image correlation of low-velocity impacts on composite plates. *Composites Part B: Engineering*, 131:153–164.

[Flores, 2016] Flores, M. D. (2016). *Damage tolerance and assessment of unidirectional carbon fiber composites: an experimental and numerical study.*

[Francfort and Marigo, 1998] Francfort, G. A. and Marigo, J.-J. (1998). Revisiting brittle fracture as an energy minimization problem. *Journal of the Mechanics and Physics of Solids*, 46(8):1319–1342.

[Gao et al., 2007] Gao, F., Jiao, G., Lu, Z., and Ning, R. (2007). Mode ii delamination and damage resistance of carbon/epoxy composite laminates interleaved with thermoplastic particles. *Journal of composite materials*, 41(1):111–123.

[García-Rodríguez et al., 2018] García-Rodríguez, S., Costa, J., Bardera, A., Singery, V., and Trias, D. (2018). A 3d tomographic investigation to elucidate the low-velocity impact resistance, tolerance and damage sequence of thin non-crimp fabric laminates: effect of ply-thickness. *Composites Part A: Applied Science and Manufacturing*, 113:53–65.

[GarciPerez, 2018] GarciPerez, P. (2018). *Méthodologie expérimentale et numérique pour la tenue résiduelle post impact des structures composites à matrice thermoplastique.* Doctorate thesis, Ecole nationale supérieure d'arts et métiers - ENSAM.

[Geers et al., 1998] Geers, M., De Borst, R., Brekelmans, W., and Peerlings, R. (1998). Strain-based transient-gradient damage model for failure analyses. *Computer methods in applied mechanics and engineering*, 160(1-2):133–153.

[Germain, 2020] Germain, J. (2020). *Évaluation des capacités prédictives d'un modèle avancé pour la prévision de la tenue de plaques stratifiées perforées.* Doctorate thesis, Université Paris-Saclay.

[Germain, 2006] Germain, N. (2006). *Modélisation non locale de l'endommagement dans les structures composites.* PhD thesis, École Nationale Supérieure des Mines de Paris.

[González et al., 2018] González, E. V., Maimí, P., Martín-Santos, E., Soto, A., Cruz, P., De La Escalera, F. M., and de Aja, J. S. (2018). Simulating drop-weight impact and compression after impact tests on composite laminates using conventional shell finite elements. *International Journal of Solids and Structures*, 144:230–247.

[Grandidier, 1991] Grandidier, J.-C. (1991). *Compression et microflambage dans les matériaux composites à fibres longues.* Doctorate thesis, Université Paul Verlaine - Metz.

[Hallett et al., 2009] Hallett, S., Green, B., Jiang, W., and Wisnom, M. (2009). An experimental and numerical investigation into the damage mechanisms in notched composites. *Composites Part A: Applied Science and Manufacturing*, 40(5):613–624.

[Hamdi et al., 2021] Hamdi, K., Moreau, G., and Aboura, Z. (2021). Digital image correlation, acoustic emission and in-situ microscopy in order to understand composite compression damage behavior. *Composite Structures*, 258:113424.

[Hashin, 1980] Hashin, Z. (1980). Failure Criteria for Unidirectional Fiber Composites. *Journal of Applied Mechanics*, 47(2):329–334.

[Hawyes et al., 2001] Hawyes, V., Curtis, P., and Soutis, C. (2001). Effect of impact damage on the compressive response of composite laminates. *Composites Part A: Applied Science and Manufacturing*, 32(9):1263–1270.

[Hempe, 2010] Hempe, D. W. (2010). Ac 20-107b advisory circular composite aircraft structure. Technical report, 0-Advisory U.S. Department of Transportation Circular Federal Aviation Administration.

[Hillerborg et al., 1976] Hillerborg, A., Modéer, M., and Petersson, P.-E. (1976). Analysis of crack formation and crack growth in concrete by means of fracture mechanics and finite elements. *Cement and concrete research*, 6(6):773–781.

[Hongkarnjanakul et al., 2013] Hongkarnjanakul, N., Bouvet, C., and Rivallant, S. (2013). Validation of low velocity impact modelling on different stacking sequences of cfrp laminates and influence of fibre failure. *Composite Structures*, 106:549–559.

[Hou et al., 2001] Hou, J., Petrinic, N., and Ruiz, C. (2001). A delamination criterion for laminated composites under low-velocity impact. *Composites Science and Technology*, 61(14):2069–2074.

[Hsieh et al., 2010] Hsieh, T., Kinloch, A., Masania, K., Taylor, A., and Sprenger, S. (2010). The mechanisms and mechanics of the toughening of epoxy polymers modified with silica nanoparticles. *Polymer*, 51(26):6284–6294.

[Hughes, 2012] Hughes, T. J. (2012). *The finite element method: linear static and dynamic finite element analysis*. Courier Corporation.

[Iarve et al., 2011] Iarve, E. V., Gurvich, M. R., Mollenhauer, D. H., Rose, C. A., and Dávila, C. G. (2011). Mesh-independent matrix cracking and delamination modeling in laminated composites. *International journal for numerical methods in engineering*, 88(8):749–773.

[J.Michael Pereira, 2010] J.Michael Pereira, Gary D. Roberts, C. R. R. (2010). Experimental techniques and for evaluating and the effects and of aging and on impact and high strain and rate properties and of triaxial and braided composite and materials. Technical report, NASA/TM—2010-216763 TP 3188.

[Joel P Johnston, 2017] Joel P Johnston, J Michael Pereira, C. R. R. (2017). High speed thermal imaging on ballistic impact of triaxially braided composites. Technical report, NASA Glenn Research Center.

[Ju, 1989] Ju, J. (1989). On energy-based coupled elastoplastic damage theories: constitutive modeling and computational aspects. *International Journal of Solids and structures*, 25(7):803–833.

[Kenane and Benzeggagh, 1997] Kenane, M. and Benzeggagh, M. (1997). Mixed-mode delamination fracture toughness of unidirectional glass/epoxy composites under fatigue loading. *Composites Science and Technology*, 57(5):597–605.

[Krueger et al., 2013] Krueger, R., Shivakumar, K. N., and Raju, I. S. (2013). Fracture mechanics analyses for interface crack problems - a review.

[Ladeveze, 1992] Ladeveze, P. (1992). A damage computational method for composite structures. *Computers & Structures*, 44(1-2):79–87.

[Ladevèze et al., 2017] Ladevèze, P., Néron, D., and Bainier, H. (2017). *A Virtual Testing Approach for Laminated Composites Based on Micromechanics*, pages 667–698. Springer International Publishing, Cham.

[Laurin et al., 2013] Laurin, F., Carrere, N., Huchette, C., and Maire, J. (2013). A multiscale hybrid approach for damage and final failure predictions of composite structures. *Journal of composite materials*, 47(20-21):2713–2747.

[Le et al., 2018] Le, M. Q., Bainier, H., Néron, D., Ha-Minh, C., and Ladevèze, P. (2018). On matrix cracking and splits modeling in laminated composites. *Composites Part A: Applied Science and Manufacturing*, 115:294–301.

[Lemaitre et al., 2020] Lemaitre, J., Chaboche, J.-L., Benallal, A., and Desmorat, R. (2020). *Mécanique des matériaux solides-3e éd.* Dunod.

[Li et al., 2008] Li, X., Hallett, S. R., and Wisnom, M. R. (2008). Predicting the effect of through-thickness compressive stress on delamination using interface elements. *Composites Part A: Applied Science and Manufacturing*, 39(2):218–230.

[Lin et al., 2020] Lin, S., Thorsson, S. I., and Waas, A. M. (2020). Predicting the low velocity impact damage of a quasi-isotropic laminate using est. *Composite Structures*, 251:112530.

[Liu et al., 2018] Liu, H., Falzon, B. G., and Tan, W. (2018). Predicting the compression-after-impact (cai) strength of damage-tolerant hybrid unidirectional/woven carbon-fibre reinforced composite laminates. *Composites Part A: Applied Science and Manufacturing*, 105:189–202.

[Liu et al., 2020] Liu, H., Liu, J., Ding, Y., Zheng, J., Kong, X., Zhou, J., Harper, L., Blackman, B. R. K., Kinloch, A. J., and Dear, J. P. (2020). The behaviour of thermoplastic and thermoset carbon fibre composites subjected to low-velocity and high-velocity impact. *Journal of Materials Science*, 55(33):15741–15768.

[Liv et al., 2017] Liv, Y., Guillamet, G., Costa, J., González, E., Marín, L., and Mayugo, J. (2017). Experimental study into compression after impact strength of laminates with conventional and nonconventional ply orientations. *Composites Part B: Engineering*, 126:133–142.

[Lopes et al., 2016] Lopes, C., Sádaba, S., González, C., Llorca, J., and Camanho, P. (2016). Physically-sound simulation of low-velocity impact on fiber reinforced laminates. *International Journal of Impact Engineering*, 92:3–17.

[Maierhofer et al., 2019] Maierhofer, C., Krankenhagen, R., and Röllig, M. (2019). Application of thermographic testing for the characterization of impact damage during and after impact load. *Composites Part B: Engineering*, 173:106899.

[Maierhofer et al., 2014] Maierhofer, C., Myrach, P., and Reischel, M. (2014). Characterizing damage in cfrp structures using flash thermography in reflection and transmission configurations. *Composites Part B: Engineering*, 57:35–46.

[Maimí et al., 2007] Maimí, P., Camanho, P. P., Mayugo, J., and Dávila, C. (2007). A continuum damage model for composite laminates: Part i–constitutive model. *Mechanics of materials*, 39(10):897–908.

[Maimi et al., 2008] Maimi, P., Mayugo, J., and Camanho, P. (2008). A three-dimensional damage model for transversely isotropic composite laminates. *Journal of Composite Materials*, 42(25):2717–2745.

[Manseri, 2020] Manseri, L. (2020). *Développement d'une stratégie d'endommagement intra/interlaminaire pour une approche semi-continue: application aux stratifiés unidirectionnels et hybrides*. PhD thesis.

[McElroy et al., 2017] McElroy, M., Jackson, W., Olsson, R., Hellström, P., Tsampas, S., and Pankow, M. (2017). Interaction of delaminations and matrix cracks in a cfrp plate, part i: A test method for model validation. *Composites Part A: Applied Science and Manufacturing*, 103:314–326.

[McQuien et al., 2020] McQuien, J. S., Hoos, K. H., Ferguson, L. A., Iarve, E. V., and Mollenhauer, D. H. (2020). Geometrically nonlinear regularized extended finite element analysis of compression after impact in composite laminates. *Composites Part A: Applied Science and Manufacturing*, 134:105907.

[Médeau, 2019] Médeau, V. (2019). *Rupture des composites tissés 3D: de la caractérisation expérimentale à la simulation robuste des effets d'échelle*. PhD thesis, Institut Supérieur de l'Aéronautique et de l'Espace.

[Meola and Boccardi, 2018] Meola, C. and Boccardi, S. (2018). A quantitative approach to retrieve delamination extension from thermal images recorded during impact tests. *NDT & E International*, 100:142–152.

[Miehe et al., 2015] Miehe, C., Schänzel, L.-M., and Ulmer, H. (2015). Phase field modeling of fracture in multi-physics problems. part i. balance of crack surface and failure criteria for brittle crack propagation in thermo-elastic solids. *Computer Methods in Applied Mechanics and Engineering*, 294:449–485.

[Mollenhauer et al., 2020] Mollenhauer, D., Iarve, E., Hallett, S., Putthanarat, S., and Li, X. (2020). *Application of Discrete Damage Modeling to Laminated Composite Overheight Compact Tension Specimens*.

[Olsson, 2000] Olsson, R. (2000). Mass criterion for wave controlled impact response of composite plates. *Composites Part A: Applied Science and Manufacturing*, 31(8):879–887.

[Otsu, 1979] Otsu, N. (1979). A threshold selection method from gray-level histograms. *IEEE transactions on systems, man, and cybernetics*, 9(1):62–66.

[Parvizi and Bailey, 1978] Parvizi, A. and Bailey, J. E. (1978). On multiple transverse cracking in glass fibre epoxy cross-ply laminates. *Journal of Materials Science*, 13(10):2131–2136.

[Peerlings et al., 1996] Peerlings, R. H., de Borst, R., Brekelmans, W. M., and de Vree, J. (1996). Gradient enhanced damage for quasi-brittle materials. *International Journal for numerical methods in engineering*, 39(19):3391–3403.

[Pijaudier-Cabot and Bažant, 1987] Pijaudier-Cabot, G. and Bažant, Z. P. (1987). Nonlocal damage theory. *Journal of engineering mechanics*, 113(10):1512–1533.

[Pijaudier-Cabot and Mazars, 2001] Pijaudier-Cabot, G. and Mazars, J. (2001). Damage Models for Concrete. In Lemaitre, J., editor, *Handbook of Materials Behavior Models*, volume 2 of *Failures of materials*, pages 500–512. Elsevier.

[Pinho et al., 2006] Pinho, S., Iannucci, L., and Robinson, P. (2006). Physically based failure models and criteria for laminated fibre-reinforced composites with emphasis on fibre kinking. part ii: Fe implementation. *Composites Part A: Applied Science and Manufacturing*, 37(5):766–777.

[Poh and Sun, 2017] Poh, L. H. and Sun, G. (2017). Localizing gradient damage model with decreasing interactions. *International Journal for Numerical Methods in Engineering*, 110(6):503–522.

[Priasso, 2017] Priasso, V. (2017). *Modélisation multi-échelle de l'endommagement des composites stratifiés avec intercouches.* Doctorate thesis. Thèse de doctorat de l'université Paris-Saclay 2017.

[Puck and Schürmann, 2002] Puck, A. and Schürmann, H. (2002). Failure analysis of frp laminates by means of physically based phenomenological models. *Composites science and technology*, 62(12-13):1633–1662.

[Quintanas-Corominas et al., 2019] Quintanas-Corominas, A., Reinoso, J., Casoni, E., Turon, A., and Mayugo, J. (2019). A phase field approach to simulate intralaminar and translaminar fracture in long fiber composite materials. *Composite Structures*, 220:899–911.

[Ranatunga et al., 2019] Ranatunga, V., Crampton, S. M., and Jegley, D. C. (2019). Impact damage tolerance of composite laminates with through-the-thickness stitches. In *AIAA Scitech 2019 Forum*, page 1045.

[Rannou, 2022] Rannou, Przybyla, p. B. (2022). Simulation par champ de phase de la rupture transverse d'un cmc à l'échelle microscopique. In *Proceedings CSMA 2022 15ème Colloque National en Calcul des Structures.*

[Rivallant et al., 2014a] Rivallant, S., Bouvet, C., Abi Abdallah, E., Broll, B., and Barrau, J.-J. (2014a). Experimental analysis of cfrp laminates subjected to compression after impact: The role of impact-induced cracks in failure. *Composite Structures*, 111:147–157.

[Rivallant et al., 2014b] Rivallant, S., Bouvet, C., Abi Abdallah, E., Broll, B., and Barrau, J.-J. (2014b). Experimental analysis of cfrp laminates subjected to compression after impact: The role of impact-induced cracks in failure. *Composite Structures*, 111:147–157.

[Rivallant et al., 2013a] Rivallant, S., Bouvet, C., and Hongkarnjanakul, N. (2013a). Failure analysis of cfrp laminates subjected to compression after impact: Fe simulation using discrete interface elements. *Composites Part A: Applied Science and Manufacturing*, 55:83–93.

[Rivallant et al., 2013b] Rivallant, S., Bouvet, C., and Hongkarnjanakul, N. (2013b). Failure analysis of cfrp laminates subjected to compression after impact: Fe simulation using discrete interface elements. *Composites Part A: Applied Science and Manufacturing*, 55:83–93.

[Ronneberger et al., 2015] Ronneberger, O., Fischer, P., and Brox, T. (2015). U-net: Convolutional networks for biomedical image segmentation. In *International Conference on Medical image computing and computer-assisted intervention*, pages 234–241. Springer.

[Sasikumar et al., 2019] Sasikumar, A., Costa, J., Trias, D., González, E., García-Rodríguez, S., and Maimí, P. (2019). Unsymmetrical stacking sequences as a novel approach to tailor damage resistance under out-of-plane impact loading. *Composites Science and Technology*, 173:125–135.

[Schneider et al., 2012] Schneider, C. A., Rasband, W. S., and Eliceiri, K. W. (2012). NIH Image to ImageJ: 25 years of image analysis. *Nature Methods*, 9(7):671–675.

[Song et al., 2018] Song, K., Leone, F. A., and Rose, C. A. (2018). Analysis of progressive damage in cross-ply and quasi-isotropic panels subjected to quasi-static indentation. In *AIAA Science and Technology Forum and Exposition*, number NF1676L-27401.

[Soto et al., 2018a] Soto, A., González, E., Maimí, P., De La Escalera, F. M., De Aja, J. S., and Alvarez, E. (2018a). Low velocity impact and compression after impact simulation of thin ply laminates. *Composites Part A: Applied Science and Manufacturing*, 109:413–427.

[Soto et al., 2018b] Soto, A., González, E., Maimí, P., Mayugo, J., Pasquali, P., and Camanho, P. (2018b). A methodology to simulate low velocity impact and compression after impact in large composite stiffened panels. *Composite Structures*, 204:223–238.

[Spronk et al., 2018] Spronk, S., Kersemans, M., De Baerdemaeker, J., Gilabert, F., Sevenois, R., Garoz, D., Kassapoglou, C., and Van Paepegem, W. (2018). Comparing damage from low-velocity impact and quasi-static indentation in automotive carbon/epoxy and glass/polyamide-6 laminates. *Polymer Testing*, 65:231–241.

[Sun and Hallett, 2017] Sun, X. and Hallett, S. (2017). Barely visible impact damage in scaled composite laminates: Experiments and numerical simulations. 109:178–195.

[Sun and Hallett, 2018] Sun, X. and Hallett, S. (2018). Failure mechanisms and damage evolution of laminated composites under compression after impact (cai): Experimental and numerical study. *Composites Part A: Applied Science and Manufacturing*, 104:41–59.

[Sun et al., 2016] Sun, X., Wisnom, M., and Hallett, S. (2016). Interaction of inter-and intralaminar damage in scaled quasi-static indentation tests: Part 2–numerical simulation. *Composite Structures*, 136:727–742.

[Tabiei and Tanov, 2000] Tabiei, A. and Tanov, R. (2000). A nonlinear higher order shear deformation shell element for dynamic explicit analysis:: Part i. formulation and finite element equations. *Finite Elements in Analysis and Design*, 36(1):17–37.

[Thorsson et al., 2018] Thorsson, S. I., Waas, A. M., and Rassaian, M. (2018). Low-velocity impact predictions of composite laminates using a continuum shell based modeling approach part a: Impact study. *International Journal of Solids and Structures*, 155:185–200.

[Trousset, 2013] Trousset, E. (2013). *Prévision des dommages d'impact basse vitesse et basse énergie dans les composites à matrice organique stratifiés*. PhD thesis, Ecole nationale supérieure d'arts et métiers-ENSAM.

[Turon et al., 2010] Turon, A., Camanho, P., Costa, J., and Renart, J. (2010). Accurate simulation of delamination growth under mixed-mode loading using cohesive elements: Definition of interlaminar strengths and elastic stiffness. *Composite Structures*, 92(8):1857–1864.

[Turon et al., 2007] Turon, A., Davila, C. G., Camanho, P. P., and Costa, J. (2007). An engineering solution for mesh size effects in the simulation of delamination using cohesive zone models. *Engineering fracture mechanics*, 74(10):1665–1682.

[van der Walt et al., 2014] van der Walt, S., Schönberger, J. L., Nunez-Iglesias, J., Boulogne, F., Warner, J. D., Yager, N., Gouillart, E., Yu, T., and contributors, t. s.-i. (2014). scikit-image: image processing in Python. *PeerJ*, 2:e453.

[Vandellos, 2011] Vandellos, T. (2011). *Développement d'une stratégie de modélisation du délaminage dans les structures composites stratifiées*. Doctorate thesis.

[Wagih et al., 2016a] Wagih, A., Maimí, P., Blanco, N., and Costa, J. (2016a). A quasi-static indentation test to elucidate the sequence of damage events in low velocity impacts on composite laminates. *Composites Part A: Applied Science and Manufacturing*, 82:180–189.

[Wagih et al., 2019] Wagih, A., Maimí, P., Blanco, N., García-Rodríguez, S., Guillamet, G., Issac, R., Turon, A., and Costa, J. (2019). Improving damage resistance and load capacity of thin-ply laminates using ply clustering and small mismatch angles. *Composites Part A: Applied Science and Manufacturing*, 117:76–91.

[Wagih et al., 2016b] Wagih, A., Maimí, P., González, E., Blanco, N., de Aja, J. S., de la Escalera, F., Olsson, R., and Alvarez, E. (2016b). Damage sequence in thin-ply composite laminates under out-of-plane loading. *Composites Part A: Applied Science and Manufacturing*, 87:66–77.

[Wronkowicz-Katunin et al., 2019] Wronkowicz-Katunin, A., Katunin, A., and Dragan, K. (2019). Reconstruction of barely visible impact damage in composite structures based on non-destructive evaluation results. *Sensors*, 19(21).

[Wu and Nguyen, 2018] Wu, J.-Y. and Nguyen, V. P. (2018). A length scale insensitive phase-field damage model for brittle fracture. *Journal of the Mechanics and Physics of Solids*, 119:20–42.

Prévision des endommagements induits par un impact basse vitesse/basse énergie au sein de matériaux composites stratifiés carbone-epoxy de dernière génération

Résumé

En aéronautique, les composites stratifiés sont aujourd'hui largement utilisés pour la fabrication de structures primaires, telles que les ailes et les fuselages. Ces structures doivent être tolérantes aux dommages d'impact car de nombreuses menaces en vitesse sont possibles durant le cycle de vie de l'aéronef. La certification de ces structures est basé sur des campagnes d'essais expérimentales longues et coûteuses en raison de l'utilisation de critères phénoménologiques pour le dimensionnement dans l'industrie.

Par conséquent, ce travail consiste en une étude expérimentale et numérique du comportement et de la résistance d'une nouvelle génération de matériaux composites carbone/époxy avec une interface renforcée soumis à un impact faible vitesse/faible énergie. L'objectif principal de ces travaux porte sur le développement d'un modèle robuste capable de prévoir la réponse de composites stratifiés sous impact, en se basant sur des observations expérimentales précises. Des essais expérimentaux sur des plaques stratifiées ont été réalisés avec des méthodes d'instrumentation avancées (telles que la thermographie infrarouge et la corrélation d'images numériques associées à des caméras rapides) pour suivre l'évolution des endommagements en temps réels. De plus, des méthodes d'évaluation non destructives en 3D (tomographie à rayons X, balayage ultrasonique) ont été réalisées afin d'évaluer et de comprendre les mécanismes d'endommagement dans ce matériau spécifique. En parallèle, un modèle éléments finis 3D d'impact à solveur implicite a été développé et prend en compte les contacts (impacteur/composite et montage/composite), la non-linéarité géométrique, la fissuration transverse à l'aide d'un modèle d'endommagement continu, le délaminage en utilisant des éléments cohésifs et la rupture des fibres en considérant une approche de type champ de phase. Une attention particulière a été accordée aux couplages entre les différents mécanismes d'endommagement et de rupture, qui ont été observés expérimentalement.

Mots clés: Résistance aux chocs des composites stratifiés - Modèle d'endommagement appliqués aux matériaux composites - Comportement des composites stratifiés

---

Prediction of low-velocity/low-energy impact damage in the latest generation of carbon-epoxy laminated composites

Abstract

In aeronautics, laminated composites are now widely used for the manufacture of primary structures, such as wings and fuselages. These structures must be tolerant to impact damage as many impact threats are possible during the life cycle of the aircraft. The certification of these structures is based on lengthy and costly experimental test campaigns due to the use of phenomenological criteria for sizing in the industry.

Therefore, this work consists of an experimental and numerical study on the behavior and strength of a new generation of carbon/epoxy composite materials with reinforced interface subjected to a low-velocity/low-energy impact. The main objective of this work is to develop a robust model capable of predicting the response of laminated composites under impact, based on accurate experimental observations. Experimental tests on laminated plates have been carried out with advanced instrumentation methods (such as infrared thermography and digital image correlation associated with fast cameras) to follow the evolution of damage in real time. In addition, non-destructive 3D evaluation methods (X-ray tomography, ultrasonic scanning) have been performed to evaluate and understand the damage mechanisms in this specific material. In parallel, an impact model has been developed and consists in a 3D finite element model using an implicit solver, which takes into account contacts (impactor/composite and set-up/composite), geometrical nonlinearity, transverse cracking thanks to a continuum damage model, delamination using cohesive elements and fibre failure considering a phase-field approach. A special attention has been paid to the couplings between the different damage and failure mechanisms, which have been clearly experimentally observed.

Keywords: Impact on composite structures - Damage modeling of composites - Behavior of laminated composites.

ONERA
THE FRENCH AEROSPACE LAB

ONERA - BP 80100 - 91123 PALAISEAU CEDEX - Tél. : +33 1 80 38 60 60 - Fax : +33 1 80 38 65 10

www.onera.fr